High-Temperature Scanning Indentation (HTSI) : Compréhension des essais de nanoindentation lors des transformations physiques de matériaux métalliques à haute température

Gabrielle Tiphene

To cite this version:

Gabrielle Tiphene. High-Temperature Scanning Indentation (HTSI) : Compréhension des essais de nanoindentation lors des transformations physiques de matériaux métalliques à haute température. Autre. Ecole Centrale de Lyon, 2023. Français. NNT : 2023ECDL0008 . tel-04117610

HAL Id: tel-04117610
https://theses.hal.science/tel-04117610
Submitted on 5 Jun 2023

Numero d'ordre NNT : 2023ECDL0008 Année 2023

Thèse de doctorat

Présentée pour l'obtention du titre de

Docteur de **L'Ecole Centrale de Lyon**

membre de l'**Université de Lyon**

Spécialité **Mécanique**

Mention **Mobilité Internationale**

Ecole doctorale MEGA
Mécanique - énergétique - génie civil - acoustique

Par

Gabrielle Tiphéne

High-Temperature Scanning Indentation (HTSI)
Compréhension des essais de nanoindentation lors des transformations physiques de matériaux métalliques à haute température

High-Temperature Scanning Indentation (HTSI)
Understanding nanoindentation testing during physical transformations of metallic materials at high temperature

---

Soutenue publiquement le 1er mars 2023 devant le jury d'examen composé de :

Sandra Korte-Kerzel	Professeur	RWTH Aachen University	Rapporteure
George M. Pharr	Professeur	Texas A&M University	Rapporteur
Brigitte Bacroix	DR CNRS	LSPM - USPM	Présidente
Muriel Braccini	CR CNRS	SIMaP - Université de Grenoble	Examinatrice
Warren C. Oliver	Docteur	KLA Corporation	Examinateur
Gaylord Guillonneau	MDC	LTDS - ECL	Co-encadrant
Guillaume Kermouche	Professeur	LGF - EMSE	Co-directeur
Jean-Luc Loubet	DR CNRS	LTDS - ECL	Directeur
Jean-Michel Bergheau	Professeur	LTDS - ECL	Invité

"I never lose. I either win or learn."

Nelson Mandela

"I have not failed. I've just found 10,000 ways that won't work."

Thomas A. Edison

Abstract

This manuscript presents an investigation of the mechanical properties of materials during a thermal cycle, using instrumented nanoindentation.

Following previous studies, the research focuses on designing a new indentation technique to measure the mechanical properties of materials with temperature quasi-continuously. The present developments give more information about the behavior of materials in temperature, along with its changes.

The High-Temperature Scanning Indentation (HTSI) method has been implemented during this work. It is based on a one-second indentation cycle applied all along a thermal cycle. Such an in-situ technique allows computing the mechanical properties quasi-continuously in temperature. A one-day experiment (approximately 1000 indents) gives access to the Young's modulus, the hardness, and the creep properties of the specimen on a large temperature scale. Through the changes of those properties with temperature, one can study the modifications taking place in the materials.

Thanks to the HTSI method, the creep properties of CaF_2 single crystals and pure polycrystalline silver were investigated in temperature. From the creep activation energy and activation volume, it becomes possible to determine the deformation mechanisms happening in the samples depending on temperature. Moreover, with the equivalence between time and temperature, the materials' behaviors at different strain rates can be anticipated.

One can also focus on the microstructure modifications occurring in metals with temperature. The variations of the mechanical properties of pure cold-rolled copper and aluminum during thermal cycles allow detecting two restoration phenomena: static recovery and recrystallization. A simple analytic model is proposed to predict the changes induced by those phenomena in the materials. It enables characterizing the kinetics of the studied phenomena thanks to a few HTSI experiments. One can then predict the final microstructure of the materials whatever the applied thermal cycle.

Finally, this local-scale analysis method allows characterizing thin film metallic glasses (TFMG). The variations in mechanical properties make it possible to determine the transition temperatures characteristic of the glass (glass transition, brittle-to-ductile transition). The superplastic behaviors of the supercooled-liquid zone can also be studied. Once the temperature is high enough, the crystallization process of the glass is observed. With complimentary High-Temperature X-ray Diffraction (HT-XRD) experiments, the changes in mechanical properties may be linked with the mechanisms taking place during the crystallization.

Keywords: Nanoindentation, High-Temperature, Mechanical properties, Creep, Metals, Restoration kinetics, Thin-film, Metallic glass

Résumé

Dans l'industrie, un matériau est sélectionné pour ces propriétés (mécaniques, physiques, etc.) répondant le mieux pour une application donnée. Dans le cas d'applications en température, ces propriétés ainsi que la structure des matériaux peuvent évoluer. Il devient donc nécessaire de caractériser correctement ces propriétés à la température de travail du matériau, à l'échelle de ces changements structuraux. Les récents développements de l'indentation instrumentée permettent maintenant de déterminer les propriétés mécaniques (module de Young, dureté, propriétés de fluage) des matériaux à l'échelle du micromètre, de l'ambiante à 1000 °C.

Néanmoins, les essais usuels de nanoindentation tels que les essais CSM (mesure continue de la raideur), les essais de fluage ou ceux de relaxation sont chronophages puisqu'ils nécessitent plusieurs minutes voire plusieurs heures pour réaliser un essai. Comme établir l'équilibre thermique à la température de test prend généralement quelques dizaines de minutes, il est difficile de réaliser plus d'une dizaine d'essais à une température donnée sur une journée. De fait, caractériser les propriétés d'un matériau sur une large gamme de température peut prendre plusieurs semaines.

De plus, la structure du matériau peut également changer en température. Ces évolutions vont impacter les propriétés mécaniques du matériau. Pour bien déterminer de tels changements, il est nécessaire d'avoir accès à suffisamment de données. Les essais d'indentations classiques, de par leur temps de mise en œuvre, ne permettent de ne caractériser que des évolutions du matériau lentes par rapport au temps d'essai.

L'objectif du présent travail est d'utiliser la méthode de nanoindentation instrumentée pour caractériser de tels changements en température. La réalisation de tels essais passe par le développement d'une nouvelle méthode de nanoindentation permettant de déterminer rapidement les propriétés des matériaux et leurs variations lors de rampes en température. Les travaux proposés dans ce manuscrit présentent cette nouvelle approche : la méthode dite de High-Temperature Scanning Indentation (HTSI) est ainsi développée. Appliquée à différents matériaux (matériaux métalliques amorphes ou cristallins, céramiques), elle permet d'obtenir rapidement ces propriétés ainsi que les changements structuraux des différents matériaux en température.

Le premier chapitre présente l'état de l'art sur plusieurs sujets. Nous nous concentrerons tout

d'abord sur l'essai de nanoindentation à l'ambiante et la détermination du module de Young, de la dureté ainsi que des propriétés viscoplastiques. Se pose ensuite la question de son adaptation pour la haute température. En effet, l'environnement de test (équilibre thermique du système, vide, etc.) doit être bien maitrisé pour permettre la bonne réalisation des essais. Le choix du matériau de la pointe est également critique pour caractériser les propriétés du matériau à haute température. En effet, du fait de l'augmentation en température, celle-ci peut être dégradée (oxydation, réaction avec le matériau à tester, etc.).
Nous aborderons ensuite l'impact de la température sur deux types de matériaux : les métaux cristallins et les verres métalliques. Dans le cas des métaux cristallins, la température induit des phénomènes de modifications structurales, impactant les propriétés mécaniques du matériau. Dans le cadre de ce manuscrit, nous nous limiterons à l'étude des phénomènes de restauration statique et de recristallisation de ces matériaux. Nous nous pencherons ensuite sur les verres métalliques. Du fait de leur structure amorphes, ces matériaux présentent un grand intérêt pour l'industrie : leurs propriétés mécaniques, anti-corrosion, etc. sont souvent plus intéressantes que celles de leur pendant cristallin. Néanmoins, la température impacte également leurs propriétés et leur structure (ce sont des matériaux thermodynamiquement métastables). Ils présentent en effet différentes transitions en température du fait de leur structure de verre (transition vitreuse, transition fragile/ductile). Il devient donc intéressant de caractériser ces différents matériaux en température et à l'échelle locale pour mieux étudier tous ces changements.

Le deuxième chapitre de ce manuscrit s'intéresse en détails au développement de la méthode d'indentation High-Temperature Scanning Indentation (HTSI), utilisée pour ces travaux. Nous commencerons par nous intéresser au cycle d'indentation utilisé. Ce cycle de 1 seconde permet d'obtenir rapidement le module d'Young, la dureté et les propriétés de fluage du matériau étudié. Il est basé sur une charge rapide (0.5 s) en demi-sinus suivi d'un maintien de la charge (de 0.1 s à 0.3 s) puis d'une décharge rapide par paliers (0.2 s). Du fait de sa vitesse, les problématiques liées à la dérive thermique sont limitées lors de la réalisation de cet essai. Il est ainsi possible de l'appliquer non seulement pendant un maintien isotherme du système mais également pendant les phases de chauffage et de refroidissement. Cela permet de déterminer quasi-continument les propriétés mécaniques des matériaux sur une large gamme de température avec une unique rampe en température. Une unique journée d'expérience donne ainsi accès aux propriétés du matériau.
Afin de vérifier la validité des résultats obtenus par cette méthode, des essais ont été réalisés sur différents matériaux. De la silice fondue a été caractérisée de l'ambiante à 350 °C, du cuivre pur, de l'ambiante à 600 °C et de l'aluminium pur de l'ambiante à 325 °C. Ces différents essais ont permis de vérifier que la méthode donnait bien accès au module d'Young, à la dureté et aux propriétés de fluage attendus pour les matériaux étudiés, sur les gammes de température étudiées.

Dans le troisième chapitre, la méthode HTSI est utilisée pour caractériser les propriétés de fluage des matériaux. En effet, cette méthode est facile à implémenter en température, contrairement

aux méthodes plus classiques (essais de fluage et de relaxation en indentation) qui nécessitent plusieurs heures pour être réalisées en température. Cependant, ces méthodes donnent accès aux propriétés de fluage du matériau sur une large gamme de vitesse de déformation, ce que ne permet pas notre méthode.
On étudie ici deux matériaux : la céramique monocristalline $\mathrm{CaF_2}$ et l'argent pur polycristallin. Grâce à l'équivalence entre le temps et la température observée sur ces deux matériaux, il est possible d'utiliser la méthode HTSI pour caractériser le comportement en fluage de ces matériaux à haute température ou à faible vitesse de déformation. De plus, en déterminant des paramètres caractéristiques du fluage (énergie d'activation, volume d'activation, etc.), il est également possible de s'intéresser aux mécanismes de déformations prenant place lors du fluage du matériau en fonction de la température et de la vitesse de déformation.

Dans le quatrième chapitre, l'objectif est de caractériser les changements de microstructure dans les métaux pendant un cycle en température en utilisant la méthode HTSI. Via les évolutions de la dureté du cuivre pur, on peut observer la recristallisation du matériau. Quand nous appliquons cette méthode à de l'aluminium pur, nous pouvons observer la restauration statique du matériau, suivi par sa recristallisation. Ces observations ont été confirmées par des essais EBSD (Electron Back-Scattering Diffraction) post-mortem.
Un modèle analytique simple est proposé pour quantifier les cinétiques de ces phénomènes. En caractérisant les paramètres de ce modèle, il devient possible de prédire les évolutions de la microstructure des matériaux étudiés grâce à quelques essais HTSI bien pensés.

Dans le dernier chapitre, nous nous intéressons à l'étude en température des verres métalliques ZrCu en couches minces. En appliquant la méthode HTSI, nous obtenons l'évolution de la dureté et des propriétés de fluage en température. Via leurs changements, nous pouvons détecter des températures caractéristiques du matériau (transition ductile-fragile, transition vitreuse). Les résultats obtenus sont cohérents avec les mesures DSC effectués.
Il est également possible étudier la zone superplastique du matériau ainsi que la cristallisation du verre. Grâce à des essais complémentaires de diffraction des rayons-X en température (HT-XRD) sur ces matériaux, il est possible de proposer un mécanisme de cristallisation du matériau.

Ces travaux présentent un fort intérêt pour la caractérisation de matériau à l'échelle locale en température. Avec le développement de la méthode HTSI, il est de fait possible de caractériser très rapidement sur une large gamme de température les propriétés mécaniques (module de Young, dureté, propriétés de fluage) des matériaux. Avec des vitesses de chauffage de quelques degrés par minute, on obtient ainsi une valeur de ces propriétés tous les degrés sur la gamme étudiée. Aux regards du temps nécessaire pour déterminer aussi finement ces évolutions avec des essais classiques, nous avons ici un énorme avantage technique pour caractériser nos matériaux.

Une telle méthode permet l'étude de différents matériaux. Si nous nous intéressons au $\mathrm{CaF_2}$,

nous pouvons caractériser ses propriétés de fluage sur une large gamme de température. Cela nous donne accès aux mécanismes régissant le fluage sur la gamme de température étudié, nous permettant ainsi d'expliquer les variations de propriétés mécaniques observées avec la vitesse de déformation.

De plus, les essais réalisés sur argent pur montrent l'importance de l'état de surface pour caractériser ces propriétés. Ajoutés aux changements de microstructure observés, ils compliquent l'interprétation des résultats.

Néanmoins, l'obtention d'une courbe maîtresse du fluage pour ces deux matériaux permet d'utiliser l'équivalence temps-température pour caractériser plus facilement, avec des essais haute température, l'impact de la vitesse de déformation sur le matériau. Il est même possible d'étudier des états correspondants à de très basses vitesses de déformations, difficilement caractérisables expérimentalement, en réalisant des essais à très haute température.

En s'intéressant à l'évolution de la dureté du cuivre pur initialement déformé lors d'un cycle thermique complet, cette méthode permet de caractériser la cinétique de recristallisation du matériau. En prenant en compte les évolutions anisothermes de la température lors du cycle, un modèle simple a été proposé pour quantifier cette cinétique.

Ce modèle peut être enrichi grâce à l'étude d'aluminium pur déformé. Ce dernier voit sa microstructure évoluée du fait de la recristallisation mais également de la restauration statique. Nous observons même l'impact de ce phénomène sur la cinétique de recristallisation, ainsi que celui de l'état de déformation initial.

Grâce à de tels essais, il devient possible de prédire les évolutions de la structure des matériaux avec un nombre restreint d'essais HTSI bien paramétrés. Cela peut grandement intéresser le domaine du développement de nouveaux matériaux. Nous pouvons également envisager d'utiliser cette technique pour mieux comprendre le comportement de matériaux mal connus.

Enfin, les essais sur verres métalliques en couches minces montrent l'intérêt d'une telle technique pour caractériser les matériaux amorphes et leurs évolutions en température. En effet, cette technique permet de déterminer des évolutions du verre très différente (transition vitreuse, cristallisation). D'autre part elle présente un fort intérêt pour l'étude des films minces : ces matériaux nécessitent des méthodes de caractérisation locales, ce que cette technique permet.

Keywords: Nanoindentation, Haute-Température, Propriétés mécaniques, Fluage, Métaux, Cinétiques de restauration, Films minces, Verres métalliques

Remerciements

Ces travaux de recherche ont été réalisés au sein du groupe COMpréhension des Phénomènes Élémentaires en Tribologie du Laboratoire de Tribologie et de Dynamique des Systèmes, situé à l'École Centrale de Lyon.

Je tiens tout d'abord à remercier mes directeurs de thèse pour la confiance qui m'a été accordée tous aux longs de ces 3 ans et demi. Cette confiance m'a permis de mener doucement ma barque dans une direction qui m'intéressait particulièrement. Nul doute que je continuerai dans les années à venir.

Je commencerais par toi, Jean-Luc, pour toutes nos discussions scientifiques sur mon sujet et bien au-delà. Comme tu le dis souvent : *La thèse c'est une aventure. La destination importe peu, c'est le voyage qui compte !*. C'est particulièrement vrai, nous nous sommes élancés vers des terres inconnues, nous avons essuyé une crise mondiale réduisant les échanges avec le monde scientifique et puis nous avons finalement décidé de complètement changer de voie après quelques temps. C'est grâce à ta confiance en mes capacités que je continue de prendre conscience de ce que je peux apporter au monde qui nous entoure.

Ensuite j'aimerais te remercie Guillaume, pour ton enthousiasme dès que je te présentais de nouveaux résultats. Cela paraît peu mais cela m'a permis de voir au-delà de mes données et de comprendre que ce que nous avons mis en place en trois ans est extrêmement intéressant pour le monde académique et industriel. Merci également de ton implication et ton soutien lorsque j'avais des petites baisses de morale suite à des résultats pas très compréhensibles. Et enfin, merci d'avoir eu confiance en moi en sortie du cycle ICM et de fait d'avoir donné mon nom à Jean-Luc pour que je puisse postuler sur cette thèse.

Enfin, merci à toi Gaylord pour nos discussions scientifiques et tes questions qui m'ont poussées à aller plus loin sur de nombreux sujets. Merci également pour ton aide sur les essais sur les verres métalliques, qui nous ont confirmé qu'on ne comprenait pas du tout ce que l'on avait mesuré…

Je souhaiterais également remercier Jean-Michel pour les échanges que nous avons eu, notamment sur les questions de thermique du nanoindenteur.

Je souhaiterais ensuite remercier les membres de mon jury. Merci à George M. Pharr et Sandra Korte-Kerzel pour avoir rapporté avec soin mon manuscrit, ainsi que pour vos questions très intéressantes lors de ma soutenance. Votre intérêt pour mes travaux est une véritable récompense. De même je remercie Brigitte Bacroix, Muriel Braccini et Warren C. Oliver pour vous être déplacés à l'Ecole centrale de Lyon lors de ma soutenance. Nos échanges soulignent bien l'intérêt de nombreuses communautés pour ces travaux et les nombreux axes de développements possibles. Voir son travail reconnu et apprécié par ses pairs est d'une grande importance pour la jeune chercheuse que je suis.

Je souhaiterais continuer en te remerciant Paul, pour m'avoir accueillie et formée sur le nanoindenteur à chaud. A peine arrivée, nous commencions déjà à voir des effets très intéressants à étudier. Merci aussi à toi Solène, tu es arrivée en nous proposant une étude sur un verre métallique, matériau que je ne connaissais pas du tout. Et nous sommes parties à faire de longues sessions d'essais pour mieux comprendre. Très clairement, certains essais restent encore très obscurs.

Je voudrais ensuite remercier particulièrement Warren C. Oliver pour m'avoir invité à venir passer 3 mois à KLA Corporation dans le Tennessee au printemps 2022 et Bryan Crawford pour avoir gérer toute la partie administrative, rendant ce séjour possible malgré les difficultés liées au Covid-19 qui rendaient les voyages à l'international compliqués. Ce séjour m'a permis de m'immerger dans un environnement scientifique différent et d'appréhender d'autres problématiques. Je tiens à remercier mes collègues rencontrés durant ce séjour (Warren, Marc, Bryan, Kurt, Jacob, Jennifer, Doral) pour leur accueil très chaleureux lors de mon arrivée et sur toute la durée de mon séjour.

Je souhaiterais ensuite remercier mes collègues des Mines de Saint-Etienne, notamment Jolan pour l'accueil au labo en temps de Covid-19. Merci tout particulièrement à Gilles Blanc pour son aide pour préparer mes échantillons (notamment pour les EBSD). Cette étape pas si simple est primordiale pour obtenir des résultats exploitables par la suite. Encore une fois merci. De même, merci à Maryline Mondon pour la réalisation des cartographies EBSD de mes échantillons. Enfin, merci à tous les collègues et notamment les doctorants Yvan, Lisa, Mathieu, Maxence, Maxime, Aubin G., Quentin, Sarah, Emeline, Jeanne, Maydine, Morgan et Jolan, pour l'accueil et les échanges que nous avons eu les rares dois où je suis venue vous déranger aux Mines.

Merci également à mes collègues de Centrale Lyon pour leur accueil durant ces trois années. Je tiens à remercier Sylvie, Hélène et Elodie pour leur aide sur toutes les questions administratives à gérer pour partir en conf ou autres. Et merci à Sophie pour son aide lors des essais sur l'argent. Merci également à Emmanuel, Manuel, Fred, Clotilde Joël et Alain pour les moments sympas de discussions au coin café après déjeuner ou les sorties pour prendre un ou plusieurs verres (on se souviendra du repas choucroute et de ces 10 viandes).

Merci à Camille, Youness, Karl, Thibaut, Paul, Mariana, Cristobal et Amal pour votre accueil au 4ième de la nouvelle doctorante que j'étais alors. On ne s'est pas forcément beaucoup croisé hors du labo au début mais votre bonne humeur et nos échanges au coin café me suivront longtemps.
Et à Adrien, Antoine A. Antoine N. et Victor, copains du 4ième, vous avec qui j'ai traversé ces trois années de thèse durant lesquelles nous avons tous avancés tant bien que mal. La période Covid aura clairement marquée nos thèses mais ne nous aura pas empêcher de passer des bons moments ensemble au coin café, au bar ou en WE (avec quelques estropiés parfois).
Une pensée également aux doctorants et stagiaires que j'ai vu arriver et parfois repartir : Vito, Chloé, Valentin (tu l'aura ta bourse de thèse, j'en suis sûre !), Héloïse, Samuel, Alexandre, Rémi. Bon courage à tous pour vos futurs projets !

Une pensée pour Yvan et Sébastien : on a commencé et vécu nos thèses ensemble. Je prends un peu d'avance en soutenant mais je ne doute pas que vous me suivrez sous peu !
Merci aux anciens mineurs Bastien, Aubin G. et Florian, discuter de tous et de rien de temps en temps est toujours agréable. Une pensée toute particulière pour Victor, parti bien trop tôt.
Merci également à Yvan, Sébastien, Arnauld, Alexandre, Maxence, Alexandre, Mathilde, les anciens du club de jeux de société des Mines. Les soirées jeux online et les semaines de vacances jeux sont toujours un plaisir.
Merci à Lucile, Martin, Murielle, Léa, Blanche, Malorie, Daphné, Julie, Marie-Claude. C'est toujours un plaisir de vous revoir même si la vie nous emmène dans des directions différentes.
Merci enfin à ma famille, notamment mes parents, mon frère et ma sœur pour votre soutien toutes ses années.

Notations and symbols

Constant

k_B	Boltzmann's constant	$1.380649 \times 10^{-23}\,\mathrm{J\,K^{-1}}$
N_A	Avogadro's constant	$6.02214076 \times 10^{23}\,\mathrm{mol^{-1}}$
R	Universal gas constant	$8.314\,462\,618\,\mathrm{J\,mol^{-1}\,K^{-1}}$

Material's properties

ν_D	Debye frequency	Hz
T_g	Glass transition temperature (polymer, glass)	°C
T_m	Melting temperature	°C
ν	Poisson ratio	
E	Young's modulus	GPa
G	Shear modulus	GPa
b	Burger's vector	nm
η	Work hardening rate	
m	Strain rate sensitivity	

Tip's properties

ν_{ind}	Poisson ratio of the tip	
E_{ind}	Young's modulus of the tip	GPa
θ	Conical equivalent angle	°
h_0	Tip defect	nm

Indentation parameters

t	time	min
T	Temperature	°C

F	Applied force in a nanoindentation test	mN
u	Measured raw displacement in a nanoindentation test	nm
h	Measured depth in a nanoindentation test	nm
P	Measured load in a nanoindentation test	mN
h_c	Contact depth	nm
h_e	Elastic deflection	nm
h'_r	Plastic depth	nm
A_c	Contact area	nm^2
a_c	Contact radius	nm
S	Contact stiffness	$\mathrm{N\,m^{-1}}$
S_u	Unloading contact stiffness	$\mathrm{N\,m^{-1}}$
S_{LF}	Load frame stiffness	$\mathrm{N\,m^{-1}}$
E_r	Reduced modulus	GPa
H	Hardness	GPa

Stress and strain

σ	Stress	GPa
σ_i	Internal stress	GPa
σ_r	Representative stress	GPa
ε	Strain	
ε_r	Representative strain	
$\dot{\varepsilon}_r$	Representative strain rate	$\mathrm{s^{-1}}$
ρ	Dislocation density	$\mathrm{m^{-2}}$

Modeling parameters

U_0	Activation energy of static recovery	$\mathrm{kJ\,mol^{-1}}$
v_0	Activation volume of static recovery	$\mathrm{nm^3}$
Q_t	Activation energy of nucleation	$\mathrm{kJ\,mol^{-1}}$
t_0	Characteristic time of germination	min

b_0	Characteristic time of growth	min^{-1}
Q_b	Activation energy of growth	$\mathrm{kJ\,mol}^{-1}$
n	Avrami exponent	

Abbreviations

DMA	Dynamic Mechanical Analysis
DSC	Differential Scanning Calorimetry
EBSD	Electron Back-Scattering Diffraction
HT	High Temperature
HTSI	High Temperature Scanning Indentation
IR	Infra-Red
ISE	Indentation Size Effect
OFHC	Oxygen-Free High Thermal Conductivity
PGS	Principle of Geometric Similarity
RT	Room Temperature
SEM	Scanning Electron Microscopy
TEM	Transmission Electron Microscope
TMA	Thermo-Mechanical Analysis
XRD	X-ray Diffraction

Contents

Introduction

The temperature may greatly impact the mechanical properties and the structure of materials. Being able to characterize such changes correctly with time and temperature is key for industrial applications. The recent developments of nanoindentation now allow determining the mechanical properties (Young's modulus, hardness, creep parameters) of materials at the micron scale up to 1000 °C.

However, the classically used indentation tests (CSM measurements, indentation creep tests, indentation relaxation tests, etc.) are time-consuming since they required minutes to hours of experiments for each test. As time is also necessary to establish thermal equilibrium before conducting experimentations in temperature, one usually only gets a few results at one temperature after one-day experiments. It can easily be understood that collecting data on a large temperature scale takes weeks.

Moreover, as the structure of the material may vary with temperature, it is complicated to assess the properties changes in temperature due to intrinsic modifications in the material. How to characterize a phase transformation or a recrystallization phenomenon if one only has a little information describing such events?

So, the main goal here is to use nanoindentation to determine and quantify such changes with temperature. In this manuscript, a proposed solution is the development of a new indentation methodology.

The first chapter presents the state-of-art on this question. It starts with the principle of nanoindentation measurement and the development of those tests at high temperatures. As explained here, lots of precautions have to be taken to get correct results. Then, the chapter focuses more on materials. The first point concerns crystalline metals and the influence of temperature on their structure and properties. Next, the amorphous metallic glasses are analyzed. Same, the temperature greatly impacts them.

The second chapter focuses on the development of the methodology named High-Temperature Scanning Indentation (HTSI). The indentation cycle used in this technique is detailed, as well as the thermal cycle. Validation is conducted on three distinct materials: fused silica (FS), pure copper, and pure aluminum. It is verified that such methodology gives access to the correct mechanical properties of the sample (Young's modulus, hardness and creep properties) with temperature. As this approach is confirmed, it is used in the following chapters to characterize specific behaviors of different materials.

The focus of chapter 3 is to assess the creep properties of materials. The goal is to present the interest in the HTSI technique to determine the creep properties of a material in temperature. Classical indentation creep and relaxation experiments are of great interest at room temperature but are complicated to conduct at temperature, contrary to the HTSI method.
Tests are carried out on CaF_2 single crystals from RT to 400 °C and on pure polycrystal silver samples from RT to 450 °C. The equivalence between time and temperature is observed in the two materials. This method is of significant interest for determining the creep properties of materials at high temperatures or low strain rates.

Examining the microstructural changes of metals during a thermal cycle is the aim of chapter 4. The present analysis focuses on the static recovery and recrystallization taking place in pure deformed copper or aluminum. The HTSI technique enables one to detect those phenomena. A simple analytical model to quantify their kinetic is proposed. It allows the prediction of the final microstructure of a sample subjected to a thermal cycle.

Finally, chapter 5 presents the study of ZrCu-based thin-film metallic glasses with temperature. As nanoindentation is a micron-scale testing method, it is an interesting approach to characterize such samples.
The HTSI technique gives access to the transition temperatures of the specimen (brittle to ductile transition, glass transition) as well as information on the supercooled liquid state of the sample. Through the variations of the hardness and strain rate sensitivity during the thermal cycle, the crystallization of the specimen can be observed. Thanks to a comparison with High-Temperature X-ray Diffraction (HT-XRD), a mechanism is proposed to explain the crystallization of the sample.

1

State of art

The aim of this chapter is to introduce all the needed notions about instrumented indentation and mechanics of materials.

Chapter's content

I. Instrumented nanoindentation

I.A. Some historical considerations

Even if humanity uses hard materials for various applications for thousands of years, the quantification of hardness is quite recent. In 1812, Mohs proposes a scale to differentiate the hardness of minerals through scratch measurements. The idea was to determine which material was harder than the other by scratching samples together. Table 1.1 gives examples of Mohs' scale. Unfortunately, it is irregular.

Table 1.1: Mohs scale for materials.

Mohs hardness	Material	Absolute hardness (Turner-sclerometer)
1	Talc	1
2	Gypsum	2
3	Calcite	14
4	Fluorite	21
5	Apatite	48
6	Orthoclase feldspar	72
7	Quartz	100
8	Topaz	200
9	Corundum	400
10	Diamond	1500

In the following years, numerous apparatus such as the Turner-sclerometer [1] (see figure 1.1) were developed to conduct more precise quantification of hardness through scratch tests.

Nevertheless, the formal definition of hardness as it is used nowadays was proposed by Hertz in 1882 in his work on the contact of rigid elastic solids [2]: "The hardness of a body is to be calculated by the normal pressure per unit area." Hardness is the ratio between an applied force on the material and the corresponding area.

With the work of Brinell in the 1900s and the development of his indentation test, standardization of hardness measurements started. The principle of measure is to push a hard non-deformable sphere inside the studied material under a specific static load during a specific time. The Brinell hardness number (BHN) is then obtained as the ratio of the applied load over the

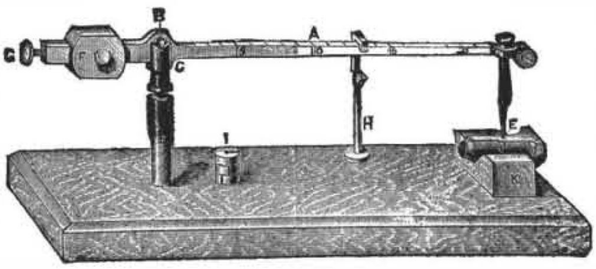

Figure 1.1: The hardness scratch measurement device from [1].

size of the residual imprint.

In the following years, numerous standard micro-indentation tests [3] were established. They are still classically used to characterize hardness. For instance, Rockwell's hardness evaluates hardness through a difference of depth, employing a conical diamond (HRC) or a steel ball (HRB) indenter depending on the tested material. Vickers hardness (HV) [4] and Knoop's hardness (HK) [5] utilize a similar process than Brinell hardness with a square-based or lozenge-based diamond pyramid indenter. All those procedures are standardized.

Micro-indentation being a "non-destructive" technique, it is wildly used to characterize materials. However, the methodologies presented above require the determination of the size of the post-mortem residual imprint. As it is usually evaluated optically, those tests are made at the macroscopic scale (100 µm to 1 mm). Such dimensions are problematic: it does not allow characterizing thin films, for instance. Thin film [6, 7] is a new technology with interesting properties and advantages compared to bulk materials. But classical characterization techniques could not be applied at such low scales (1 nm to 100 nm). It is impossible to determine optically imprint size at this scale: it should be assessed through other methods. An idea could be to measure the post-mortem imprint using a Scanning Electron Microscopy (SEM). Unfortunately, SEM is not made for precise evaluations. And on hyper-elastic materials such as elastomers, no residual imprint can be measured: hardness would be infinite if such procedures were used.

To overcome these issues, Tabor [8, 9] proposes to define the hardness as the ratio between the applied load and the area under the contact. It becomes compulsory to quantify the contact area during the test and not post-mortem. This approach leads to the development of the instrumented indentation where the load and the depth are recorded all together during the indentation test.

I.B. How to assess mechanical properties using nanoindentation experiment?

After those historical considerations, let's now focus on the nanoindentation test. The load-displacement curve being the basement of the nanoindentation measurement, it will be addressed first. Then the principle of geometric similarity will be described before detailing how the hardness and Young's modulus are obtained from those measurements. In the following, the issue of the contact area determination will be deal with. In the end, dynamic measurements will be compared to static ones.

I.B.1. The load-displacement curve

Since the '70s, new indentation devices[10–12] were developed: they allow measuring the load and depth all along the indentation test. Lots of improvements to the tool were made during the past fifty years, but the principle of the technique stays the same.

The apparatus considered in this work is the InSEM HT from KLA Nanomechanics. The system (see figure 1.2) is constituted of two distinct parts: one link with the specimen and the other with the tip. The sample is clamped on its support. In front of it, the tip is fixated on an axis that moves depending on the applied force. The force is applied with a coil and the

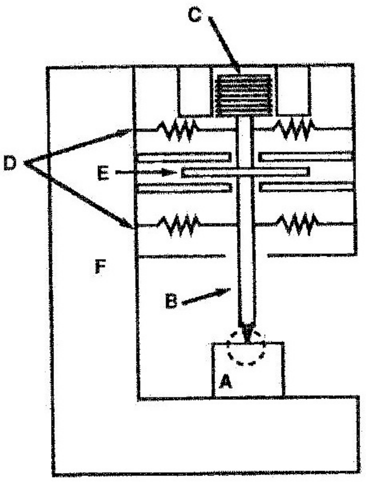

A : sample (stiffness S; damping coefficient C)
B : indentor loading column (mass M)
C : solenoid applying the force
D : springs supporting the column (stiffness S_{spring})
E : capacitive gauge measuring the displacement (damping coefficent Cl)
F : indenter load frame (stiffness S_{LF})

Figure 1.2: Schematic indentation device adapted from [13].

corresponding displacement is measured through capacitance gauges. Other constructors utilize various technologies: Femto tools employ mEMS to control the movements, Alemnis uses piezo actuators to apply displacement, etc.

The Berkovich diamond one (triangle-based pyramid) is widely used during the nanoindentation tests. However, tips made of other hard materials and/or different geometries (see figure 1.3) can also be utilized depending on applications.

The indentation test is then performed as follows (see figure 1.4): the tip is put in contact with the surface of the specimen, giving the initial force and displacement point. It is then pushed inside the sample up to the maximum applied force and displacement and maintains a specific time at this position. Next the tip is unloaded: a residual imprint can be observed if plastic deformation happened in the material. The complete measurement of the load and of the displacement during the indentation cycle gives the load-displacement curve. The mechanical properties of the sample can now be determined from this curve.

During the indentation test, the raw displacement u and the applied force F are measured. From those values, the displacement h and the load P are defined [15]:

$$P = F - S_{spring} u \tag{1.1}$$

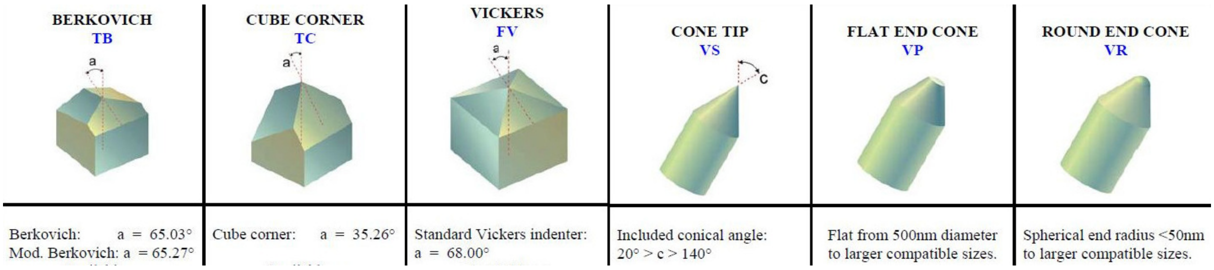

Figure 1.3: Examples of tip geometries that are proposed by a constructor [14]

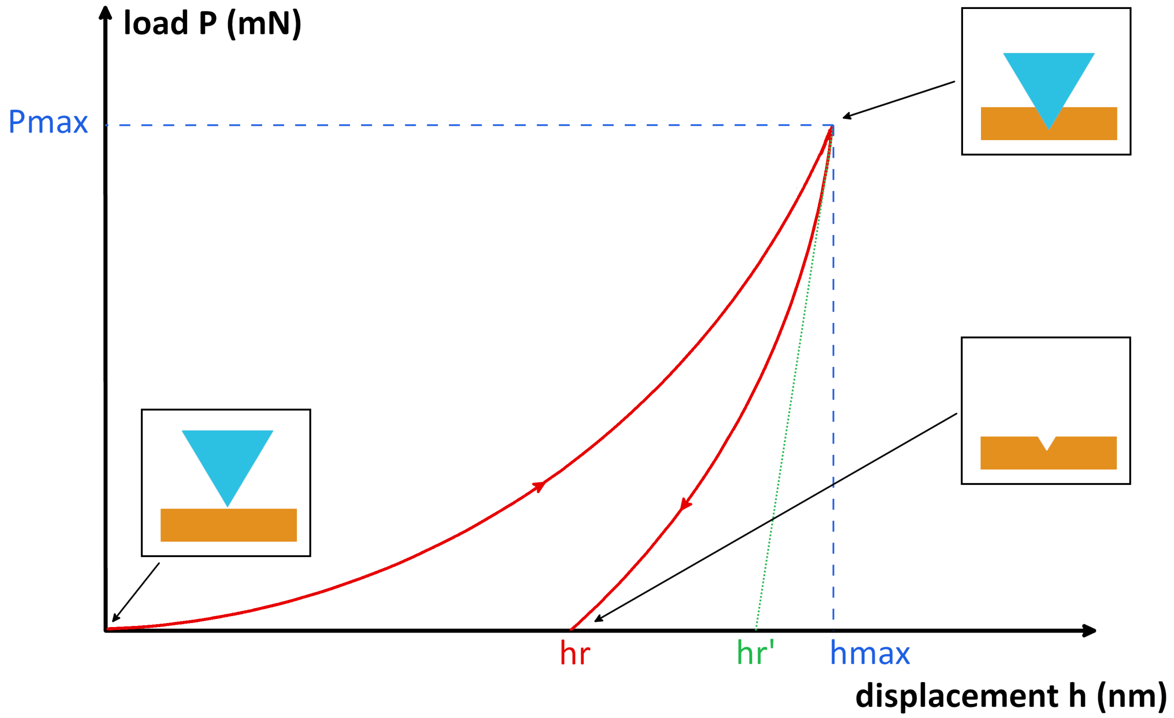

Figure 1.4: Load-displacement curve (red) obtained during an indentation test. The arrows indicate the loading and unloading. In green is the tangent of the unloading curve at the maximum depth. The beginning of the unloading is fully elastic.

and

$$h = u - \frac{P}{S_{LF}} \tag{1.2}$$

where S_{spring} is the stiffness of the springs and S_{LF} is the load frame stiffness (see figure 1.2). The contact stiffness K is then defined as:

$$K = \left.\frac{dP}{du}\right|_{u=u_{max}} \tag{1.3}$$

The unloading contact stiffness S can be linked with K and S_{LF}:

$$\frac{1}{K} = \frac{1}{S} + \frac{1}{S_{LF}} \tag{1.4}$$

For a really stiff device ($S_{LF} >> K$), the contact stiffness and the unloading contact stiffness are equal. However, if S_{LF} and K are of the same order of magnitude, not taking into account S_{LF} would lead to false values of the mechanical properties.

I.B.2. The principle of geometrical similarity

The principle of geometric similarity was first enunciated by Tabor [9]. The "principle of geometric similarity states that if two indentations are made of the same geometric shape, then,

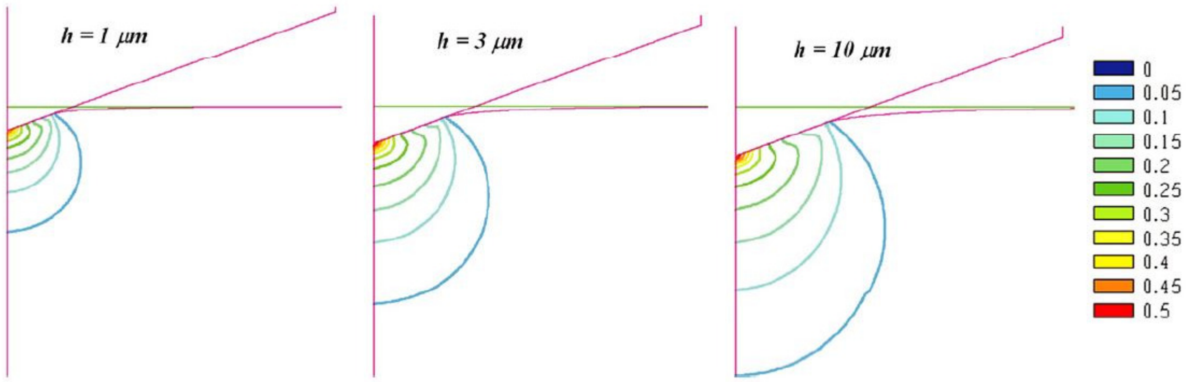

Figure 1.5: Illustration of the principle of geometric similarity from [16].

whatever their size, the strain distribution and the stress distribution around the indentations will be geometrically similar." It is correct for a homogeneous and uniform material. So with an indenter with no characteristic length, hardness should be independent of the indentation's dimension. This principle is valid for pyramidal or conical indenters. On the opposite, for spherical tips defined by a specific radius, hardness will change with the contact height.

Figure 1.5 presents this principle. It can clearly be noticed that the plastic strain distribution is geometrically the same in the three cases when the indentation depths are different. The indenter employed here is a conical one.

I.B.3. Hardness and Young's Modulus

Computation of the hardness and Young's modulus using the load-displacement curve is the next focus point.

Hardness As seen previously, hardness is defined as the ratio between an applied force and the corresponding contact area. It is measured by nanoindentation as:

$$H = \frac{P}{A_c} \tag{1.5}$$

where P is the maximum applied load (assessed in figure 1.4) and A_c is the corresponding contact area. Quantifying precisely the contact area is a tricky question. It will be addressed in a specific paragraph (see I.B.4.).

Young's modulus Determining the Young's modulus requires spending more time on the load-displacement curve. In [11], Loubet *et al.* explain the type of deformations that take place during the whole cycle. During loading, deformation is elasto-plastic, not only elastic. On the opposite, the beginning of the unloading part is fully elastic: it allows getting information on the elastic properties of the sample.

Thanks to the work of Sneddon [17], the unloading contact stiffness S can be linked to the reduced modulus E_r [11, 12, 15, 18, 19]:

$$E_r = \frac{S}{2\beta}\sqrt{\frac{\pi}{A_c}} \tag{1.6}$$

β being equal to 1 for axisymmetric tips [19]. Unfortunately, Berkovich and Vickers's tips do not respect this hypothesis. However, equation 1.6 stays valid when taking β equal to 1.034 and 1.012 respectively [19]. Moreover, taking β equal to 1 does not lead to large errors compared to the measurement ones: in the rest of this manuscript, it will consider that $\beta = 1$.

The reduced modulus is linked with the Young's modulus E through the elastic properties of the tip:

$$\frac{1}{E_r} = \frac{1-\nu^2}{E} + \frac{1-\nu_{ind}^2}{E_{ind}} \tag{1.7}$$

with ν and ν_{ind} the Poisson ratio of the sample and the tip respectively. As for the hardness, the Young's modulus depends on the contact area. If one already knows the Young's modulus of its specimens, one can evaluate the contact area using equations 1.6 and 1.7 and then computes the hardness [20]. Nevertheless, most of the time, one wants to determine hardness and Young's modulus using indentation testing: quantifying A_c precisely is then compulsory.

I.B.4. Determination of the contact area

Unfortunately, it is impossible to evaluate the contact area directly from the load-displacement curve contrary to the contact stiffness. Models should be applied to quantify the contact depth h_c and the contact area from the measurement of the displacement. To do so, one should first understand what happens under the tip during the contact.

Pile-up versus sink-in Two phenomena [9, 21] have been detected when indenting a specimen: pile-up and sink-in. Those phenomena are illustrated in figure 1.6. On the cold-rolled sample (a, b), a pile-up effect can be observed around the tip. On the opposite, on the annealed specimen (c, d), sink-in occurs.

To quantify the contact depth properly, those effects have to be considered. Let's study two models to determine the contact area between a sample and a conical tip. The contact is non-adhesive and without friction.

The model of Oliver and Pharr Presented thirty years ago in [18], the model of Oliver and Pharr is the most used in literature since then. This model is based on the representation proposed in figure 1.7 on the left part. First, the measured displacement h all along the indentation cycle is the sum of the real contact depth h_c and the elastic deflection around the contact due to sink-in h_e:

$$h = h_c + h_e \tag{1.8}$$

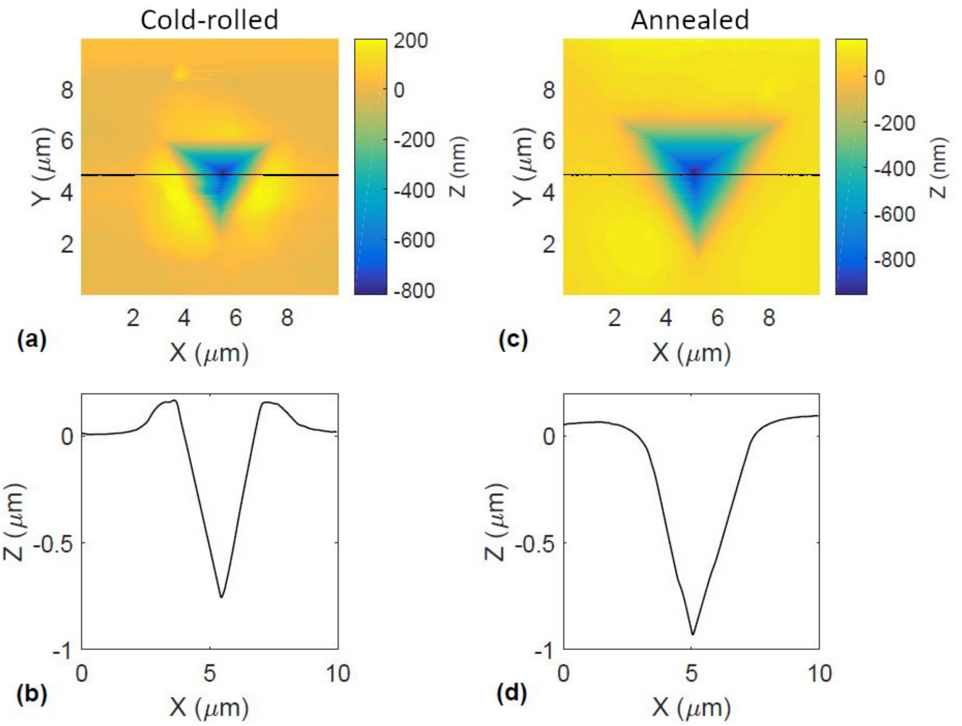

Figure 1.6: Topographies and indents' depth profiles from [22]. On (a) and (c) are the post-mortem Berkovich indents realized on a cold-rolled aluminum alloy before and after annealing at 380 °C during 2 h, observed in SEM. (b) and (d) are the corresponding depth profiles obtained by AFM measurements. Clear pile-up can be detected in (b) while (d) shows sink-in.

Thanks to Sneddon's work [17], the elastic deflection can be linked to the load and the unloading contact stiffness [18]:

$$h_e = \varepsilon_{OP} \frac{P_{max}}{S} \tag{1.9}$$

where ε_{OP} is a constant describing the indenter. The value of ε_{OP} depends on the tip geometry (see table 1.2).

So the contact depth at the maximum depth is:

$$h_c = h_{max} - \varepsilon_{OP} \frac{P_{max}}{S} \tag{1.10}$$

Table 1.2: Values of ε_{OP} in the model of Oliver and Pharr depending on the tip

Tip	ε_{OP}
Flat punch	1
Paraboloid of revolution	0.75
Conical indenter	0.72

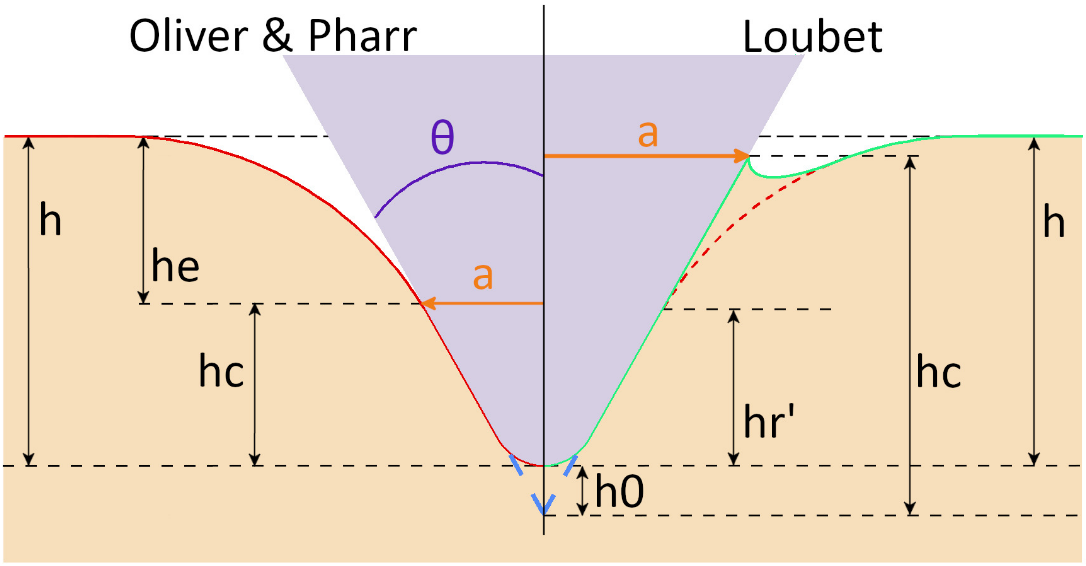

Figure 1.7: Description of the models introduced by Oliver and Pharr (left) and by Loubet (right). Unfortunately, a conical tip is never perfect: the tip defect should be accounted for when determining the contact area.

For a perfect conical tip, the area function A_c is:

$$A_c = c_0 h_c^2 \tag{1.11}$$

c_0 being a constant. For a Berkovich tip of equivalent conical angle $\theta = 70.32°$, $c_0 = 24.5$.
This function works quite well for large indentations when the tip behaves as a perfect one. However, tips are never perfect: their end is always a little blunted. This phenomenon should be accounted to obtain consistent results when performing really small indentations. So Oliver and Pharr used a more complicated function to describe the tip geometry:

$$A_c = \sum_{i=0}^{7} m_i h_c^{2/2^i} \tag{1.12}$$

where the m_i are the fitting coefficients, determined through a calibration process (see section I.B.5.).
This model is quite good for materials that present sink-in. However, it does not consider the pile-up phenomena: it is forbidden by equation 1.10. On samples presenting pile-up, the contact area would be underestimated leading to false values of mechanical properties. Kese *et al.* [23] propose a correction of Oliver and Pharr's model to take into account the pile-up phenomenon.

The model of Loubet Also presented thirty years ago in [24], the model of Loubet is less utilized in literature even if it has interesting characteristics. This model is based on the representation proposed in figure 1.7 on the right part. A perfectly conical tip is indenting an elastic, perfectly plastic sample. The determination of the contact depth h_c using the plastic indentation depth h'_r gives:

$$h_c = \alpha_L h'_r \tag{1.13}$$

The plastic depth is defined as:

$$h'_r = h_{max} - \frac{P_{max}}{S} \tag{1.14}$$

α_L, the coefficient from equation 1.13, was assessed experimentally on various materials. Its value will depend on the geometry of the tip. For a Berkovich tip, it gives $\alpha_L = 1.2$ [25, 26]. This value has been validated theoretically for purely elastic and purely plastic material [27] and was confirmed by numerical studies [27].

To take a blunted tip into account, Loubet adds a tip defect term h_0 [25] in the definition of the contact depth:

$$h_c = \alpha_L \left(h_{max} - \frac{P_{max}}{S} + h_0 \right) \tag{1.15}$$

Determination of the value of the tip defect is done by calibration (see section I.B.5.).

The contact area is then obtained through:

$$A_c = \pi \left(h_c tan(\theta) \right)^2 \tag{1.16}$$

where θ is the equivalent conical angle. $\theta = 70.32°$ for a Berkovich tip.

It should be noticed that h_c could be higher or lower than the maximum depth h_{max}, contrary to Oliver and Pharr's model. Equation 1.15 allows both pile-up and sink-in.

As it is explained in [28], hardness is independent of the load frame stiffness S_{LF}. Let's write the plastic depth h'_r using u the measured raw displacement.

$$h'_r = u - \frac{P}{S_{LF}} - \frac{P}{S} + h_0 \tag{1.17}$$

So,

$$h'_r = u - \frac{P}{K} + h_0 \tag{1.18}$$

Thanks to this, an error made during the calibration of the load frame stiffness would not impact the plastic depth determined by Loubet's model. So the contact depth h_c, the contact area A_c, and the hardness H are independent of this stiffness. It is really interesting when studying the hardness of very stiff materials or when utilizing devices that have low load frame stiffness.

How to choose the model that best describes the behavior of the material? To determine which model should be used, McElhaney [29] suggests observing the post-mortem indents (as in figure 1.8) and to evaluate if pile-up or sink-in arose. Time should be spent to do such measurements [30].

Another way was proposed by Bolshakov [31]. According to him, if the value of h_r/h_{max} is

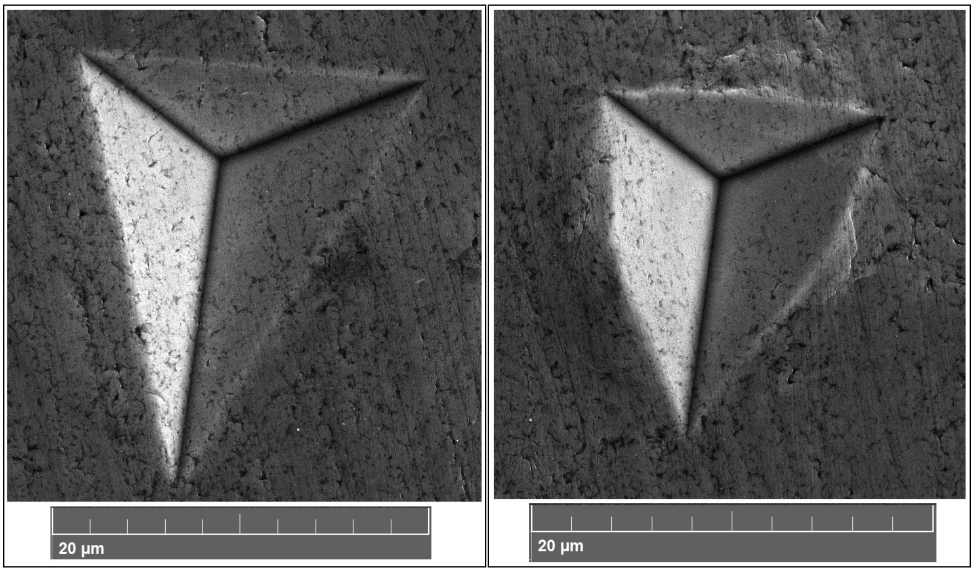

Figure 1.8: Post-mortem Berkovich indents made on aluminum, observed inside a SEM. Sink-in happens on the left one while pile-up is detected on the right one.

higher than 0.7 and if the specimen is not work-hardened, pile-up is expected. If h_r/h_{max} is lower than 0.7 or if the sample is moderately work-hardened, sink-in would occur. Roudet [32] indicates that if h_r/h_{max} is higher than 0.83 pile-up would be anticipated. Knowing that one can then choose to apply Oliver and Pharr's model or Loubet's model.

Experimental determination of A_c during indentation measurements To overcome the issue of the modeling of the real contact area using the load-displacement curve, an idea would be to evaluate it during the indentation test performing complementary measurements.

For instance, Kleesattel proposes to assess this area by quantifying the resonance frequency during the indentation test [33, 34]. The variation of the resonance frequency during the contact can be linked with the Young's modulus and the contact area.

More recently, with the work of Comby-Dassonneville [35], nanoindentation was coupled with resistive measurements. Through the modifications in the resistance during the test, the contact area can be computed, independently of the load-displacement curve.

Another way would be to perform experiments with two different tips (Berkovich and Cube Corner for instance), and combine the results to eliminate the contact area in the equations [36].

I.B.5. From static measurements to dynamics one

All the properties studied until now are evaluated using static measurements: hardness and Young's modulus are determined at the maximum load and depth point. So to access the change of the properties against depth, numerous measurements have to be performed, which is really time-consuming.

New techniques were developed to compute the hardness and Young's modulus not only at the maximum load and depth point but also during the loading part of the indentation cycle. A first

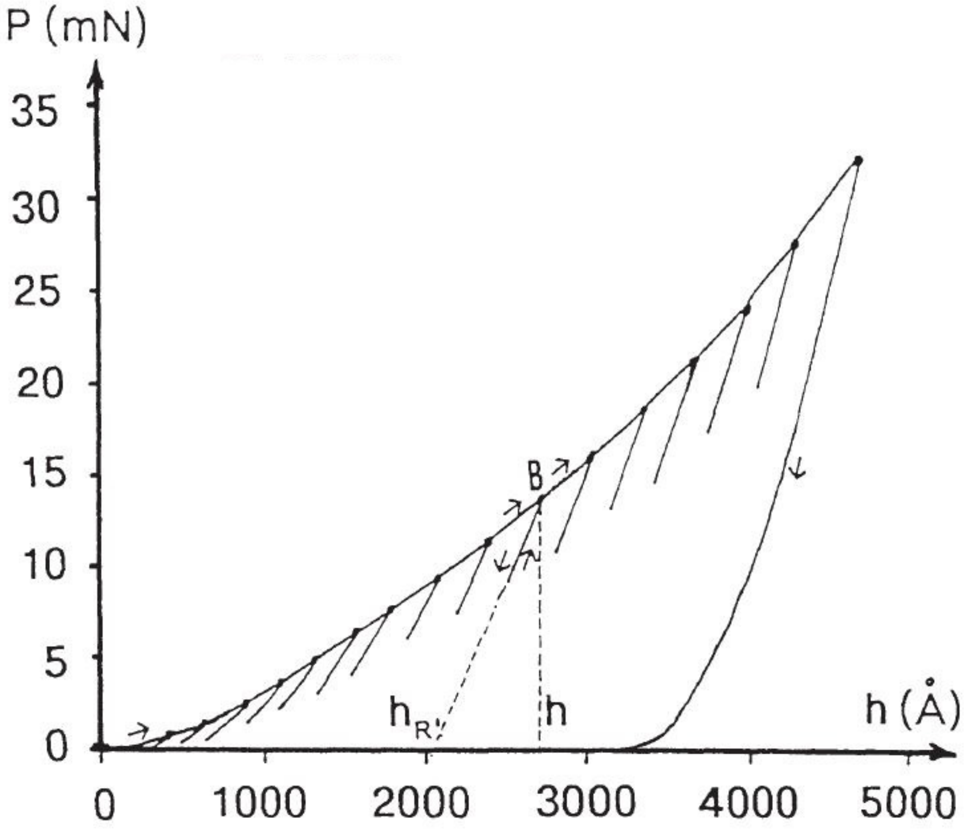

Figure 1.9: Loading-partial unloading indentation cycle performed on sapphire, from [24].

method based on partial unloading allows one to obtain those values at some discrete depths. A second method, widely used nowadays, gives those properties all along the depth utilizing only one indentation test: it is the Continuous Stiffness Measurement (CSM) methodology.

Loading-partial unloading cycles The principle of the method, presents in figure 1.9, consists in making regular unloading during the loading phase. This enables the calculation of contact stiffness at different depths using a single indentation test. Employing the equations defined in the previous sections, one can then obtain discrete values of hardness and Young's modulus against depth.

Continuous Stiffness Measurement (CSM) The Continuous Stiffness Measurement consists in adding an oscillation of frequency ω and of low amplitude in force or displacement to the static signal during the loading [13, 18, 20, 24], as presented in figure 1.10. Let's considered a force-controlled indentation device. The oscillation signal in force P_{osc} would be:

$$P_{osc}(t) = P_A \exp j\omega t \tag{1.19}$$

with P_A the amplitude of the oscillating signal and ω its frequency.

Such oscillation in force would add an oscillation signal $h_{osc}(t)$ of the same frequency to the

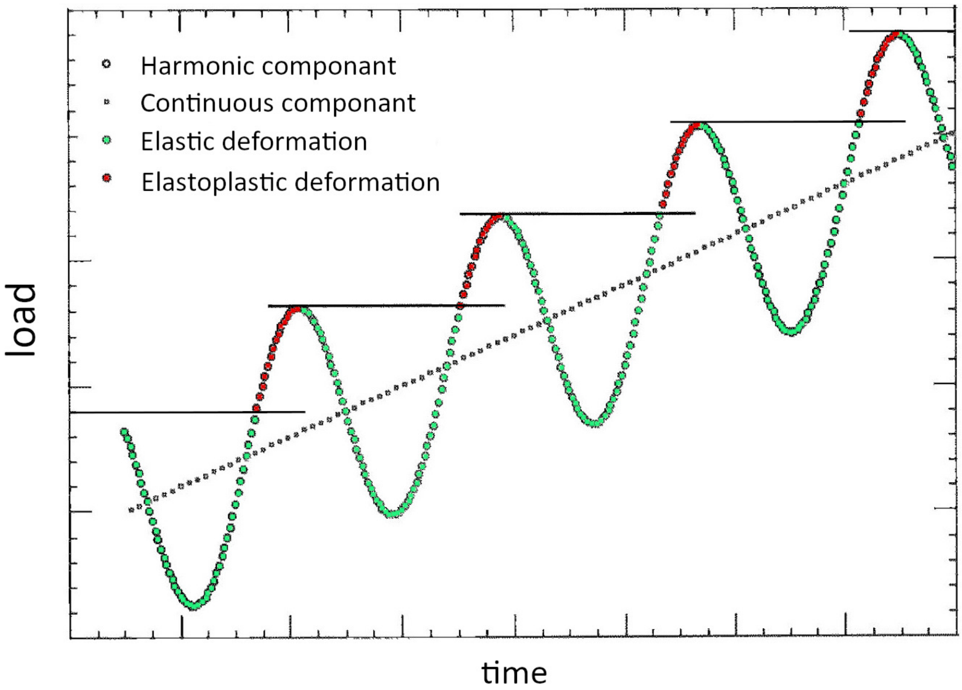

Figure 1.10: Graphical representation of the principle of the CSM measurement adapted from [13]. An oscillation is added to the initial continuous signal to allow continuous determination of the contact stiffness.

static measured displacement:

$$h_{osc}(t) = h_A \exp j(\omega t - \phi) \tag{1.20}$$

with h_A the amplitude of the oscillating signal and ϕ the phase difference between the two signals.

The simplified equation governing the response of the indenter to such oscillation is:

$$M\ddot{h}_{osc}(t) + C_{eq}\dot{h}_{osc}(t) + K_{eq}h_{osc}(t) = P_{osc}(t) \tag{1.21}$$

where M, C_{eq}, and K_{eq} are the mass, the damping coefficient, and the stiffness of the system. Those coefficients can be identified through the rheological model presented in figure 1.11.

Applying equations 1.19 to 1.21, the transfer function of the system can be evaluated:

$$\frac{P_A}{h_A} \exp -j\phi = K_{eq} - \omega^2 M + jC_{eq}M \tag{1.22}$$

$$\tan(\phi) = \frac{C_{eq}\omega}{K_{eq} - \omega^2 M} \tag{1.23}$$

By studying the idle movement of the indentation column, its stiffness and damping coefficients can be calibrated. Once they are known, the contact's parameters can be determined. The load and depth values are used to compute the contact stiffness and depth.

Thanks to this oscillation, one obtains the complete changes of Young's modulus and hardness

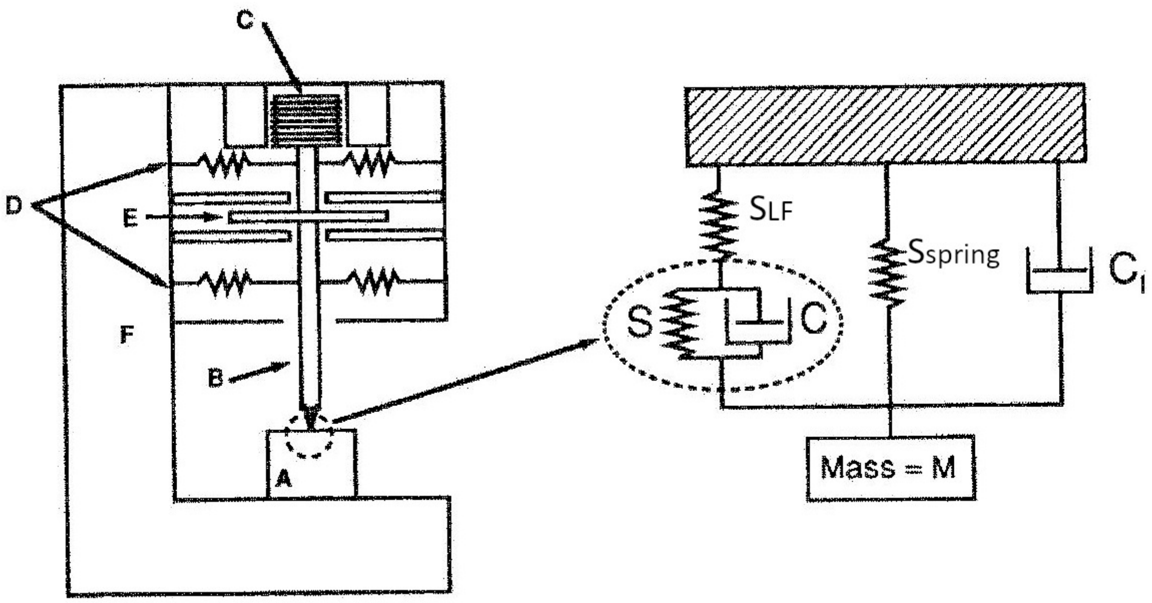

A : sample (stiffness S; damping coefficient C)
B : indentor loading column (mass M)
C : solenoid applying the force
D : springs supporting the column (stiffness S_{spring})
E : capacitive gauge measuring the displacement (damping coefficent Cl)
F : indenter load frame (stiffness S_{LF})

Figure 1.11: Rheological model describing the dynamic indention, adapted from [13].

versus displacement. Moreover, the frequency of the oscillations is in the range of 10 Hz to 100 Hz: the calculated contact stiffness is less sensitive to thermal drift [37].

Nevertheless, some drawbacks have been identified: when applying this technique, one has to take some precautions. In fact, the addition of the amplitude of oscillations could impact the measured properties. Cordill *et al.* [38] have shown that on nickel samples, softening happens on the first 200 nm-depth compared to static indentation results. The CSM method modifies the dynamic of dislocations by bringing more energy leading to unexpected changes in the mechanical properties. Siu *et al.* [37] noted that this softening effect of CSM was seen if $h/h_{osc} < 150$ while making experiments of aluminum. Pharr *et al.* [39] also observe its influence on copper when working on the impact of the amplitude of those oscillations on the load, depth, and contact stiffness determination. Those effects increase on materials with a high E/H ratio. They proposed a correction of those parameters to decrease the errors. The amplitude of the oscillation should be lowered to reduce those errors.

More recently, Merle *et al.* [40–42] studied this issue while trying to significantly increase the applied strain rate in those tests. As it can be observed in figure 1.10, because the static load increases with time, the deformation is not always elastic. Increasing the loading rate in CSM mode greatly amplifies this effect and leads to wrong results. They recommended examining the phase difference ϕ against depth to validate the measurements. Phani *et al.* [43, 44] have

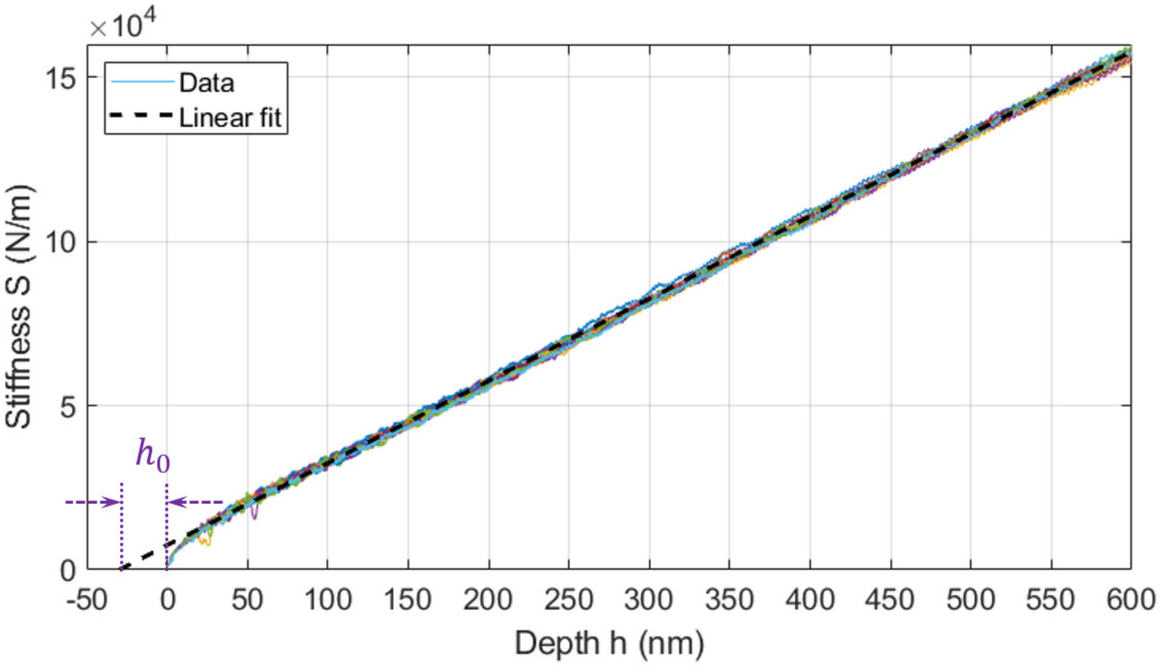

Figure 1.12: Stiffness plots against depth for a fused silica specimen, from [28]. From those CSM measurements, the tip defect h_0 can be determined.

recently proposed some methods to correct the data or to lower the errors coming from the CSM procedure. One of the suggested solutions is to use an oscillation amplitude that varies with depth.

CSM is a really worthwhile technique yet some precautions have to be taken, especially when conducting "high-speed" CSM tests ($\geq 1\,\mathrm{s}$) on materials with a high E/H ratio. A high oscillation amplitude reduces the noise/signal ratio but can lead to inaccurate values of the mechanical properties: a compromise must be made when choosing its value.

Calibrations using CSM Even if precautions should be taken when performing CSM measurements, this technique is widely used to calibrate the contact area parameters when applying Oliver and Pharr or Loubet's model.

The idea is to utilize a homogeneous material with a known constant hardness and Young's modulus against depth to calibrate the tip contact area [24]. Before evaluating the m_i of equation 1.12 or the h_0 of equation 1.15, the load frame stiffness S_{LF} of equation 1.4 has to be calibrated. Oliver and Pharr [45] proposed to quantify it using the ratio P/S^2:

$$\frac{P}{S^2} = \frac{\pi}{4\beta^2}\frac{H}{E_r^2} \tag{1.24}$$

If H and E are constant against depth, this ratio is also a constant against depth. So the value of S_{LF} is determined when this condition is reached. The m_i are then calculating to achieve the correct values of the Young's modulus against depth.

The tip defect h_0 can be obtained by plotting the evolution of stiffness against depth. From equation 1.6, for a constant modulus, the stiffness should be proportional to the depth: $S(h) = ah$. As it can be seen in figure 1.12, because the tip is not perfect, the relation is $S(h) = a(h+h_0)$. Calibration is usually performed on fused silica, a reference sample in nanoindentation. This material is known to have constant values of Young's modulus and hardness against depth. Moreover, its hardness is equal to 10 GPa, its Young's modulus is 72 GPa and its Poisson ratio is 0.188. $E/H = 8$: it has a low E/H ratio which is a plus when utilizing the CSM technique.

Because the studied material can be really stiff or soft compared to fused silica, it is also recommended to calibrate the system stiffness on other materials [15, 32] (sapphire or silicon for instance).

Some authors use AFM measurements to calibrate the tip area function [46] but such quantification is time-consuming.

I.C. Time-dependent mechanical properties

Obtaining information on the hardness and Young's modulus is quite easy thanks to nanoindentation tests. However, some properties of materials are time-dependent. Let's now focus on a way to characterize those properties.

Before analyzing methods to determine the impact of the strain rate on the properties of the samples, the notions of representative stress, representative strain, and representative strain rate are introduced to compare indentation measurements with uniaxial ones.

I.C.1. A little reminder on the mechanical behaviors of materials

Usually, one performs uniaxial traction tests to evaluate the mechanical behavior of materials. The objective is to compute the changes of stress σ depending on the level of deformation ε. Figure 1.13 presents a stress-strain curve obtained on steel at 725 °C. On the elastic part of the curve, stress σ and strain ε are proportional and related through Hooke's law (in isotropy):

$$\sigma = E\varepsilon \tag{1.25}$$

However, plasticity quickly appears as the sample is deformed and stress-strain changes are no longer proportional. Once the yield stress σ_y is reached, the material will deform plastically and the flow stress σ is generally computed as [9]:

$$\sigma = b\varepsilon^x \tag{1.26}$$

with b a constant and x the work-hardening index.

As it can be observed in figure 1.13, the yield stress value and the plastic deformation are greatly affected by the strain rate $\dot{\varepsilon}$. This is a viscoplastic effect on the material: irreversible deformations occur and depend on time. Let's focus on the way to study those time-dependent effects after defining some representative values.

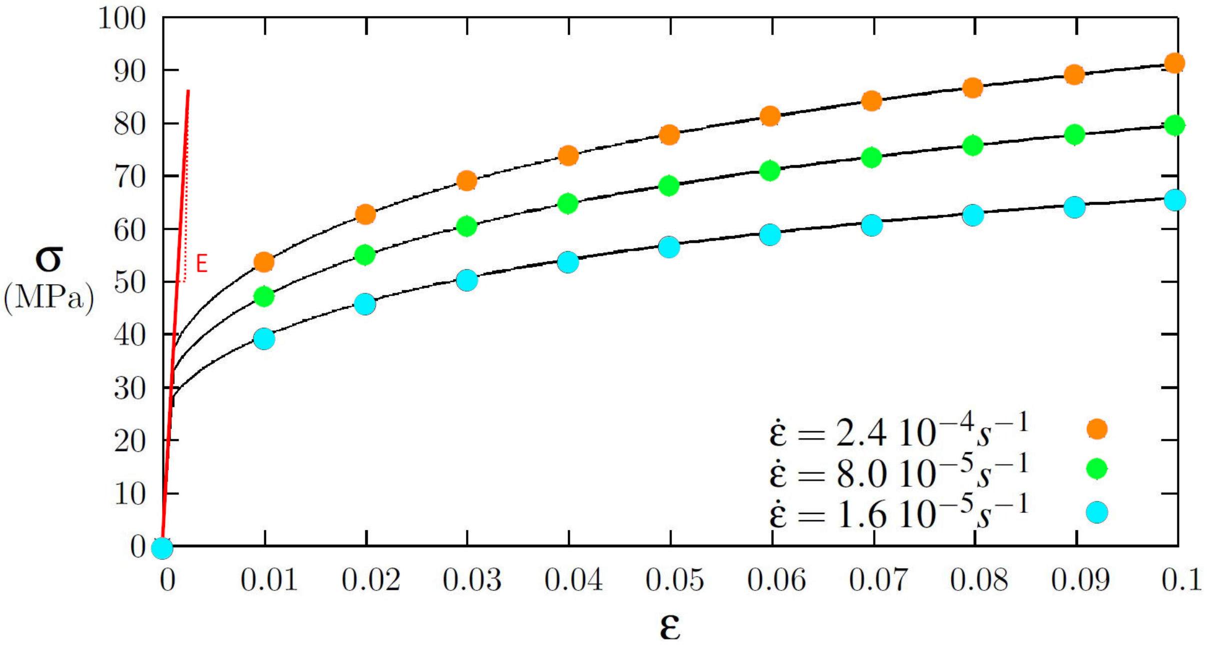

Figure 1.13: Stress-strain curve on an austenitic steel at 725 °C from uniaxial traction adapted from [47].

I.C.2. Representative stress and representative strain

In nanoindentation, the load-displacement curve gives information about the hardness and the Young's modulus of the material. For indenters verifying the principle of geometric similarity, one indentation curve will correspond to one point of the stress-strain curve. This point will depend on the characteristic of the tip [9, 16].

It becomes compulsory to define representative stress σ_r and representative strain ε_r to be able to compare indentation measurements with uniaxial traction. Those notions were introduced by Tabor [9].

Contrary to uniaxial traction tests, indentation measurements present a really complex stress distribution. However, as explained by Tabor [9], when considering a homogeneous perfectly plastic material, hydrostatic pressure does not produce plastic flow. So hardness can be related to the representative stress by:

$$H = C\sigma_r \tag{1.27}$$

where C is a constant between 2.6 and 3 for metals. For elasto-plastic materials, Tabor proposed modifications considering the Young's modulus of the material and the shape of the indenter (for instance a glass material would have a value of C around 2).

Moreover, he also introduces an expression of the representative strain for a Brinell indenter in the case of a fully plastic regime:

$$\varepsilon_r = 0.2\frac{d}{D} \tag{1.28}$$

where d is the chordal diameter of the indentation and D the diameter of the indent.

For a conical equivalent tip, this deformation is linked with the equivalent angle θ:

$$\varepsilon_r = 0.2\cot(\theta) \tag{1.29}$$

This equation is valid for rigid plastic material yet fails once elastic deformation occurs [48]. When studying a sphere-plane or a cone-plane contact, Odoni [13] compute the variation of the ratio H/σ_r with Poisson's ratio. Not only did he get the value of $C = 3$ for metals, but he also gives the formula to determine C for other types of materials.

Moreover, he also computes the values of the representative strain depending on the tip shape (see table 1.3). Making indentations with a Berkovich or a Vicker tip increases the deformation in the specimen of 8% while a trigonal tip deforms the sample up to 13.5%. Here is the expression of the principle of geometric similarity: when using one of those tips, the deformation will always be the same whatever the applied load and depth. On the opposite, a spherical tip has a representative stress that varies with a the contact radius. Deformation (and stress) increases all along the test.

To take into account elasto-plasticity in material, Kermouche *et al.* [49] propose new definitions of the representative stress and strain:

$$\sigma_r = \frac{\xi_3\cot(\theta)}{\xi_1\cot(\theta) - (1-\xi_2)H/E}H = \gamma H \tag{1.30}$$

$$\varepsilon_r = (1-\xi_2)\frac{\sigma_r}{E} + \xi_3\cot(\theta) \tag{1.31}$$

where ξ_1, ξ_2 and ξ_3 are constant depending on the tip shape. For a Berkovich indenter, $\xi_1 = 0.66$, $\xi_2 = 0.216$ and $\xi_3 = 0.24$. Values for other tips can be found in [16]. γ is the constraint factor, depending of the hardness over Young's modulus ratio. Those expressions will be used in the rest of this manuscript when representative strain and stress are required.

I.C.3. Strain rate in indentation

As it was seen in figure 1.13, the stress-strain curve in uniaxial traction depends on the strain rate. It would be expected that in indentation, such behavior would also be observed. But how is the strain rate defined in indentation experiments? Moreover, because the mechanical properties of materials would depend on various parameters, such as the strain rate, it becomes essential to perform tests at constant strain rates. Such tests would allow characterizing the

Table 1.3: Representative strain for different indenter shapes, from [13].

Tip	angle α	angle θ	ε_r
Sphere	/	/	$0.2a/R$
Berkovich	65.3°	70.32°	$0.194\cot\theta = 8.3\%$
Trigonal	35.3°	42.3°	$0.123\cot\theta = 13.6\%$
Vickers	68°	70.32°	$0.246\cot\theta = 8.8\%$

mechanical properties as a function of this strain rate.
Strain rate in indentation is generally defined as [12, 50]:

$$\dot{\varepsilon}_{ind} = \frac{\dot{h}}{h} \tag{1.32}$$

Because h/a is a constant, this definition verifies the principle of geometric similarity [22, 51].
As indenter are usually controlled in force, the indentation strain rate is also defined as [52]:

$$\dot{\varepsilon}_{ind} = \frac{1}{2}\frac{\dot{P}}{P} \tag{1.33}$$

when performing exponential loading and when the plastic flow becomes stationary.
In [52], Lucas *et al.* compared the influence of two loading protocols on the strain rate: constant loading rate $\dot{P} = cste$ and constant loading rate over load $\dot{P}/P = cste$. For a Berkovich tip, the $\dot{P}/P = cste$ loading procedure leads to a constant strain rate during the experiment. To characterize the impact of the loading rate on mechanical properties, one should carry out constant strain rate indentation tests using a Berkovich tip.

As for stress and strain, the question of comparison with uniaxial testing can be asked. How to define a representative strain rate knowing the indentation strain rate? Authors [52, 53] usually consider that $\dot{\varepsilon}_{ind}$ is equivalent to $\dot{\varepsilon}_r$. It is expected that they would be related but the equivalence is not certain.
In [16], Kermouche *et al.* introduces a more complex link between the two:

$$\dot{\varepsilon}_r \approx \xi(m)\cot(\theta)\frac{\dot{h}}{h} \tag{1.34}$$

where $\xi(m)$ is a function of the strain rate sensitivity of the material m, determined by creep experiments (see subsection I.C.4.). From numerical simulations, they propose an expression for $\xi(m)$:

$$\xi(m) = 0.44\exp\left(\frac{0.2}{m}\right) \tag{1.35}$$

For materials with a low strain rate sensitivity, such a function leads to $\dot{\varepsilon}_r \approx \dot{h}/h$.

I.C.4. Determination of creep properties

The creep phenomenon Creep in metals is a viscoplastic mechanism appearing under a constant load: the sample will continuously deform while the load is maintained constant. This phenomenon happens at all temperatures [54] but is greatly activated by temperature. It is linked with the diffusion of the atoms at grain boundaries or inside the lattice [22].
Classically, when performing creep tests, the plastic deformation evolves following three stages (see figure 1.14). The first phase, named primary creep, means a rise in plastic deformation. It has a plastic deformation rate that tends to stabilize the deformation process. The latter one is a stationary creep and corresponds to a constant plastic deformation rate. When the ternary

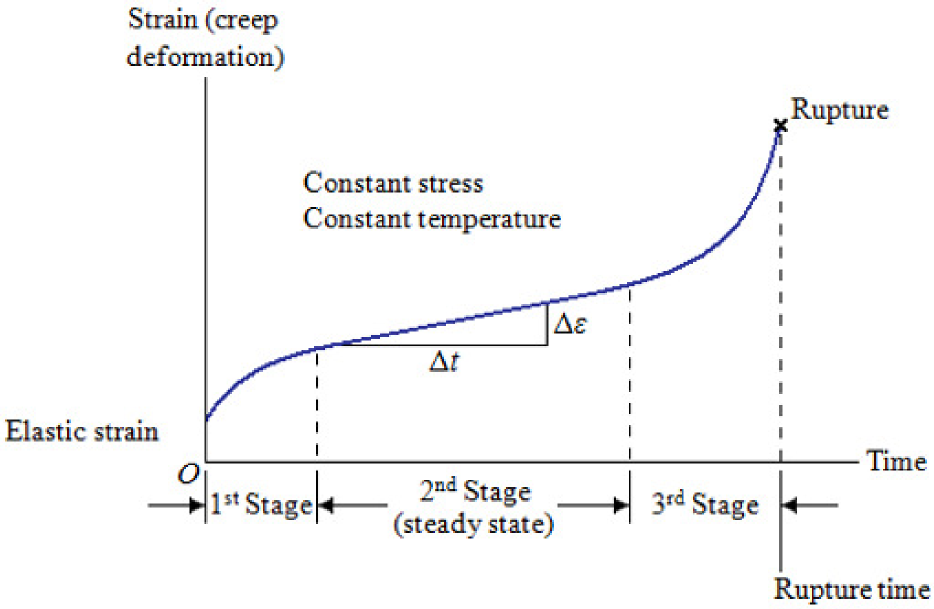

Figure 1.14: Classical evolution of the plastic deformation of a material under creep tests, from [55].

creep happens, the plastic deformation rate increases, the material is damaged and failure will occur soon.

When secondary creep is happening, Norton-Hoff's law allows determining parameters describing the viscoplastic behavior of the studied material [54]:

$$\dot{\varepsilon}_p = \alpha\sigma^n \exp\left(-\frac{Q}{RT}\right) \tag{1.36}$$

with α a constant, Q the activation energy of creep, R the universal gas constant, and T the absolute temperature. The viscoplasticity index $n = 1/m$ is obtained through:

$$n = \frac{d\ln(\dot{\varepsilon}_p)}{d\ln(\sigma)} \tag{1.37}$$

Creep tests in nanoindentation In conventional creep testing, a force is applied to the sample and held constant. As it is shown in figure 1.15, during those experiments, the force stays constant. At a given temperature, in uniaxial tests, steady-state strain rate $\dot{\varepsilon}$ is correlated to uniaxial stress σ through the power law:

$$\dot{\varepsilon} = \alpha_T\sigma^n \tag{1.38}$$

Because stress and hardness are related to each other, a similar expression should be observed in nanoindentation experiments [56]:

$$\dot{\varepsilon}_{ind} = \alpha_{ind}H^N \tag{1.39}$$

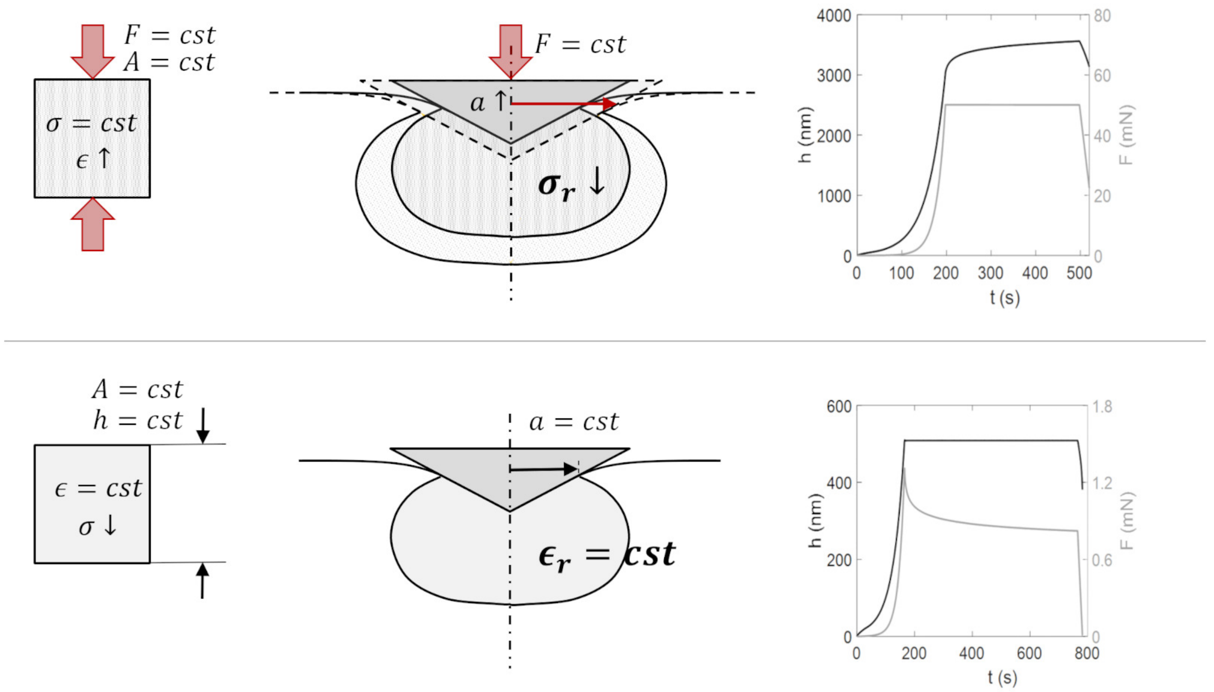

Figure 1.15: Comparison of creep and relaxation experiments adapted from [22, 57]. On top are the representations of uniaxial and indentation creep testing and the changes of load and depth during indentation creep testing. During such tests, the load is kept constant which leads to an increase in the contact depth and so of the tested volume. On the bottom are the representations of uniaxial and indentation relaxation testing and the evolution of load and depth during indentation relaxation testing. During such tests, the depth is maintained constant which leads to a decrease in the load: the tested volume stays constant.

where α_{ind} and N are material constants, linked to α_T and n respectively. If steady-state creep is reached, $N = n$. So, using equations 1.32 and 1.39, one can determine the creep properties of its samples.

To be able to perform long-term creep measurements (a few minutes to a few hours), one should take rid of the thermal drift that impacts the displacement. Maier *et al.* [58] propose to apply the CSM method not only during the loading phase of the indentation test but also through the loading-creep segment. It enables defining the indentation creep rate thanks to Sneddon's equation:

$$\dot{\varepsilon}_{creep} = \frac{\dot{S}}{S} \tag{1.40}$$

Moreover, hardness during the creep segment is also expressed as:

$$H_{creep} = \frac{4\beta^2}{\pi}\frac{PE_r^2}{S^2} \tag{1.41}$$

Fortunately, stiffness is not really sensitive to thermal drift which allows for more precise long-term experiments. The strain rate sensitivity m is then obtained through:

$$m = \frac{\partial H_{creep}}{\partial \dot{\varepsilon}_{creep}} \tag{1.42}$$

The activation volume of creep V can be computed:

$$m = \frac{\sqrt{3} k_B T}{V \sigma_r} = \frac{\gamma \sqrt{3} k_B T}{V H_{creep}} \tag{1.43}$$

where k_B is Boltzmann's constant and γ is the constraint factor previously defined.
Some improvements to the classical creep tests have been lately proposed. For instance, Maier *et al.* [59] developed strain rate jump experiments. Abrupt variations of $\dot{P}/P$ are carried out during the indentation experiment. It leads to measurements of different hardness using only one indentation test. Such tests "only" allow to go down to strain rate of $10^{-3}s^{-1}$. More recently, Prach *et al.* [60] proposed a constant contact pressure creep test. By keeping the value of P/S^2 constant, the hardness stays constant at a chosen value. Through those tests, they reach strain rate value down to $10^{-6}s^{-1}$. However such tests greatly increase the contact area.
Because of the creep test conception in indentation, there are very huge increases in the depth and so of the contact area during the creep segment (see figure 1.15). The tested volume during creep indentation tests increases. This could impact the results if the tests are performed at low depths, where hardness is not a constant, and where the tip area function is really dependent on calibration. To overcome this issue, one should then conduct relaxation experiments, presented in the next section.

Relaxation experiments in nanoindentation In relaxation tests, the idea is to maintain the contact area constant during the holding segment [61–63]. As it can be seen in figure 1.15, in course of relaxation experiments, the depth is kept constant and the load decreases during the holding. If one considers the cavity model proposed in [48], one can observed that the ratio c/a (with c the limit of the plastic zone) is proportional to $(E/H)^{1/3}$. As hardness decreases during relaxation tests, the plastic zone expands during the relaxation segment. There is a small increase of tested volume in indentation relaxation tests, but negligible compared to the one observed in indentation creep tests. Indeed, its variations with hardness ($\Delta c/c = -1/3 \Delta H/H$) are much lower compared to the one in the indentation creep test ($\Delta c/c = -5/6 \Delta H/H$). As for creep tests, once the strain rate and stress are computed, strain rate sensitivity and activation volume can be determined.
In [64], Baral *et al.* analyzed in more detail the relaxation experiments. Their main conclusion was that one should conduct the constant strain rate loading procedure to remove the effect of the maximum depth on measurements. Their next development now allows them to perform long-time relaxation tests [57] with low impact of the thermal drift. Unfortunately, displacement is very sensitive to the thermal drift: keeping it constant leads to high fluctuations in load and stiffness measurements. Through equation 1.6, one should remember that the contact area is proportional to $(S/E_r)^2$. If one maintained S constant, the contact area should also remain

constant. But if S stays constant, how to define the strain rate? Following their analysis, the relaxation strain rate $\dot{\varepsilon}_{rel}$ is computed using the representative stress variations during the holding phase:

$$\dot{\varepsilon}_{rel} = \frac{1}{E}\left|\frac{d\sigma_r}{dt}\right| \tag{1.44}$$

When performing such tests on fused silica and PMMA, consistent results with previous creep data were obtained [57]. Moreover, those tests allow going down to strain rates around $10^{-8}s^{-1}$. Relaxation experiments are complementary to creep ones.

I.D. Critical depth impacting the mechanical properties

To calibrate the system (see section I.B.5.), fused silica is usually used because it is known to have a constant Young's modulus and hardness in depth. However, on other materials, the mechanical properties could depend on depth. It then asks the following question: at which depth should the tests be carried out? Let's now focus on two phenomena linked with depth: the pop-in phenomenon and the Indentation Size Effect (ISE).

I.D.1. The pop-in phenomenon

The pop-in phenomenon is detected by outbursts on the load-displacement curve (see figure 1.16 performed on CaF_2 samples). On the CaF_2 (111) cleavage plane after abrasive polishing, the load-displacement curve is continuous. On the opposite, on the CaF_2 (111) cleavage plane, the load-displacement curve presents a jump at $0.2mN$ load. The load-displacement curves then merge at higher loads. This burst marks the change in the deformation mechanism in the sample. Before the pop-in event, the loading and unloading curves made on the sample overlap: the deformation is purely elastic and can be described using Hertz's theory [65]. Therefore, after the pop-in, the deformation becomes elasto-plastic. Schuh *et al.* [65] proposed a model to study the pop-in probability depending on the applied load on the sample, temperature, and loading rate.

Caution has to be taken when analyzing the origin of the pop-in in samples: it could come to the nucleation of dislocations to accommodate the deformation. However, on aluminum samples, for instance, it could also be linked with the oxide film breakdown [67]. Moreover, it is impacted by the dislocations' distribution in the sample before the experiment [68], as shown in figure 1.16.

I.D.2. The Indentation Size Effect

In section I.B.2., the Principle of Geometric Similarity is explained. This principle states that for a self-similar indenter (with no characteristic length) the stress and strain fields during indentation are geometrically similar whatever the depth. So, for homogeneous materials, Young's modulus and hardness should be independent of the depth. However, as it can be seen in figure 1.17, even if the constant strain rate tests ($\dot{P}/P = cste$) are performed with a Berkovich tip, the hardness of CaF_2 decreases with increasing depth. This "smaller is stronger" effect is the Indentation Size Effect (ISE) [69].

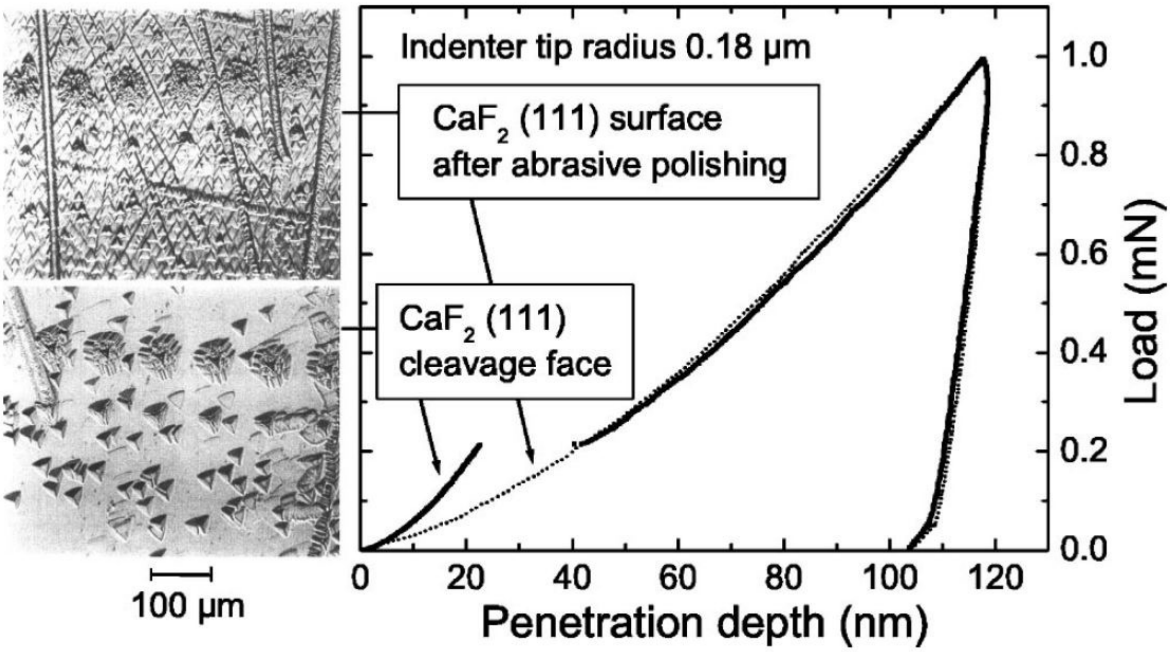

Figure 1.16: Load-displacement indentation curve on CaF_2 samples, from [66]. As can be seen, the load curves of the two samples are superimposed at large depths but are really different at shallow depths. An outburst can be observed on the CaF_2 (111) cleavage plan: this is a pop-in.

Under a critical depth, the tested volume is no longer a representative volume of the bulk material. The defects in this volume are not representative of those presented in the bulk material. Nix and Gao[73] introduced a model based on geometrically necessary dislocations to quantify this phenomenon. Worldly used to describe this phenomenon, some improvements have been proposed to define the characteristic length [74]. In [69], Pharr *et al.* compute all the results previously obtained on the topic. To analyze this effect, one should pay attention to some points: first, the surface preparation has to be properly controlled. Moreover, as this effect depends greatly on the depth, the tip area function must be well calibrated. At last, as CSM applied an oscillation on the specimen, it could induce a hardening or a softening at the low depths. CSM measurements are not recommended if one wishes to study this effect.

I.E. Conclusions on indentations tests

Since the last century, macro-indentation experiments have been democratized with Brinell's, Vicker's, and Rockwell's hardness tests. Because one want to characterize smaller samples at smaller scales, instrumented nanoindentation has been developed. Based on the measurement of the load-displacement curve and the use of a contact model, mechanical properties such as hardness, Young's modulus, and viscoplastic properties can be computed. Thanks to the implementation of the CSM mode, such properties can also be obtained against depth. Nevertheless, some precautions have to be taken when analyzing the data: some pop-in events and the Indentation Size Effect can occur. If there is no measurement artifacts, such effects give information about the sample state and response to mechanical loading.

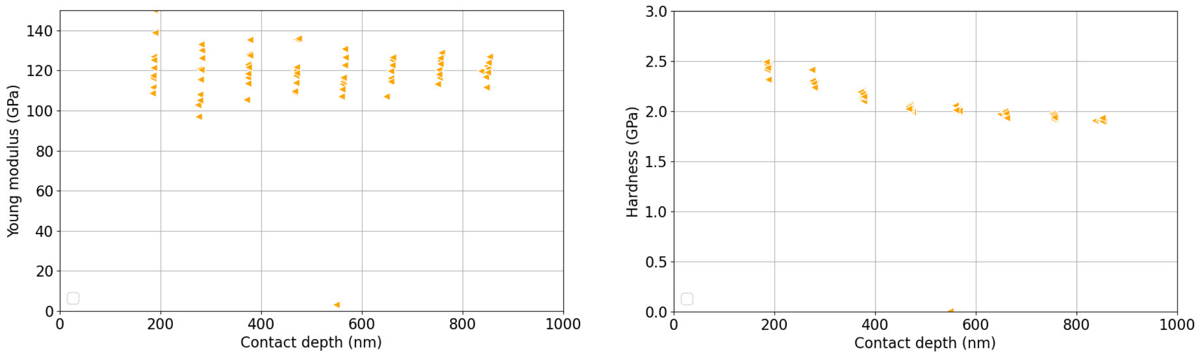

Figure 1.17: Evolution of Young's's modulus and hardness against depth on CaF_2 samples determined using a constant loading rate $\dot{P}/P$ mode with a Berkovich tip. Although P/S^2 is a constant at large depths ($> 500nm$) on this sample, hardness falls as depth increases. This effect was observed on diverse materials [70–72].

Until now, the tests are carried out at room temperature. However, the mechanical properties of materials can change with temperature. To be able to characterize such changes in properties with temperature, it becomes compulsory to perform indentation experiments at low and high temperatures. Nanoindentation at high temperatures will be the next focus point.

II. High-temperature nanoindentation

As at room temperature, high-temperature nanoindentation consists in measuring the load-displacement curve and using it to obtain the mechanical properties of the studied material. The determination of the material's properties is carried out the same way at room and high temperatures. However, whereas the load-displacement curve's measurement is quite simple at the ambiance, it becomes more complicated when temperature increases.

This section focuses first on the development of high-temperature nanoindentation instruments before addressing the issues of the heating system, the control of the environment during the indentation test, the tip choice in temperature, and the stiffness of the device.

II.A. The development of the high-temperature systems

The development of high-temperature nanoindentation tools starts in the 1990s. With their apparatus, the High-Temperature Mechanical Properties Microprobe, Lucas and Oliver [75] could carry out measurements under high vacuum between −100 °C and 300 °C. They mechanically characterized indium samples from −100 °C to 75 °C.

In 2000, Smith and Zheng [76] modify a NanoTest 600 (Micro Materials Ltd) tool to head up to 500 °C, under inert gas. To protect the column behind the tip, a copper shield was used. Before performing tests at 200 °C, the tip and specimens were maintained for 3 hours at the set temperature to achieve thermal equilibrium, and calibration was conducted before the experiments.

Currently, after new implementations, the nanoindentation devices allow going up to 1000 °C

[77–79]. As high temperature becomes more popular, the number of apparatus greatly increases. However, some features remain: the atmosphere has to be controlled, the sample and the tip have to be heated, some time should be taken to reach thermal equilibrium, etc.

II.B. How to heat the whole system

The heating system is the first point to address. In [75], Lucas and Oliver heated the tip and the sample utilizing two independent heating systems. On the opposite, in [80], the system used by Schuh *et al.* only heated the sample. The tip was heated through thermal contact with the sample. What is the best solution? To answer, one need to understand why thermal equilibrium is compulsory to obtain good results.

Thermal dilatation Let's consider a tip that is at a lower temperature compared to a sample. When the contact between the two happens, the tip will be heated a little and the sample cooled a little. So the tip will thermally dilate and the sample thermally contract. As linear dilatation coefficients are of the order of $1 \times 10^{-6}\,\mathrm{K}^{-1}$ to $1 \times 10^{-5}\,\mathrm{K}^{-1}$, for a tip of 1 mm long, a rise of temperature of 5 K leads to an increase of the length of 5 nm to 50 nm. Moreover, the sample surface will also change by a few nanometers during the contact. Such variations are huge and can greatly modify the contact and so the measured mechanical properties. To decrease this effect, one should be sure that the sample and the tip are at the same temperature near the contact [81].

Thermal drift and equilibrium in temperature At room temperature, the entire system is usually allowed to stabilize for a few hours inside a SEM or environmental chamber before conducting any experiments. This reduces thermal drift during the test. The classical way to correct thermal drift [27] is to determine it at 90% of the unloading segment. Supposing that it is constant during the test, one can redress his data (see figure 1.18).
At high temperatures, achieving thermal equilibrium in a reasonable time is a little more touchy. A first solution [82] would be to heat the whole test chamber to have all the pieces at the same temperature and to get rid of the thermal drift. Unfortunately, the electronics that control the system could not work at really high temperatures. This solution is only feasible at less than 100 °C.
To go up to higher temperatures, the tip and the sample should be locally heated up while the rest of the system should be maintained near room temperature and protected from infrared radiation. In [80], Schuh *et al.* proposed to heat only the specimen. The tip would be heated through thermal contact with the sample before each experiment. In [81], Everitt *et al.* conducted numerical simulations on the contact between a cold tip and a hot specimen (gold or fused silica). They showed that if such an apparatus allows heating a diamond tip against the fused silica sample, it doesn't work with the gold sample. As gold is a good thermal conductor, it is cooled down by the cold tip.
So to ensure better thermal stability, the tip and the sample should be heated up independently [83]. As they need to be at the same temperature at the contact, a thermal calibration should

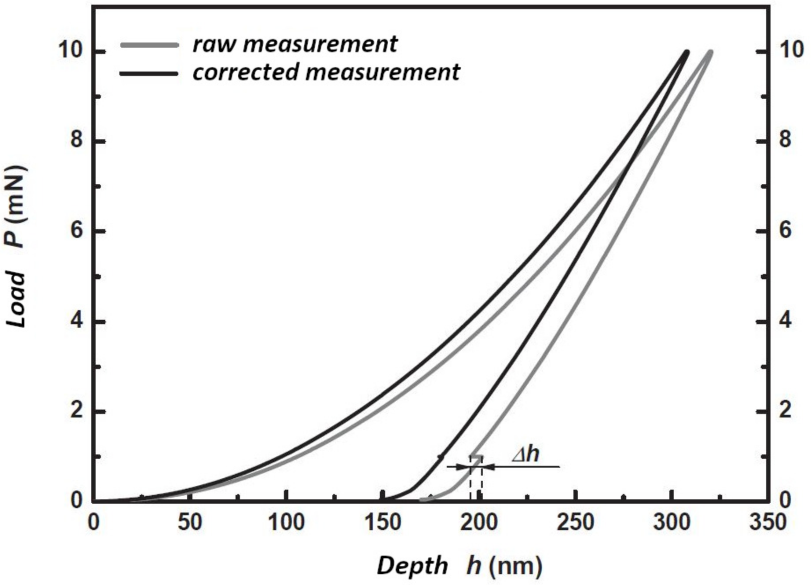

Figure 1.18: Load-displacement curve on fused silica from [27]. The thermal drift measurement is performed during unloading on the gray curve. Once corrected, the black curve can be exploited to obtain the properties of the sample.

be carried out to adjust the temperature set points of the specimen and the tip heating systems. Diverse methods exist to do so. The technique of KLA Nanomechanics [79] (see figure 1.19) consists of square signals applied on the tip. The tip will indent the same point of the sample multiple times. If temperatures equal at the surface, the tip should not dilate nor contract during the contact. If some displacement variations are observed, the set points should be adjusted until the match is obtained. The method used by Alemnis is different [84].

Once the set point is obtained, thermal stability should be established prior to making experiments at room temperature. Again, thermal drift should be characterized to minimize errors in hardness and Young's modulus determination.

II.C. Test environment for high-temperature experiment

As one want to reach really high temperatures, the environment of tests should be controlled to prevent oxidation. The heating parts of the heater are usually in metals: such materials will be oxidized if tests are performed in the air. This will considerably reduce the lifetime of the system.

Moreover, in the air, metal samples will also be oxidized. Oxidation leads to the creation of an oxide at the surface of the specimen. As nanoindentation gives mechanical information near the surface of the sampling, it becomes complicated to obtain the properties of the sample. Oxidation is greatly favored by high temperatures: it is important to control the environment of testing to lessen this phenomenon, especially when doing high-temperature tests.

One answer is to conduct tests in an inert environment, for instance, high-purity nitrogen or argon. This solution increases the time before the detection of oxidation on silicon in an argon

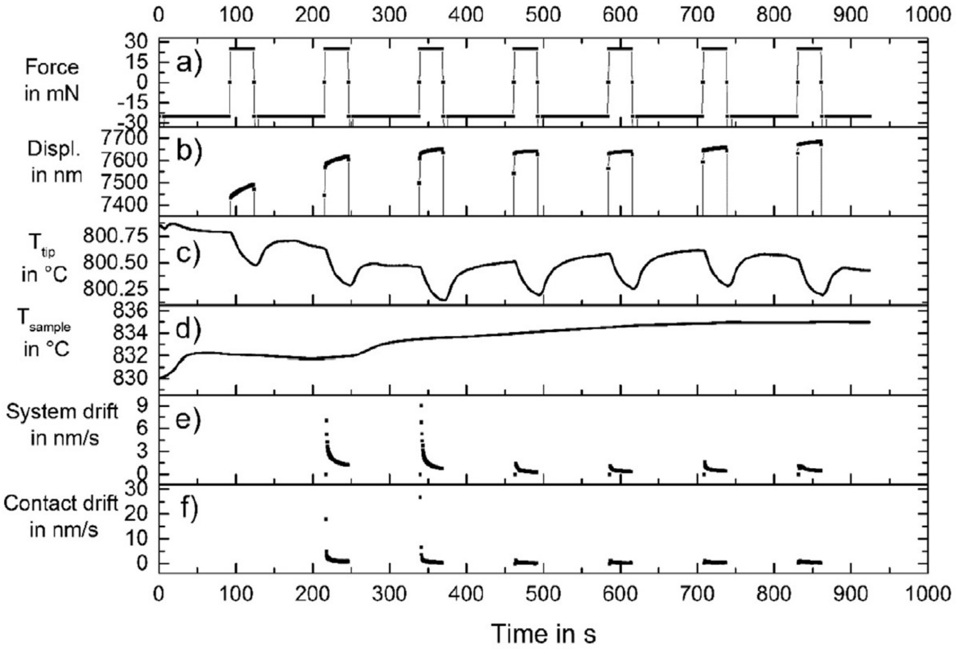

Figure 1.19: Procedure implemented to evaluate the temperature settings of a sapphire tip and a nickel sample to have thermal equilibrium at the contact, from [79]. A rectangular signal in force is applied on the tip. During the contact, the displacement and the drift are monitored. By calibrating the temperature setting, thermal equilibrium is achieved.

atmosphere at 500 °C and increases the thermal stability [85]. Unfortunately, even if it is a simple answer to implement, it is not enough to go to 1000 °C. It "only" works for materials that are not reactive to oxygen and for temperatures up to 400 °C to 500 °C. In [83], Wheeler *et al.* showed that oxidation occurs on tungsten at 700 °C for 1 h under argon.

Another idea is to perform the test under vacuum. As illustrated on tungsten at 700 °C during 100 h in [83] or on nickel at 630 °C during 48 h in [86], oxidation was greatly reduced on those samples. No surface degradation was detected. To carry out nanoindentation experiments at high temperatures, the system has to be under vacuum.

II.D. Choosing a tip to go to 1000 °C

As all materials soften in temperature, the tip's mechanical properties evolve in temperature. Unfortunately, it can also be oxidized or react chemically with the specimen. This will guide the choice of the tip for the high-temperature tests.

II.D.1. Mechanical properties in temperature

Hardness To be sure that indentation experiments are correctly carried out, the tip has to be harder than the sample: the objective is that the tip generates plasticity in the sample. The hardness of the tip should be 20% higher than the one of the samples. To limit tip deformation, Wheeler *et al.* [87] advise having $H_{tip}/H_{sample} >$ 100–1000%. As diamond is the hardest material at room temperature, using a diamond tip to conduct nanoindentation testing is very common at this temperature.

When doing experiments at high temperatures, one has to verify that its tip remains hard enough to limit the damage (see table 1.4). As it can be seen, diamond stays the hardest material in this temperature range. However, one can also employ tungsten carbide or sapphire to perform high-temperature measurements as their hardness is still high.

Young's modulus As hardness, Young's modulus also changes with temperature. As seen in equation 1.7, the Young's modulus is determined from the measured reduced modulus and the tip modulus. So one has to take the tip modulus variations (see table 1.4) into account to reduce errors. Wheeler *et al.* [87] have quantified these errors on Young's modulus: it can be of a few percent at 700 °C.

II.D.2. Structure and chemical reactivity

Diamond structure The diamond structure is an unstable crystallographic structure at room temperature and atmospheric pressure (see figure 1.20). It is progressively evolving back to its stable phase which is graphite. However, at 25 °C this phenomenon is so slow that it takes thousands of years. Nevertheless, when increasing temperatures, as diffusion becomes easier, the atoms can reorganize more quickly. So it should be verified that at the testing temperature, the diamond tip does not transform into coal.

In literature, the graphitization of diamonds was analyzed a lot. In the case of diamond single crystal, the studies [89–94] pointed out that graphitization of diamonds starts to be detected around 1500 °C after 30 min and that this phenomenon is thermally activated. So for applications up to 1000 °C under vacuum, graphitization is not expected.

Oxidation Oxidation is a chemical reaction with oxygen that will damage the tip. As the tip geometry is of primary importance to determine the material's mechanical behaviors, tips have to be inert to oxidation at the testing temperature.

Oxidation of diamond single crystal in diverse atmospheres with different oxygen contents was studied [95–100]. They found out that natural diamond starts to oxidize in the air at 500 °C to 700 °C. The results of Ando *et al.* [101] and of Pehrsson *et al.* [102] on hydrogenated

Table 1.4: Evolution of Vicker's hardness and Young's modulus in temperature for divers tip materials, from [87].

Material	Diamond		Tungsten Carbide WC		Sapphire Al_2O_3	
T (°C)	H (GPa)	E (GPa)	H (GPa)	E (GPa)	H (GPa)	E (GPa)
25	100	1140	25	700	20	460
400	87	1130	15	690	12	450
700	75	1110	10	680	8	430

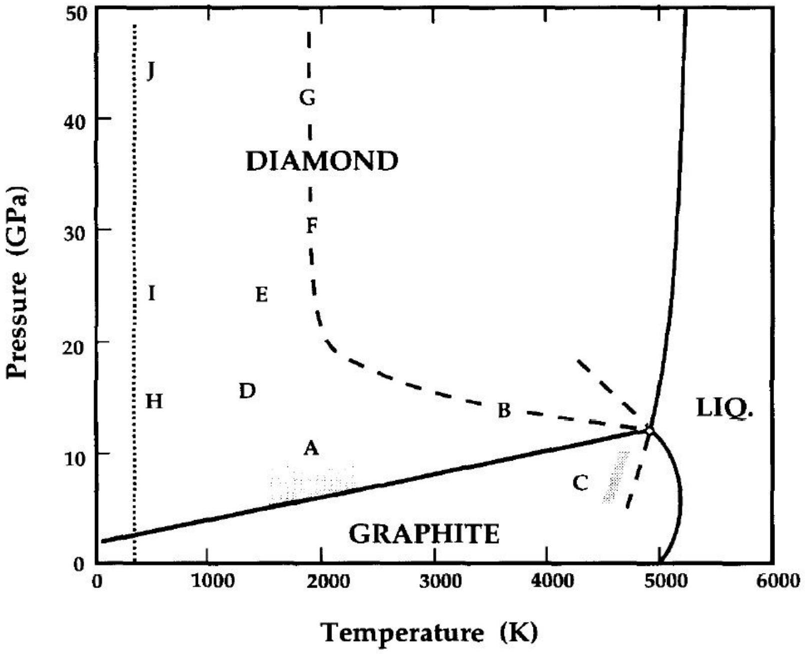

Figure 1.20: Pressure-temperature phase diagram of carbon from [88]. As it can be seen, the diamond is not a stable structure in ambient conditions.

diamond clearly point out the influence of the vacuum: when Ando indicates oxidation at 300 °C in 20%O_2 in Ar, Pehrsson sees oxidation at 850 °C to 950 °C in dry O_2 in Ultra High Vacuum. As shown in [103], diamond is very sensitive to oxidation in the air or commercial purity argon. If one wants to conduct tests with a diamond tip to take advantage of its high hardness in temperature, one has to pay attention to this problem.

Moreover, tungsten carbide or sapphire has correct hardness values in temperature. As pointed out in [103], sapphire is inert in presence of oxygen: it is a good compromise to carried out nanoindentation at high temperatures.

Chemical reactivity A last important issue is the chemical reactivity between the sample and the tip. The classical example is the indentation of steel using a diamond tip. During the contact, the carbon will diffuse inside the iron structure to form Fe_3C: the tip will be greatly degraded by this process (see figure 1.21). Moreover, Minnert *et al.* [79] show that the tip area function of a sapphire tip changes when performing indentation tests at high temperatures on nickel.

Wheeler *et al.* [87] have studied the chemical reactivity of tip/sample couples. One should use their work to verify the compatibility of a tip with a sample before making experiments.

II.E. Load-frame stiffness in temperature

As seen in equation 1.4, the contact stiffness depends on the load frame stiffness. One has to verify that the system stays stiff enough in temperature to get corrected results.

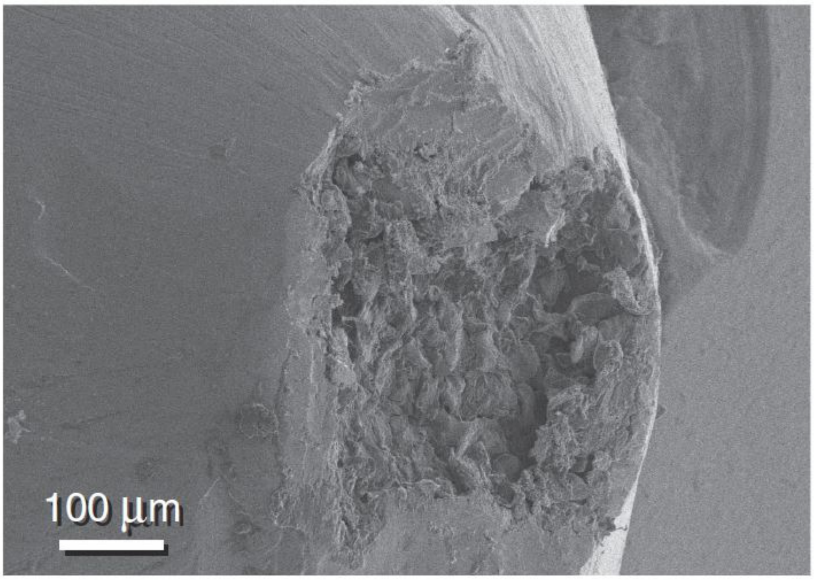

Figure 1.21: SEM observation of the damage of a diamond tip after indentation performed on steel at 500 °C, from [87].

The sample holding has to stay stiff with temperature. During room temperature experiments, the specimen is usually glued on its holder. Nevertheless, classical cyanoacrylate glues are not temperature resistant. Another system has to be utilized to retain the specimen. A solution would be to use high-temperature ceramic glue instead. Minnert *et al.* [79] propose a different strategy: they clamp the specimen on the sample holder to mechanically maintained it in temperature. As shown in their paper, the stiffness of the system stays high even at really high temperatures.

II.F. Conclusions on indentation tests in temperature

To carry out high-temperature nanoindentation experiments, recent developments in devices now allow making tests up to 1000 °C. To ensure thermal stability, the tip and the sample have to be heated independently. So, one should perform temperature matching between the tip and the sample to reduce thermal drift. As the control of the sample surface is important, tests are usually conducted in vacuum to lessen its oxidation. Moreover, the tip is vital to obtain correct mechanical properties. Controlling its area function is compulsory: one should verify that the selected tip will not evolve in temperature. The article by Wheeler *et al.* [87] is a good reference to choose a tip.

As temperature increases, the mechanical properties of the sample could vary. For instance, Schuh *et al.* [104] presents the effect of temperature on the pop-in phenomenon. Same, Franke *et al.* [105] analyze the impact of temperature on the Indentation Size Effect on copper at 200 °C. Moreover, at high temperatures, the structure of the material could change. Using nanoindentation in temperature, one would be able to characterize such variation. For instance, in [106], Baral *et al.* study isotherm recrystallization of a cold-rolled A1050 aluminum through

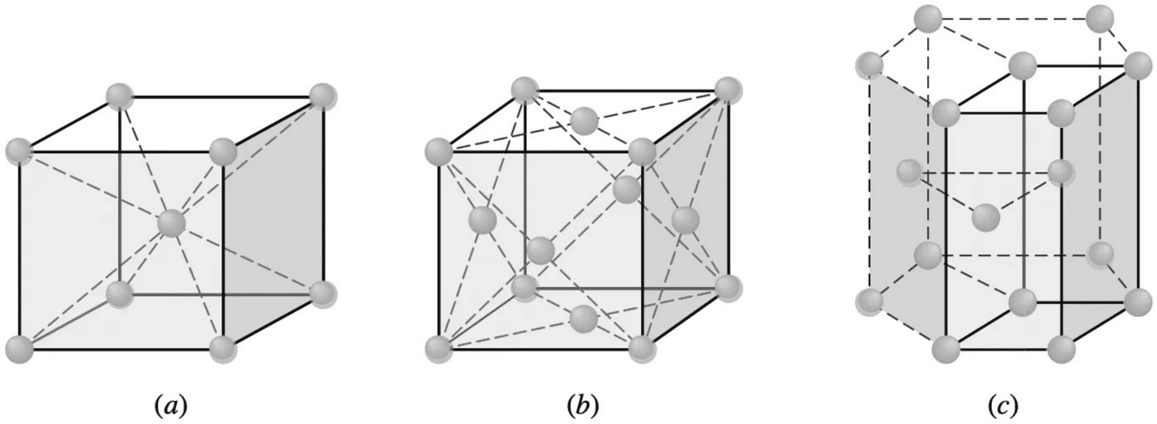

Figure 1.22: (a) BCC, (b) FCC, and (c) HCP crystalline systems, from [107].

in-situ nanoindentation measurement. The microstructural evolution of crystalline structures is the next focus point.

III. Structural changes in crystalline metals

Steel is a material that is widely employed nowadays, in a huge number of applications. Depending on its chemical composition, the applications change a lot. Moreover, depending on the thermal treatment, the same grade could have really distinct properties and so different applications. Such effect is due to the relation between the microstructure of the material and its mechanical properties.

Let's analyze the characteristic of a crystalline structure before focusing on the link between the microstructure and the properties of the corresponding material. In the end, the phenomena that make the microstructure of a metal changes with temperature will be studied.

III.A. Microstructure, you said microstructure

Crystal lattice A crystalline structure is a long-range ordered arrangement. Atoms are organized in such a manner as to get this long-range order. Three systems are classically defined when studying metals: the Face-Centered Cubic (FCC), the Body-Centered Cubic (BCC), and the Hexagonal Close-Packed (HCP) systems (see figure 1.22). Those lattices are characterized by the way atoms are arranged in the material. The FCC and HCP structures are dense structures since every atom has 6 neighbors in the plane. They differ by the number of stacking planes: 3 in the FCC structure and 2 in the HCP structure. The BCC structure is less dense: each atom has 4 neighbors in the plan [108].

If all the atoms are packed according to a crystalline structure everywhere in the material, it is a perfect crystal with no defect. This structure would be the less energetic one. However, there are faults when the material is produced: the perfect structure is never obtained. When there is a defect, other atoms should reorganize near the defect. As they are no longer in the more

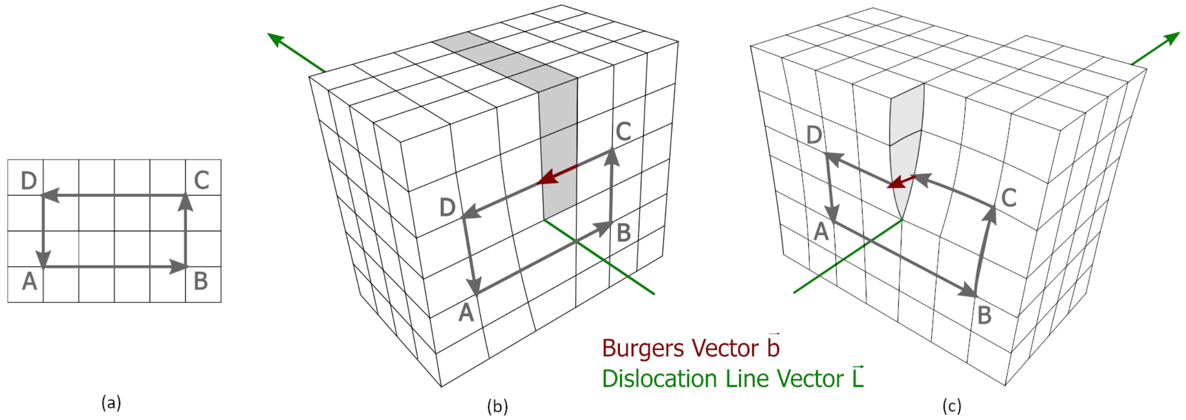

Figure 1.23: Schematic representation of (a) perfect crystal, (b) edge, and (c) screw dislocations, adapted from [109].

stable position, locally the energy increases.

Defect in the crystals Different defects can be observed in a crystalline structure. The first one is the vacancy: an atom is missing in the structure. The atoms around this vacancy miss a neighbor: as on the surface, they are in a less stable position.

Then one can find a linear defect, the dislocation, defined by Orowan [111], Polanyi [112] and Taylor [113] in the 1930s. Let's consider a perfect lattice as in figure 1.23 a). Atoms are at the node of the lattice. As it can be seen in b), a half-plan of atoms was added between points C and D but does not exist between A and B. This plane forms a linear defect, named an edge dislocation in this case. In c), a half-plan of the atoms was slipped: a screw dislocation was created. Each dislocation is characterized by a dislocation line $\vec{L}$. The Burger vector $\vec{b}$ is defined as the required vector to complete the cycle ABCD compared to the perfect crystal. If $\vec{L}$ and $\vec{b}$ are co-linear, the dislocation is a perfect screw one. If they are perpendicular, it is an edge dislocation. Usually, in materials, dislocations are mixed, constituted of a combination of edge and screw dislocations.

Let's now consider the planar defect: the grain boundary. A liquid metal that is cooled down will crystallize: atoms should organize to form crystals that will grow until the whole structure is solid. The thing is that multiple crystals grow at the same time: the final structure is not composed of a single crystal but of a polycrystal with multiple grains. Each grain has a crystalline structure with a specific orientation. Two consecutive grains have a distinct orientation: at their boundary, atoms do not really know how to arrange because of this difference in orientation. In figure 1.24, it is clear that at the junction of the two grains, the atoms cannot arrange completely: it is a grain boundary.

Finally, 3D defects such as inclusion can be found. During the solidification process, some particles (e.g., oxide) can be trapped inside the material. As they have different properties compared to the solid, they could be fatigue crack nucleator or areas of high-stress intensity which is deficient in the material.

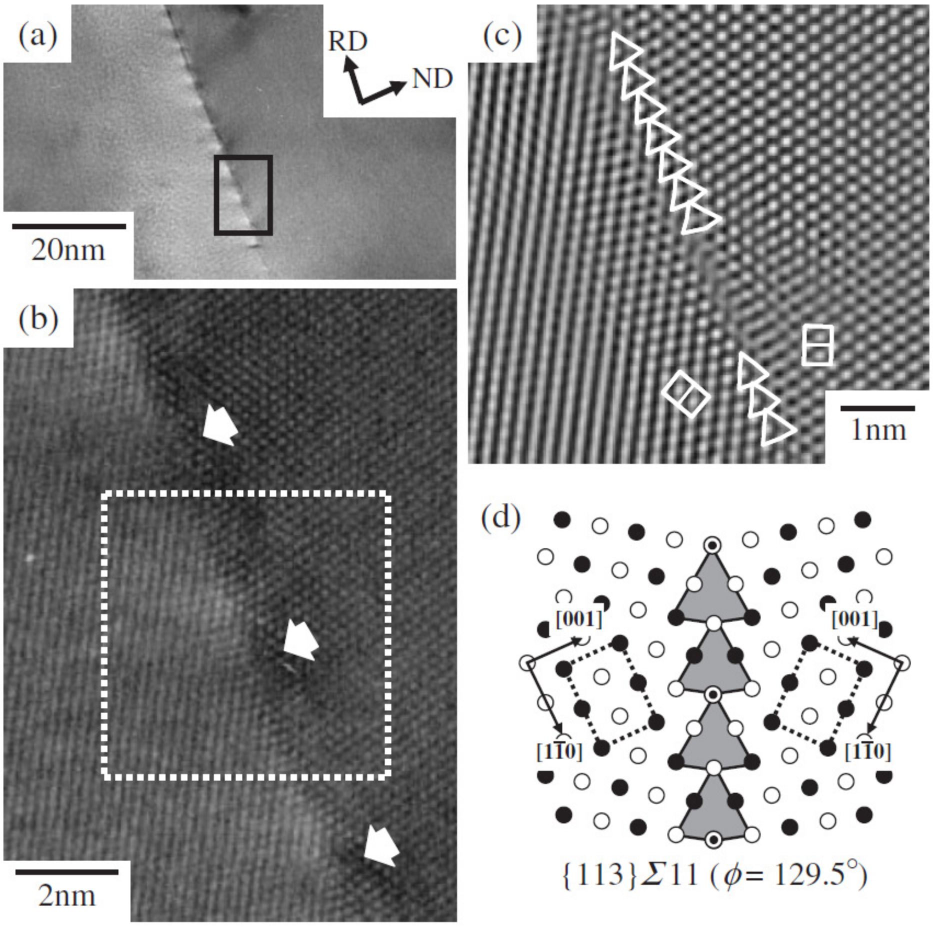

Figure 1.24: (a) TEM image and (b) HR-TEM image of a high angle grain boundary close to Σ11 STGB in 6cARB-Cu, (c) the FFT image of the dotted square region in (b) and (d) the atomic structure of the 113 Σ11 STGB obtained by MD simulations. From [110].

III.B. Links between microstructure and mechanical properties

The mechanical properties of a metal can be correlated with its microstructure. For instance, the grain size of a sample impacts its hardness [9, 114], following the Hall-Petch's relation:

$$\sigma = \sigma_y + \frac{\alpha_1}{\sqrt{d}} \tag{1.45}$$

with d the diameter of the grain and σ_y the yield stress of a large single crystal. It is not difficult for a dislocation to slip inside a grain. However, when a dislocation encounters a grain boundary, it has to pass forward this boundary to slip to the next grain. It is more complicated than sliding inside the grain. Having little grains increases the grain boundary amount and so the hardness of a material.

According to Taylor's relation, one can link the rise of flow stress σ to the dislocation density ρ [115, 116]:

$$\sigma = \sigma_y + \alpha M G b \sqrt{\rho} \tag{1.46}$$

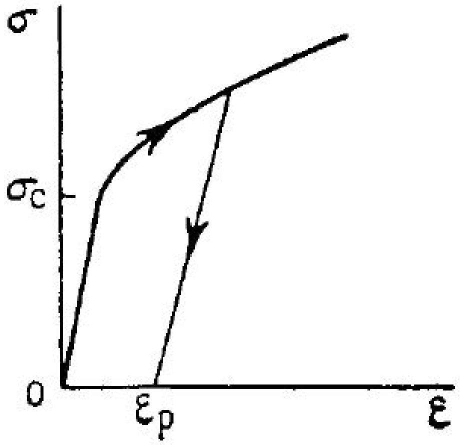

Figure 1.25: Stress versus strain curve, from [117]. When following the deformation path, as plastic deformation occurs, the sample was hardened.

where M is Taylor constant, α is a constant around 0.3, G is the shear modulus and b the Burger's vector of the material. Increasing the number of dislocations will increase their interactions. As they will be blocked by the others, it will mechanically increase the hardness of the material. The internal stress σ_i is usually defined as:

$$\sigma_i = \sigma - \sigma_y = \alpha M G b \sqrt{\rho} \tag{1.47}$$

Those relations explain why the microstructure of a specimen greatly impacts its mechanical properties.

Hardening When deforming a sample (as during cold-rolling), the material will first behave elastically, up to it yield stress σ_y (see figure 1.25). It corresponds to 0.2% of deformation in the case of metals. If the specimen is deformed to higher strains, plastic deformation and hardening happen. In this mechanism, dislocations are emitted to accommodate the deformation [117].

Anisotropy Samples are generally deformed by cold-rolling or hot-rolling: grains are deformed in specific directions. This leads to an anisotropic structure and so anisotropic behaviors. Such changes in grain shape increase the surface of grain boundaries [118].

Stored energy If the dislocation density can be quantified (usually using TEM measurements), the stored energy E_D can be roughly estimated [118]:

$$E_D = c_2 \rho G b^2 \tag{1.48}$$

with c_2 a constant around 0.5. Increasing the dislocation density increases the stored energy in the specimen: the deformed microstructural state is more energetic compared to the non-deformed one.

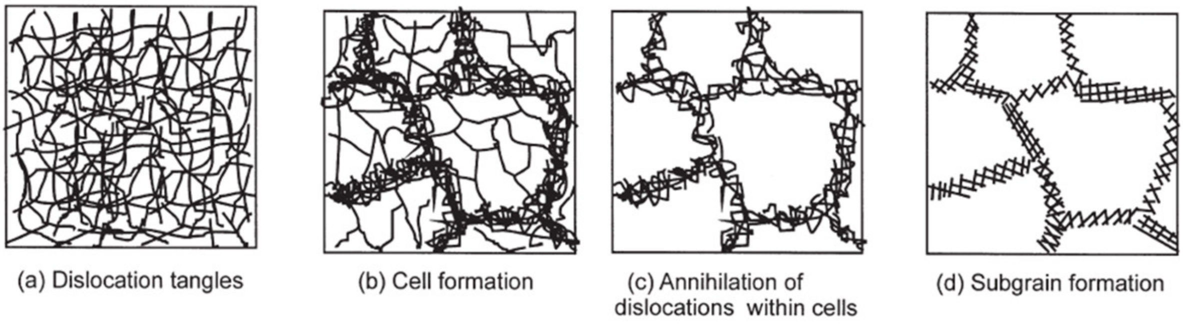
(a) Dislocation tangles (b) Cell formation (c) Annihilation of dislocations within cells (d) Subgrain formation

Figure 1.26: The recovery process in a deformed material, from [118]: inside a grain, the dislocation structure rearranges to form dislocations cells and subgrain boundaries. Such formations allow decreasing the energy stored in the sample: the plastic behavior of the material is partly restored.

III.C. Going back to a stable structure

Friedel [117] considered that two competing diffusion mechanisms will allow a deformed sample to go back to a more stable state. Through the dislocation motion inside the structure, polygonization (recovery) takes place. Once the grain boundaries start to move, the recrystallization process occurs.

III.C.1. Recovery process

Recovery [118] of a metal is a phenomenon that will restore partially the mechanical behaviors of the material, before any recrystallization. It is the annihilation and the reorganization of dislocations inside the grains structure that leads the structure to a more stable state (see figure 1.26).

This phenomenon is homogeneous: it happens everywhere in the structure. As it is a reorganization of the dislocation structure inside the grains, the grain structure is not modified by this mechanism. To reorganize the structure, the atoms should be able to move: recovery is a thermally activated process. Moreover, as it can be intuited, high stored energy levels greatly favor this phenomenon.

Usually, a distinction is made between static and dynamic recovery. Static recovery takes place after the deformation process, during the annealing of the sample. On the opposite, dynamic recovery occurs during the deformation process. Only the static recovery process will be considered in the following.

Static recovery As said, static recovery is the reorganization of dislocations inside the grain structure after the deformation process. Depending on the material, this process could arise at room temperature (for high-purity aluminum for instance) or during annealing at high temperature.

All materials cannot restore a lot. It is monitored by the stacking fault energy γ_{SFE}. As explained in [118], this energy controls the rate of dislocation climb and cross slip, which are

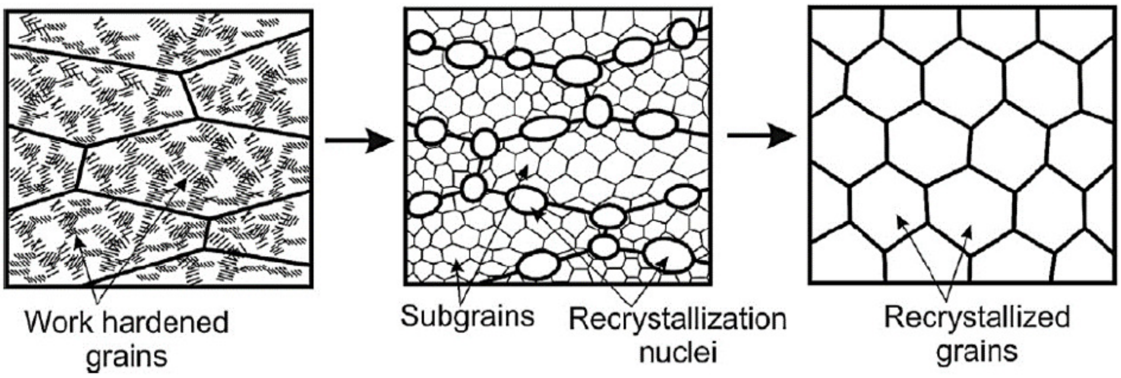

Figure 1.27: Recrystallization process in a deformed material, from [118]. The initial structure is work-hardened. While nucleation happens, recovery is also occurring inside the structure. Once nuclei grow, the new recrystallized structure supplants the old deformed one.

the mechanisms that take place during recovery. Having a high-stacking fault energy favors the recovery mechanism prior to recrystallization. Seen table 1.5, pure zirconium, aluminum, and zinc are anticipated showing the recovery process before recrystallization. On the opposite, 91Cu:9Si, cobalt (FCC), and 70Cu:30Zn are expected to only recrystallize.

III.C.2. Recrystallization process

Recrystallization is a process involving grain boundary migration [117]. It usually takes place in two phases (see figure 1.27): the nucleation and the growth of new grains [118]. Nucleation is the phase where new nuclei, free of dislocation, will form in the old structure. Growth can then occur, replacing the old grain structure with a new one, free of dislocation.

Nucleation Nucleation is the first stage of recrystallization, where new nuclei are created. A new nucleus is a structure with a high surface-over-volume ratio, which means that if too small, it is unstable. Because of the energy of its grain boundaries, it will have difficulties forming in a structure with low defect density (inside a grain with low dislocation density for instance). On the opposite, as grain boundaries or highly deformed grains have lots of defects, it is easier for a nucleus to be the more stable structure here: they are preferred nucleation sites.

Table 1.5: Stacking fault energy of metals, from [119]

Metal	γ_{SFE} (mJ/m^2)	Metal	γ_{SFE} (mJ/m^2)
Aluminum	166	Zirconium	240
Nickel	128	Zinc	140
Copper	78	Magnesium	125
Gold	45	304 Stainless Steel	21
Silver	22	70Cu:30Zn	20
Cobalt (FCC)	15	91Cu:9Si	5

Growth Once nuclei are stable, they start to grow to replace the whole old structure with a new one, free of dislocations. According to Taylor's equation (equation 1.46), as the dislocation density greatly decreases, the stress and the hardness of the system will also decrease.

Here the impact of the initial deformation state and temperature is clearly seen. The more the structure is deformed, the easier it is to form a lot of nuclei that will then grow. Moreover, as temperature increases, diffusion is easier: it also promotes recrystallization. Depending on the temperature, the annealing time, and the initial deformed state, the final microstructure could change a lot. If the deformed state is high and the annealing time is not so long, a fine microstructure with a lot of new fine grains is expected. On the opposite, a low deformed structure annealed for a long time would favor a microstructure with a few large grains. Moreover, recrystallization is a heterogeneous process: it depends on where the nucleation takes place.

Recovery can also arise and is a thermally activated process. If the structure had time to recover, the dislocation density lowers, and dislocations reorganize themselves in the structure. It becomes more difficult to begin nucleation. Nevertheless, once recrystallization has started, the dislocation density is drastically decreased. Recovery is no longer happening. The recovery and recrystallization processes are competing phenomena [117, 118].

Same as for recovery, a distinction is done between static and dynamic recrystallization. Static recrystallization occurs during annealing, after the deformation of the structure. Dynamic recrystallization will take place when the structure recrystallizes during the deformation process.

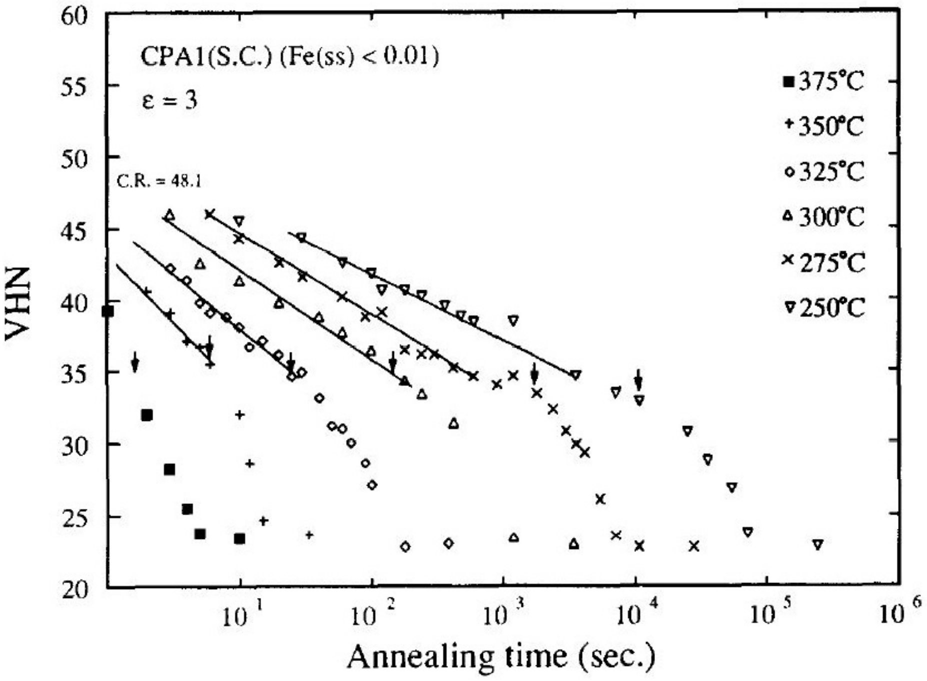

Figure 1.28: Hardness modifications during annealing of a commercial purity cold-rolled aluminum at different annealing temperatures, from [120]. As it can be seen, hardness decreases when static recovery and recrystallization occur in the samples. The arrows indicate the point where recrystallization is detected at the annealing temperature.

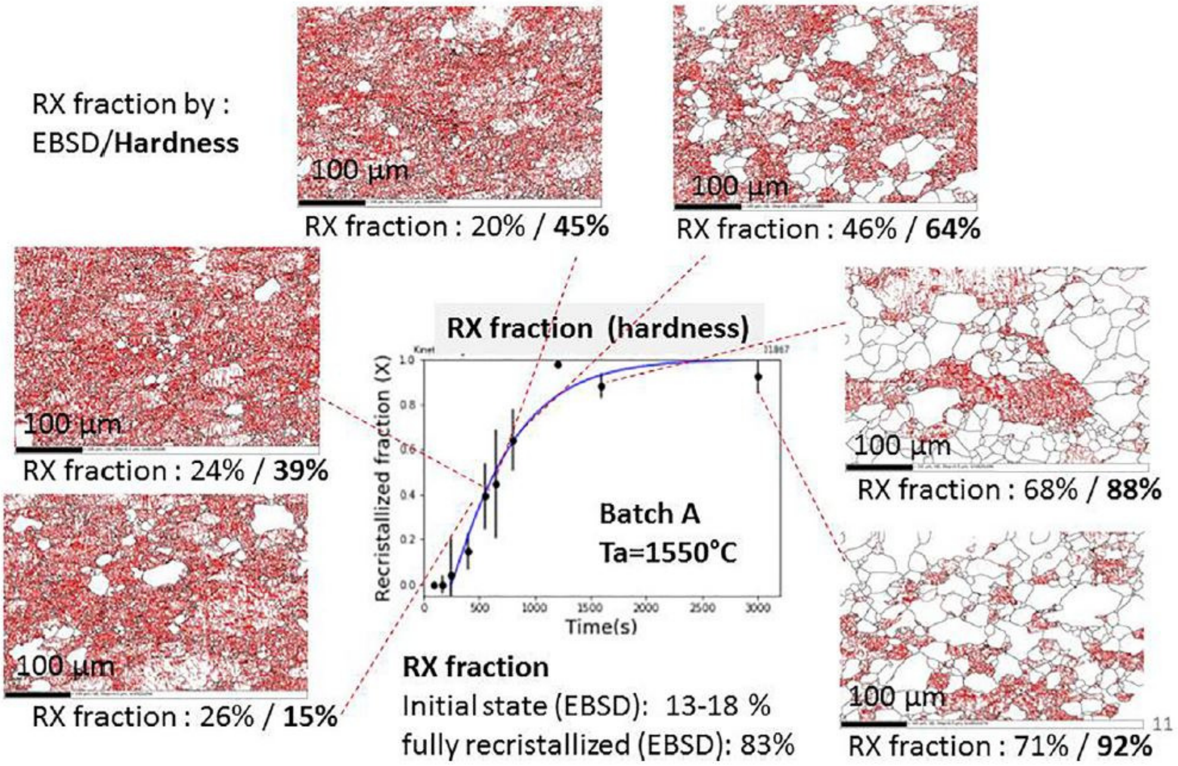

Figure 1.29: Recrystallized fraction in time during annealing of tungsten, computed from hardness and EBSD measurements, from [121].

Only static recrystallization is investigated in this manuscript.

III.D. Classical determination methods

To study the static recovery and recrystallization phenomena, various techniques are frequently used. Usually, as one wants to determine the kinetics of the phenomenon, measurements are carried out through isothermal annealing.

Post-mortem hardness As shown by Taylor's equation (equation 1.46), the density of dislocations is linked with the hardness of the sample. Classically, to detect static recovery or recrystallization, one will conduct isotherm annealing of samples. By quenching the specimens at various annealing times and performing post-mortem indentation tests, one can observe the hardness evolution due to those phenomena (see figure 1.28).

Electron Back-Scattering Diffraction EBSD is classically used to determine the microstructure of the material before and after the annealing. This confirms the microstructure changes due to those phenomena. As for post-mortem hardness data, one can either quench the samples after annealing a certain time at a given temperature and then characterize those changes [121–123]. Richou *et al.* [121] compared their EBSD results with recrystallized fraction obtained through hardness measurements (see figure 1.29). However, one can also perform in-situ EBSD

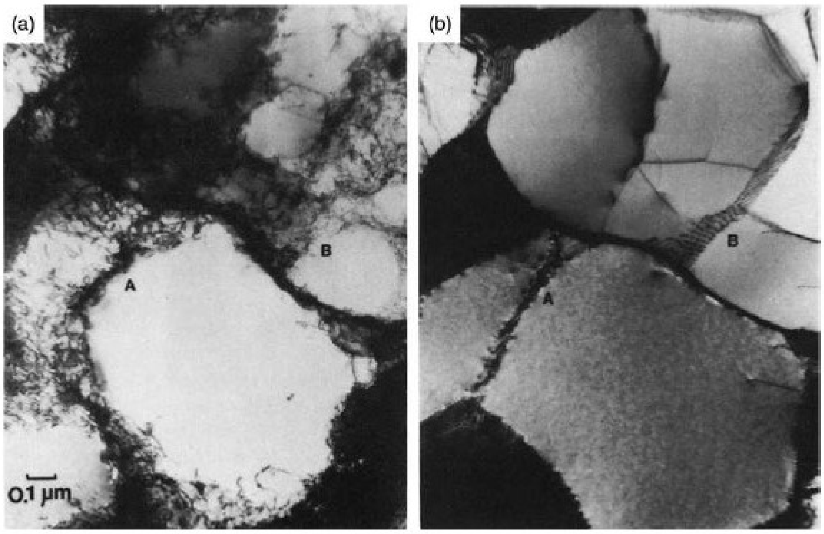

Figure 1.30: Recovery of a 10% deformed aluminum during in situ annealing at 250 °C (a) deformed structure, (b) after 2 min, from [118]. The reorganization of the dislocation is clearly noticed.

measurements during annealing inside a SEM to characterize the evolution of the sample [124, 125]. The problem here is the definition of the recrystallized grains compared to the deformed and recovered ones. In EBSD, the definitions of the recovered and recrystallized fractions are still in discussion.

Transmission Electron Microscopy Some in situ TEM measurements can also be conducted to study more specifically what happens at the dislocation levels during annealing. In figure 1.30, one can observe the dislocations organizing into cell structure during in situ annealing inside a TEM. However, such measurements are really complicated to perform.

Differential Scanning Calorimetry Finally, as phase transformations are phenomena that release or absorb heat, one can use DSC to study them. In figure 1.31, a clear peak on the calorimetric data around 300 °C is present and corresponds to the recrystallization of the aluminum specimen. However, it is usually not simple to study recovery and recrystallization of metals via DSC.

III.E. Modeling

Once the modifications in the microstructure and properties of the samples are observed, one wants to quantify the kinetic of the phenomena responsible for the changes. Modeling is then performed to understand and describe it. Let's examine the classical models of static recovery and static recrystallization.

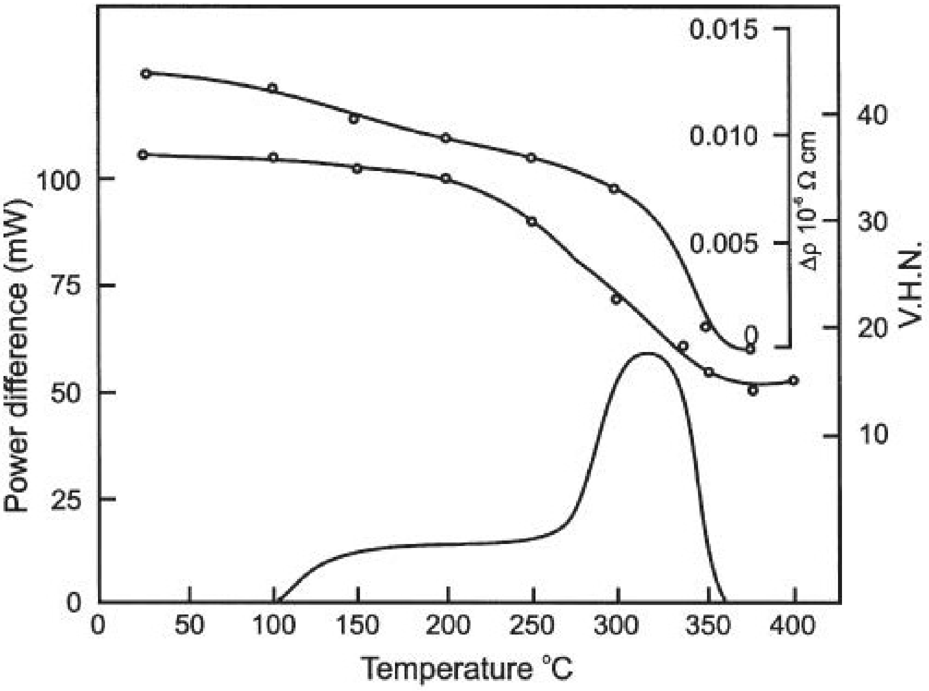

Figure 1.31: Recovery and recrystallization of a 75% deformed aluminum during DSC measurements (heating at 6 °C/min), from [118]. Comparison is done with electrical resistivity and hardness evolution on the samples.

III.E.1. Modeling of static recovery

As it is important to assess the kinetic of static recovery, numerous studies introduce models to analyze it. It is usually based on the rate of changes of the internal stress of the specimen.

Kuhlmann's model In [126], Kuhlmann *et al.* consider that deformation creates a uniform distribution of dislocations in the structure. They suggest a simple equation governing the internal stress evolution rate [120, 126]:

$$\frac{d\sigma_i}{dt} = -K \exp\left(-\frac{U_0 - \beta\sigma_i}{RT}\right) \tag{1.49}$$

where K and β are constants, R is the universal gas constant and U_0 is an activation energy. This equation indicates that recovery is a thermally activated process and is favored by a high number of dislocations.

Friedel's model For Friedel [117], the model proposed by Kuhlmann *et al.* illustrates the static recovery occurring at low temperature, by cross-slip mechanism. However, at high temperatures where climb would be the dominant mechanism of dislocation movements, the equation would become:

$$\frac{d\sigma_i}{dt} = -K\frac{\sigma_i^m}{RT} \exp\left(-\frac{U(\sigma_i, T)}{RT}\right) \tag{1.50}$$

where K is a constant and $m = 3$. $U(\sigma_i, T)$ is an activation energy whose expression depends on the internal stress and temperature.

Verdier's model To better understand what the parameters β and U_0 in Kuhlmann's model represent, Verdier *et al.* [116] propose another approach, based on observations on aluminum alloys. For them, internal stress relaxation is linked with the plastic relaxation of the structure. So:

$$\frac{d\sigma_i}{dt} = -\dot{\varepsilon}_p E \tag{1.51}$$

Using Orowan's law, they obtained the plastic relaxation rate and then the internal stress relaxation rate:

$$\frac{d\sigma_i}{dt} = -\frac{64\nu_D}{9M^3\alpha^2}\frac{\sigma_i^2}{E}\exp\left(-\frac{U_0}{RT}\right)\sinh\left(-\frac{\sigma_i v_0 N_A}{RT}\right) \tag{1.52}$$

with ν_D the Debye frequency, N_A the Avogadro constant, U_0 the activation energy at the end of the recovery process, and v_0 the activation volume of recovery. Through experiments performed on various prestrain samples, they show that the activation volume would depend on the prestrain and that U_0 for their aluminum alloy was around 170 kJ/mol to 210 kJ/mol. On other aluminum alloys [127, 128], the same activation energy range was found. The activation volume greatly depends on the alloy but is still dependent on the stress level.

III.E.2. Modeling of static recrystallization

The recrystallized fraction To model the recrystallization process, people start by defining the recrystallized fraction X. Under the equivalent strain assumption, a mixture law allows relating the measured properties with those of the initial and final state. For instance, when carrying out hardness measurements:

$$H_m = XH_{ReX} + (1 - X)H_{def} \tag{1.53}$$

where H_m is the measured hardness, H_{ReX} the hardness of the fully recrystallized state and H_{def} the hardness of the initially deformed state. By extracting the recrystallized fraction X from this mixture law, one can then model it. During annealing experiments, the recrystallized fraction behaves like in figure 1.32.

JMAK For isotherm annealing, the static recrystallization process is generally described by the Johnson-Mehl-Avrami-Kolmogorov [129–131] equation:

$$X = 1 - \exp(-[B(t - t_{inc})]^n) \tag{1.54}$$

with X the recrystallized fraction, the factor B depending on the annealing temperature, t_{inc} the incubation time needed to nucleate the new grains, and n the Avrami exponent, between 1 and

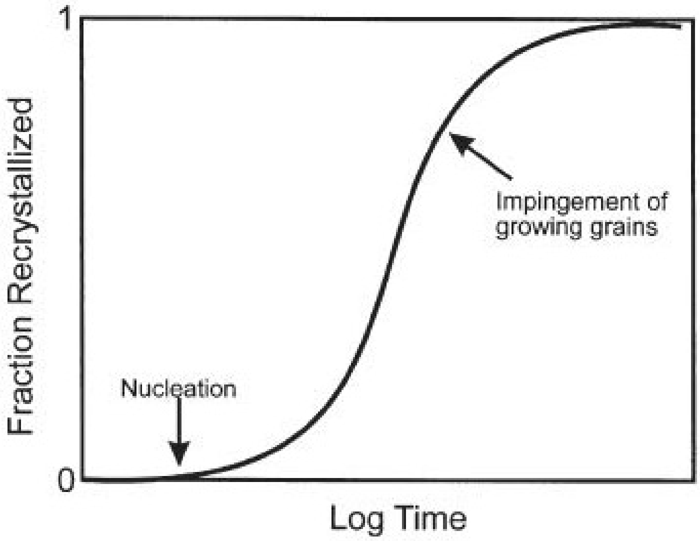

Figure 1.32: Examples of recrystallized fraction changes against the logarithm of time, from [118].

4. n characterize the nucleation mechanism [118]. The B factor is usually thermally activated:

$$B(T) = B_0 \exp\left(-\frac{Q_b}{RT}\right) \tag{1.55}$$

with B_0 the pre-exponential factor and Q_b an activation energy.

Derivative JMAK When doing non-isotherm tests (as in DSC for instance), the JMAK model cannot be used like this. Some modifications have to be done before being able to apply it. The first idea is to derive equation 1.54 to obtain the recrystallized fraction rate [132, 133]:

$$\frac{dX}{dt} = -nB(1-X)[-\ln(1-X)]^{(n-1)/n} \tag{1.56}$$

This rate equation is the base to determine kinetic parameters of phase transformation depending on the heating rate in DSC measurements [132, 133].

Integrated JMAK Another approach comes from the work of Fernandes *et al.* [134] during linear heating or cooling of the specimen. As in isotherm measurements, nucleation and growth will take place, one after the other. During a linear heating ramp, a certain amount of heating is needed to nucleate stable nuclei. Once it is done, growth happens. The recrystallized fraction will increase, depending on temperature and time.

III.E.3. Separating both contributions on measurements

The main issue for equation 1.53 is that it made the hypothesis that only recrystallization occurs at the annealing temperature. However, as shown in [120, 127, 135], some recovery can happen

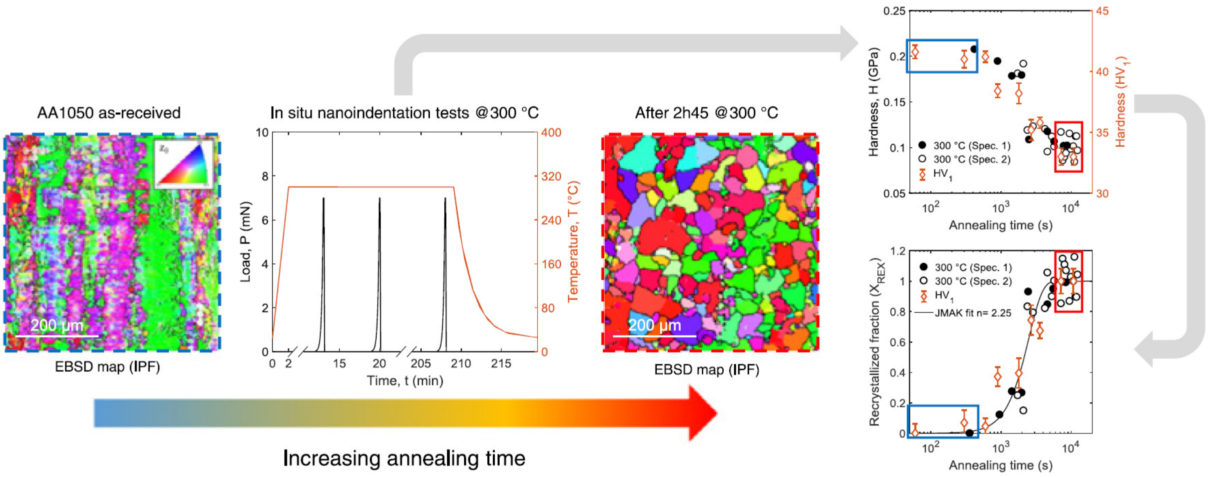

Figure 1.33: Proof of concept of applying in-situ nanoindentation to study the recrystallization kinetics of aluminum, from [106].

before recrystallization. To take this point into account, one can modify equation 1.53:

$$H_m = XH_{ReX} + (1 - X)H_{recov} \tag{1.57}$$

where H_{recov} is the hardness of the sample that would only recover and not recrystallized. Then, as in [127, 135], the two phenomena are taken into account in the modeling process. Such formulation gives consistent results for isotherm [135] and non-isotherm [127] experiments.

III.F. Conclusions on metallic materials

In crystalline metals, two phenomena are responsible for the microstructural changes considered here: static recovery and static recrystallization. Static recovery is related with dislocation motions inside the initial grain structure and leads to a metastable structure. Static recrystallization is the nucleation and growth of a new grain structure that will replace the old one. It is linked with grain boundary movements and leads to a stable microstructural state.

Those two phenomena were widely analyzed on materials during isotherm annealing utilizing diverse characterization techniques. The modeling shows that each is thermally activated and favored by high stored energy levels: both are competing during the annealing. Recent developments in modeling have opened the possibility to model non-isotherm measurements through thermal ramping tests.

In [106], Baral *et al.* applied in-situ nanoindentation measurements to characterize the recrystallization kinetics of a cold-rolled aluminum during isotherm measurements (see figure 1.33). This opens the path to using nanoindentation to quantify those kinetics utilizing in-situ measurements. Moreover, if one can perform thermal ramping in nanoindentation devices, he would be able to characterize those kinetic using a few non-isotherm experiments. It will be the main focus of chapter 4 of this manuscript.

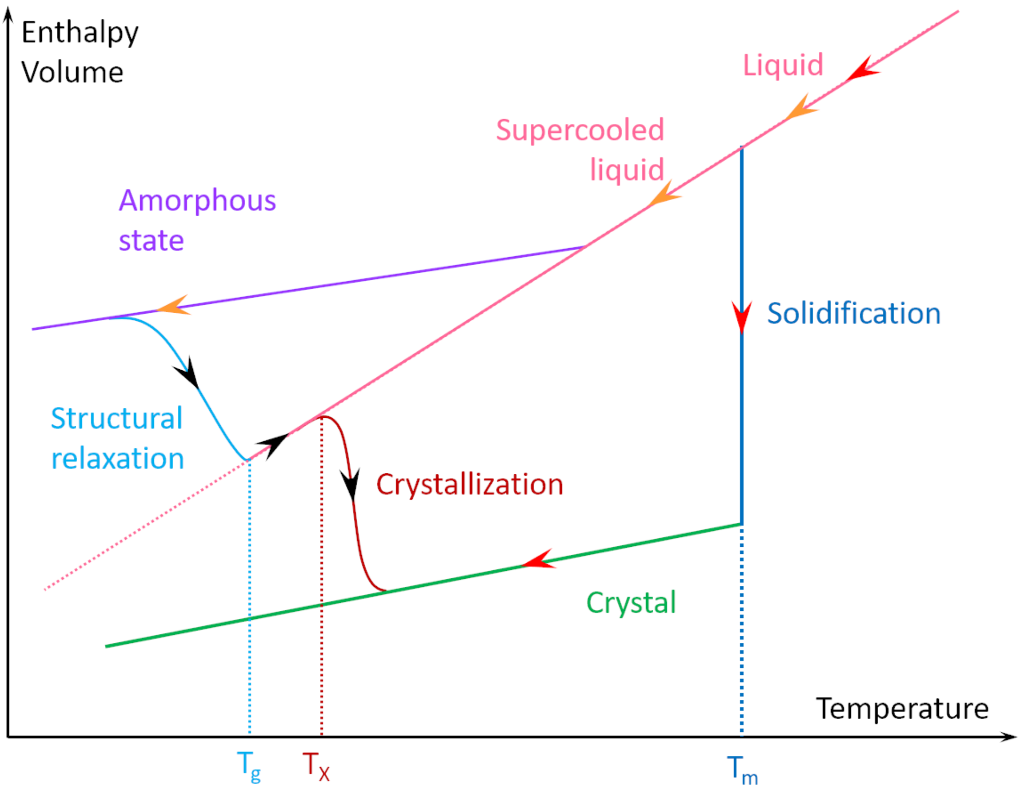

Figure 1.34: Variation of the volume or enthalpy of a material depending on its physical state, adapted from [7, 137]. Let considered a material initially in the liquid state. If the cooling is slow, solidification happens at the melting temperature and one gets a crystal (red arrows). On the opposite, if the cooling is quick enough (orange arrows), the liquid state will be frozen. A metastable state is obtained. If the amorphous structure is heated (black arrows), structural relaxation will take place. Local reorganization of the atoms appends to obtain a more stable structure. If the temperature becomes higher than the glass transition temperature T_g, the material is in the superplastic state, and crystallization is expected to happen sooner or later. The glass transition temperature T_g and crystallization temperature T_X depends on the heating rate [138].

IV. Amorphous structures: metallic glasses

IV.A. Amorphous structure in metals?

Amorphous structures are commonly used: the best known is glass. However, it was only in the ’60s that amorphous metallic structures were first obtained. Klement *et al.* [6, 136] reported the first metallic glass made of Au75Si25. To get it, they had to apply a cooling rate of 1×10^6 K/s. Contrary to crystalline structures, amorphous structures do not present long-range orders. This out-of-equilibrium structure results from the fast cooling of the structure from a liquid state, without undergoing crystallization. So, in order to obtain a metallic glass (MG), one should freeze the metal in its liquid state, without allowing it to crystallize.

As seen in figure 1.34, under the melting temperature T_m, the amorphous structure is a metastable configuration. The glass transition temperature T$_g$ is defined as the temperature separating the supercooled liquid state and the amorphous state, a state where the liquid state is frozen. This separation can be observed while studying property changes of the material (viscosity [137], ductility [139], etc.).

As the amorphous state is unstable, it is of higher energy than the crystalline one. If the temperature is increased, the sample will slowly go back to a more stable state, via structural relaxation (under T$_g$) and/or crystallization.

IV.B. Amorphous properties versus crystalline ones

Such formation's mechanisms leads to a structure that is chemically homogeneous and that does not present crystallographic defects. This greatly impacts the properties of the material compared to the crystalline state.

IV.B.1. Properties of amorphous state

Such an amorphous structure gives metallic glasses interesting properties compared to the crystalline state. It can be mechanical or magnetic properties, super-formability at high temperatures and high corrosion resistance, etc. [7, 140–144].

IV.B.2. Deformation mechanism

As the metal is not in the crystalline structure, the deformation mechanisms are not the same. There is no dislocation in metallic glasses!

Deformation takes place via Shear Transformation Zone (STZ) [145–147]. Two complementary models explain this deformation mechanism: Eshelby or free volume [147]. Localization of the deformation in the shear band leads to catastrophic failures at RT [136]. Usually, when increasing the temperature around $0.7 - 1.1T_g$, a brittle-to-ductile transition is observed on those materials.

Depending on the strain rate, the deformation in MG is homogeneous or heterogeneous [145–147]. Under low deformation rate, once the stress level is high enough, a shear band will localize the deformation and make the sample deform. If the level of stress increases again, a second shear band will be triggered. Such heterogeneous behavior is detected via pop-in during nanoindentation experiments [148–150]

If the increase of stress is quick, multiple shear bands will be activated in a small time and deformation will look homogeneous. Schuh *et al.* [146, 147] proposed a deformation map depending on the strain rate and temperature. Using it, one can understand what deformation mode in the tested conditions is expected (see figure 1.35).

When T> T$_g$, the sample is in the supercooled liquid state: the strain rate sensitivity of the specimen increases a lot [145, 151]. Its value generally reaches values near 1: it has a Newtonian comportment. However, if nanocrystals appear in the structure, this behavior is lost: the material becomes non-Newtonian.

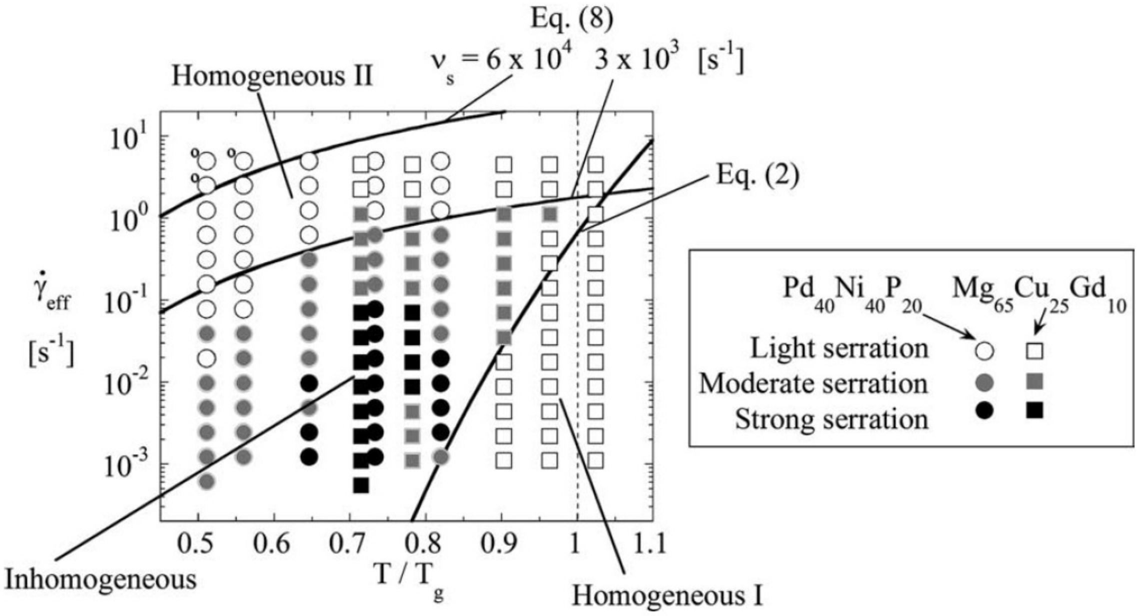

Figure 1.35: Deformation map of metallic glasses, from [146]. Depending on the strain rate and temperature, a metallic glass will flow homogeneously or heterogeneously.

IV.B.3. Impact of temperature on mechanical properties

When heating the amorphous sample, Young's modulus and shear modulus usually decrease [138, 152, 153]. In the case of Zr-based MG, hardness and Young's modulus are typically lower in the amorphous state compared to the crystalline one [153, 154] (see figure 1.36). Using DMA (Dynamic Mechanical Analysis), TMA (Thermo-Mechanical Analysis) or DSC experiments, one can determine the glass transition temperature of the specimen and its crystallization temperature (see figure 1.37). Those temperatures depend on the heating rate and T_g is also sensitive to the tested frequency.

Structural relaxation under glass transition temperature Structural relaxation is a reorganization of atoms on short distances [7, 137, 138, 155, 156]. It can be observed in hardness and Young's modulus changes during isotherm annealing (see figure 1.36).
A distinction is generally made between the alpha and beta relaxation [7]: during the alpha relaxation, the deformation is permanent while during the beta deformation it is reversible and takes place at a lower temperature. DMA measurements allow determining the temperature of the alpha relaxation, which is impacted by frequency.

Crystallization Crystallization is usually detected when performing DSC or DMA at a constant heating rate on the specimen. By studying the Young's modulus changes in temperature, Idriss *et al.* [153] observed it. Figure 1.36 presents their work. Firstly, the Young's modulus decreases with temperature. Annealing of the amorphous glass leads here to an increase of the Young's modulus compared to the as-cast sample. More, if heating at a temperature higher than T_g is carried out, a sudden increase of the Young's modulus can be linked with the crystallization of

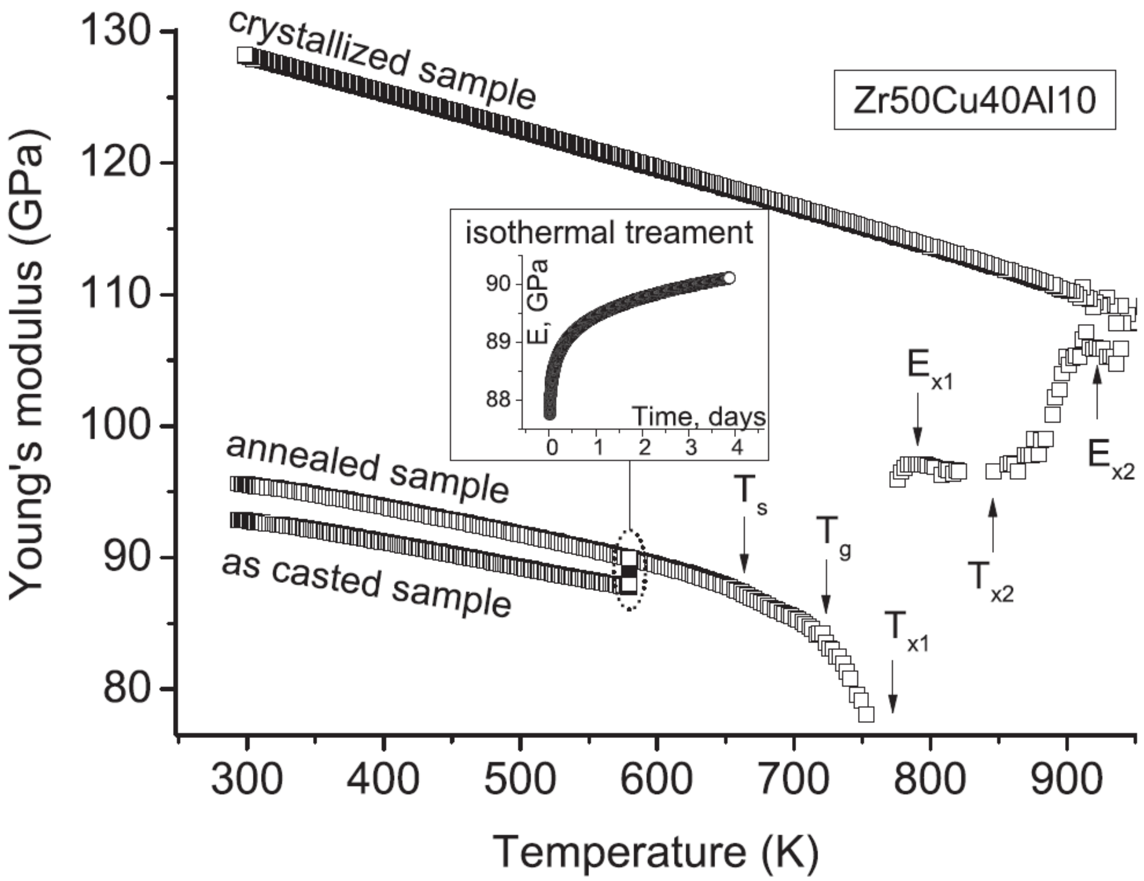

Figure 1.36: Variations of the Young's modulus during heating for a Zr-based metallic, from [153].

the specimen.

Through the changes of the strain rate sensitivity and so of the flow of the material, one can also detect that crystallization is taking place [145]. As for the glass transition, the crystallization temperature depends on the heating rate. Crystallization can arise at a temperature lower or higher than T_g. Below T_g, its kinetics depend on the number of nuclei that were frozen before cooling. Above T_g, a delay time will determine when crystallization suddenly occurs, during a short temperature scale.

To analyze crystallization kinetics, one can apply the JMAK equation (equation 1.54) during isotherm annealing. However, the values of the Avrami exponent n presented in papers are not between 1 and 4, but sometimes higher [157, 158]. This makes those results complicated to interpret. For non-isotherm measurements, like in DSC measurements, authors usually use the Kissinger method for instance. They are based on the rate equation of the JMAK formulation (equation 1.56).

IV.C. Conclusions on metallic glasses

Metallic glasses are particularly interesting materials, with really outstanding properties compared to the ones of their corresponding crystalline structure. Unfortunately, due to the high

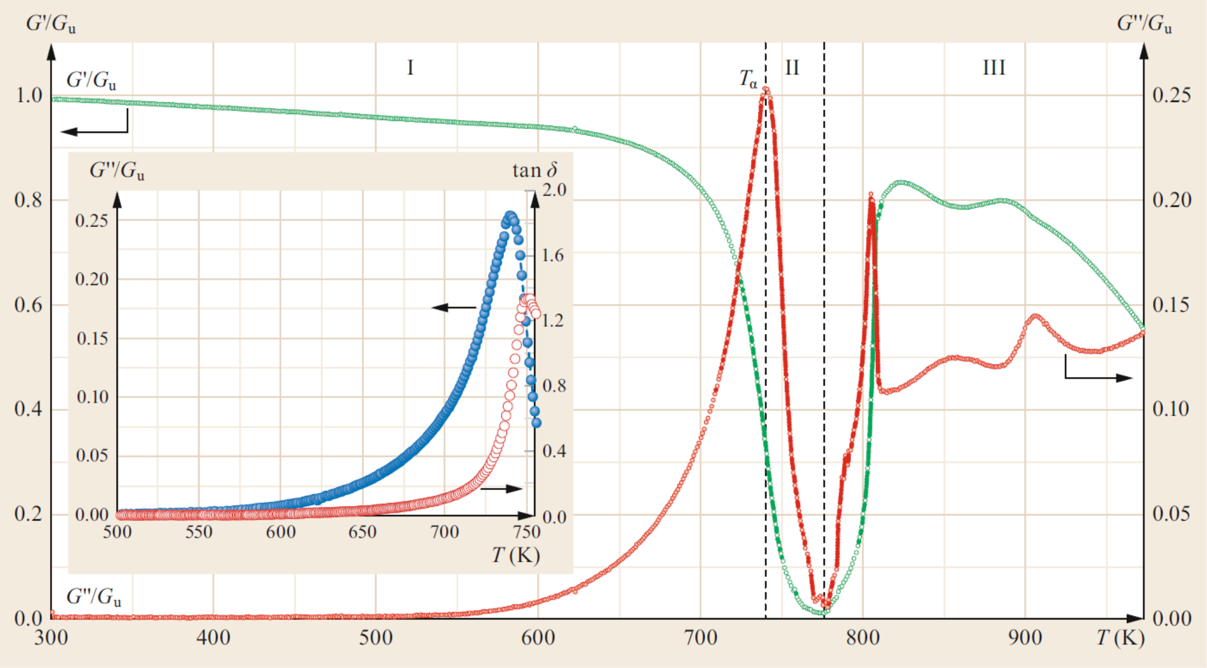

Figure 1.37: DMA experiments on a $Cu_{36}Zr_{46}Ag_8Al_8$, from [7]. The changes in the ratio G'/G and G''/G give information on the glass transition and the crystallization of the sample.

cooling rates that are required to fabricate them, bulk metallic glasses have a limited maximum size. The record is 80mm x 85mm [7]. To take advantage of those properties, one can then use thin films rather than bulk samples.

As bulk metallic glasses, thin film metallic glasses are expected to see their properties depend on temperature and strain rate. Determining the properties of a model thin-film metallic glasses (TFMG) will be the main focus of chapter 5 of this manuscript.

V. Conclusions of the chapter

As seen, nanoindentation is an easy test giving quite a lot of data on the mechanical properties of a sample. Not only does it give the hardness and Young's modulus but creep properties could also be determined. This approach allows collecting information on the strain rate sensitivity of a material.

Thanks to the last fifteen years of development, nanoindentation is no longer limited to room temperature testing. One is now able to get in-situ hardness, Young's modulus, and creep properties from room temperature up to 1000 °C. Such tests become more complex to run but open great perspectives to characterize material properties in temperature. Some studies [22, 106] propose to apply such temperature experiments to measure really-time microstructure modifications in temperature via in-situ nanoindentation.

As the microstructure or physical structure of metals and metallic glasses is linked with their plastic properties, one should be able to use the modifications of their properties to observe such changes. Moreover, one would need to model those phenomena in temperature to quantify them.

Through the development of the High-Temperature Scanning Indentation method, presented in the next chapter, one can collect information on the hardness, Young's modulus and stain rate sensitivity of materials in temperature. Complementary to creep and relaxation indentation tests, one could then get information about deformation mechanisms during creep on a large strain rate and temperature scale (cf chapter 3). Moreover, quantification of static recovery and static recrystallization of model metals using the HTSI experiments would be carried out in chapter 4. Finally, by studying hardness and strain rate sensitivity variations during a ramp in temperature, one is able to follow the physical changes of a thin-film metallic glass (cf chapter 5).

2

Development of the High-Temperature Scanning Indentation method

Let's now focus on the development of the High-Temperature Scanning Indentation (HTSI) technique.

Chapter's content

I. Implementation of the High-Temperature Scanning Indentation

As explained in chapter 1 section III.F., in-situ nanoindentation allows determining the kinetics of microstructure changes of materials. However, the methodology used in [22, 106] is really time-consuming: the time between experiments is around 5 min to 10 min. And as can be seen in figure 1.33, the modifications in hardness happen quite early in the experiment. Hopefully, it is enough to quantify the kinetic of recrystallization of the studied aluminum. But if the tests were conducted at higher temperatures, the methodology would be too slow to characterize this kinetic correctly.

Moreover, performing tests in temperature is complicated because of the issue of thermal drift. Lowering the time of thermal stabilization before carrying out classical indentation tests is not possible: doing that would lead to errors in properties characterization. To reduce the impact of thermal drift on measurements, it is thought to change the way of doing experiments. Instead of doing long indentation tests that need good thermal equilibrium, quick indentation tests that would be less affected by the thermal drift could be carried out. This methodology should allow conducting testing during heating ramps and not only during isotherm experiments. So, a new technique is developed: High-Temperature Scanning Indentation. This chapter will focus on the indentation cycle that is the basis of the HTSI method. The apparatus and the materials that were used to validate the results are then presented and the verification is finally performed.

I.A. The indentation cycle

To implement the HTSI method, a specific indentation cycle was designed. This is the first focus point. Little time is then spent on the applied thermal cycle.

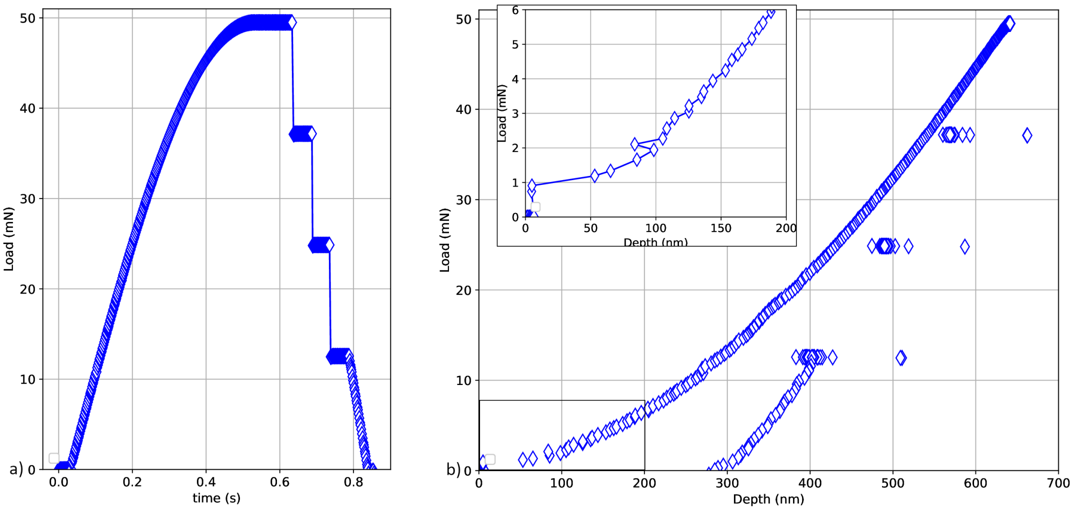

Figure 2.1: (b) Load-displacement curve on fused silica at RT, obtained when applying the quarter-sinus loading indentation cycle (a). In the zoomed picture, a jump in displacement, reminding a pop-in effect, is observed. Such behavior is not expected on FS: this effect comes from the indentation cycle.

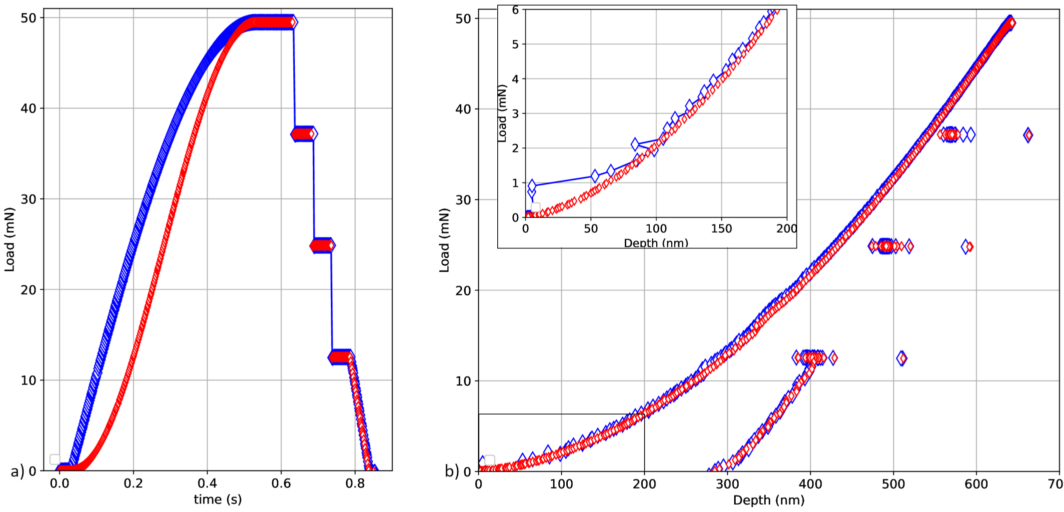

Figure 2.2: (b) Load-displacement curves on fused silica at RT, obtained when applying the (blue) quarter-sinus or (red) half-sinus loading indentation cycles (a). In the zoomed picture, the "pop-in effect" previously detected is no longer observed. On the other parts, the load-displacement curves are identical: the two cycles give the same mechanical properties.

Experimental constraints To overcome the issues identified by Baral *et al.* [106], important properties of the newly used indentation cycle are highlighted. First, one wants to determine the hardness and Young's modulus, as well as the creep properties. Secondly, the cycle should be as fast as possible so it could be applied not only during isotherm measurements but also during thermal ramping. This impacts the design of the cycle.

Loading part An exponential loading (constant strain rate) function using a quick loading rate could be used but such loading methodology would greatly affect a short creep segment and so the measured creep properties. A loading function that could perform a fast loading and have a slow derivative when arriving at the maximum load to do the creep segment is required. The chosen function is a quarter sinus function (see figure 2.1 (a)):

$$P(t) = P_{max} \sin\left(\frac{\pi}{2t_{load}} t\right) \tag{2.1}$$

with P_{max} the maximum load ant t_{load} the time of the loading segment.

Such loading procedure allows getting a low inertia impact when arriving to do the creep segment. Moreover, the used nanoindentation device required a loading in 0.5 s: it is really quick compared to the usual nanoindentation methodologies. The main drawback of this procedure is that the constant strain rate properties of the exponential loading are lost.

Experiments are started applying this loading procedure but an issue is detected on fused silica. As can be seen on the loading curve on fused silica (figure 2.1 (b)), some instabilities are observed on the loading part. One can think that "pop-ins" are detected yet no "pop-in phenomenon" is expected on fused silica. It is an instability due to the infinite value of the derivative of the used loading function when touching the surface.

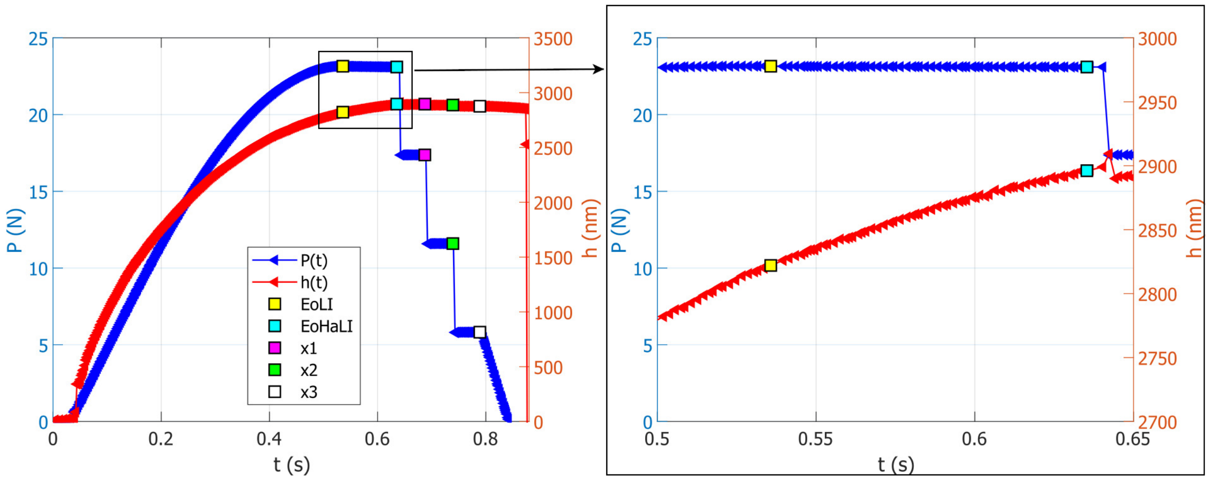

Figure 2.3: Applied load and measured depth versus time on aluminum at 300 °C. The end of loading EoLI, the end of holding EoHaLI, and the 3 steps during the unloading segment are identified. When zooming on the creep segment, it is clear that the sample creeps.

As one is interested in the detection of pop-in in the material, a half-sinus loading function is implemented (equation 2.2). Such an approach solves the pop-in issue while staying OK for the creep segment (figure 2.2). The pop-ins that are now detected on materials are no longer related to the methodology.

$$P(t) = \frac{P_{max}}{2}\left(1 + \sin\left(\frac{\pi}{t_{load}}t - \frac{\pi}{2}\right)\right) \tag{2.2}$$

Creep segment To determine the creep properties, a creep segment is required in the loading procedure. As the cycle should be as quick as possible, the creep segment is short: 0.1 s to 0.3 s after loading. Such low time asks the question of reaching steady-state creep when performing the tests, especially at RT.

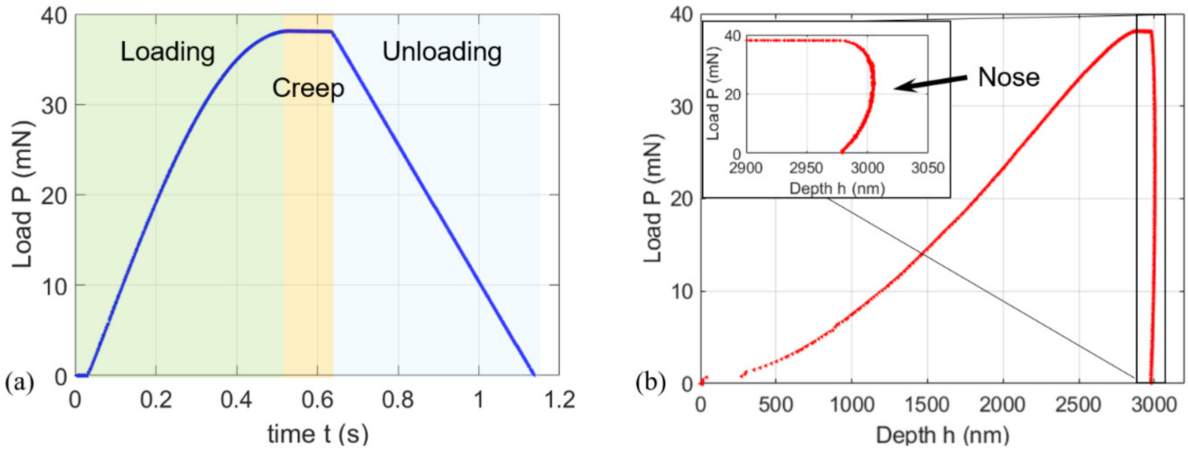

Figure 2.4: (a) Indentation cycle applied on a pure aluminum at 300 °C. (b) Corresponding load-displacement cycle. As can be noticed, a nose is presented on the unloading part. It is an issue to compute the stiffness and so hardness and Young's modulus.

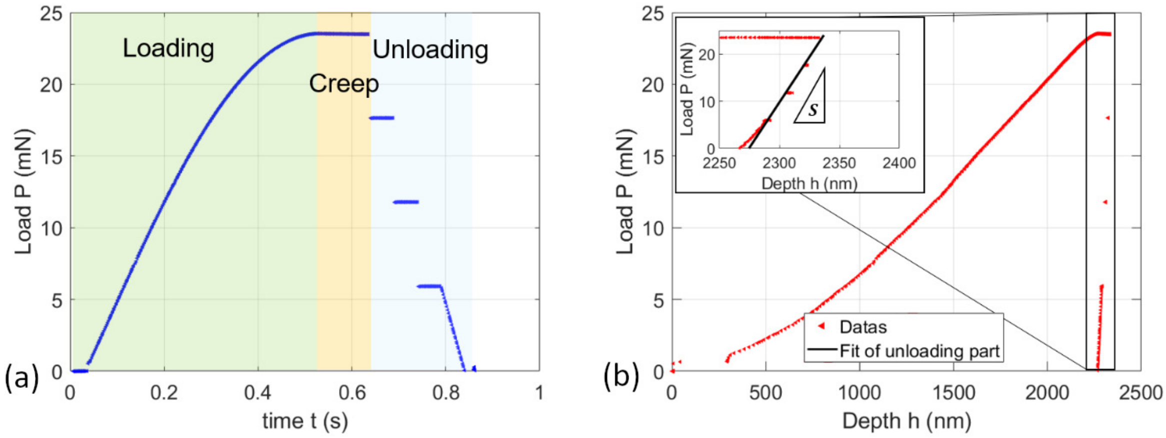

Figure 2.5: (a) Indentation cycle applied on a pure aluminum at 300 °C. (b) Corresponding load-displacement cycle. As can be seen, the nose is no longer present on the unloading part. Stiffness and so hardness and Young's modulus can be computed.

Contrary to the creep methodology of Maier *et al.* [58], CSM is not conducted during loading. Only the depth h and load P are saved against time. So the strain rate is computed through:

$$\dot{\varepsilon} = \frac{\dot{h}}{h} \tag{2.3}$$

As it can be seen in figure 2.3, during the creep segment, the displacement increases. To calculate the strain rate, the displacement is fitted against time using a degree 2 polynomial function. Deriving it gives the $\dot{h}$.

Unloading part Initially, a linear unloading function (0.5 s) is used to get the Young's modulus and the hardness of the material at the maximum depth. Unfortunately, as it can be seen in figure 2.4 (b), a nose is visible on the unloading curve of aluminum at 300 °C. Some creep happens during the unloading and impacts the determination of E and H [159]. Ngan *et al.* [160, 161] propose some methodologies to correct this effect during the unloading. Sadly, applying them to the samples does not solve the issue.

To reduce creep during the unloading, the load should be decreased really quickly while having enough data to compute the hardness and Young's modulus. Unfortunately, increasing the unloading speed during the linear unloading while having enough data points was not possible. So, it is decided to change the unloading function to do a quick unloading to determine the stiffness correctly and so the Young modulus (through equations 1.6 and 1.7) of the specimen. As hardness is not directly proportional to stiffness (equation 1.5), the error on the stiffness hopefully does not impact its value that much.

To reduce this effect, the idea is to decrease the load using steps (see figure 2.5). The brutal drop of the load allows to no longer have creep during the unloading and the steps give us data to compute the stiffness.

In figure 2.6, the load and displacement versus time on aluminum at 300 °C are plotted. If one

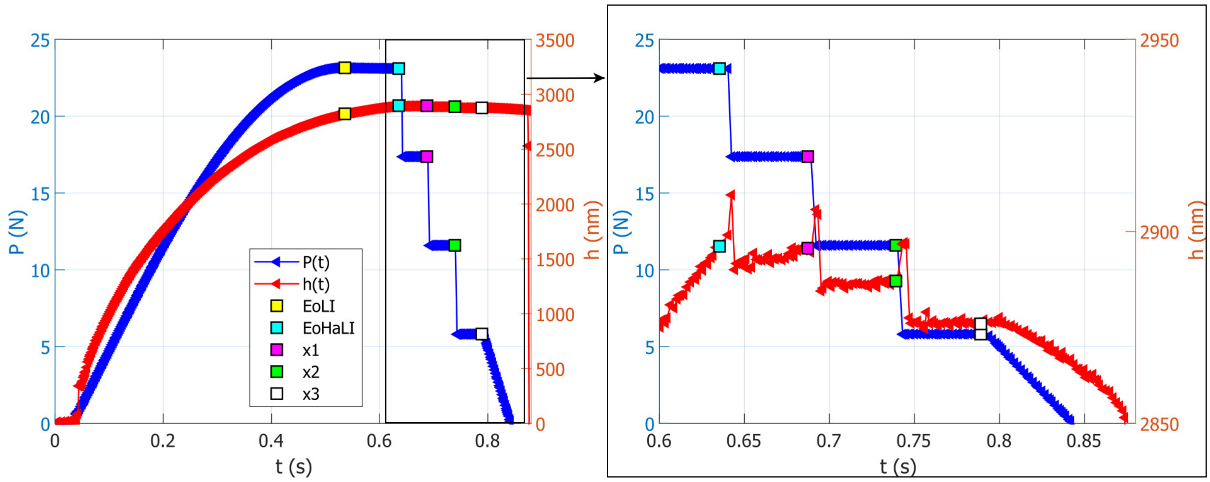

Figure 2.6: Applied load and measured depth versus time on aluminum at 300 °C. The end of loading EoLI, the end of holding EoHaLI, and the 3 steps during the unloading segment are identified. When zooming on the unloading, the steps in displacement are observed.

focuses on the unloading part, one observes the steps applied here. As there are little movements just after the decrease in load, the end of a step is used to determine the load and displacement values used to calculate the stiffness. A linear decrease of the load against depth during this unloading is considered: computing a correct contact stiffness is now possible.

The two indentation cycles presented in figure 2.2 are used in the following work. The red one allows avoiding the instability effect detected on fused silica in figure 2.1. Unfortunately, it was not implemented at the beginning of the present work.

I.B. The thermal cycle

The idea of the High-Temperature Scanning Indentation method is to couple a thermal ramping with the previously defined indentation cycles (see figure 2.7). One will heat his sample at a given heating rate and perform as many indentation cycles as possible. This allows computing the hardness, the Young's modulus, and the creep properties versus temperature. To be sure

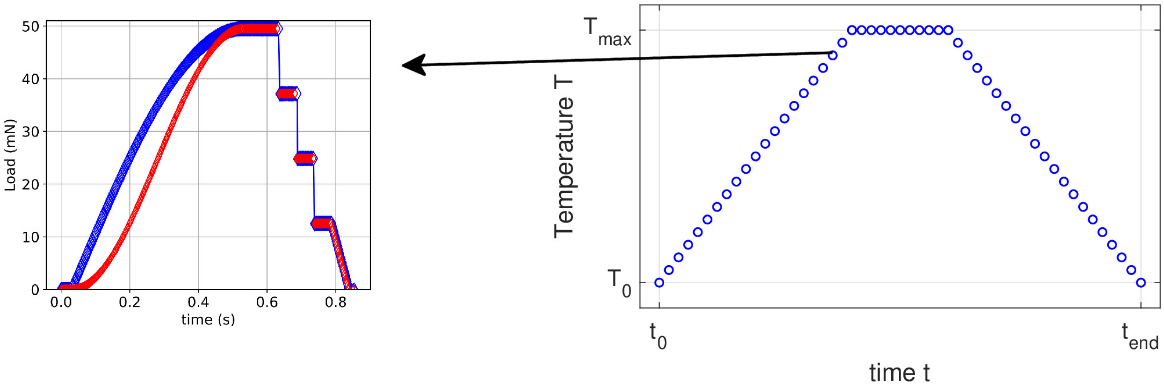

Figure 2.7: Principle of the High-Temperature Scanning Indentation: one applies as many indentation cycles as possible during a thermal cycle.

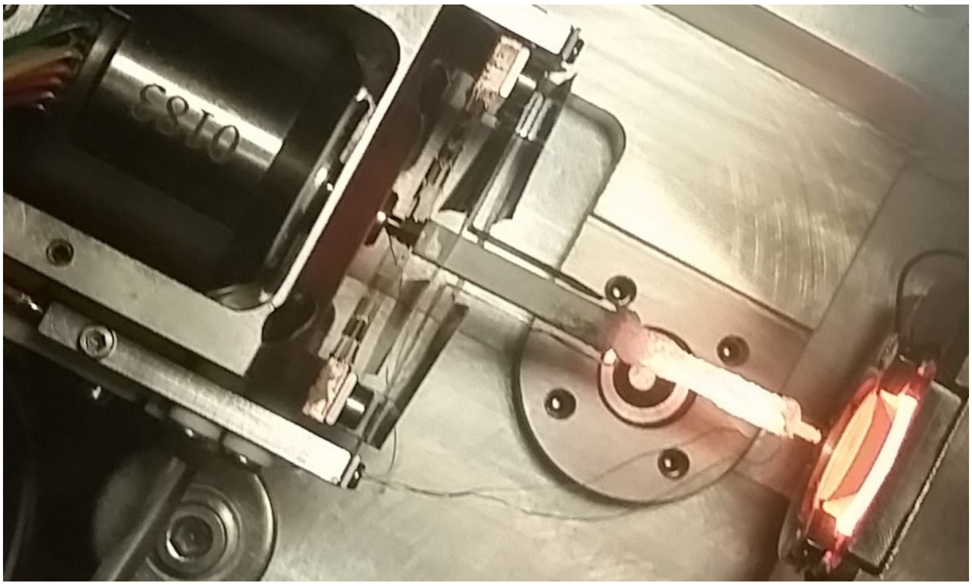

Figure 2.8: InSEM HT system developed by KLA Nanomechanics. The system is heated at 1000 °C under vacuum.

the temperature does not impact significantly the measurement, the heating (or cooling) rate must be low in comparison to the indentation test time. A theoretical temperature increase of less than 0.05 °C during one indentation cycle is used as a criterion to determine the maximum heating rate.

The control of the thermal ramp is of prior importance to get corrected values of Young's modulus. Thermal calibration (see section II.A.2.) and PID settings are compulsory.

II. Materials and methods

II.A. The nanoindentation device

To carry out the validation of the HTSI method, experiments are conducted using the InSEM HT nanoindenter at the LTDS, provided by KLA Nanomechanics (figure 2.8).

This nanoindentation system allows conducting experiments from RT up to 1000 °C. The tip and the sample are heated independently. Very local heating is performed to protect all the electronics. The tests are carried out under vacuum (1×10^{-2} Pa) to prevent oxidation of the whole system. The system is inside a VEGA 3 SEM (Tescan) that enables in-situ observation of the indentation tests.

II.A.1. Calibration of the load frame stiffness

The first step is to calibrate the load frame stiffness. One should perform CSM tests on a fused silica sample as it is the calibration material for nanoindentation experiments. Using equations 1.4 and 1.24, one can determine the load frame stiffness S_{LF} of the system. Moreover, the tip area function is also calibrated. As the maximum load is 50 mN (the maximum depth when

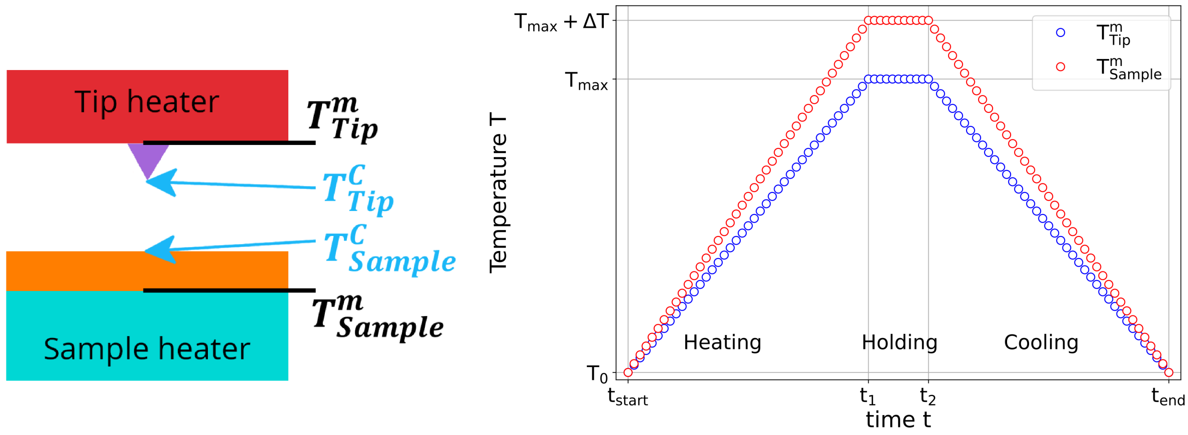

Figure 2.9: (left) Schematic representation near the contact and (right) thermal cycle applied during the High-Temperature Scanning Indentation experiments. Usually, the tip and the specimen temperature settings at the maximum temperature are not the same. One should take that into account to set the HTSI tests correctly.

calibrating on FS is 700 nm) and as suggested by Roudet [32], it is recommended to perform CSM measurements on the studied specimens at RT before doing any HT tests. This allows one to verify the properties at this temperature. As the load frame stiffness may vary a little when changing the sample, corrections can then be done if required.

II.A.2. Temperatures settings

To compute the hardness and the Young's modulus correctly, the temperature of the tip and of the specimen at the contact point should be equal. As presented on the left in figure 2.9, one will measure the temperatures at the back of the sample T^m_{sample} and of the tip T^m_{tip}. Nevertheless, one want the tip and sample temperatures at the contact point to be equal all along the thermal cycle: $T^c_{sample} = T^c_{tip} = T^c$. First, the temperature at the contact point is supposed to be equal to the one at the back of the tip since the tip is quite small and usually in conductive material (diamond, SiC, etc.). So one can plan the thermal cycle that one want to apply on the tip (in blue in the thermal cycle in figure 2.9). Then, thermal calibration at the maximum temperature is performed to determined T^m_{sample} so that $T^c_{sample} = T^c_{tip}$. The method proposed by Minnert *et al.* [79] is carried out to determine this temperature. The idea to calibrate the temperatures is to adjust the temperatures until the tip does not dilate nor contract during contact with the sample, using the displacement measurement. Finally, it is supposed that the difference between T^m_{sample} and T^m_{tip} at the maximum temperature varies linearly in temperature. One can then plan the thermal cycle to apply at the back of the sample (in red in the thermal cycle in figure 2.9).

II.A.3. Indentation parameters

Now that the thermal ramp is planned, the indentation cycles can also be prepared. The method is implemented to have the same maximum load for each test. This means that, as hardness usually decreases with increasing temperature, the maximum depth increases. Experiments are

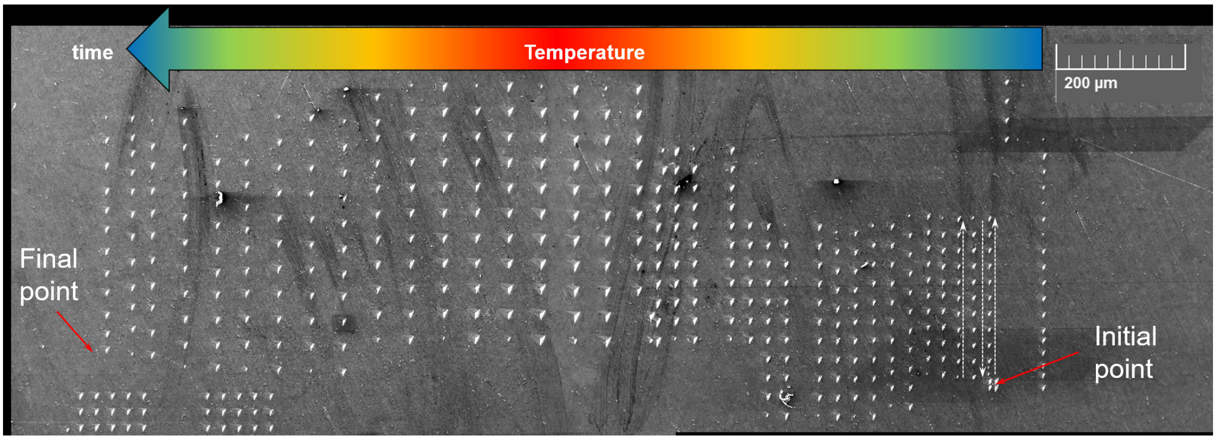

Figure 2.10: Example of HTSI grid applied on a pure aluminum sample during a ramping from RT to 300 °C back to RT at 3 °C/min. The experiment was performed entirely by the user. The imprint size changes due to temperature.

performed verifying that the distance between two indents is higher than $10h_{max}$ [162]. As the indentation tests were initially made by hand (see figure 2.10), this distance was adapted by the experimenter. Recent developments now allow conducting the tests automatically. So, the distance between indents has to be determined prior to the tests, considering this increase of h_{max} with temperature. Further developments would be to adapt the cycle to conduct tests at a given maximum depth.

II.B. Materials

To validate the methodology, experiments are carried out on fused silica, pure aluminum, and pure copper.

Fused silica samples Fused silica samples of 12.5 mm diameter and 2.0 mm thick were provided by Edmund Optic. The samples have parallelism better than 5″. No more polishing was conducted on these samples. Quarter sinus indentation tests are carried out. The maximum applied load is 50 mN, which corresponds to maximum depth of 700 nm at RT and 1000 nm at 350 °C. Loubet's model is used to analyze the data. According to [30], applying Oliver and Pharr's model should give the same results.

Aluminum and copper samples One plate of pure OFHC copper and one of pure aluminum were cut and deformed using a thickness reduction ratio of 85%. Samples cut from those plates have a final diameter of 10 mm to 12 mm for a final thickness of 3 mm. One of the aluminum samples was then annealed at 400 °C for 2 h while the copper sample was annealed at 500 °C for 1 h. The grains size of the recrystallized samples is from 20 µm to 100 µm on both aluminum and copper. Samples were then polished by hand using SiC papers (P460, P600, P1200) before being finished with diamond solution down to 0.5 µm.

Quarter sinus indentation tests are carried out on aluminum. The maximum applied load is 25 mN, which corresponds to a maximum depth of 1000 nm at RT and 3000 nm at 300 °C. Half

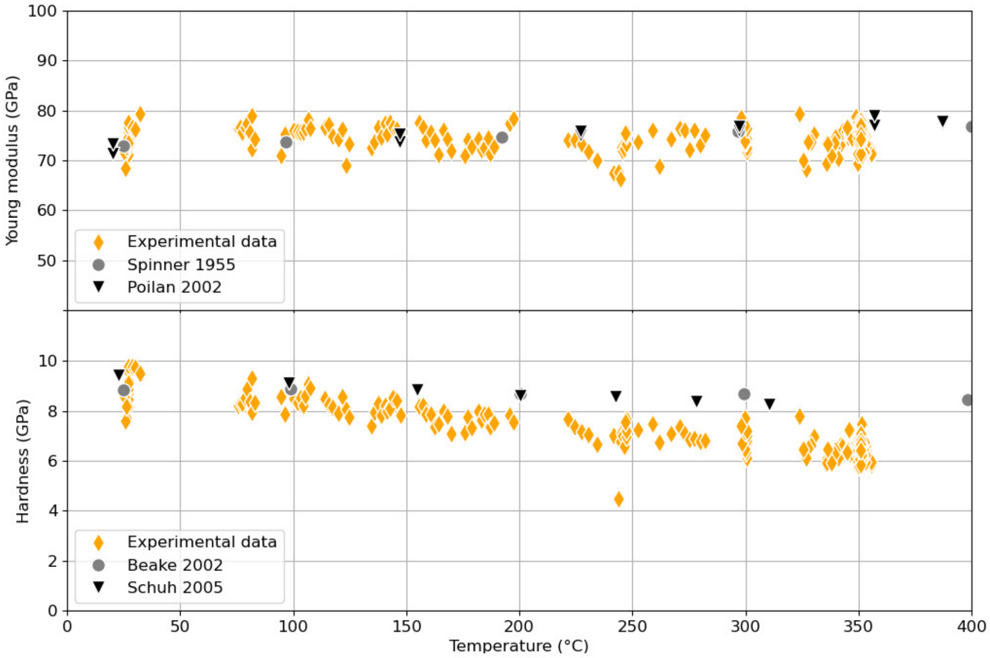

Figure 2.11: Young's modulus and hardness of fused silica, obtained by HTSI experiments. The sample and the tip were heated from RT to 350 °C at 3 °C/min. Results are consistent with literature data [80, 163–165].

sinus indentation tests are carried out on copper. The maximum applied load is 25 mN, which corresponds to a maximum depth of 1000 nm at RT and 2500 nm at 600 °C. As the copper sample was recrystallized, the model of Oliver and Pharr is applied to analyze the copper results. As an aluminum sample was cold-rolled, Loubet's model is applied to evaluate the aluminum data (see Appendix A).

III. Validation of the High-Temperature Scanning Indentation method

Validation is performed on multiple samples. First, tests are conducted on fused silica, the reference material in nanoindentation. Then, verification is carried out on pure aluminum and pure copper.

III.A. Hardness and Young's modulus in temperature

On fused silica The impact of temperature on the hardness and Young's modulus is studied first in fused silica. According to literature [80, 163–165], Young's modulus should increase in temperature while hardness should decrease. The tests are conducted under vacuum. A Berkovich diamond tip is calibrated at RT. The system is heated from RT to 350 °C at 3 °C/min and the indentation cycles are applied as quickly as possible to follow hardness and Young's modulus changes in temperature.

As it can be seen in figure 2.11, the mechanical properties of the specimen are measured quasi-continuously in temperature. The results are consistent with the literature data [80, 163–165].

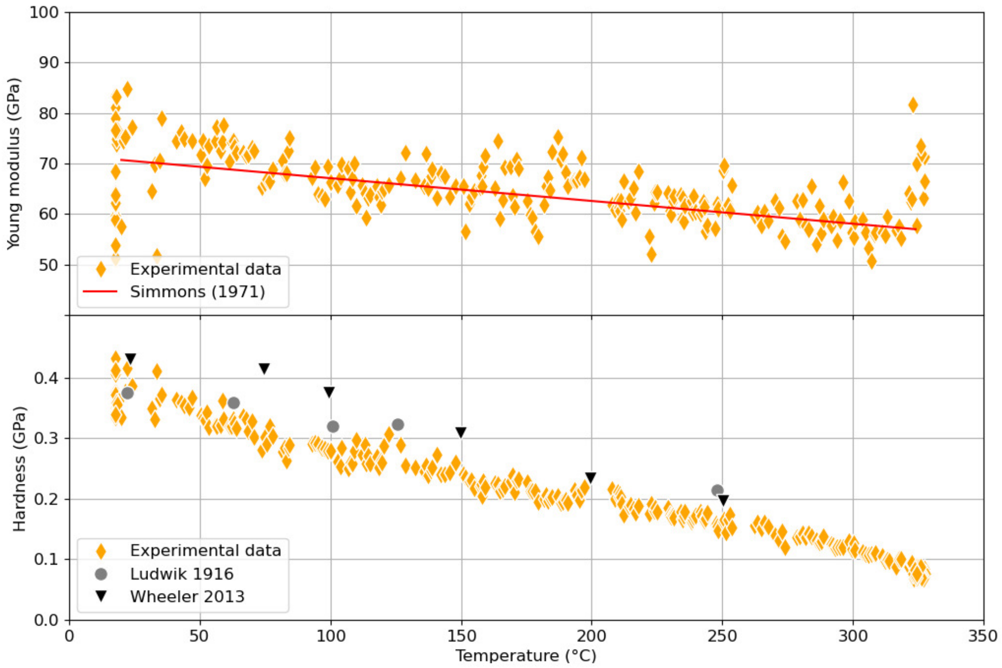

Figure 2.12: Young's modulus and hardness of a cold-rolled pure aluminum sample obtained by HTSI experiments. The specimen and the tip are heated from RT to 325 °C at 3 °C/min. Results are consistent with literature data [166–168].

This High-Temperature Scanning Indentation allows getting those changes really quickly compared to classical isotherm experiments.

On pure aluminum To confirm the validation process, tests are performed on pure metals. Through experiments on pure aluminum, it is verified that once again consistent hardness and Young's modulus changes in temperature are determined.

Young's modulus is expected to decrease. As it can be seen in [166], hardness values in temperature depend a lot on the microstructure. A reduction in hardness is anticipated but caution should be taken when comparing the absolute values with literature data. As it can be noted in figure 2.12 on the cold-rolled sample, such changes are consistent with literature data [166–168].

When performing the experiments, it is observed that the applied PID does not allow the specimen to follow its setting correctly at low temperatures. Moreover, when arriving near the maximum temperature, some overshoots happen for the tip and the sample. So during the thermal cycle, some high-temperature mismatches between the tip and sample surface occurred. It leads to incorrect determination of the contact stiffness and so to wrong Young's modulus values. So, it becomes obvious that the control of temperature during ramping is quite important. Having a really good PID regulation is compulsory to get the Young's modulus changes in temperature. Hopefully, hardness is less sensitive to this control: it is easier to study hardness modifications applying this technique.

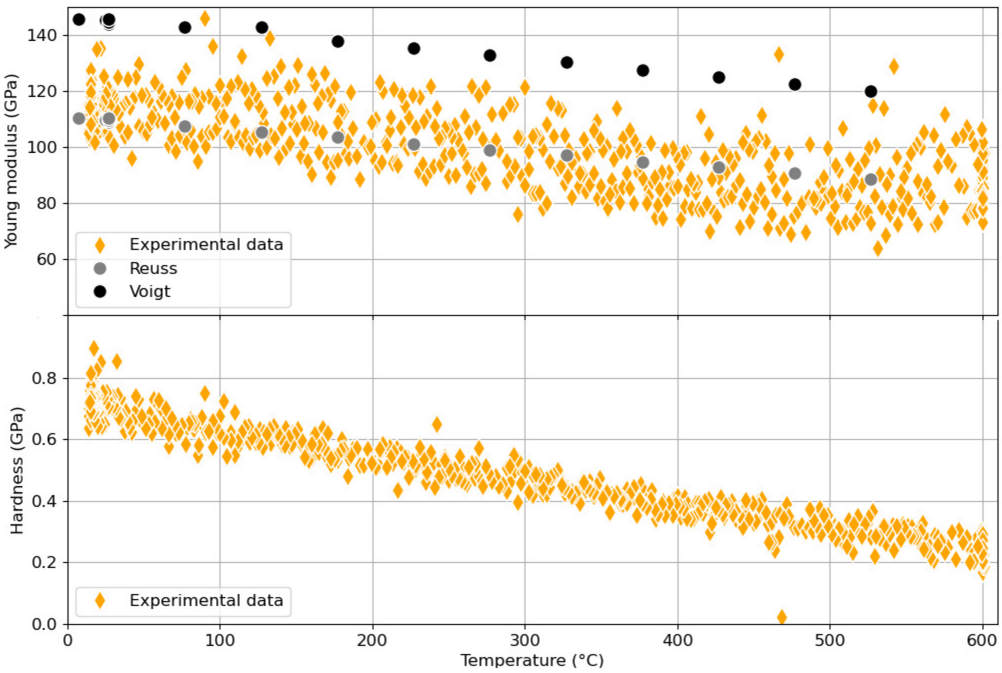

Figure 2.13: Young's modulus and hardness of an annealed pure copper sample, obtained by HTSI experiments. The specimen and the tip are heated from RT to 600 °C at 5 °C/min. Results are consistent with literature data [167, 169].

On pure copper Using a copper sample, results are verified up to higher temperature, utilizing a Berkovich sapphire tip this time. Young's modulus and hardness are expected to decrease [167, 169]. As seen in figure 2.13, the variations are consistent with what is predicted.

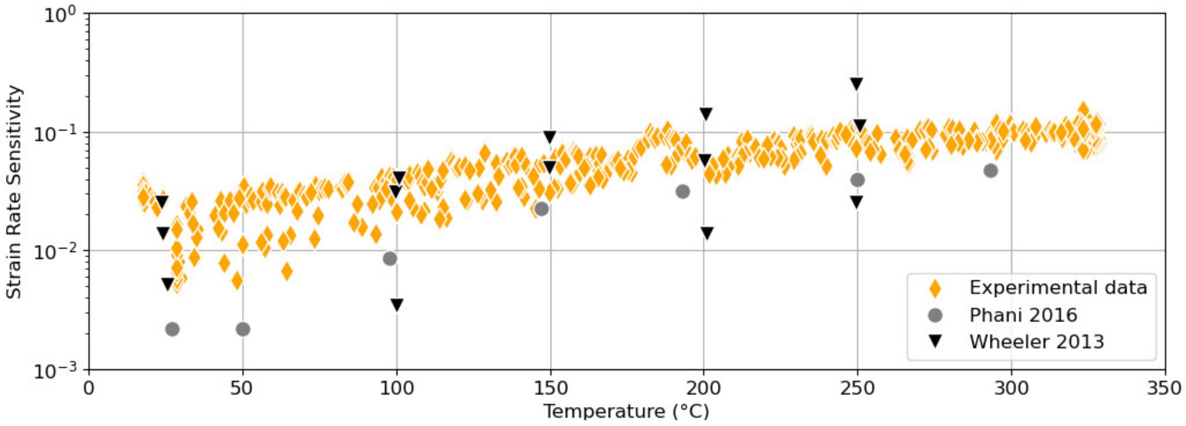

Figure 2.14: Strain rate sensitivity of an annealed pure aluminum sample, obtained by HTSI experiments. The specimen and the tip are heated from RT to 325 °C at 3 °C/min. Results are consistent with literature data [166, 170].

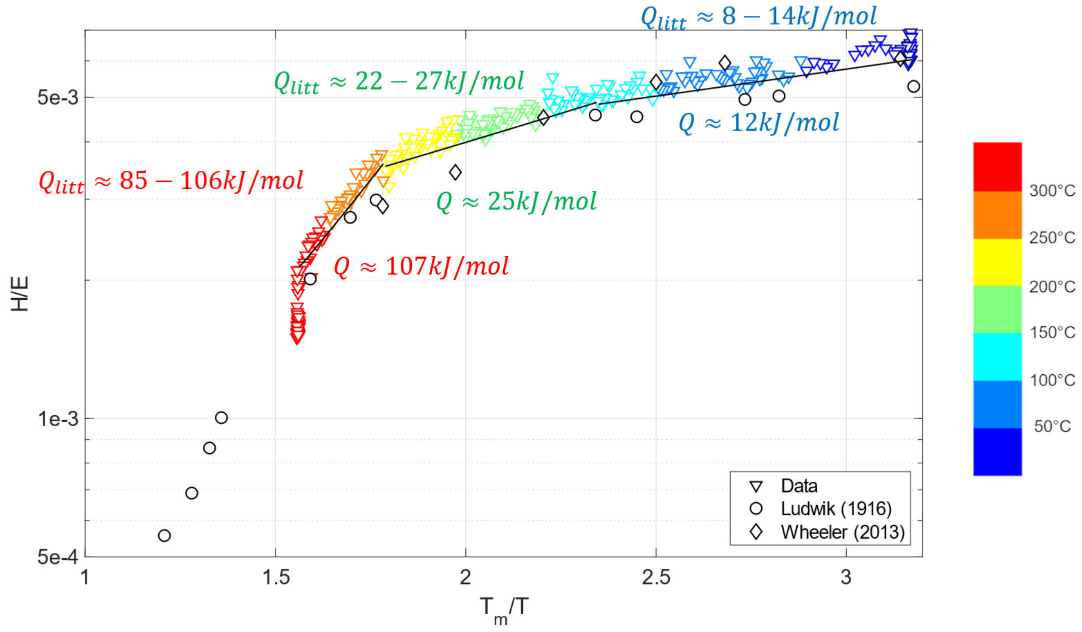

Figure 2.15: Young's modulus-compensated hardness versus melting temperature over temperature on aluminum during heating from RT to 325 °C at 3 °C/min. The slope gives the activation energy of creep according to Sherby and Armstrong analysis. It is consistent with literature data [166].

III.B. Creep in temperature

The indentation cycle was designed to get the hardness and Young's modulus but also creep properties of the specimen.

The strain rate sensitivity By applying the analysis developed in chapter 1 section I.C.4., the creep properties of aluminum are computed in temperature. As for the other properties, quasi-continuous changes of this property are determined in temperature. They are consistent with literature data [166, 170] (figure 2.14).

Sherby and Armstrong analysis According to Sherby and Armstrong analysis [171], the changes in the hardness over the Young modulus ratio are thermally activated. The activation energy depends on the temperature:

$$\frac{H}{E} = C_0 \exp \frac{Q}{nRT} \tag{2.4}$$

where C_0 is a pre-exponential factor, R the universal gas constant, T the absolute temperature and n the stress exponent previously defined. Through Sherby and Armstrong's analysis, the apparent activation energy of creep can be assessed (see figure 2.15). The variations of the determined activation energy with temperature are consistent with those in [166].

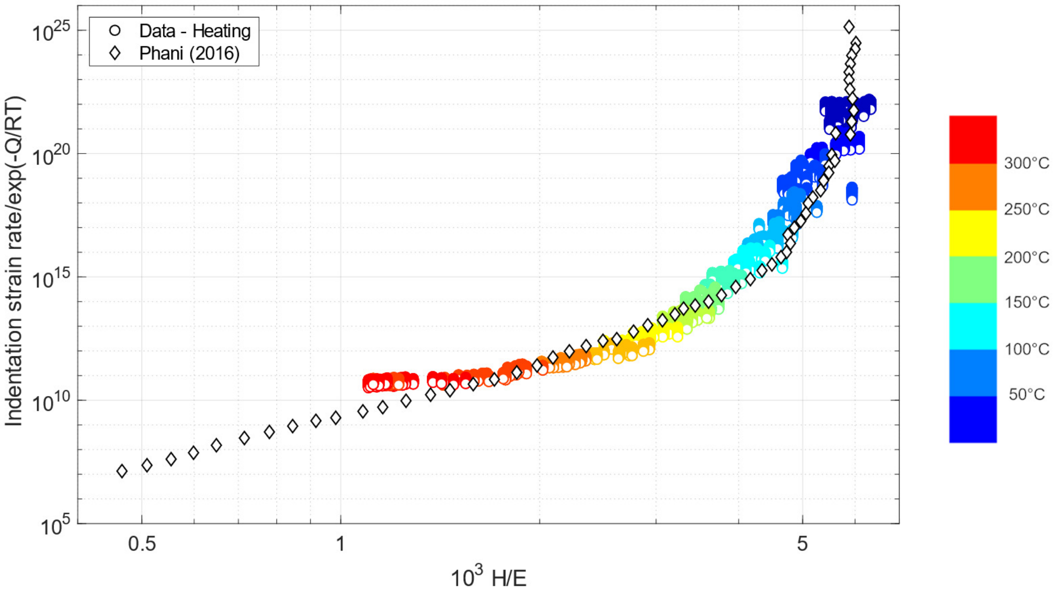

Figure 2.16: Master curve based on Norton-Hoff's law. The apparent activation energy of creep is 130 kJ/mol, which is close to the value of 142 kJ/mol found by Phani and Oliver [170].

Norton-Hoff's law According to Norton-Hoff's law, the relation between stress and strain rate is thermally activated:

$$\dot{\varepsilon}_p = \alpha \sigma^n \exp\left(-\frac{Q_{creep}}{RT}\right) \tag{2.5}$$

By plotting the changes of the temperature-compensated strain rate versus the Young's modulus-compensated stress, the activation energy of creep Q_{creep} can be evaluated (see figure 2.16). On aluminum, an activation energy of 130 kJ/mol is determined which is consistent with the activation energy of 142 kJ/mol obtained by Phani and Oliver [170].

Primary and secondary creep To perform all those analysis, a huge hypothesis is done: it is considered that a secondary creep regime is taking place in the sample. Nevertheless, it is not certain. For instance, Phani and Oliver [170] explain a discrepancy observed on their results by the fact that the aluminum sample does not reach this secondary creep regime at low temperature with a Berkovich tip. Classically, it is considered that reaching a steady-state where $\dot{h}$ is constant during the creep segment is the sign of a secondary creep regime [172] and so primary creep is neglected. Such approach has been criticized [173–176], saying that strain rate and stress in indentation are really high compared to classical values obtained in secondary creep measured by uniaxial testing. Those authors propose another approach, based on Miller-Norton law, to model creep in indentation tests, taking into account both the primary and the secondary creep. Unfortunately, such law breaks in plasticity and does not allow to determine a criterion to separate both contributions.

Determining the creep properties by indentation testing is an open question. It seems necessary to determine criteria to characterize the creep state(s) under the indents to validate the used methodology. So first, it would required a theoretical analysis. A simple representation is

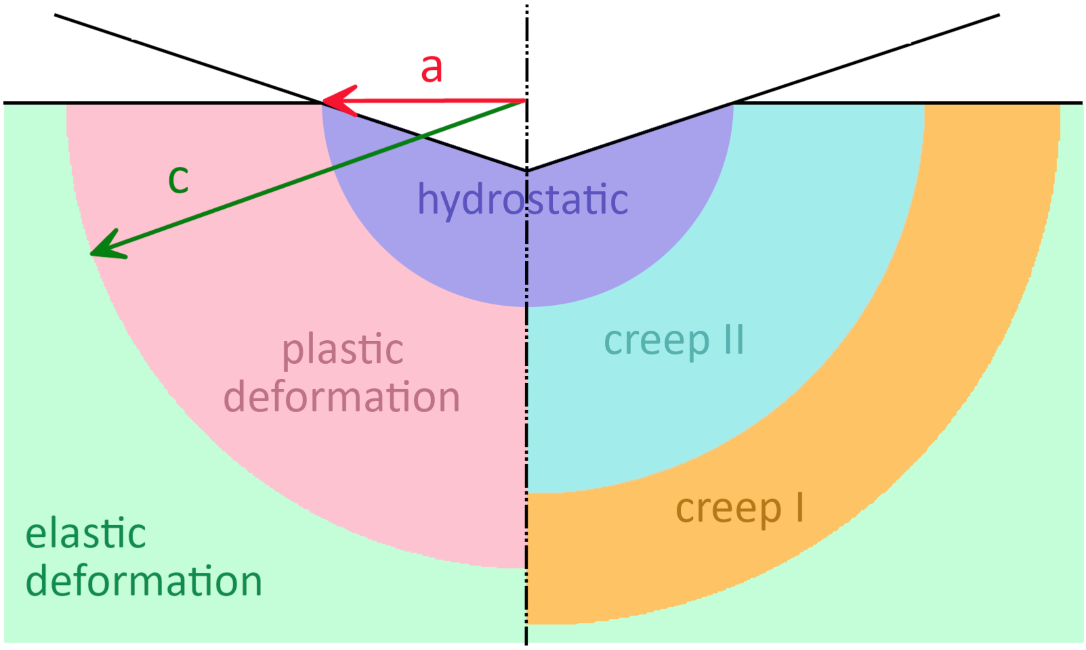

Figure 2.17: (Left) Johnson's model for indentation in an elastic-perfectly plastic material [48]. (Right) possible simple adaptation of the cavity model to visualize the creep zones. Theoretical analysis is required to determine the size of each zone and its variations during the tests.

proposed in figure 2.17. During an indentation creep experiment, primary and secondary creep are expected under the indent. The question is to know exactly where they are taking place. So a theoretical analysis should give criteria (characteristic strain rate, stress level, deformation level, etc.) to define the transition between the elastic zone and the primary creep one as well as the one between primary and secondary creep zones. As the plastic zone expanses during creep tests, it is expected that the creep cavities also expanse during the tests. Characterizing such expansions is also required to go further in the analysis. Moreover, quantifying the contribution of both creep states to the measurements is also essential.

Performing finite element modeling would then give access to the deformed state under the indent during the test. Comparing the obtained stress and strain rate with the theoretical analysis should allows one to quantify the contribution of primary creep to the results in the studied state. It would allow to determine in which case the classical approach can be applied and in which caution should be taken.

IV. Conclusions of the chapter

Through the development of the High-Temperature Scanning Indentation method, one can now compute quasi-continuously the changes in the mechanical properties (Young's modulus, hardness and creep properties) of a material in temperature. Moreover, with creep analysis, one can acquire information on creep parameters such as the activation energy in temperature.

This methodology is based on a specific high-speed indentation cycle applied all along the thermal cycle. Using this approach to determine those properties in temperature is really less time-consuming compared to conducting classical indentation experiments. When it takes one day to get results with the HTSI method, it may require a month to obtain equivalent data through classical testing. However, good care should be taken in the temperature regulation to measure the Young's modulus. Unfortunately, it is really sensitive to thermal equilibrium.

The indentation cycle applied here is controlled by force: during a thermal ramp, the maximum force remains constant. As the hardness of materials decreases with temperature, the indentation depth increases. Caution should be taken if an Indentation Size Effect happen in a sample in temperature. An improvement of the technique would be to implement an indentation cycle where it would be the maximum depth that would stay the same all along the thermal cycle. Nevertheless, the impact of ISE is not too important if tests are performed at large depths. Moreover, it decreases with increasing temperature [105, 177]. So in the following work, it is considered that it does not affect too much the results.

Now that the mechanical properties of a sample are easily determined all along a thermal cycle, one can focus on the signification of their variations. For instance, by studying hardness changes on metals, characterization of static recovery and recrystallization can be performed (see chapter 4). Furthermore, by combining the modifications in hardness and strain rate sensitivity, the physical changes inside thin-film metallic glasses can be analyzed (see chapter 5). However, the next chapter will focus on the interest of the HTSI method to assess the creep properties of a material in temperature.

3

Creep properties in temperature: advantages and drawbacks

Let's use the HTSI method to study the creep properties of materials depending on temperature and strain rate.

Chapter's content

I. Aims

To get the creep properties of a material, one can use classical creep or relaxation uni-axial tests. As they are easy to implement at RT, indentation creep tests are also classically used to get creep properties of materials [56, 58, 170]. Recent developments [22, 57, 61, 64] lead to the implementation of indentation relaxation tests to get creep properties. With the HTSI method, one once again is able to determine those properties. As indentation creep tests are quite easy to implement, it is interesting to measure the creep properties using such a method. However, the question of comparison of the various techniques is still open. The aim of this chapter is to compare indentation creep tests, indentation relaxation tests, HTSI creep tests, and uniaxial tests.

II. Indentation creep versus relaxation tests

The difference between creep and relaxation was presented in chapter 1 (see figure 1.15). During creep tests, the load is kept constant and the increase of displacement allows getting the indentation strain rate [58]. On the opposite, during relaxation tests, the displacement is maintained constant and the decrease of load gives the relaxation strain rate [22, 57]. As presented in [57], relaxation tests enable assessing creep properties on fused silica and PMMA at lower strain rates compared to indentation creep tests.

Unfortunately, as shown in figure 3.1 from [178], comparing indentation creep and relaxation tests gives good results at 27 °C and 30 °C on amorphous selenium but a discrepancy can be observed at higher temperatures. Such behavior is also noted on other materials [179]. Amorphous selenium is known to exhibit a huge increase in strain rate sensitivity near its glass transition. This increase is clearly detected in [178], where it changes from near 0.2 at 27 °C to around 0.5 at 36 °C, depending on the strain rate. The authors propose to use the creep representative strain rate to better compare those tests with relaxation one. As they want to compare such results with literature one, they introduced a new definition of the representative strain rate [178]. Based on the analysis of Bower *et al.* [180], they use the expressions of Kermouche *et al.* [16] (equations 1.34 and 1.35) to define the representative strain rate of creep:

$$\dot{\varepsilon}_r(creep) = 0.44 \exp\left(\frac{0.2}{m}\right) \cot(\theta)\dot{\varepsilon}_{ind} \tag{3.1}$$

According to the definition of the strain rate in the relaxation test (equation 1.44):

$$\dot{\varepsilon}_{rel} = \frac{1}{E}\left|\frac{d\sigma_r}{dt}\right| \tag{3.2}$$

one has:

$$\dot{\varepsilon}_r(relaxation) = \dot{\varepsilon}_{rel} \tag{3.3}$$

When applying those definitions, the comparison between indentation creep tests, indentation relaxation tests and compression tests (from [56]) gives consistent results, as presented in figure

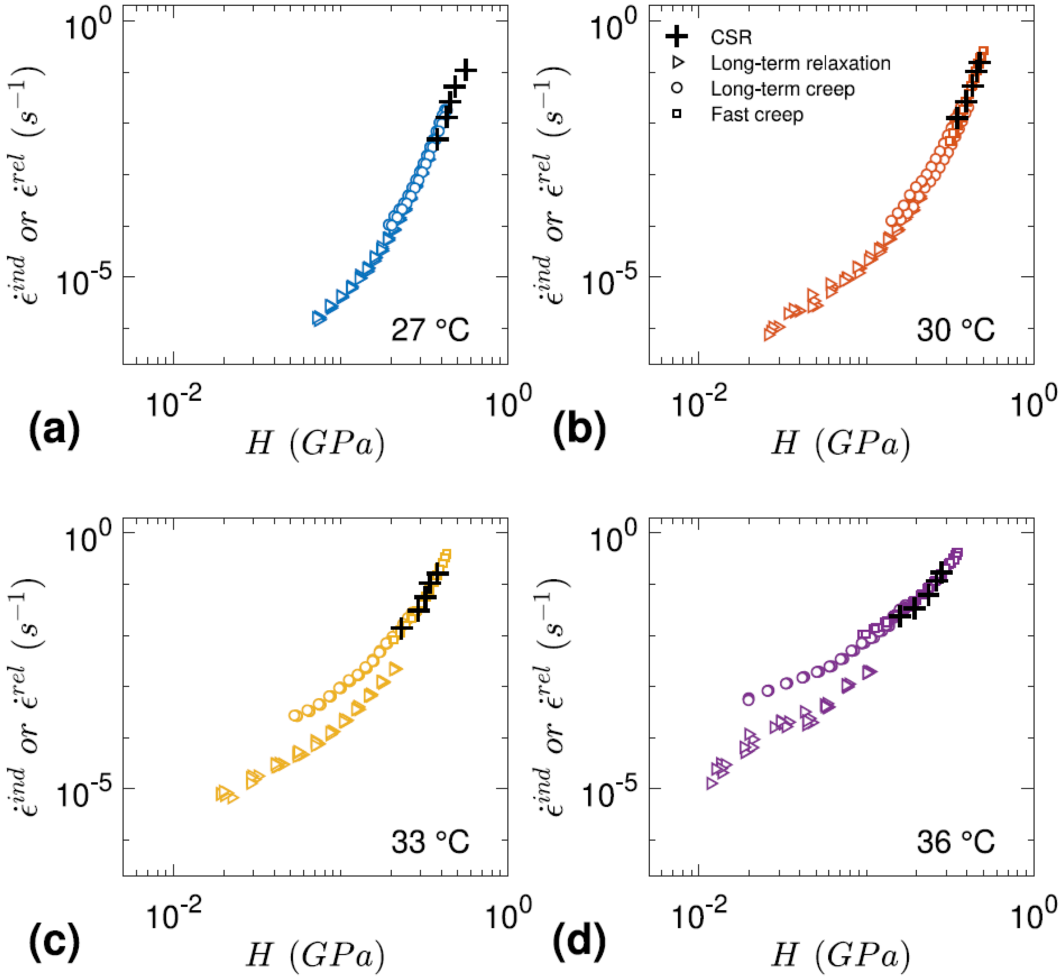

Figure 3.1: Indentation creep behavior of amorphous selenium measured from constant strain rate (CSR) (plus symbols), fast creep (square symbols), long-term creep (circle symbols) and relaxation (triangle symbols) at distinct temperatures: (a) 27 °C, (b) 30 °C, (c) 33 °C and (d) 36 °C, from [178].

3.2, from [178].

As this discrepancy effect is observed when the strain rate sensitivity is high enough, they recommend switching to the creep representative strain rate when $m > 0.1$. For the majority of materials, the strain rate is lower than this value at room temperature so such a definition is not necessary. Nevertheless, when conducting experiments in temperature, it is expected to reach such strain rate sensitivity values: such a definition would be necessary in this case.

Then, assuming that amorphous selenium can be described by Norton-Hoff's law, one can determine the activation energy of creep Q:

$$\dot{\varepsilon}_r = \alpha \sigma_r^{1/m} \exp\left(-\frac{Q}{RT}\right) \tag{3.4}$$

In their article, Baral *et al.* [178] evaluate an activation energy around 500 kJ for amorphous selenium. Using this value and their data, one can then plot the master curve corresponding

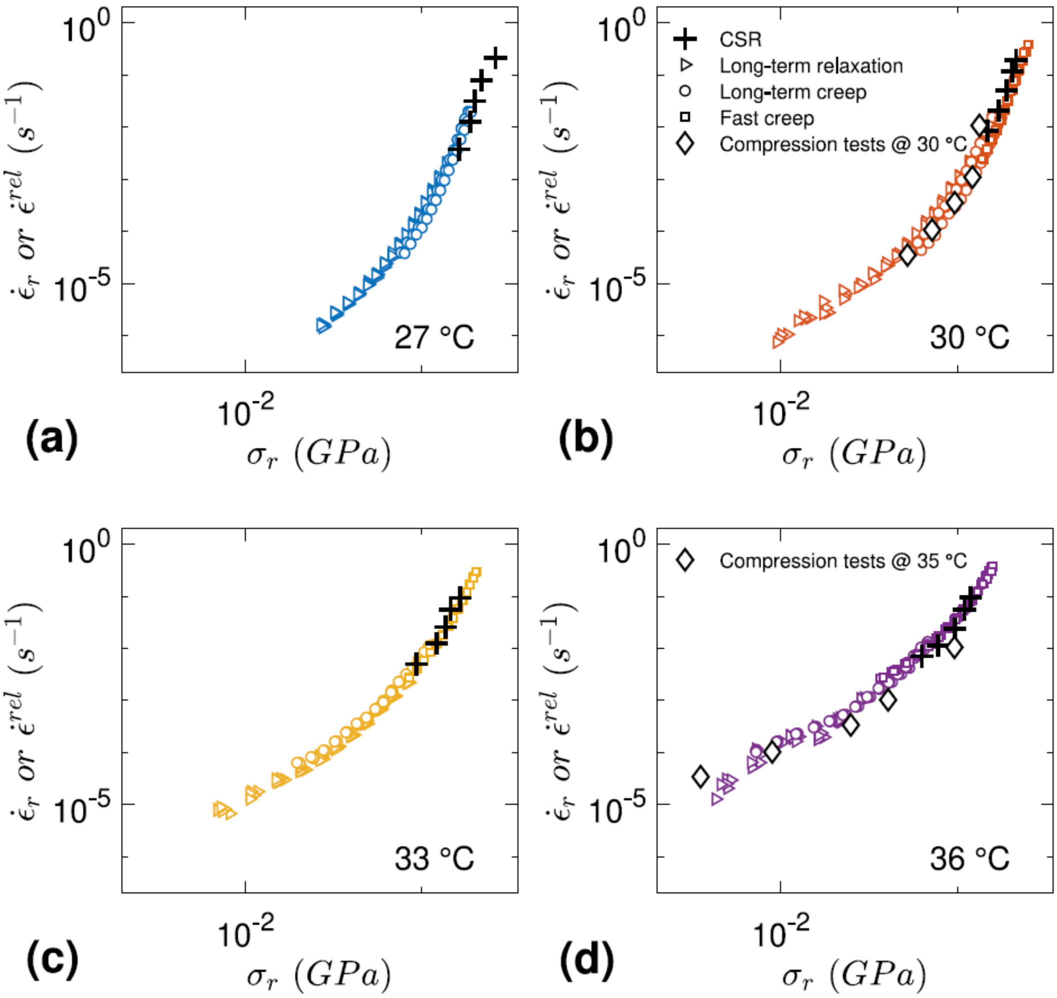

Figure 3.2: Indentation creep behavior of amorphous selenium expressed with the representative strain rate $\dot{\varepsilon}_r$ and stress σ_r and measured from CSR (plus symbols), fast creep (square symbols), long-term creep (circle symbols), and relaxation (triangle symbols) at different temperatures: (a) 27 °C, (b) 30 °C, (c) 33 °C and (d) 36 °C, from [178]. Diamond symbols are compression data from [56].

to Norton-Hoff's law (see figure 3.3). Thanks to the utilization of the representative stress and strain rate, a master curve consistent between indentation tests and literature data is obtained. As it can be observed, there is an equivalence between time and temperature: conducting experiments at a lower strain rate is equivalent to carrying out tests at a higher temperature.

Such equivalence is a really promising tool to study the creep properties of a sample at temperatures or strain rates difficult to reach through classical methods. Thanks to indentation relaxation tests, one can get data at low strain rates compared to classical creep tests. However, performing creep or relaxation tests in temperature requires extremely good control of temperature. As the load or the displacement have to be maintained constant for a few minutes to a few hours, thermal drift can really lead to uncorrected properties. For instance, Baral *et al.* [178] had to let the temperature stabilize for 12 h before conducting any experiments. Such thermal stabilization coupled with the type of experiments makes those characterizations really

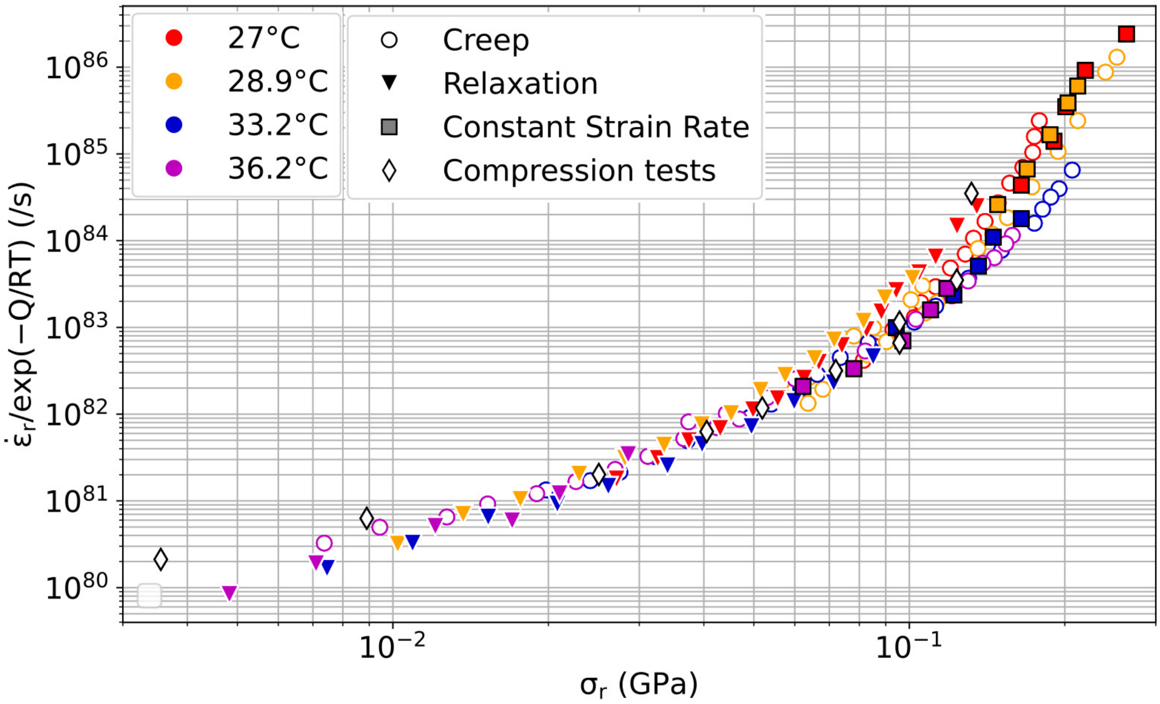

Figure 3.3: Master curve of creep for amorphous selenium. The indentation data are from [178] and the compression data from [56].

time-consuming. As the newly developed High-Temperature Scanning Indentation method is a fast methodology, it can be used to determine those properties in temperature.

III. Materials and methods

III.A. Materials

Silver samples Polycrystal pure silver samples of 10 mm diameter and 0.3 mm thick were provided by Technetics. They were glued on AU4G shelves of 12.5 mm diameter and 3 mm thick using a sliver-based temperature-resistant glue provided by Polytec (Pyro-Duct 597-A). This allows clamping of the sample in the InSEM system. Unfortunately, it was not possible to polish the samples more than what was provided. Moreover, such system greatly decreases the load frame stiffness of the system.

CaF_2 samples CaF_2 single-crystal samples of 10 mm to 12 mm diameter and 2 mm thick were provided by Edmund Optics. No more polishing was conducted on the samples.

III.B. Indenters

Two nanoindentation devices are used for those experiments. All the tests on silver are conducted using the InSEM HT nanoindenter at the LTDS, provided by KLA Nanomechanics. This system is under vacuum (1×10^{-2} Pa), inside a VEGA 3 SEM (Tescan). A Berkovich diamond tip is

Table 3.1: Tests conducted on silver samples

Type of test	Pre-annealing	Temperature	Heating rate	$\dot{P}/P$	$t_{loading}$	$t_{holding}$
CSR	na	RT	na	$0.1\,s^{-1}$	na	na
	2 h at 350 °C	185 °C	na	$0.1\,s^{-1}$	na	na
	1 h at 400 °C	350 °C	na	$0.1\,s^{-1}$	na	na
Creep	na	RT	na	$0.1\,s^{-1}$	na	10 h
	2 h at 350 °C	185 °C	na	$0.1\,s^{-1}$	na	1000 s
	1 h at 400 °C	350 °C	na	$0.1\,s^{-1}$	na	1000 s
Relaxation	na	RT	na	$0.1\,s^{-1}$	na	10 h
	2 h at 350 °C	185 °C	na	$0.1\,s^{-1}$	na	1000 s
HSTI	na	RT → 450 °C	3 °C/min	na	0.5 s	0.3 s
	1 h at 400 °C	RT → 350 °C	3 °C/min	na	0.5 s	0.5 s

used to perform the tests. Tests with constant loading rate before doing long creep or relaxation segments are carried out during isotherm heating at RT, 185 °C and 350 °C. Moreover, two HTSI measurements are conducted. Initially, the maximum temperature applied should have been 350 °C. Due to an issue with a thermocouple that has been identified after the first HTSI test, one of the samples is heated up to 450 °C. The temperature control during those cycles is quite bad, the temperatures are not following well enough their settings. The Young's modulus could not be correctly determined during those experiments. Table 3.1 summarizes what tests are conducted on the silver specimens.

All the tests on CaF_2 are conducted using the InSEM HT nanoindenter at KLA Nanomechanics. This system is under vacuum (1×10^{-2} Pa) inside a vacuum chamber. A Berkovich sapphire tip is used to make those tests. Tests with constant loading rate (CSR) before doing long creep or relaxation segments are carried out during isotherm heating at RT, 100 °C, 200 °C, and 400 °C. As the sample sticks to the tip at 400 °C, it is not possible to perform tests at higher temperatures. Moreover, two HTSI measurements are conducted: one heating at 2 °C/min up to 250 °C and the other at 0.2 °C/min up to 100 °C. To get results at higher strain rates at RT, tests at constant strain rates are performed using the Alemnis system [181]. Table 3.2 summarizes the different tests realized on those samples.

Before doing high-temperature experiments, a thermal matching step was conducted on the sample to achieve thermal equilibrium. As it was quite difficult to reduce the variation of temperature under 0.5 °C around the temperature setting, creep and relaxation tests could not be carried out for more than 15 min in temperature.

IV. Application on CaF_2

Let's start the analysis with CaF_2 samples. This ceramic is said to present interesting properties at RT and in temperature, for industrial applications [182, 183].

It has a cubic structure with calcium ions in a FCC structure and fluorite ions in the tetrahedral sites. Its bonds are ionic ones [184]. Contrary to classical FCC structures, the activated slip

Table 3.2: Tests conducted on CaF_2 samples

Type of test	Temperature	Heating rate	$\dot{P}/P$	$\dot{h}/h$	$t_{loading}$	$t_{holding}$
CSR	RT	na	$0.01 \rightarrow 0.2\,\mathrm{s}^{-1}$	na	na	na
	100 °C	na	$0.01 - 0.2\,\mathrm{s}^{-1}$	na	na	na
	200 °C	na	$0.01 - 0.2\,\mathrm{s}^{-1}$	na	na	na
	400 °C	na	$0.2\,\mathrm{s}^{-1}$	na	na	na
Creep	RT	na	$0.01 - 0.2\,\mathrm{s}$	na	na	1000 s
	100 °C	na	$0.01 - 0.2\,\mathrm{s}^{-1}$	na	na	1000 s
	200 °C	na	$0.2\,\mathrm{s}^{-1}$	na	na	1000 s
	400 °C	na	$0.2\,\mathrm{s}^{-1}$	na	na	1000 s
Relaxation	RT	na	$0.01 - 0.2\,\mathrm{s}^{-1}$	na	na	1000 s
	100 °C	na	$0.2\,\mathrm{s}^{-1}$	na	na	1000 s
	200 °C	na	$0.2\,\mathrm{s}^{-1}$	na	na	1000 s
High Strain Rate	RT	na	na	$1 \rightarrow 100\,\mathrm{s}^{-1}$	na	na
HTSI	RT	na	na	na	0.5 s	0.3 s
	RT	na	na	na	5 s	3 s
	RT → 250 °C	2 °C/min	na	na	0.5 s	0.3 s
	RT → 100 °C	0.2 °C/min	na	na	5 s	0.3 s

systems at RT are $\{100\} < 110 >$ [185, 186]. Those slip systems control the deformation mechanism up to around 260 °C [187]. Finally, as the samples are single crystals, some anisotropy is expected here.

IV.A. Results

IV.A.1. At RT

Let's first study this material at room temperature.

Indentation Size Effect According to [188, 189], the Young's modulus value of a single-crystal of CaF_2 goes from 90 GPa in the $< 111 >$ directions to 140 GPa in the $< 100 >$ directions. The Young's modulus values here are consistent with those values. As it can be observed in figure 3.4, an ISE effect is detected on the hardness of the material [188–190]. To analyze the data correctly, one has to perform tests at a specific maximal depth to compare the values.

Strain rate Let's now work on the impact of the strain rate on the results. As it can be noticed in figure 3.5, increasing the loading rate clearly affects the Indentation Size Effect previously detected on the material. For instance, at 800 nm, the hardness varies from 1.8 GPa to 2.7 GPa because the constant loading rate rises from $0.01\,\mathrm{s}^{-1}$ to $0.2\,\mathrm{s}^{-1}$.

Creep As hardness depends on the strain rate, let's see how it impacts the creep properties of CaF_2 samples at RT. To determine the creep properties on a large strain rate scale, various tests

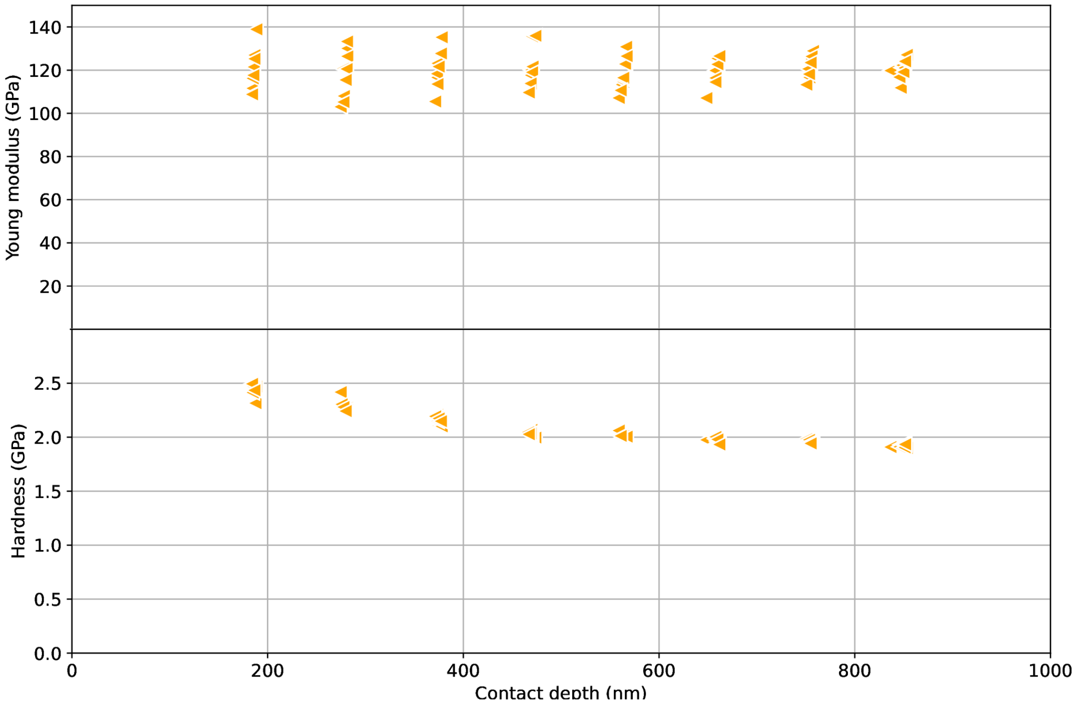

Figure 3.4: Hardness and Young's modulus of CaF_2 versus depth measured by constant strain rate indentation tests ($\dot{P}/P = 0.01\,\mathrm{s}^{-1}$). An ISE effect is detected on hardness but not on Young's modulus.

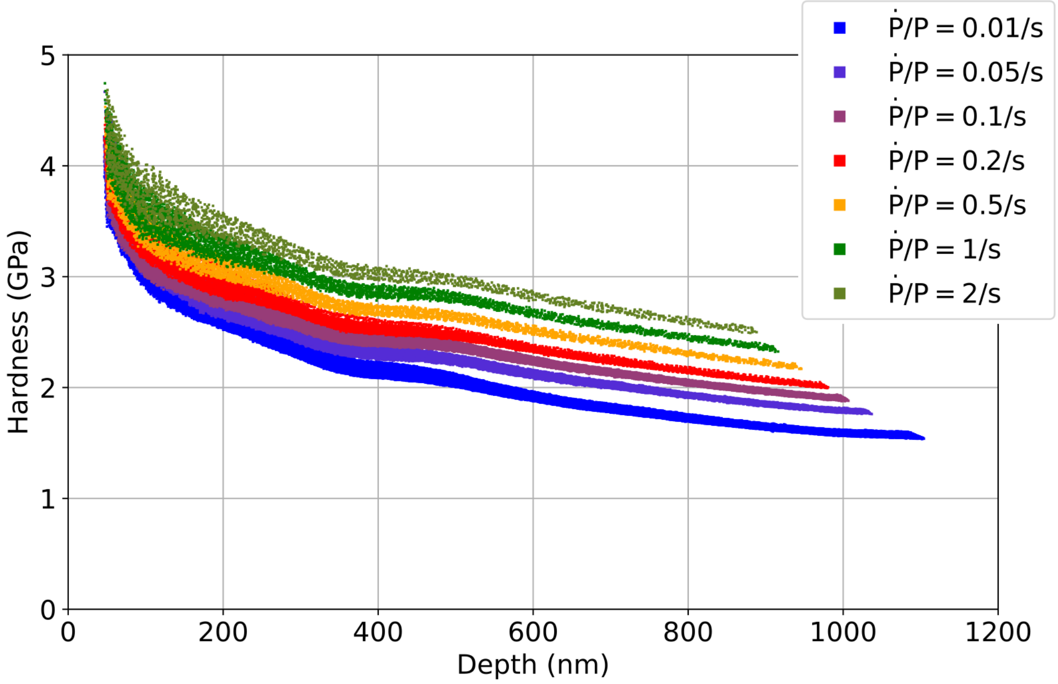

Figure 3.5: Hardness versus depth measured by constant strain rate indentation experiments.

were carried out. In figure 3.6, different tests are plotted. The symbols correspond to the type of experiments, while the color gives information on the time of loading or the constant loading

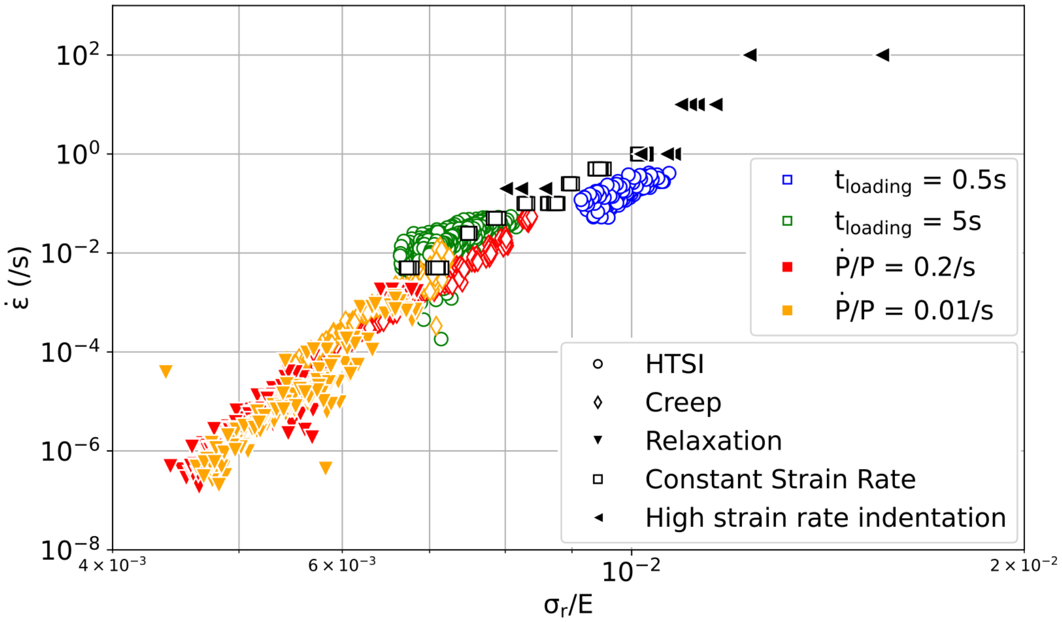

Figure 3.6: Strain rate versus Young's modulus compensated stress for CaF_2 at RT. The symbols correspond to the type of tests, while the color gives information on the time of loading or the constant loading rate.

rate. To reduce the influence of the ISE on the results, the values are taken at a depth of 850 nm. The open squares represent the value obtained from constant strain rates ($5 \times 10^{-3}\,s^{-1}$ to $1\,s^{-1}$). The open circles refer to high-speed indentation cycles used in the HTSI method, with a loading segment in 0.5 s or 5 s. The open diamonds correspond to the creep segment data: after a constant loading rate ($0.01\,s^{-1}$ or $0.2\,s^{-1}$), a creep segment of 1000 s is performed. The close-colored triangles stand for the relaxation segment data: after a constant loading rate ($0.01\,s^{-1}$ or $0.2\,s^{-1}$), a relaxation segment of 1000 s is conducted. Finally, the close-black triangles represent the high constant loading rate tests ($1\,s^{-1}$ to $100\,s^{-1}$), carried out on the Alemnis indenter.

As can be seen on the strain rate—stress curve, the different tests are consistent with each other. The stress changes depending on the strain rate are then obtained on a large strain rate scale: $1 \times 10^{-8}\,s^{-1}$ to $100\,s^{-1}$. However, even if the variations between the two seem linear, it is not.

At a specify temperature:

$$\dot{\varepsilon} = \alpha \sigma_r^{1/m} \tag{3.5}$$

In figure 3.6, the values are in log scale: a linear evolution would require a constant strain rate sensitivity m. As it can be observed on the strain rate sensitivity depending on the strain rate, in figure 3.7, it is not the case. The strain rate sensitivity decreases linearly with lowering strain rate: at higher strain rates, this material is more sensitive to the strain rate. To verify this behavior, it would be necessary to perform tests at higher strain rates. Recent developments [181, 191, 192] may allow to do so.

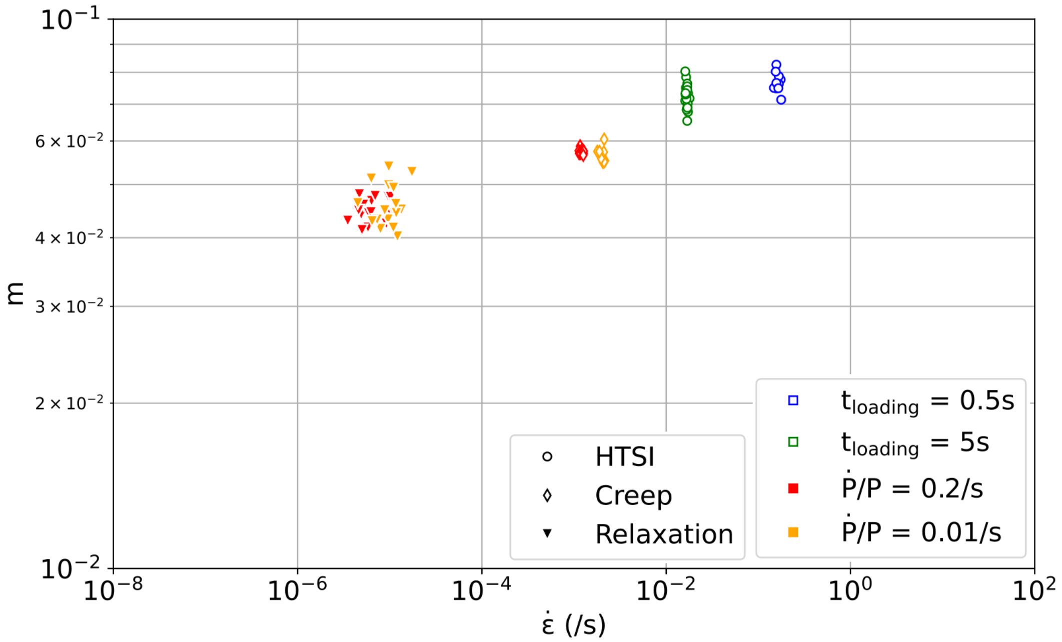

Figure 3.7: Strain rate sensitivity versus strain rate for CaF_2 at RT. The symbols correspond to the type of tests, while the color gives information on the time of loading or the constant loading rate.

IV.A.2. At high temperature

Hardness According to [182], hardness of CaF_2 should decreases with increasing temperature. As it can be observed in figure 3.8, this is the case. Hardness clearly decreases during the HTSI experiment. Unfortunately, as those tests were carried out at a constant load, the maximum depth was not constant: the hardness diminution may be caused by the temperature but also by the Indentation Size Effect. When examining the constant strain rate tests, where hardness is evaluated at the same depth whatever the temperature, the hardness decrease is clearly linked with temperature. There is a huge decrease from RT to 200 °C. According to [182], a second one is expected around 500 °C or 600 °C.

Moreover, the impact of the strain rate is very clear at RT: as previously observed, the hardness values are quite scattered depending on the strain rate. When increasing temperature, this effect is still present. With increasing temperature, the strain rate dependence of hardness is getting lower (0.7 GPa at RT to 0.5 GPa at 100 °C when passing from $0.01\,s^{-1}$ to $0.2\,s^{-1}$). As hardness literature data are from Vickers measurements [182], it is expected that the strain rate is not that important during the tests. The indentation experiment results seem to merge with those values at high temperatures when a huge difference is observed at RT.

Creep in T Indentation creep and relaxation tests were carried out to study the creep properties of the CaF_2 in temperature, for comparison with the HTSI experiments. As seen in figure 3.9, increasing temperature decreases the Young modulus compensated stress value for a given strain rate. As it was observed at room temperature, increasing the strain rate increases the strain

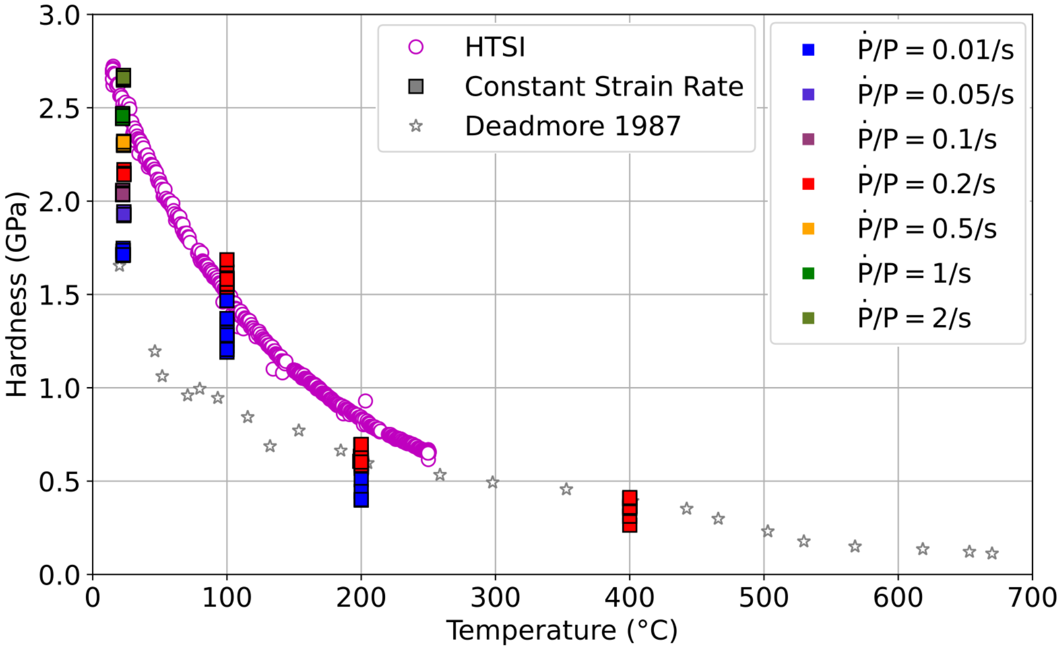

Figure 3.8: Hardness changes of CaF_2 in temperature. Indentation results are from HTSI and constant strain rate tests. They are compared with high-temperature hardness measurements from [182]. A clear impact of the strain rate is assessed at RT and it seems to reduce with increasing temperature.

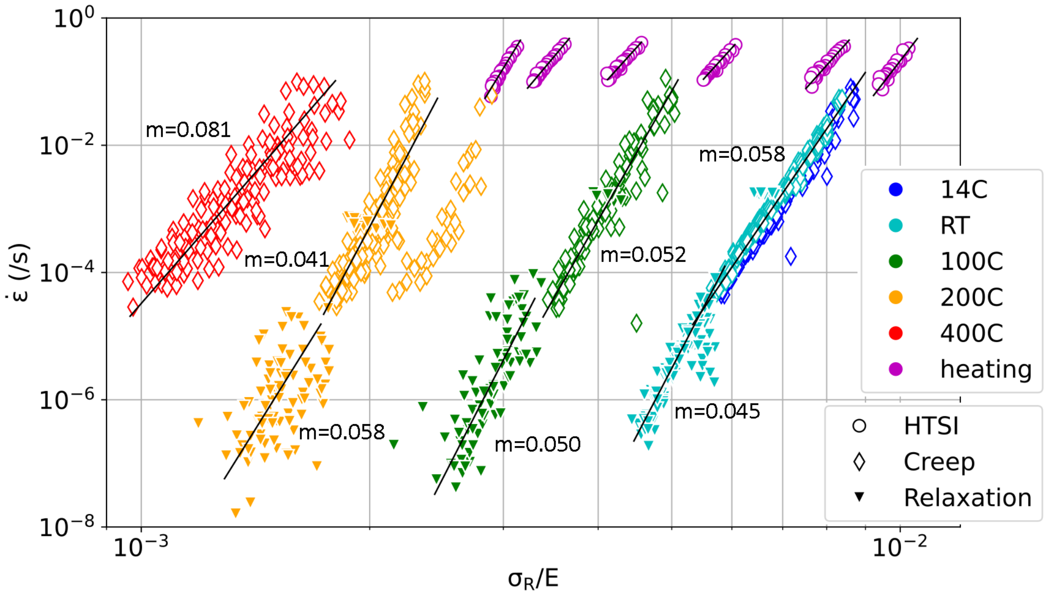

Figure 3.9: Strain rate versus Young's modulus compensated stress at various temperatures on CaF_2. Isotherm indentation creep tests are compared to isotherm indentation relaxation tests and HTSI experiments. Only the HTSI tests at 20 °C, 50 °C, 100 °C, 150 °C, 200 °C and 250 °C (6 of the 400 tests) are plotted here. The slope of the curve yields the strain rate sensitivity. As observed, temperature and strain rate impact those properties.

Table 3.3: Strain rate sensitivity determined on CaF_2, depending on temperature and strain rate.

Temperature	$\dot{\varepsilon}$	Strain rate sensitivity
RT	$10^{-1}s^{-1}$	0.072
	$10^{-1} \rightarrow 10^{-4}s^{-1}$	0.058±0.001
	$10^{-5} \rightarrow 10^{-7}s^{-1}$	0.045±0.002
50 °C	$10^{-1}s^{-1}$	0.078
100 °C	$10^{-1}s^{-1}$	0.080
	$10^{-1} \rightarrow 10^{-4}s^{-1}$	0.052±0.003
	$10^{-5} \rightarrow 10^{-7}s^{-1}$	0.050±0.009
150 °C	$10^{-1}s^{-1}$	0.082
200 °C	$10^{-1}s^{-1}$	0.070
	$10^{-1} \rightarrow 10^{-4}s^{-1}$	0.041±0.004
	$10^{-5} \rightarrow 10^{-7}s^{-1}$	0.058±0.001
250 °C	$10^{-1}s^{-1}$	0.049
400 °C	$10^{-1} \rightarrow 10^{-4}s^{-1}$	0.081±0.005

rate sensitivity. However, this tendency seems to reverse with temperature. Moreover, seeing the slope of HTSI tests, the impact of the strain rate is clear: this inversion happens at a higher temperature compared to what is observed on relaxation tests (see table 3.3).

Finally, assuming that CaF_2 follows the Norton-Hoff's law, one can plot the master curve of its creep behavior depending on the strain rate and temperature. This is done in figure 3.10, for an activation energy of 110 kJ mol^{-1}. The data merge quite well on a unique master curve, the different tests (indentation creep, indentation relaxation, and HTSI) giving consistent results in temperature. There is an equivalence between time and temperature: conducting tests at a higher temperature is equivalent to perform experiments at a lower strain rate. Let's notice the scale on the ordinate scale: it is on 20 orders of magnitude. If the equivalence stays valid, it is possible to get information at really low strain rates "only" by doing experiments at higher temperatures. To verify the value of activation energy, the Norton-Hoff's law is used. The slope between $\log\left(\frac{\dot{\varepsilon}}{\sigma^{1/m}}\right)$ and $1/T$ gives the activation energy of creep. An energy of 100 kJ mol^{-1} for temperature under 200 °C is obtained through HTSI tests, quite close to what is applied in figure 3.10.

IV.B. Discussion

IV.B.1. Deformation mechanisms taking place in the sample

The consistent master curve is plotted using a constant activation energy of 110 kJ mol^{-1}. However, it seems that this energy may change with temperature and strain rate. For comparison, O'Neil *et al.* [187] obtain an activation energy of 42 kJ mol^{-1} between RT and 300 °C, leading them to conclude that vacuum diffusion of fluorite ions (52 kJ mol^{-1} [193]) is the controlling mechanism for creep. Nevertheless, this value is quite low compared to what is measured here.

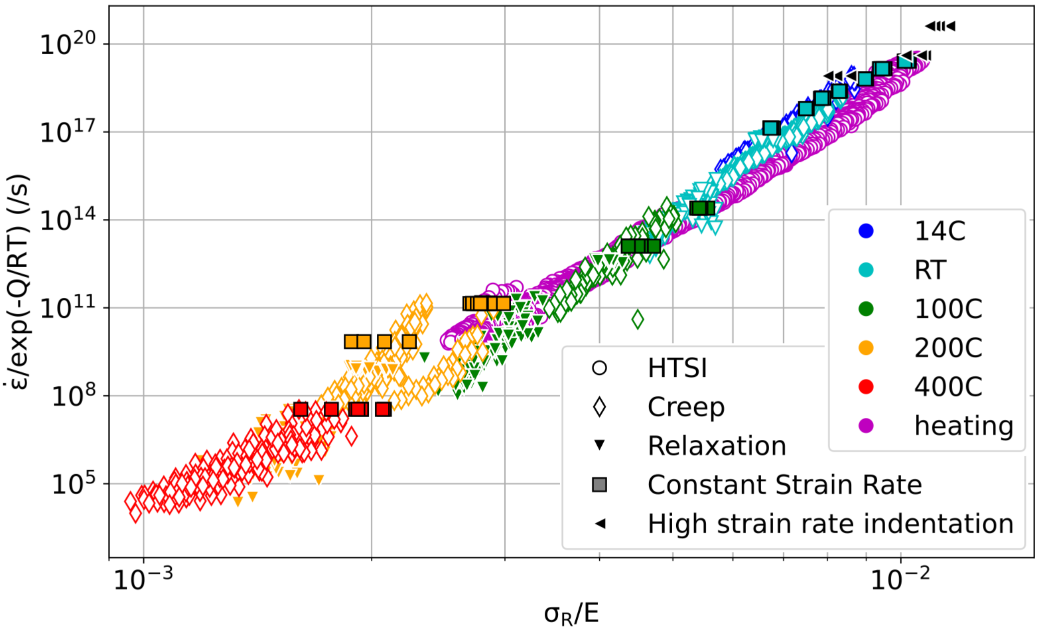

Figure 3.10: Creep master curve on CaF_2. All the indentation tests nicely merge into a unique master curve. The activation energy of creep is 110 kJ/mol.

Melaka [194] proposes an expression for the apparent activation energy ($J\,mol^{-1}$) of creep between 673 K and 1200 K:

$$Q(T) = 8.31(20.8T + 7640) \tag{3.6}$$

A linear extrapolation of this expression gives a value of $115\,kJ\,mol^{-1}$ at RT, consistent with what is obtained here.

To determine the deformation mechanism taking place in the sample during creep, one could focus on the activation volume of creep.

$$m = \frac{\sqrt{3}k_BT}{V\sigma_r} = \frac{\gamma\sqrt{3}k_BT}{VH_{creep}} \tag{3.7}$$

where k_B is Boltzmann's constant and γ is the constraint factor. As observed in figure 3.11, the master curve obtained at low temperature is consistent with what is measured at high temperature by Sadrabadi *et al.* [195]. Moreover, at RT, the activation volume is quite low (1–5 b^3 depending on the strain rate). Increasing temperature or decreasing strain rate leads to an increase in this volume. There is a first increase from RT to 200 °C approximately ($1 \rightarrow 30b^3$). Then between 200 °C and 400 °C, the activation volume seems to be more or less stable before increasing once again at higher temperatures. Table 3.4 gives typical activation volume for classical deformation mechanisms, according to [54]. According to [193, 196], edge dislocations have a really low speed compared to screw dislocations at RT. The edge dislocation gliding mechanism is expected to control creep.

Seen the low values of the activation volume at RT, one can think that climb of edge dislocations would be the dominant mechanism for creep here. This is consistent with what Feltham *et al.*

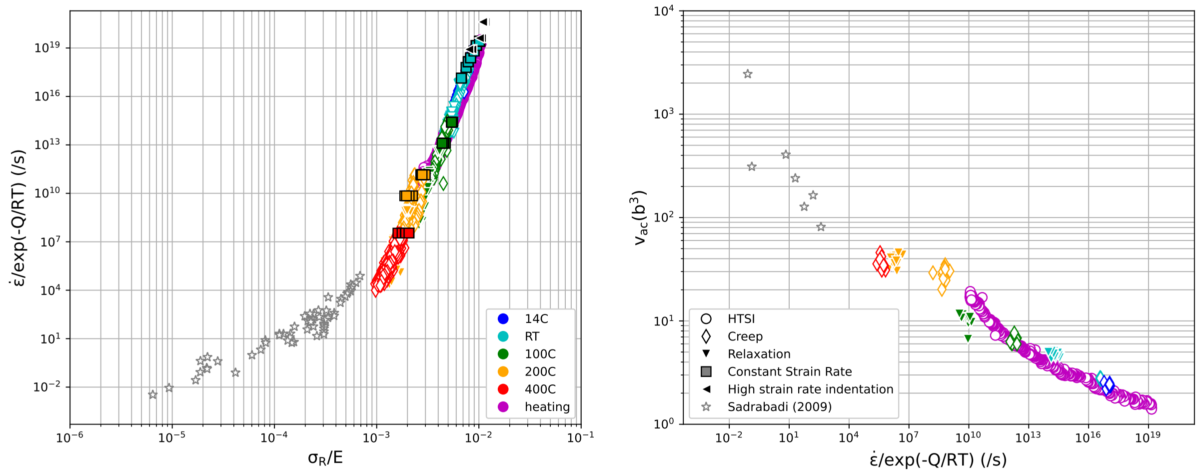

Figure 3.11: (Left) Creep master curve and (right) activation volume of creep in CaF_2 depending on temperature and strain rate. Data at high temperatures comes from compression tests [195].

[197] get: an activation energy of 183 kJ mol^{-1} between 400 °C and 600 °C and a mechanism of dislocation climb. Moreover, it seems that these dislocation movements lead to formations of complexes that trap the electrons [197]. However, climb is a thermally activated mechanism [198]: it is more expected at high temperatures. Having it at RT is unexpected. According to Evans *et al.* [196], a probable controlling mechanism near RT would be the interaction of edge dislocations with local charges. So, the edge dislocations would have to overcome those electronic barriers to move in the structure. It may remind the behavior of screw dislocations overcoming Peierls stress in BCC structures at low temperatures [198]. The deformation mechanism ruling creep in CaF_2 is still an open question.

IV.B.2. Impact of strain rates at low temperature

If the deformation mechanism for creep on CaF_2 resembles the deformation of BCC structures at room temperature, other behaviors may be similar.

Indentation Size Effect and strain rates The sample is a single-crystal: at RT, only a few slip systems (up to six systems $\{100\} < 110 >$ [186]) can be activated. It can be through that depending on the strain rate, more or less slip systems are activated, which impacts the

Table 3.4: Typical activation volume depending on the deformation mechanism, from [54]

Deformation mechanism	Typical activation volume (b^3)
Overcoming Peierls-Nabarro stress	$10^1 - 10^2$
Intersection of dislocations	$10^2 - 10^4$
Nonconservative motion of jogs	$10^2 - 10^4$
Cross-slip	$10^1 - 10^3$
Climb	1

measured hardness of the specimen. Tian *et al.* [199] observed the activation of slip systems non-predicted by Schmid's law when increasing the strain rate on ferrite. Such behavior seems to increase the hardness of a material [200]. Moreover, Maier *et al.* [201] notice that BCC structures at RT are sensitive to strain rate because of their high lattice friction. According to Sadrabadi [190], CaF_2 may present high internal friction at RT. This may explain the behavior noted on the ISE on hardness in figure 3.5.

Strain rate sensitivity depending on strain rate As observed in figure 3.7, the strain rate sensitivity decreases linearly with lowering strain rate. At higher strain rates, this material is more sensitive to the strain rate. Similar behavior is predicted by El Ters *et al.* [202] on BCC iron. Once again it seems that this behavior is explained by a similar deformation mechanism between CaF_2 and BCC crystals at low temperatures.

Impact of strain rate on hardness at high temperature According to literature [187, 203, 204], the slip system $\{100\} < 110 >$ is the primary slip system in CaF_2. However, with increasing temperature, other slips systems are activated in temperature [203]. And at high temperatures (>400–600 °C), cross-slip and other slip systems take place in the structure [183, 203, 204]. Such behavior may explain the decrease of strain rate impact on the hardness value with increasing temperature. This reduces the anisotropy of the material [187], the plasticity being isotropic at 600 °C [203]. Moreover, it could explain the second decrease of hardness observed around 500 °C or 600 °C [182].

IV.C. Conclusion on CaF_2

Creep properties of CaF_2 at RT and HT can be surprising. To study such properties correctly, one has to perform experiments on large strain rates and temperature scales. The nanoindentation technique allows doing so: by using creep [59], relaxation [57, 178] and high constant strain rate tests, one can get information on a really large strain rate scale (10^{-8} s^{-1} up to 10^{2} s^{-1}). Seen the recent developments, one can also hope to go up to strain rate of 10^{4} s^{-1} [181, 191, 192]. Utilizing such measurements enable to observe the impact of the strain rate on the plastic behaviors of CaF_2 single-crystal at RT.

To determine those properties in temperature, one can perform those tests (creep and relaxation) during isotherm experiments. However, such tests are difficult to implement and quite time-consuming. Nevertheless, the HTSI method that gives information at a given strain rate (1/s) allows getting properties in temperature quite easily compared to those methods. Using the equivalence between time and temperature, one can then obtain the creep properties expected at low strain rates through HTSI experiments at higher temperatures. On CaF_2, it can thus be observed that the impact of the strain rate, quite important at RT, is no longer that affecting at high temperatures. Finally, this methodology also allows getting information on activation energy and volume. Such data can help understand the deformation mechanisms taking place in the sample submitted to high temperatures. However, more studies seem necessary to understand better the detected behavior at RT and high temperatures. Moreover, a constant activation energy has been used in the present analysis. Understanding the impact of temperature and strain rate is compulsory to go further in the analysis. Finally, CaF_2 presents pop-ins in its load-displacement curves. Examining them may lead to the detection of the brittle to ductile transition of this material in temperature [182].

V. Application on silver

The equivalence between time and temperature works well on CaF_2: applying the HTSI method allows getting data much faster than with alternative testing methods. Let's now verify that consistent results are also obtained on other materials. To do so, experiments were carried out on pure silver samples in temperature.

V.A. Hardness and Young's modulus

Firstly, let's focus on the hardness and Young's modulus of silver with temperature. As no pile-up was observed on post-mortem indents on an annealed specimen, the analysis was conducted using Oliver and Pharr method. When examining the hardness and Young's modulus (see 3.12), one can detect an ISE effect on hardness and no ISE on the Young's modulus. However, when performing the same experiments on another glued sample, a huge ISE is observed on the Young's modulus. Unfortunately, the glue employed for that study tends to impact the system stiffness. As the samples are rough and an ISE effect may be present on the Young's modulus

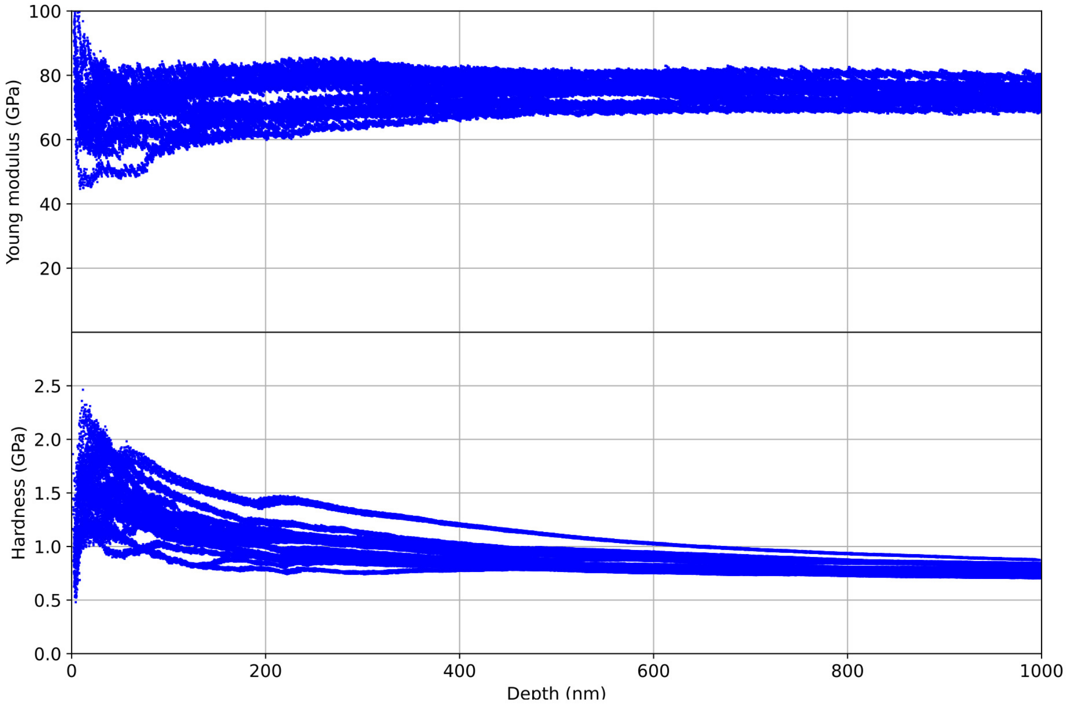

Figure 3.12: Hardness and Young's modulus against the depth of silver samples at RT. An ISE effect is observed on hardness and not on Young's modulus here.

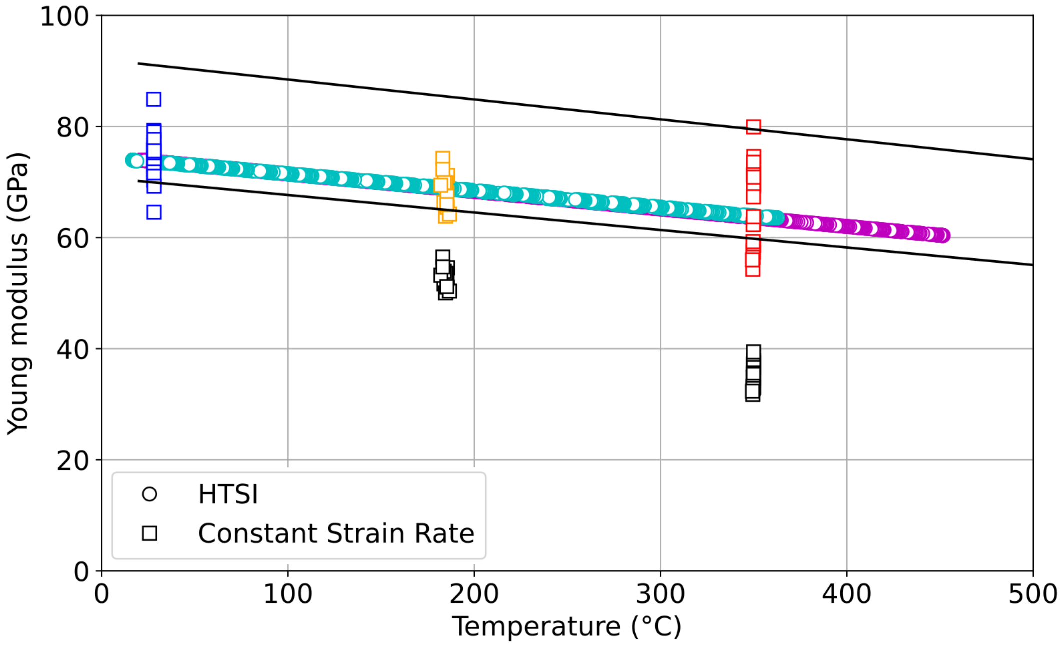

Figure 3.13: Young's modulus of silver in temperature. The results in black are determined using the load frame stiffness calibrated on fused silica. The load frame stiffness was then modified to get consistent Young's modulus data (color). The black line corresponds to (high) Voigt and (low) Reuss boundaries.

of silver, it is not possible to correct the system stiffness easily. Moreover, the data are quite scattered. The specimens were rough before being glued, and polishing them to get a better roughness was quite complicated. This effect, with the polycrystalline microstructure, explain this scattering.

Let's now verify those properties in temperature, plotted in figures 3.13 and 3.14. If taking the system frame calibrated on fused silica (in black), it is clear that something happens in temperature. The Young's modulus values decrease a lot. To get consistent values, one should greatly lower the system stiffness with temperature. This effect may come from the glue employed to glue the sample on the aluminum subtract. For this reason, the Young's modulus data were useless and had to be corrected for future uses.

If the same analysis is performed on the hardness data, no effect is observed (see 3.14). The impact of the system stiffness noted on Young's modulus is not present on hardness. Hopefully, even if the Young's modulus of silver is not exploitable, one has consistent hardness data. However, one notices that, depending on the initial state of the silver specimen (annealed or not), the hardness values at low temperatures change. The non-annealed samples (blue and purple) have a hardness of 0.8 GPa at RT while the annealed one (cyan) has a hardness of 0.6 GPa at this temperature. Then, at temperatures higher than 300 °C, the purple and cyan samples have the same hardness changes. And if focusing on the HTSI results, some purple data can be observed at values between 0.4 GPa and 0.6 GPa at low temperatures. In the figure, the hardness data correspond to the whole thermal cycle applied to the sampling. Something happens on the non-annealed specimen during the thermal cycle. As silver is a metal with a low

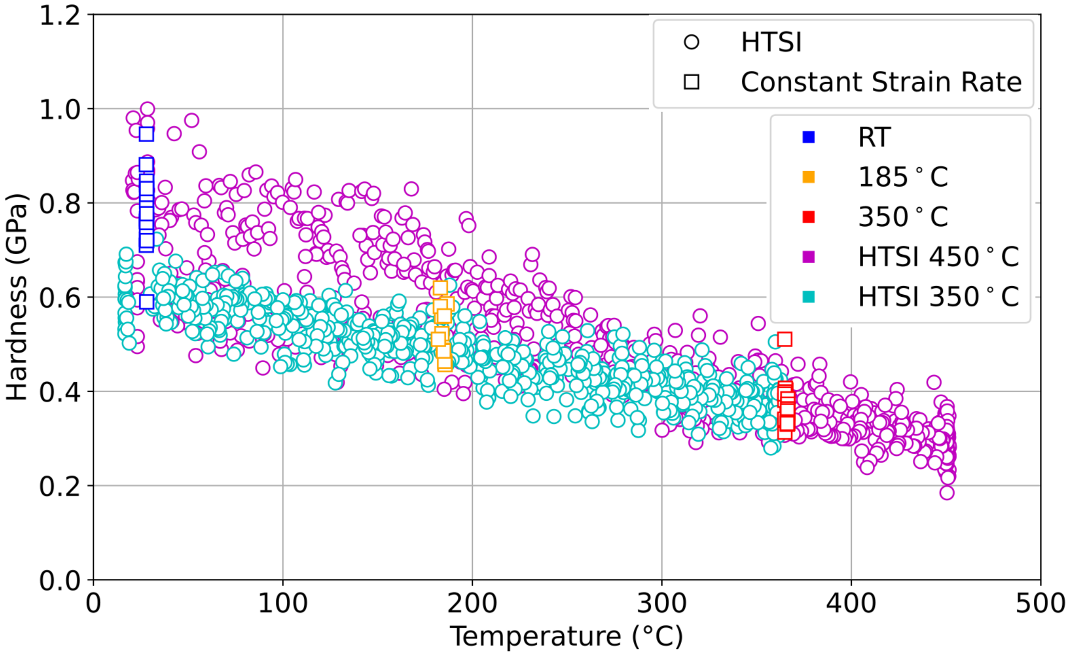

Figure 3.14: Hardness of silver samples in temperature. Contrary to what was observed on Young's modulus data, the non-corrected (black) and corrected (colored) stiffness data overlap each other.

stacking fault energy, it is believed that the sample recrystallized during the heating phase. It would explain the difference in behavior at RT and the consistency assessed at the end of heating and during cooling. The microstructure changes detected here are not the focus of this chapter. However, a substantial analysis of those phenomena observed on model metallic materials, using the HTSI method, is conducted in the following chapter.

V.B. Creep properties

As for CaF_2, the main interest here is to get the creep master curve of the silver sample. Let's first focus on the strain rate versus stress curve in temperature (see figure 3.15). Data from HTSI (plotted only at RT, 100 °C, 200 °C, 300 °C, and 400 °C), indentation creep and relaxation tests are compared with literature data. Goods and Nix [205] studied creep properties from 200 °C to 500 °C. Logan *et al.* [206] performed tensile creep tests from RT to 200 °C. Finally, Kassner [207] gets creep data from torsion experiments, from −70 °C to 100 °C.
At RT, the results from HTSI, creep and relaxation tests are consistent one with the other, and also with literature data. Moreover, the strain rate sensitivity of the sample seems to increase with decreasing strain rate (see table 3.5). At higher temperatures, creep and relaxation data are once again consistent one with each other. Here again, it appears that strain rate sensibility increases with decreasing strain rate. Finally, at the highest temperatures, the creep results are consistent with the HTSI creep tests. However, the data do not follow the slope observed by Goods [205] in this range. The strain rate sensitivity seems quite high on those tests at 350 °C (see table 3.5). According to Baral *et al.* [178], one should apply their representative strain rate

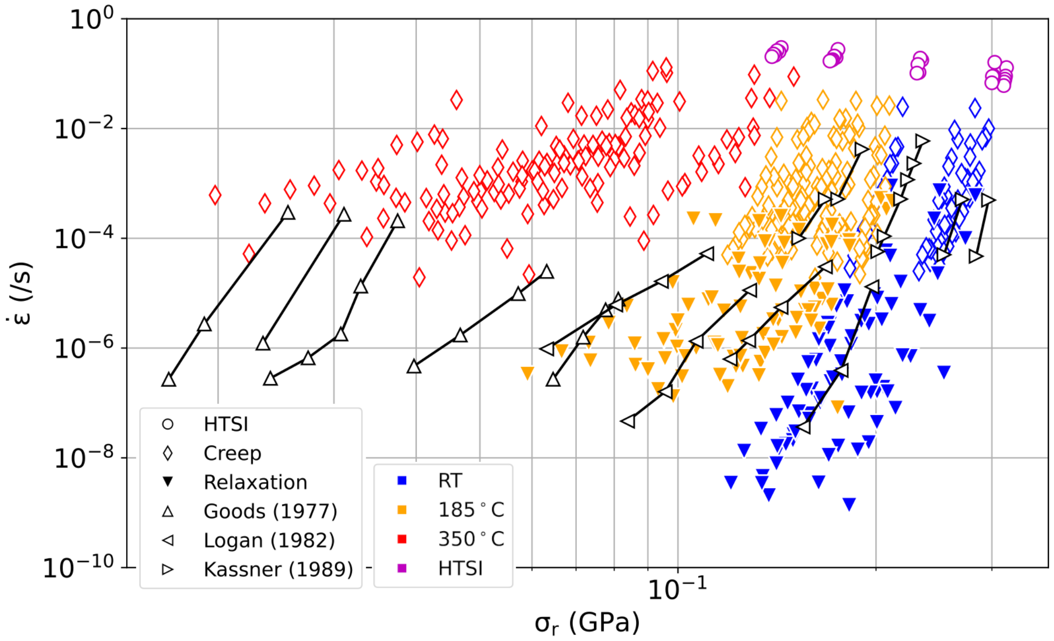

Figure 3.15: Strain rate versus stress curves from indentation creep or relaxation experiments at different temperatures. Only the HTSI tests at RT, 100 °C, 200 °C, 300 °C, and 400 °C were plotted. Literature data come from [205–207] .

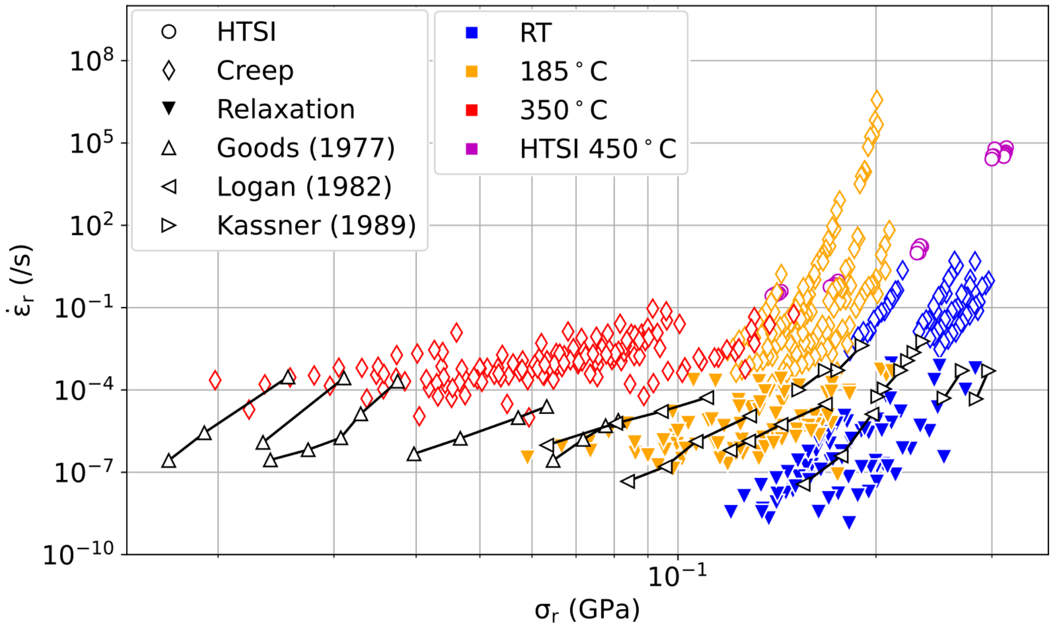

Figure 3.16: Representative strain rate versus stress curves from indentation creep or relaxation tests at different temperatures. Only the HTSI tests at RT, 100 °C, 200 °C, 300 °C, and 400 °C were plotted. Literature data come from [205–207] .

definition to indentation creep results with literature data.

Using this definition, one can correct the data to compare the indentation results with literature

Table 3.5: Strain rate sensitivity on pure silver, depending on temperature and strain rate.

Test	Temperature (°C)	mean ($\dot{\varepsilon}$) (s^{-1})	Strain Rate Sensitivity
HTSI	RT	1×10^{-1}	0.013
	100	1×10^{-1}	0.014
	200	2×10^{-1}	0.031
	300	2×10^{-1}	0.065
	400	2×10^{-1}	0.094
Creep	RT	2×10^{-3}	0.029 ± 0.003
	185	2×10^{-3}	0.033 ± 0.018
	350	6×10^{-3}	0.183 ± 0.043
Relaxation	RT	5×10^{-5}	0.045 ± 0.007
	185	4×10^{-5}	0.085 ± 0.018
Kassner	-70	5×10^{-4}	0.017
	-40	5×10^{-4}	0.025
	23	5×10^{-4}	0.031
	100	5×10^{-4}	0.056
	400	5×10^{-4}	0.2
	500	5×10^{-4}	0.2
	600	5×10^{-4}	0.2
Logan	20	6×10^{-5}	0.045
	96	6×10^{-5}	0.10
	153	6×10^{-5}	0.09
	200	6×10^{-5}	0.14
Goods	200	5×10^{-7}	0.069
	300	5×10^{-7}	0.054
	400	2×10^{-6}	0.14
	450	4×10^{-6}	0.20
	500	4×10^{-6}	0.21

data. In figure 3.16, the representative strain rate is plotted against the corresponding stress. The data at high temperatures seem more consistent with the results of Goods [205]. It can be noticed that at low temperatures, such definition leads to really high representative strain rates. This effect is an artifact coming from the proposed definition and the low strain rate sensitivity values at this temperature.

Supposing that silver follows the Norton-Hoff's law, one can plot the master curve of creep for silver. The activation energy of creep employed here is 70 kJ/mol. Such value is consistent with what is observed by Kassner [207]. The indentation results and literature data compare quite nicely. However, the values at low temperatures correspond to high representative strain rates. Examining the strain rate sensitivity values (figure 3.18), they go from 0.01 near RT to values near 0.1-0.2 at high temperatures. According to Baral *et al.* [178], their definition of the representative strain rate should be used if the strain rate sensitivity is high enough. It is coherent with the observations on the master curve.

Finally, let's discuss the changes in strain rate sensitivity. As noted in the literature, the strain

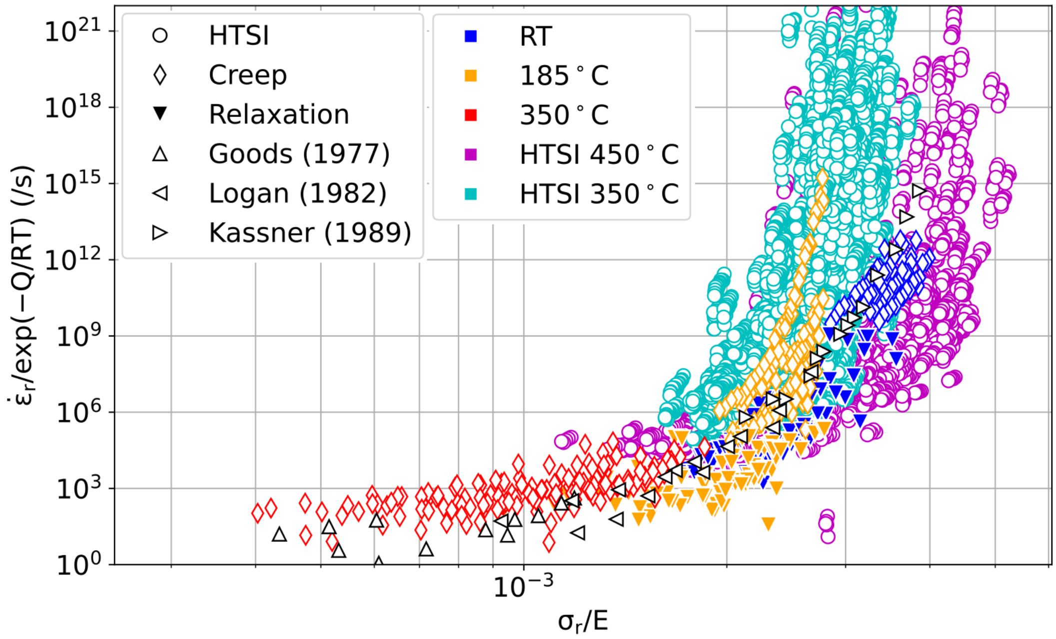

Figure 3.17: Master curve obtained on silver for an activation energy of creep of 70 kJ/mol, using the representative strain rate definition introduced by Baral *et al.* [178].

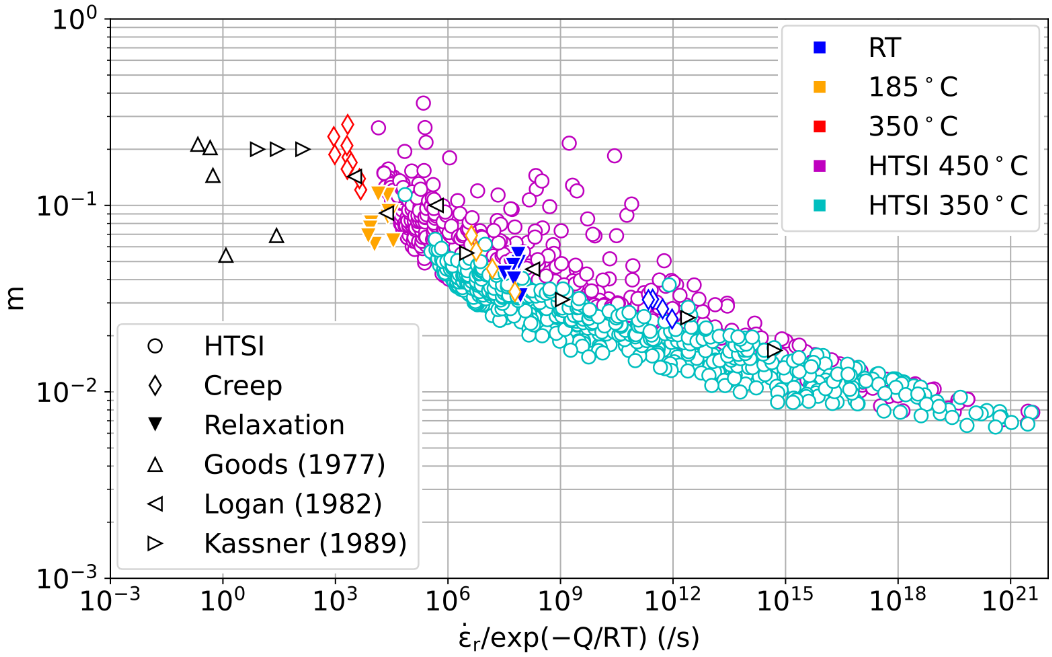

Figure 3.18: Strain rate sensitivity versus temperature-compensated representative strain rate for silver.

rate sensitivity increases with temperature (see figure 3.18). Moreover, as seen in figure 3.15, at a given temperature, strain rate sensitivity seems to increase with decreasing strain rate. However, if comparing the two HTSI tests, the microstructure also impacts the strain rate sensitivity [208]. The values obtained here are consistent with the literature data. Seen the trend of those data, the strain rate sensitivity is expected to go to values around 0.2 at high temperatures.

V.C. Conclusion on silver

As for CaF_2, one can conduct various indentation tests to characterize the creep properties of silver depending on temperature and strain rate. As observed on the master curves, time and temperature are equivalent. As indentation creep and relaxation tests are quite difficult to perform in temperature, one can use the HTSI method and this equivalence to predict the behavior of this material at different temperatures and strain rates. As the strain rate sensitivity of the sample in temperature increases to values near 0.1, one should also apply the representative strain rate definition to compare correctly the results and predict such properties.

A limit observed here comes from the polishing state of the specimens. A polycrystalline state leads to some scattering of the properties, due to the indentation size compared to the grain size. Adding roughness increases this scattering. It makes the characterization more complicated, especially in temperature.

VI. Conclusions of the chapter

Performing nanoindentation tests allow getting the impact of temperatures and strain rates on the mechanical properties of a sample. As creep properties are important, one can use this technique to quantify their characteristics. Different indentation tests give access to those properties: indentation creep tests, indentation relaxation tests, and HTSI tests. Creep and relaxation experiments are quite interesting since they enable having access to a really large strain rate scale (10^{-8} to 1/s usually). Adding the new high-speed indentation tests enlarge this scale up to 10^4/s. However, as some tests required really low thermal drift, they are complicated to implement in temperature. The HTSI method also gives access to the creep properties of a sample. It allows getting them on a large temperature scale but only at a strain rate of around 1/s. Thanks to the equivalence between time and temperature, doing tests at high temperatures gives information on the properties at a lower strain rate. So, to complete the knowledge on a specimen, one can conduct HTSI experiments at high temperatures.

As presented here, indentation creep, relaxation, and HTSI experiments were carried out for comparison purposes. It gives consistent results on CaF_2 and pure silver samples. On the master curves, the equivalence between time and temperature is clearly observed. Moreover, one gets the strain rate sensitivity, the activation energy, and the activation volume of the sample. All of this may help to determine the deformation mechanisms taking place in the material, depending on temperature and strain rate.

The analysis presented here is still quite simple: the creep activation energy used for the equivalence is supposed to stay constant during the whole temperature scale. However, as observed in the literature on CaF_2 [194] and on silver [205] it is not the case at all temperatures. Moreover, seeing the change of deformation mechanisms on CaF_2 (figure 3.11), one clearly expects an effect of temperature. So, for better characterization, the impact of temperature and strain rate sensibility on those parameters should be investigated.

Furthermore, the indentation tests at really high temperatures are still quite touchy. As already mentioned, the tip is a critical factor for indentation tests. And unfortunately, even using the article by Wheeler *et al.* [87], it was not possible to find one allowing conducting tests on CaF_2 at temperatures higher than $400\,^\circ C$. The development of high-temperature tips is critical to continue those characterizations at high temperatures.

Finally, as observed on silver, the properties of a material may vary in temperature. Here the irreversible changes are expected to be due to the recrystallization of the sample during an HTSI test. Characterizing the mechanisms taking place here is of great interest for material design. This is the main concern of the upcoming chapter.

4

Characterization of microstructure changes in metals

This chapter aims to use the High-Temperature Scanning Indentation technique to characterize microstructure changes in metals.

Chapter's content

I. Goals

The HTSI method allows following the variations in mechanical properties of samples quasi-continuously with temperature. The thing is that for metals, those properties depend on temperature but also on microstructure. Yet, microstructures are modified in temperature too. This chapter aims to apply the HTSI technique to predict the microstructure changes of metals. Using only a few HTSI tests, one should be able to determine the microstructure state of the specimen knowing the applied thermal cycle.

II. Materials and methods

II.A. Samples

To do so, two model materials (pure aluminum and pure copper) have been selected. As specimens were initially cold-rolled, Loubet's model is used to analyze the indentation data. Here, the variations of the hardness are more interesting than its absolute values against temperature.

Aluminum samples An initial pure aluminum plate was cut and deformed applying 3 different thickness reduction ratios r. Samples were cut for those plates, the final diameter is 10 mm to 12 mm for a final thickness of 3 mm. A few specimens were annealed at 400 °C during 2 h.
Samples were then polished by hand using SiC papers (P460, P600, P1200) before being finished with diamond solution down to 0.5 µm.

Copper samples An initial pure OFHC copper plate was cut and deformed using a thickness reduction ratio of 85%. Specimens were cut for this plate, with the final diameter being 10 mm to 12 mm for a final thickness of 3 mm.
Samples were then polished by hand using SiC papers (P460, P600, P1200) before being finished with diamond solution down to 0.5 µm.

Table 4.1: Thermal cycle applied on the different aluminum samples

Sample	r	Annealing	T_{max} (°C)	Heating rate (°C/min)	Holding time (min)
#1	85%	2 h at 380 °C	325	3	30
#2	85%	no	325	3	60
#3	85%	no	300	3	30
#4	85%	no	325	3	120
#5	60%	no	325	3	120
#6	40%	no	325	3	120
#7	40%	no	300	3	2
#8	85%	no	325	1	60

Table 4.2: Thermal cycle applied on the different copper samples

Sample	r	Annealing	T_{max} (°C)	Heating rate (°C/min)	Holding time (min)
#1	85%	no	600	5	60
#1a	85%	ramping #1	600	5	60
#2	85%	no	400	1	0
#3	85%	no	200	5	2
#4	85%	no	250	5	120

Those two materials have really different stalking fault energy: 142 kJ/mol for aluminum and 78 kJ/mol for copper. Static recovery and recrystallization are expected on aluminum. However, static recovery is not anticipated prior to recrystallization on copper.

II.B. Indentation devices

Nanoindentation testing Two nanoindentation devices were used for those experiments. All the tests on aluminum were conducted utilizing the InSEM HT nanoindenter at the LTDS, provided by KLA Nanomechanics. This system is under vacuum (1×10^{-2} Pa), inside a VEGA 3 SEM (Tescan). A Berkovich diamond tip was employed to make those tests. Samples were heated up to 325 °C at 1 °C/min to 3 °C/min depending on the HTSI tests. The tests were made manually. Table 4.1 summarizes what happens to each aluminum sample.
All the tests on copper were conducted using the InSEM HT nanoindenter at KLA Nanomechanics, USA. This system is under vacuum (1×10^{-2} Pa) inside a vacuum chamber. A Berkovich sapphire tip was mounted to make those experiments. Specimens were heated up to 200-600 °C at 1 °C/min to 5 °C/min depending on the HTSI tests. The tests were performed using the automatic HTSI mode. Table 4.2 summarizes what happens to each copper specimen.

EDSB characterization Microstructure characterization was carried out on a few copper and aluminum samples before or after the indentation experiments. The specimens were electropolished prior to this characterization. EBSD measurements were conducted using a SEM-FEG from Zeiss (SUPRA 55 VP) at the LGF. Postprocessing was performed using the MTEX MATLAB ToolBox [209].

II.C. Tests settings

Before doing the HTSI experiments, the temperature settings are calibrated to know what heating rate to apply on the tip and the specimen. The settings are calibrated at the maximum temperature. It is supposed that the temperature difference between the tip and the sample changes linearly from RT to the maximum temperature.
The presence of an ISE effect is detected on the samples at RT. To reduce its impact, the tests are carried out at 1 µm depth at low temperatures. As the maximum load does not change when increasing temperature, the maximum depth increases. ISE effect usually decreases when

increasing temperature but could still be there. However, it is not expected to have an important impact on the measurements.

III. Results

III.A. Detection of microstructure changes

Copper The cold-rolled sample Cu#1 is heated from RT to 600 °C at 5 °C/min, maintained here for half an hour before being cooled down. As it can be seen in figure 4.1, the hardness of the specimen decreases with increasing temperature. However, a sudden drop is detected around 250-300 °C. Then, the hardness keeps reducing linearly with increasing temperature. Nonetheless, the slope is different than the one at low temperatures. When cooling back to RT, hardness increases, following the slope observed after the drop.

After this thermal cycle, the sample is once again submitted to the same thermal cycle. The hardness of specimen Cu#1*a* decreases with temperature, following the variations measured during cooling on specimen Cu#1. The hardness changes of sample Cu#1 are irreversible: it is a proof that the microstructure of the sample changes. On the second cycle (specimen Cu#1*a*), the hardness is reversible: the microstructure no longer changes in temperature. The drop of hardness near 250 °C on specimen Cu#1 is likely the result of the recrystallization taking place in the sample. On the EBSD characterization of the sample, the microstructure changes due to the thermal cycle are clearly observed. The HTSI measurements are consistent with the EBSD ones.

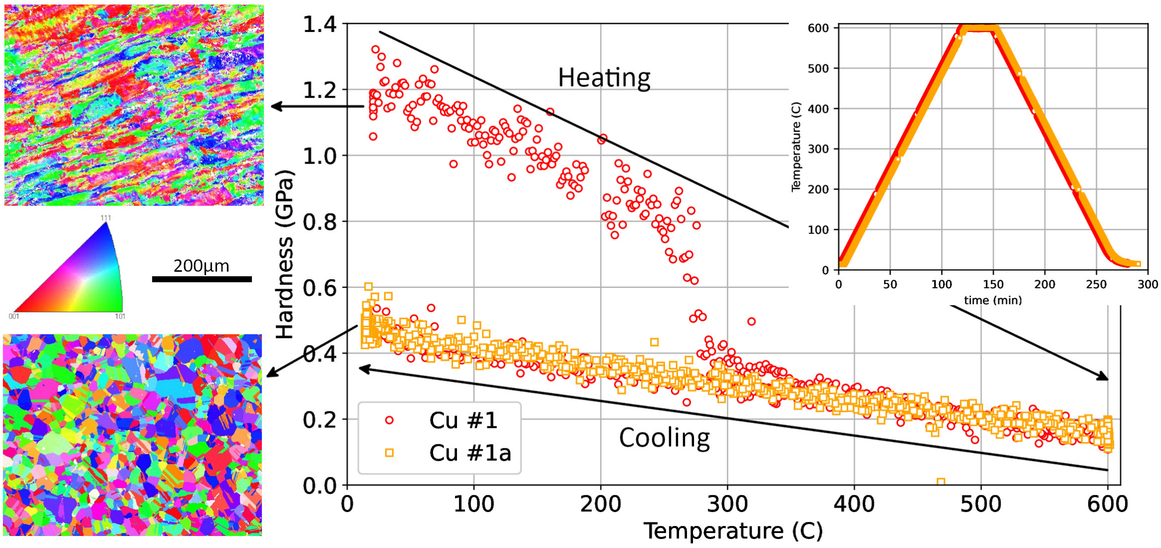

Figure 4.1: Hardness variations on copper during a thermal ramp determined by HTSI experiments. Hardness clearly decreases with increasing temperature. Sample Cu#1 was initially cold-rolled: the hardness drop around 250-300 °C is likely the consequence of the recrystallization taking place in the specimen. It is consistent with the EBSD measurements.

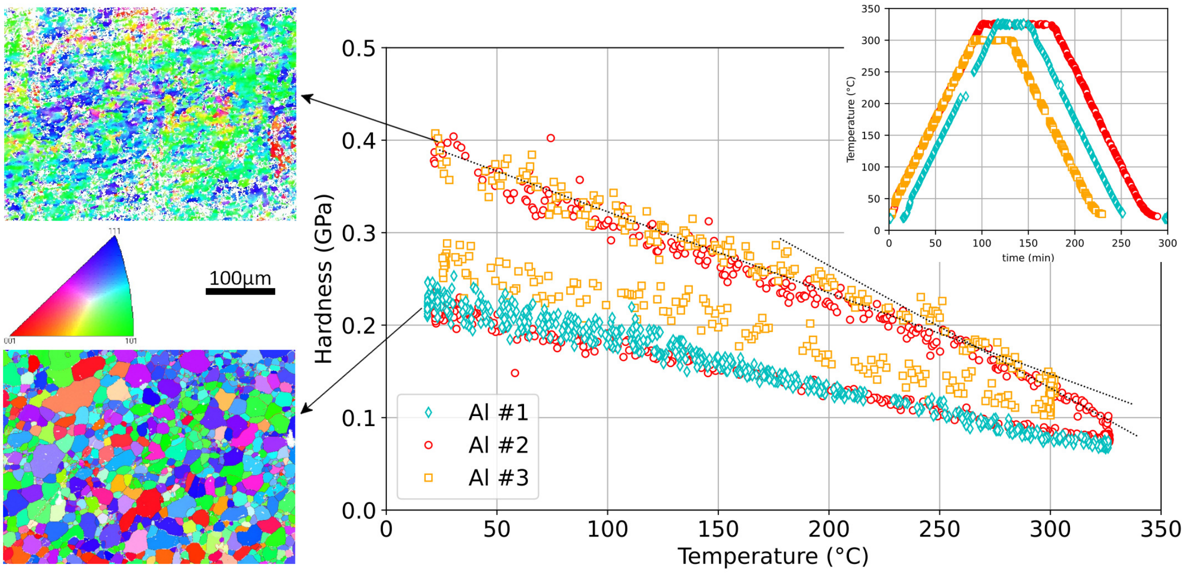

Figure 4.2: Hardness variations on aluminum during a thermal ramp evaluated by HTSI experiments. Hardness clearly lowers with increasing temperature. Samples Al#2 and Al #3 were initially cold-rolled: the modification of the hardness's slopes around 250 °C is related to the recrystallization of the specimens. It is consistent with the EBSD measurements.

Aluminum In figure 4.2, the hardness of sample Al #1 decreases linearly with increasing temperature. Sample Al#1 is an annealed sample. No microstructure changes are expected on this sample so hardness changes in temperature are reversible. On the opposite, on the cold-rolled specimen Al#2, hardness changes are irreversible. Its hardness value at RT is 0.4 GPa, quite high compared to the one of Al#1. It then decreases linearly with temperature up to 250 °C. At this temperature, the slope of hardness in temperature seems to change. During cooling, hardness follows the same path as the one of sample Al#1. As hardness changes are irreversible, the microstructure also changes during the thermal cycle. Contrary to copper, the drop in hardness is less visible. The change in the hardness slope observed around 250 °C is expected to be the sign of recrystallization of the sample, which is consistent with the microstructure modifications detected by EBSD.

Sample Al#3 presents similar variations compared to the specimen Al#2 up to 300 °C. Its hardness then decreases during the 30 minutes of annealing before increasing back during cooling. Nevertheless, it does not merge with the data of sample Al#2 during cooling. It is assumed that the recrystallization of the sample is not completed.

Two phenomena (see chapter 1, section III.) can explain the microstructure changes observed here: static recrystallization and/or static recovery. Recrystallization is expected on copper and aluminum. Static recovery is awaited on aluminum, before recrystallization, but not on copper.

III.B. What are the detected phenomena?

To verify the presence of static recovery during the HTSI tests on copper and aluminum, another experiment is conducted. Static recovery is expected to take place all along the thermal cycle,

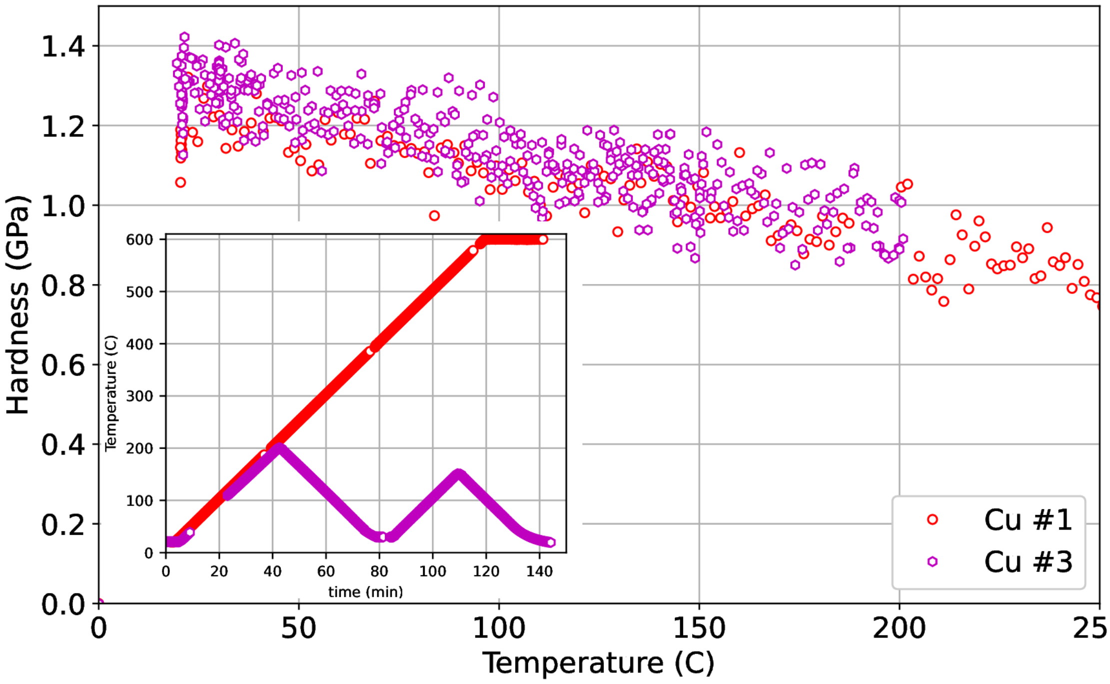

Figure 4.3: Hardness changes on cold-rolled copper samples. Hardness variations of specimen Cu#3 are reversible here: no static recovery is detected on copper.

while recrystallization is assumed to occur only at a temperature high enough because of the nucleation stage. So, tests up to a temperature not too elevated are carried out: recrystallization should not happen here. Static recovery would be the phenomenon explaining the hardness changes during such cycles.

Copper Sample Cu#3 is heated from RT to 200 °C before being cooled down, heated once again up to 150 °C, and then cooled down. As it can be seen in figure 4.3, hardness variations are reversible. No microstructure changes are detected: no recovery is found on this copper

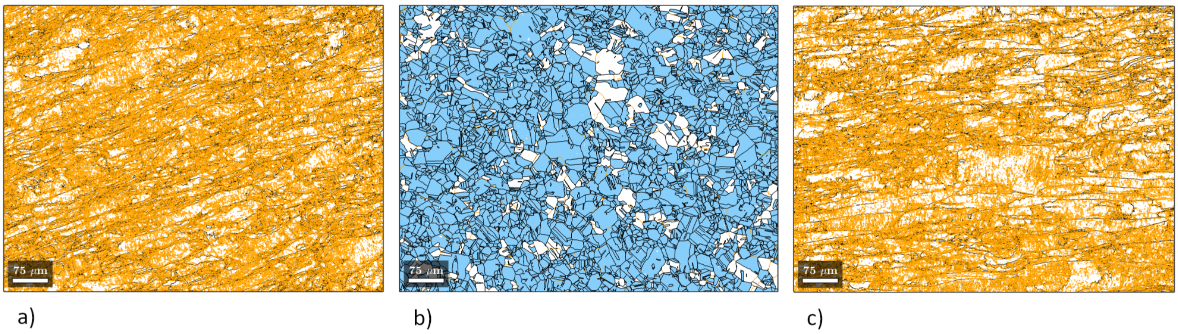

Figure 4.4: Post-mortem EBSD measurements on copper (a) initial state, (b) sample Cu#1 and (c) sample Cu#3. The grains boundaries are in black, the subgrain boundaries are in orange and the new recrystallized grains are in blue. The recrystallization of sample Cu#1 is clearly observed. Specimen #3 presents a huge number of subgrain boundaries: no recrystallization is detected.

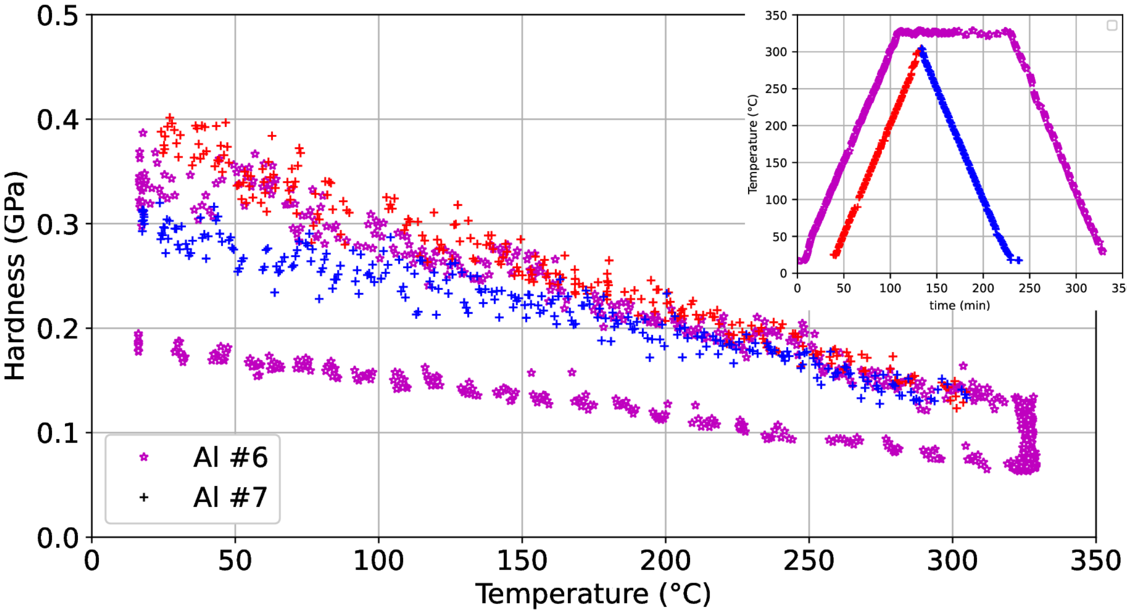

Figure 4.5: Hardness changes on cold-rolled aluminum specimens. Hardness at RT has varied during the thermal cycle on the sample Al#7: microstructure changes are detected. Recovery takes place on the aluminum specimens.

specimen. If static recovery were taking place in copper, it would be so slow that it would not be detected during these tests. On copper, it is expected that only static recrystallization is responsible for the microstructure changes observed on figure 4.1.

To verify that no recrystallization occurs on sample Cu#3, post-mortem EBSD characterization is carried out (see figure 4.4). According to [210–212], the grains boundaries are defined if the misorientation angle between pixels is higher than 15°. They are in black in the figures. In orange are the subgrain boundaries with a misorientation angle between 2° and 15°. The new recrystallized grains in blue are the grains where the mean misorientation is lower than 2°.

Specimen #3 presents a huge number of subgrain boundaries: no recrystallization is detected. At the opposite, specimen #1 presents a fully recrystallized structure.

Aluminum Sample Al#6 is heated up to 325 °C and maintained at this temperature for 2 h before being cooled down. Sample Al#7 was heated up to 300 °C before being immediately cooled down so no recrystallization is expected on this specimen. In figure 4.5, hardness changes are irreversible in the two cases.

When verifying the post-mortem EBSD of the two samples (figure 4.6), recrystallized grains are clearly visible on the specimen Al#6. They are quite big and more or less equiaxial. Moreover, only a few subgrain boundaries are found. On sample Al#7, grains are deformed. There is a large number of subgrain boundaries but a few new grains (blue arrows) are detected. However, recrystallization growth did not have the time to occur. The hardness variation cannot be explained by those nuclei alone: static recovery is taking place in those aluminum samples.

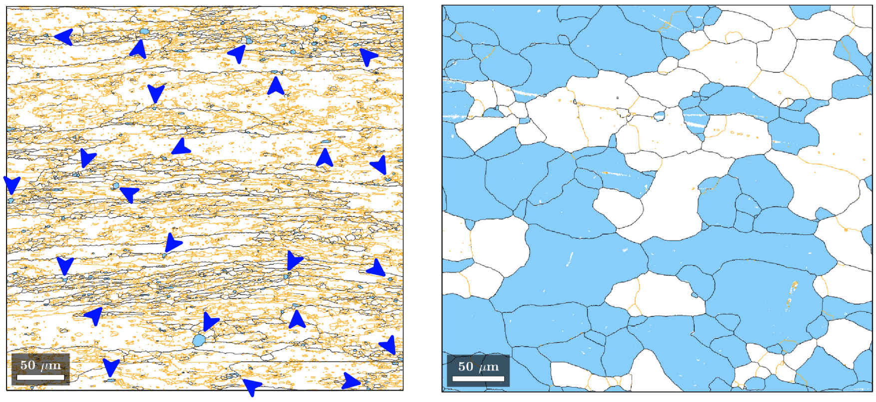

Al#7 Al#6

Figure 4.6: Post-mortem EBSD measurements on samples Al#6 and Al#7. The grains boundaries are in black, the subgrain boundaries are in orange and the new recrystallized grains are in blue. On the specimen Al#6, a recrystallized structure can be observed. Sample Al#7 presents more subgrain boundaries and some recrystallized nuclei can be viewed following the blue arrows.

III.C. Impact of the heating rates

Copper As static recovery and recrystallization may depend on the heating rate, experiments at different heating rates are carried out. On copper (see figure 4.7), the results heated at 5 °C/min (sample Cu#1) are compared with those heated at 1 °C/min (specimen Cu#2). Hardness decrease up to 220 °C is the same on the two samples. However, the temperature where hardness drop increases with the heating rate. This is consistent with the absence of static recovery

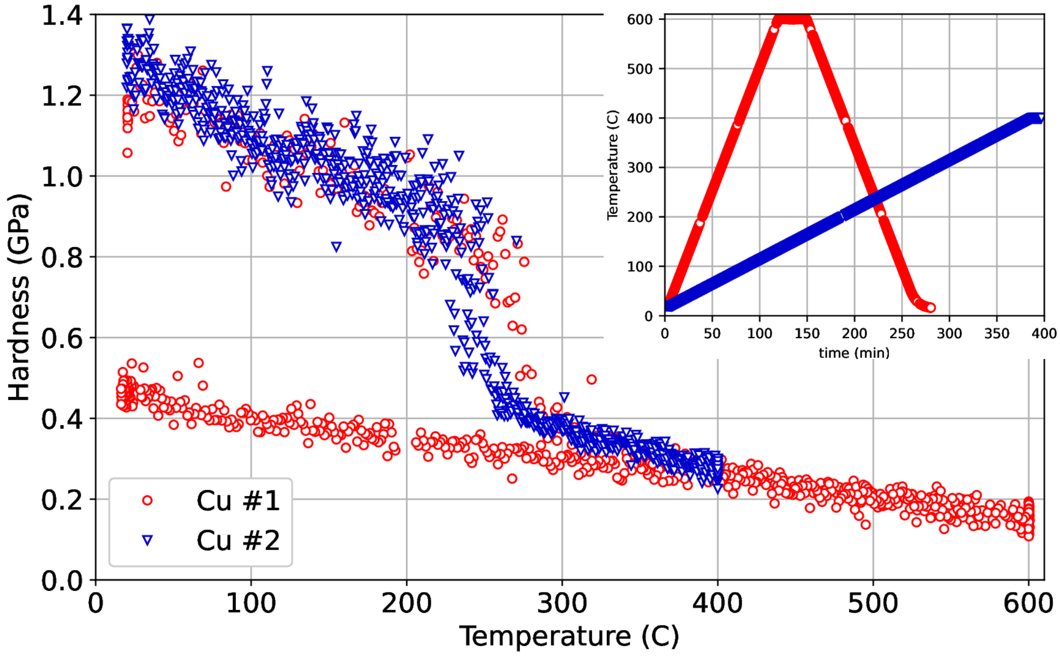

Figure 4.7: Impact of heating rates on the hardness changes on cold-rolled copper samples. Decreasing the heating rate reduces the temperature where recrystallization takes place.

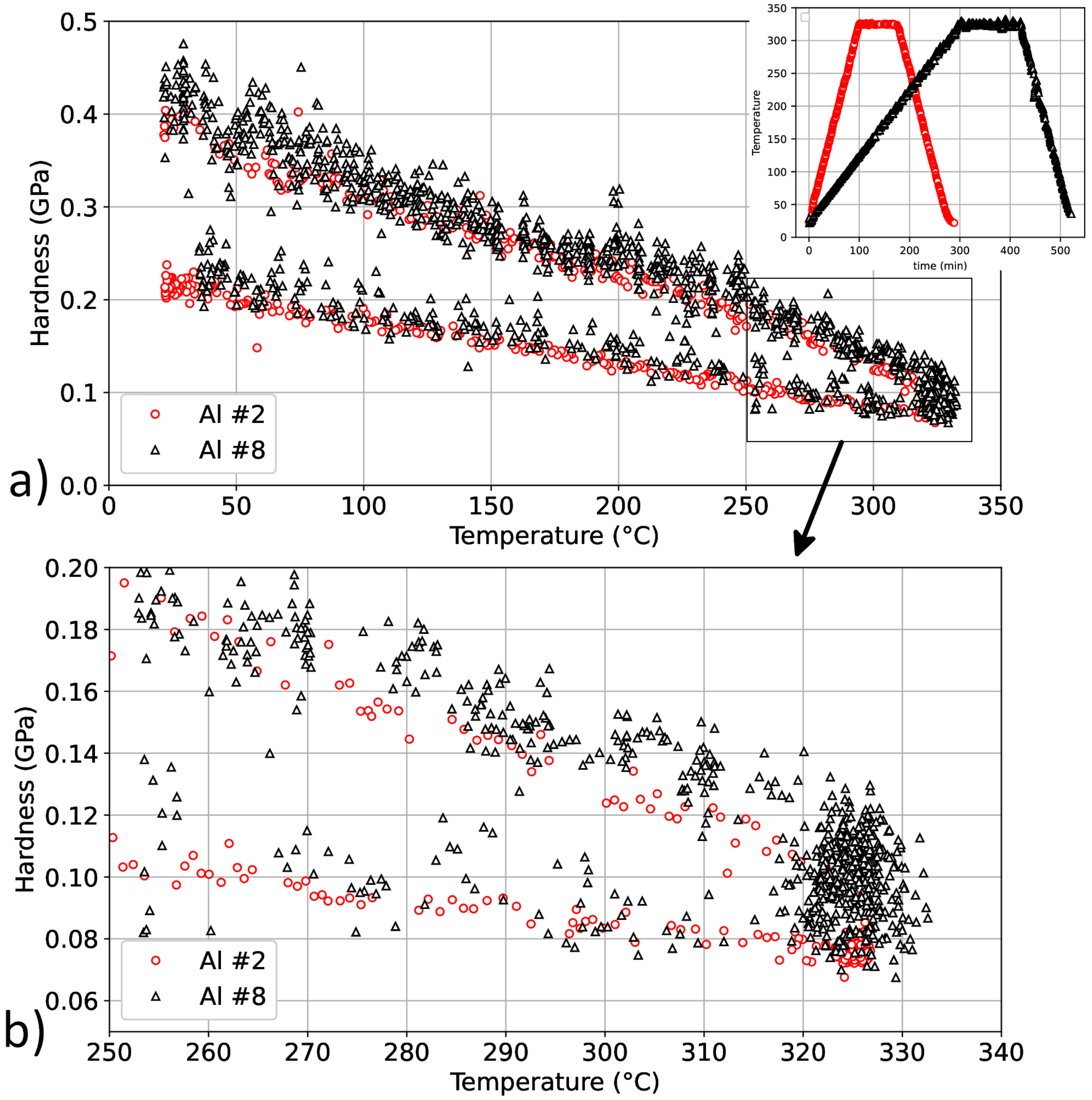

Figure 4.8: (a) Impact of heating rate on the hardness changes on cold-rolled aluminum specimens. (b) zoom at the end of the heating, where the influence of the heating rate is noted.

taking place on copper.

Aluminum On aluminum samples, the comparison is performed between heating at 3 °C/min (sample Al#2) and heating at 1 °C/min (sample Al#8). In figure 4.8 a), the variations in hardness look quite the same between the two samples. However, on the zoom at high temperature (b), the change of slope on sample Al#2 is not observed on sample Al#8. The recrystallization process is detected during the annealing at 325 °C: the increase of the heating rate decreases the recrystallization temperature. This is due to static recovery. Initially, the two samples have the same deformation level. As static recovery takes place, the stored energy is lowered. Decreasing the heating rate allows the sample to recover more before arriving at a temperature where

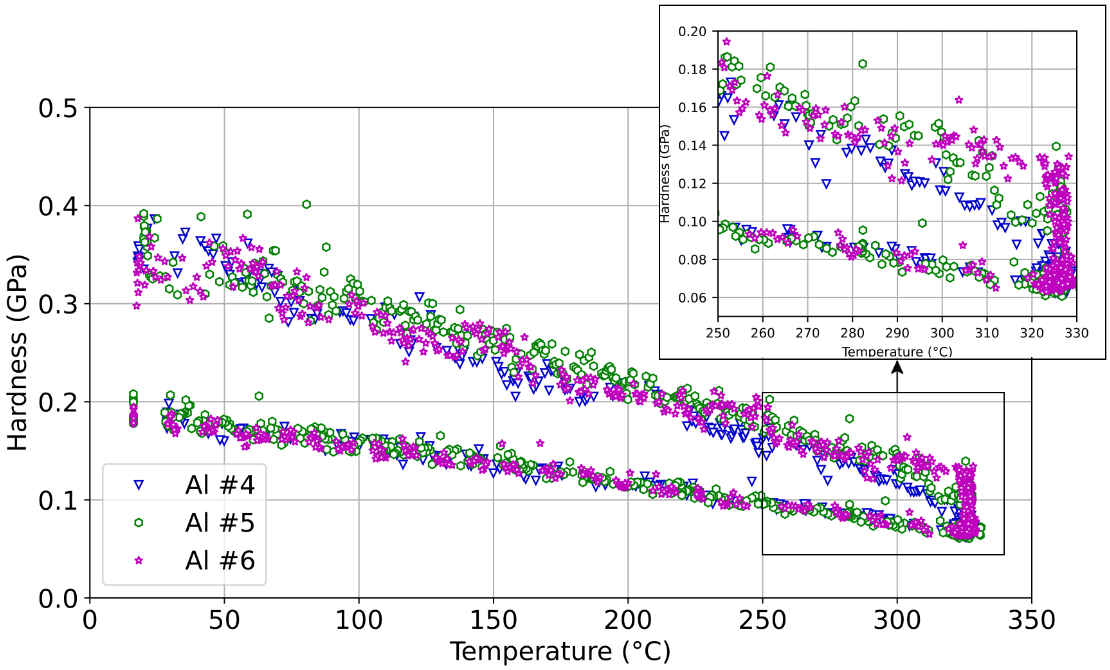

Figure 4.9: Impact of initial deformation state of aluminum samples on the hardness changes observed during HTSI experiments.

recrystallization can happen [212]. As the stored energy has been lowered, the driving force of recrystallization is reduced [213]. So, decreasing the heating rate increases the recrystallization temperature if static recovery takes place in the sample [118, 213, 214].

III.D. Impact of the initial state

Finally, the initial deformation state should also impact the kinetics of static recovery and recrystallization. Comparison between aluminum samples deformed using various thickness reduction ratios is conducted (see table 4.1). Sample Al#4 has a reduction ratio of 85%, sample Al#5 of 60% and sample Al#6 of 40%. The deformation saturates in all three samples, but the stored energy is different. As it can be seen in figure 4.9, the decrease of hardness up to 250 °C is the same in the three samples. However, at higher temperatures, the variations depend on the initial state. It is clearly observed in the zoom image: they behave differently at high temperatures. As stored energy is different initially, it will affect both static recovery and static recrystallization kinetics.

III.E. Any impact on others properties?

As noted, the hardness of pure copper and aluminum changes a lot depending on the thermal cycle, due to static recovery and recrystallization. Does those phenomena also impacts other mechanical properties ?

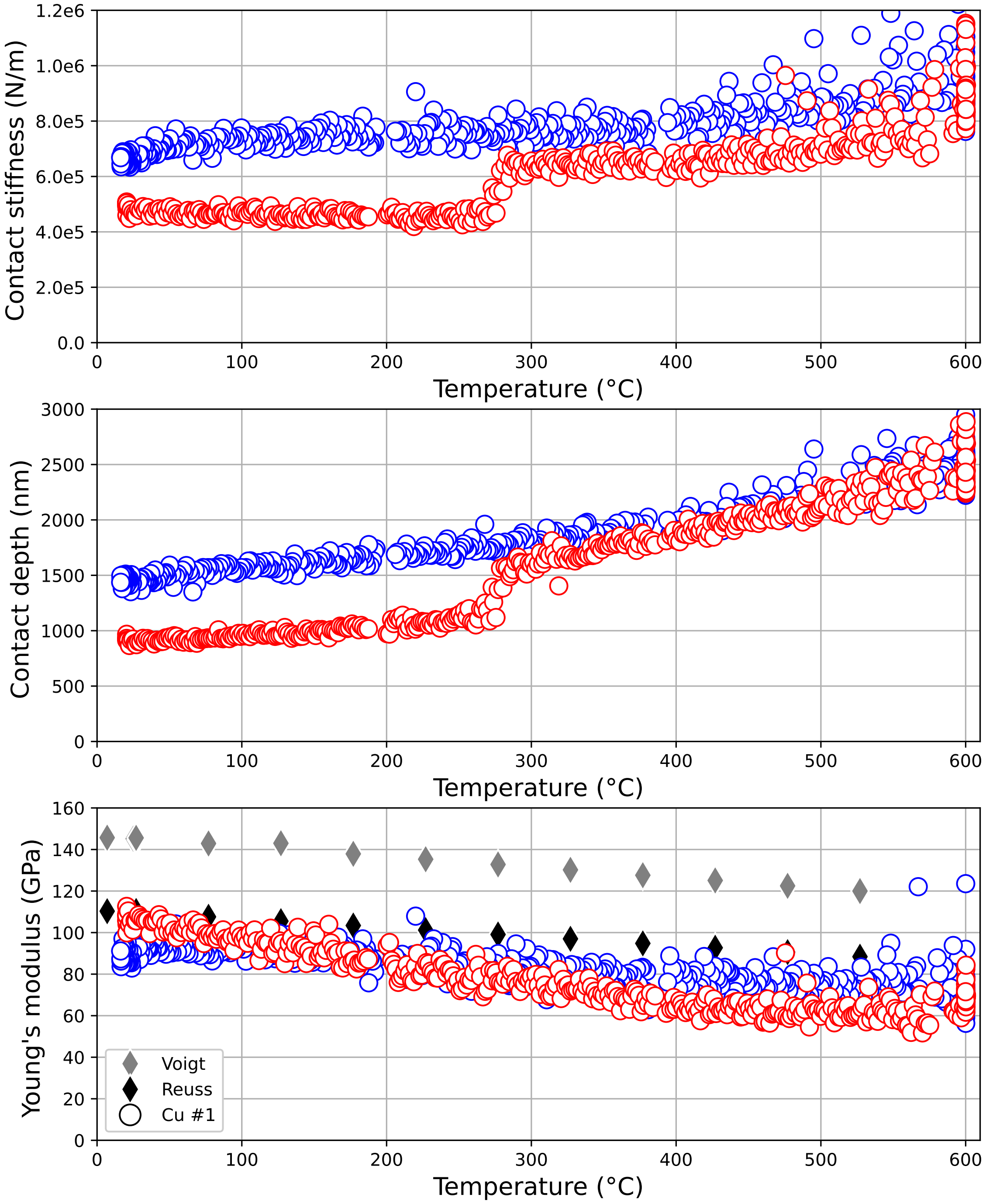

Figure 4.10: Contact stiffness, contact depth and Young's modulus versus temperature measured on sample Cu#1 (in red: heating, in blue: cooling). Loubet's model is used to model the contact under the indent. Literature data are from [167].

III.E.1. Young's modulus

Copper Let's focus on Young's modulus data of sample Cu #1 (figure 4.10). The cold-rolled sample presents consistent values of Young's modulus at low temperature ($T \leq 200\,°C$). However, when the sample is in fully recrystallized state (end of heating and cooling), the values are quite low compared to literature data [167]. It is expected to come from the contact area model: Loubet's model is used here as it described well the behaviors of cold-rolled copper but Oliver and Pharr's model would better describe the contact under the indent for recrystallized copper. This leads to an overestimation of the contact area and so an underestimation of the Young' modulus (and of hardness) after recrystallization of the sample ($t \geq 400\,\mathrm{min}$). Moreover, a difference in Young's modulus values is observed between heating and cooling at $T \geq 400\,°\mathrm{C}$. Such variation is observed to come from variations on contact stiffness (see figure 4.10), impacted by difference in temperature control between heating and cooling. Those variations are not observed on the contact depth in this temperature range: it greatly impacts the Young's modulus but not the hardness.

Much better control of the experimental temperatures is required to have better access to the Young's modulus. To study the absolute values of Young's modulus and hardness, it is also required to quantify the change in contact model during the recrystallization process. As the Young's modulus is not expected to change because of the microstructure changes of the sample, it may be used to quantify the contact area of the sample without using a contact model. Such analysis will reduce the hardness gap observed around 250 °C to 300 °C on sample Cu #1 but as contact stiffness and contact depth greatly changes in this range, a clear decrease of hardness would still be obtained.

Aluminum Due to issues with the PID controlling the temperatures and to unexpected load frame stiffness drop in temperature, it was not possible to get exploitable Young's modulus data on those aluminum samples.

III.E.2. Creep

Copper On figure 4.11, the strain rate sensibility of specimens Cu#1 (during heating) and Cu#2 is plotted against temperature. Initially, the strain rate sensitivity of sample Cu#2 is near 0.01-0.02. It then rises linearly, up to 0.04 at 220 °C. Next, a decrease back to 0.02 at 370 °C is observed. It happens when the recrystallization of the sample takes place. In the end, the strain rate sensitivity increases again linearly up to 0.05 at 400 °C.

A similar scenario is detected in sample Cu#1. Starting at 0.01, the strain rate sensitivity increases linearly, up to 0.03 at 250 °C. A low decrease to 0.02 at 320 °C is then observed. Finally, the strain rate sensitivity increases again up to 0.06-0.07 at 600 °C. The cooling phase of this sample follows the high-temperature trend: it was not plotted for clarity reasons.

Aluminum On figure 4.12, the strain rate sensibility of samples Al#1, Al#2 and Al#3 is plotted against temperature. As observed on hardness, the strain rate sensibility changes of the annealed sample are reversible in temperature. This is not the case for the cold-rolled samples: they have a strain rate sensibility of 0.03 before any experiment. Nevertheless, at the end of the HTSI tests, it is near 0.007. Moreover, the strain rate variations follow that of the annealed

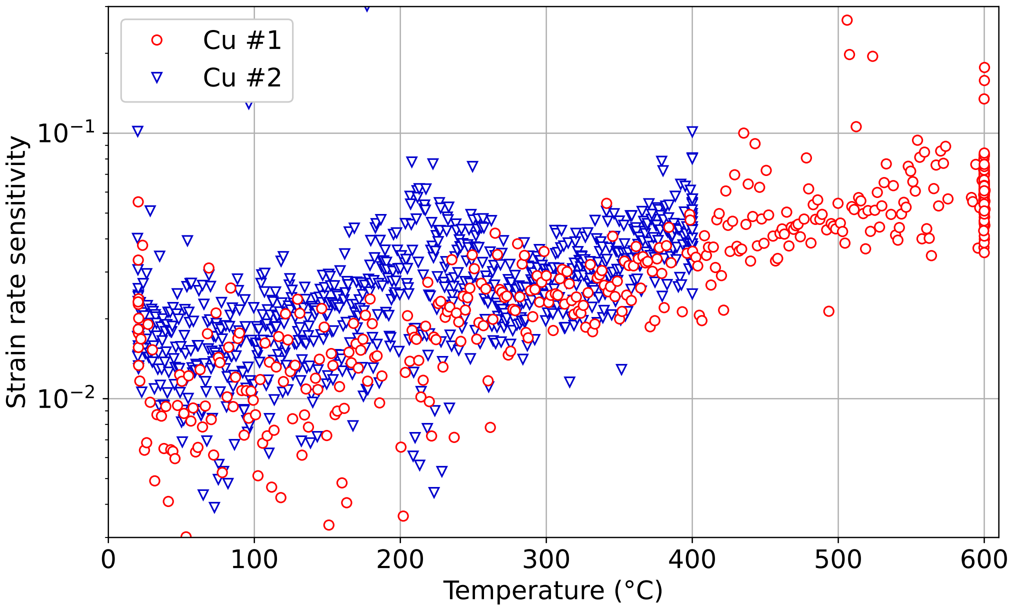

Figure 4.11: Strain rate sensitivity versus temperature on copper specimens, depending on the heating rate. For clarity, only the heating phase of sample Cu#1 is plotted.

sample during the cooling phase, whatever the applied thermal cycle. The distinction between sample Al#2 and Al#3 during cooling, observed on hardness, is not present here.

IV. Modeling and predicting

IV.A. Model

To reconstruct the hardness changes with temperature, modeling of the different phenomena taking place in the sample is required. Three phenomena are expected to be responsible for the decrease in hardness with temperature. At low temperatures, the softening is due to the thermal activation of plasticity and static recovery (if taking place). Then, at a given temperature, recrystallization takes place.

Activation of plasticity in temperature Firstly, hardness decreases with temperature because of the thermal activation of dislocation movement. When temperature increases, it is easier for dislocations to overcome the thermal barrier [54, 198].

$$\sigma = \sigma_a(\varepsilon) + \sigma_{th}(T, \dot{\varepsilon}) \tag{4.1}$$

with σ_a the athermal contribution to stress, coming from the applied deformation, and σ_{th} the thermal contribution to stress, depending on temperature and strain rate.

This phenomenon is not a change in microstructure. It is the reason why the hardness of an

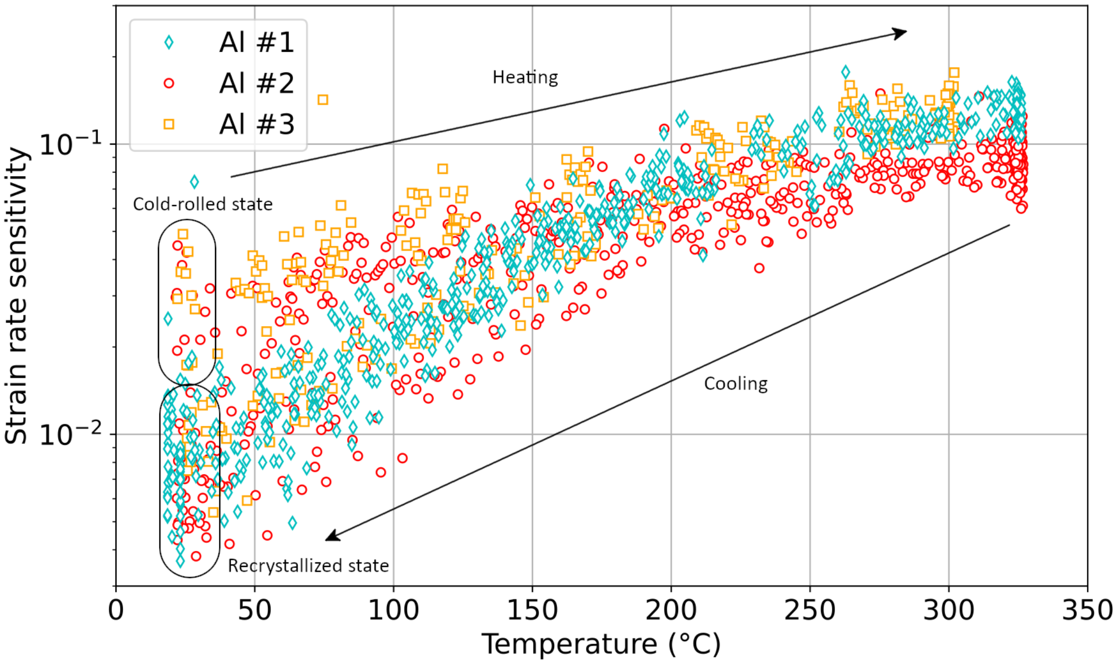

Figure 4.12: Strain rate sensitivity versus temperature on aluminum specimens.

Table 4.3: Typical activation volume depending on the deformation mechanism, from [54]

Deformation mechanism	Typical activation volume (b^3)
Overcoming Peierls-Nabarro stress	$10^1 - 10^2$
Intersection of dislocations	$10^2 - 10^4$
Nonconservative motion of jogs	$10^2 - 10^4$
Cross-slip	$10^1 - 10^3$
Climb	1

annealed sample is varying with temperature. It is modeled using equation [54, 198]:

$$\sigma = \sigma_a(\varepsilon) - \frac{\alpha k_B}{v_{ac}} T \tag{4.2}$$

with α a constant and v_{ac} an activation volume. The activation volume is not expected to be a constant in temperature. Moreover, it is linked with the activation area that a dislocation had to travel to go from one obstacle to the next one. It is characteristic of the deformation mechanism controlling the movement. As v_{ac} is characteristic of the distance between defects, it will depend on the state of the material. It is expected to be higher for an annealed sample compared to a cold-rolled one.

Static recovery As seen in chapter 1, static recovery is a mechanism of dislocation annihilation and rearrangement. This mechanism takes place in the whole structure, inside the old grains structure. The model of Verdier [116] is used to model the static recovery that happens in aluminum:

$$\frac{d\sigma_i}{dt} = -\frac{64\nu_D}{9M^3\alpha^2}\frac{\sigma_i^2}{E}\exp\left(-\frac{U_0}{RT}\right)\sinh\left(-\frac{\sigma_i v_0 N_A}{RT_a}\right) \tag{4.3}$$

with ν_D the Debye frequency, N_A the Avogadro constant, U_0 the activation energy at the end of the recovery process, v_0 the activation volume of recovery, and T_a the annealing temperature. One should remember that this model is defined with the internal stress σ_i determined at RT after annealing at T_a: the impact of the thermal activation of plasticity should be removed before applying this model. To characterize the kinetic of static recovery correctly, the activation energy U_0 and the activation volume v_0 should be evaluated.

Static recrystallization As the HTSI tests are carried out during linear heating, the classical JMAK formulation proposed for isotherm measurements [129–131] cannot be applied. The integrated JMAK approach proposed by Fernandes *et al.* [134] is utilized instead. As in isotherm measurements, nucleation and growth will take place, one after the other. During a linear heating ramp, a certain amount of heating is needed to nucleate stable nuclei. Once it is done, growth happens and the recrystallized fraction will increase. Iterative calculations are performed: step i is used to compute step $i+1$ [215].

The incubation phase linked with nucleation is described as follows:

$$\Delta inc = \sum_i \frac{\Delta t_i}{t_{inc}(T_{p_i})} \tag{4.4}$$

where $\Delta t_i = t_{i+1} - t_i$ and

$$T_{p_i} = \frac{T_i + T_{i+1}}{2} \tag{4.5}$$

As long as $\Delta inc < 1$, nuclei are not stable and do not grow. The incubation time is computed as:

$$\frac{1}{t_{inc}} = \frac{1}{t_0}\exp\left(-\frac{Q_t}{RT}\right) \tag{4.6}$$

with t_0 a characteristic time and Q_t an activation energy.

Once $\Delta inc = 1$, growth starts and recrystallized fraction changes can be modeled. However, to use the JMAK equation to determine the $i+1$ step from the i step, the increase in temperature has to be considered. To pass from $X_i(T_{p_i}, t_i)$ to $X_{i+1}(T_{p_{i+1}}, t_{i+1})$, one has to evaluate t_i^*, the fictive time corresponding to $X_i(T_{p_{i+1}}, t_i^*) = X_i(T_{p_i}, t_i)$. Then one can calculate X_{i+1}. Figure 4.13 illustrates this methodology.

The fictive time is obtained through:

$$t_i^* = \frac{(-\ln(1 - X_i(t_i, T_{p_i}))^{1/n}}{b(T_{p_i})} \tag{4.7}$$

with:

$$b(T) = b_0 \exp\left(-\frac{Q_b}{RT}\right) \tag{4.8}$$

with b_0 the pre-exponential factor and Q_b an activation energy. The recrystallized fraction is

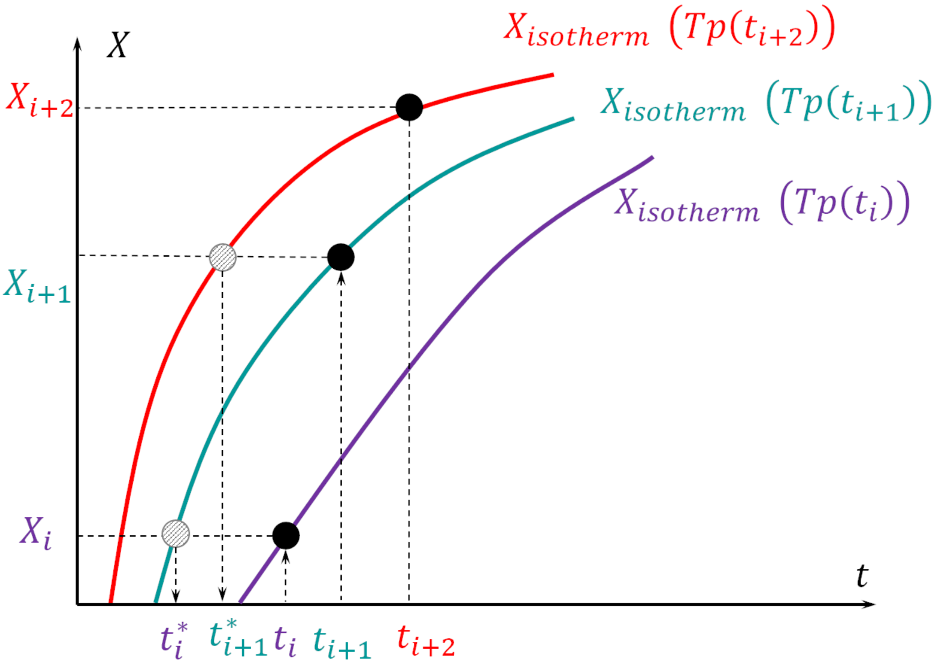

Figure 4.13: Principle of integrated JMAK. The black points are the measured data. However, to use the JMAK equation to determine the $i+1$ step from the i step, the increase in temperature has to be considered. So t_i^*, the fictive time corresponding to recrystallized fraction X_i at temperature $T_{p_{i+1}}$ is determined, prior to computing X_{i+1}.

then computed:

$$X_{i+1} = 1 - \exp(-[b(T_{p_{i+1}})(t_i^* + \Delta t_i)]^n) \tag{4.9}$$

where $\Delta t_i = t_{i+1} - t_i$. To characterize this kinetic correctly, one needs to determine the nucleation parameters t_0 and Q_t and the growth parameters b_0, Q_b, and n.

Separation of contributions for hardness reconstruction To quantify the input of those phenomena, one should start by isolating the contribution of recrystallization from those of static recovery and thermal activation of plasticity. For the modeling, the stress is calculated from hardness data using equation 1.30.

Firstly, as recrystallization is happening only at high temperatures and causes a high decrease in hardness, its contribution is separated by applying a mixture law:

$$\sigma_m(t,T) = X(t,T)\sigma_{ReX}(T) + (1 - X(t,T))\sigma_{recov}(t,T) \tag{4.10}$$

With X the recrystallized fraction, σ_m the stress coming from the measured hardness, σ_{ReX} the stress of the fully recrystallized sample in temperature and σ_{recov} the stress changes due to thermal activation of plasticity and recovery.

When a specimen is fully recrystallized, thermal activation of the plasticity is the only phenomenon that takes place in the sample:

$$\sigma_{ReX}(T) = \sigma_{ReX}(T_0) + a_{ReX}(T - T_0) \tag{4.11}$$

with $\sigma_{ReX}(T_0)$ the stress of the recrystallized specimen at T_0, near room temperature. a_{ReX} is linked with the activation volume of dislocation movement (equation 4.2).

σ_{recov} contains information on the thermal activation of the plasticity of the cold-rolled sample and static recovery. To identify both contributions, the thermal activation of plasticity is removed first (equation 4.2):

$$\sigma_{recov}(t, T) = \sigma_{recov}(t, T = T_0) + a_0(T - T_0) \tag{4.12}$$

with a_0 the slope due to thermal activation of plasticity. It is expected to depend on the microstructure. However, before recrystallization, it will be considered as constant. Then the internal stress is defined as:

$$\sigma_{recov}(t, T = T_0) = \sigma_0(T_0) + \alpha M G b \sqrt{\rho} = \sigma_0(T_0) + \sigma_i \tag{4.13}$$

with $\sigma_0(T_0)$ the yield stress at T_0 and σ_i the internal stress of the sample, measured at T_0 but changing because of heating at T. Before recrystallization, σ_i will only evolve due to static recovery. So σ_{recov} is decomposed as:

$$\sigma_{recov}(t, T) = \sigma_0(T_0) + \sigma_i + a_0(T - T_0) \tag{4.14}$$

The fluctuations of the stress due to those phenomena can be computed:

$$d\sigma_m = \left.\frac{\partial \sigma_m}{\partial t}\right|_T dt + \left.\frac{\partial \sigma_m}{\partial t}\right|_t dT \tag{4.15}$$

$$\left.\frac{\partial \sigma_m}{\partial t}\right|_T = (\sigma_{ReX} - \sigma_{recov}) \left.\frac{\partial X}{\partial t}\right|_T + (1 - X)\frac{d\sigma_i}{dt} \tag{4.16}$$

$$\left.\frac{\partial \sigma_m}{\partial T}\right|_t = (\sigma_{ReX} - \sigma_{recov}) \left.\frac{\partial X}{\partial T}\right|_t + X a_{ReX} + (1 - X) a_0 \tag{4.17}$$

The variations of the internal stress with temperature are considered negligible.

So it gives:

$$d\sigma_m = (\sigma_{ReX} - \sigma_{recov}) dX + (X a_{ReX} + (1 - X) a_0) dT + (1 - X)\frac{d\sigma_i}{dt} dt \tag{4.18}$$

with

$$dX = \left.\frac{\partial X}{\partial t}\right|_T dt + \left.\frac{\partial X}{\partial t}\right|_t dT \tag{4.19}$$

An increment in time will induce an increment in temperature and recrystallized fraction. Using this formulation, an iterative calculation is performed to reconstruct the changes of the stress and so of the hardness knowing the applied thermal cycle.

The first step is to determine the a_{ReX} and a_0 parameters from the measurements. The slope of the thermal activation of plasticity may depend on the microstructure of the sample. a_0 is assumed constant before recrystallization. Once recrystallization starts, it is supposed that the slope of the thermal activation of plasticity follows a mixture law with recrystallization fraction. Then, the kinetic of static recovery is quantified using the Verdier model. As the recrystallized fraction can now be computed, the kinetic of the static recrystallization can be determined through the integrated JMAK formulation.

IV.B. Application on pure copper

Sample Cu#1 is used to quantify the parameters of the model. As observed on sample Cu#3, no static recovery is expected in copper.

Determination of the parameters of the model The slope a_{ReX} is characterized by exploiting the hardness data coming from the cooling and a_0 on the heating between RT and $200°C$. As there is no recovery, there is no doubt about the value of a_0. The recrystallized fraction is then computed (see figure 4.14). A PSO algorithm [216–220] is used to evaluate the parameters of recrystallization on copper. To verify that the heating rate does not affect the recrystallization kinetic, its parameters are quantified on specimens Cu#1 and Cu#2, independently. The optimization is performed with 10^4 particles and 10^3 iterations (see Annexe B for more details on the algorithm). Such optimization is time-consuming: optimization of the algorithm and better hypotheses on the parameter values could enable reducing this step.
Applying the methodology previously described allows determining parameters that correctly reproduce the changes at the beginning of the recrystallization but misses the end of the curve. This is a phenomenon observed in literature: when copper recrystallized, its Avrami exponent decreases during the process [221, 222]. To take this effect into account, the JMAK formulation is modified: if the recrystallized fraction is lower than 0.5, a constant n_1 is used. If it is higher than 0.5, a constant value n_2 is applied instead. Such modification leads to a good reconstruction of the recrystallized fraction.
Moreover, according to literature [223], the activation energies of nucleation Q_t and of growth Q_b are expected to be of the same order. Unfortunately, this hypothesis does not enable determining recrystallization parameters giving a convincing reconstruction. To get a correct prediction of the hardness, it is decided to apply an activation energy of 1 J/mol during nucleation. Nevertheless, this approach gives consistent results, as presented in figure 4.14 and gives the following parameters (see table 4.4).

Analysis of the parameters The two samples give similar optimized parameters: the values of t_0 and n_2 are the same and the others are really close. Moreover, the determined activation energy of growth is consistent with literature data [222, 224, 225]. The main issue here is that for a given sample, the PSO algorithm converges to similar values but it does not give a unique solution. The data here are not enough to identify uniquely the 5 parameters here. This can be observed on the parameter I, the identification factor [226–228]. A value of I lower than 2

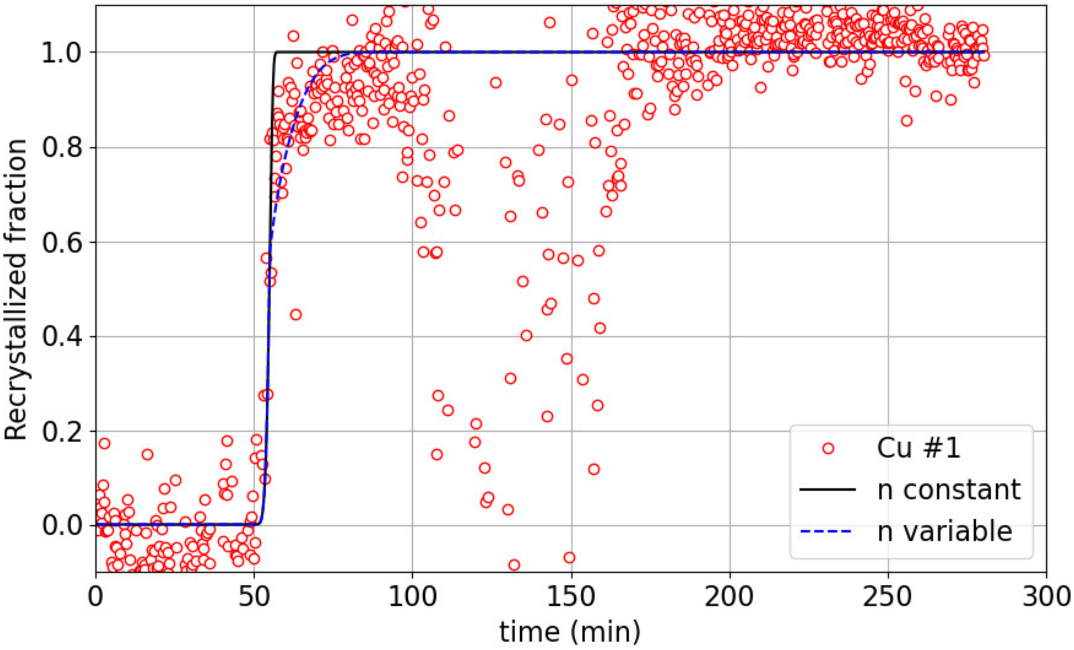

Figure 4.14: Recrystallized fraction calculated on sample Cu#1. The integrated JMAK formulation is utilized to model its changes. A variation of the Avrami exponent during the recrystallization process is considered. It allows fitting correctly the end of the recrystallization process.

indicates good identifiability of the solution (uniqueness and stability). Unfortunately, it is not the case here.

Nevertheless, the obtained parameters allow reconstructing the hardness variations of the copper samples. To compare the modeling with experimental results, the parameters determined on sample Cu#1 are used to predict hardness on a sample submitted to the thermal cycle of samples Cu#1, Cu#2, and Cu#4. As observed in figure 4.15, the proposed model yields consistent results. The impact of recrystallization on microstructure changes of the cold-rolled copper samples depending on the applied thermal cycle is well predicted.

Let's come back a little on the values of a_{ReX} and a_0, as they are linked with the characteristic activation volume. According to equations 4.2 and 4.11, they should be related to the activation volume of the deformation mechanism. From hardness measurements, $\frac{v_{ReX}}{v_{cold-rolled}} \propto \frac{a_0}{a_{ReX}} = 3.2$: an increase of the activation volume is expected since the density of defects decreases upon recrystallization.

Table 4.4: Recrystallization parameters of copper obtained by PSO optimization.

Sample	Heating rate (°C min^{-1})	t_0 (min)	b_0 (min^{-1})	Q_b (kJ/mol)	n	n_2	I
Cu#1	5	50	3.45×10^9	106	3.58	0.34	4.42
Cu#2	1	50	2.82×10^9	104	3.32	0.34	4.36

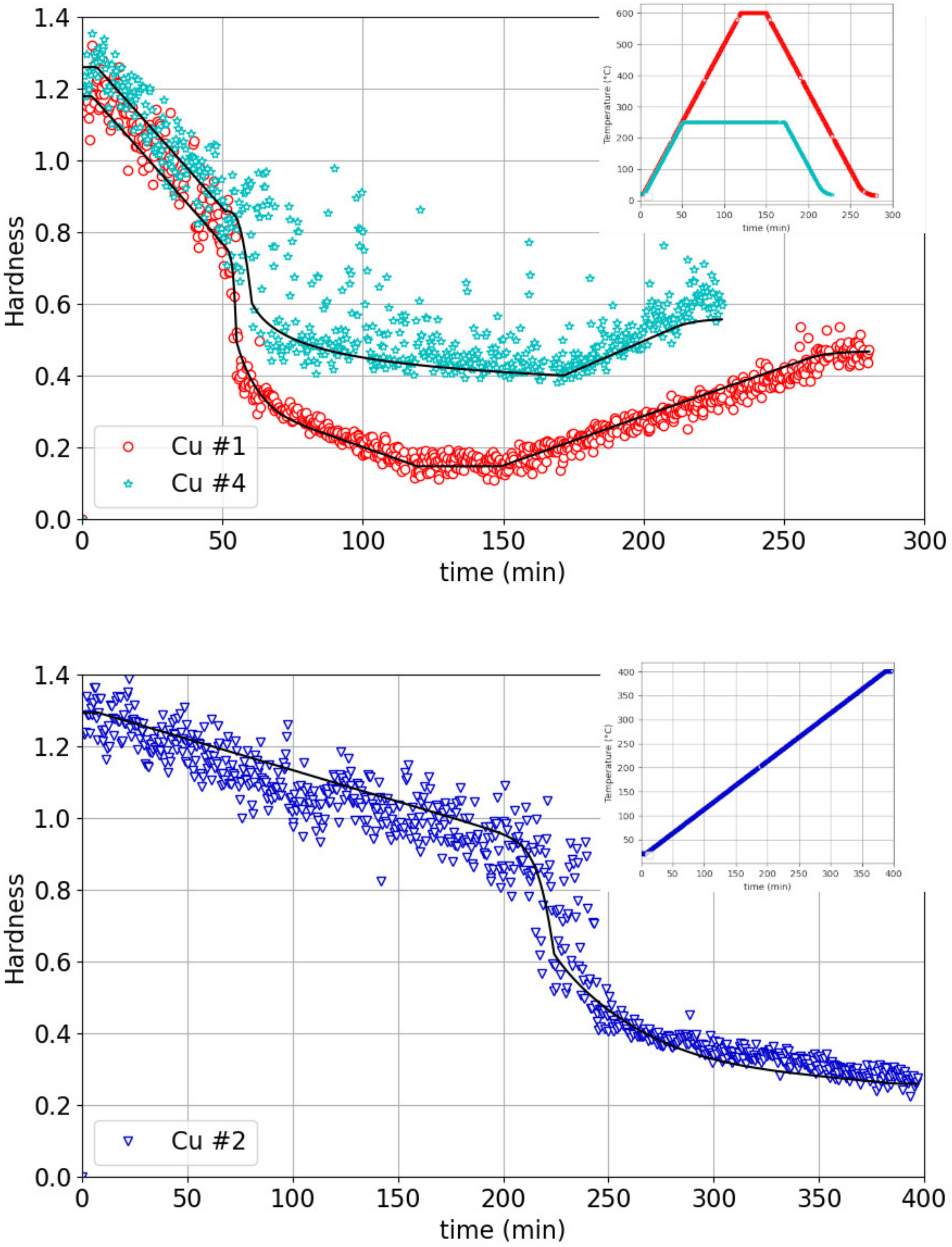

Figure 4.15: Reconstruction of hardness when applying the thermal cycle of samples Cu#1, Cu#2, and Cu#4. The model gives a really good prediction of the hardness variations compared to the experiments.

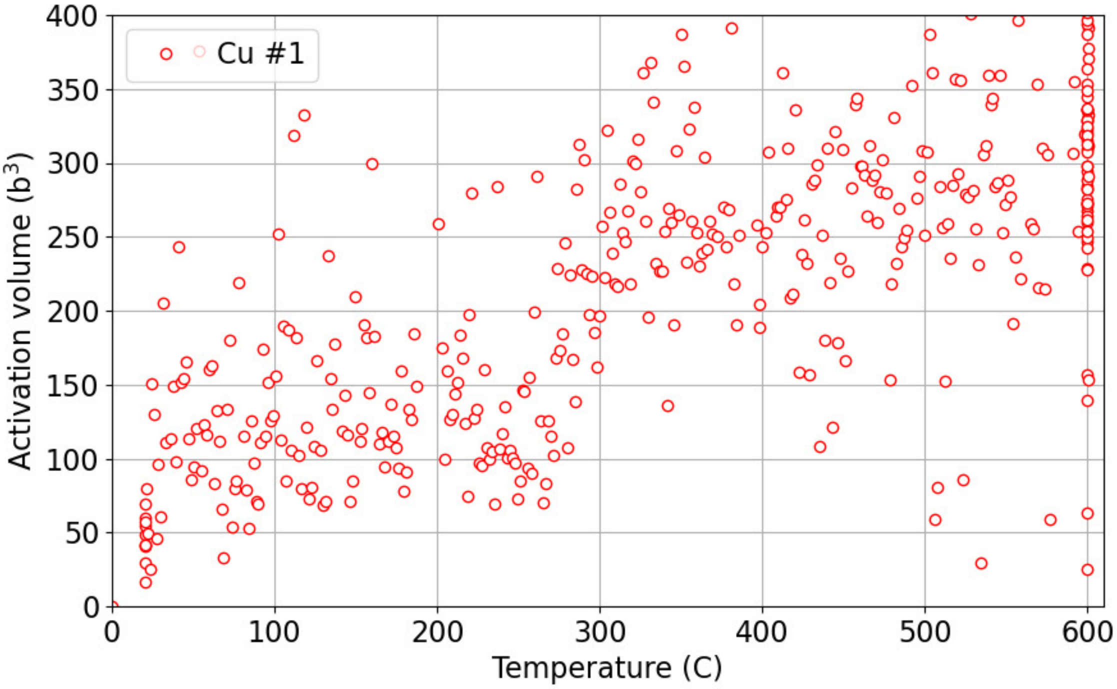

Figure 4.16: Activation volume of Cu#1 during heating determined through the analysis of the creep segment. Around 300 °C the activation volume rises significantly. It is a sign that recrystallization occurred here.

The creep properties also give access to the activation volume with temperature. Analyzing the creep properties of the sample Cu#1 (see figure 4.16), a rise of this volume around 300 °C is observed, after recrystallization. The increase seems to be around a factor of 3. The creep analysis confirms the increase noted using a linear thermal model for the thermal activation of plasticity.

According to equation 4.2, the activation volume is not expected to be constant with temperature. However, when studying figure 4.16, it stays roughly constant before and after recrystallization: it explains the linear behavior of hardness in temperature, viewed in figure 4.1.

IV.C. Application on pure aluminum

It is quite easy to assess the kinetic of static recrystallization if it is the only mechanism responsible for microstructure changes. However, what happens if two mechanisms in competition take place? The next step is the quantification of the kinetics of static recovery and recrystallization on pure aluminum.

Thermal activation of plasticity versus static recovery Contrary to copper, the changes in hardness at low temperatures are due to the thermal activation of plasticity and to static recovery taking place in the sample. Their contributions are determined on specimen Al#7 (see figure 4.5). This sample was heated up to 300 °C and then cooled down before any significant recrystallization occurs. As static recovery is promoted by high dislocation density and high

temperature, it is considered that during the cooling, there is not that much recovery. This part should give an estimation of the parameter a_0 (thermal activation of plasticity). It is supposed that this value does not change with static recovery nor with the initial state of the sample.
The value of a_{ReX} is determined on samples Al#4, Al#5 and Al#6. As it can be seen in figure 4.9, during the cooling, the hardness of all samples has the same trend in temperature.

Determination of the parameters of static recovery As there is no static recrystallization, the variations of internal stress σ_i with time and temperature can be computed. Static recovery kinetic can now be quantified. As previously, a PSO algorithm [216–220] is used to assess the parameters U_0 and v_0 (see table 4.5). The optimization is performed with 2000 particles and 10^3 iterations. It takes a few minutes to get static recovery parameters.
As it was expected, those parameters depend on the initial state, as this phenomenon is favored by a high density of dislocation. The activation energy is constant with the initial state and in the scale of what is observed in the literature on other aluminum grades [116, 127, 128]. Moreover, a decrease in the activation volume when increasing the thickness deformation ratio is noticed. It is consistent with the product $v_0\sigma_0$ which is more or less constant. The identification factor I is lower than 2 when trying to determine the two parameters of the static recovery model: a good identification is possible here. As observed in figure 4.17, the parameters quantified on sample Al#6 allow reconstructing the changes correctly noted on sample Al#7.

Determination of the parameters of static recrystallization As the hardness changes due to the activation of plasticity and static recovery are quantified, the recrystallized fraction can now be computed. Its parameters can also be evaluated, once again using a PSO algorithm [216–220]. The optimization is performed with 10^4 particles and 5×10^3 iterations.
The parameters characterizing the recrystallization kinetic are computed in the table 4.6. As it could be expected, the incubation time increases with decreasing deformation state: it is more difficult to obtain stable nuclei to start the growth. Once again, it is decided to apply an activation energy of 1 J/mol during nucleation.
When heating at 3 °C/min, it seems that there is no impact of the initial state on the growth parameters: the same prefactor b_0, the activation energy of growth Q_b, and the Avrami coefficient n were accessed on the samples. Moreover, the activation energy of growth is of the same order as the activation energy of self-diffusion inside aluminum alloys [166].
As for copper, it is not possible to obtain a unique stable solution for the parameters of the

Table 4.5: Static recovery parameters of cold-rolled aluminum obtained by PSO optimization.

Sample	r	U_0 (kJ/mol)	v_0 (b^3)	$v_0\sigma_0$ (eV)	I
Al#4	85%	207	133	2.68	1.19
Al#5	60%	207	148	2.93	1.70
Al#6	40%	207	153	2.78	1.61

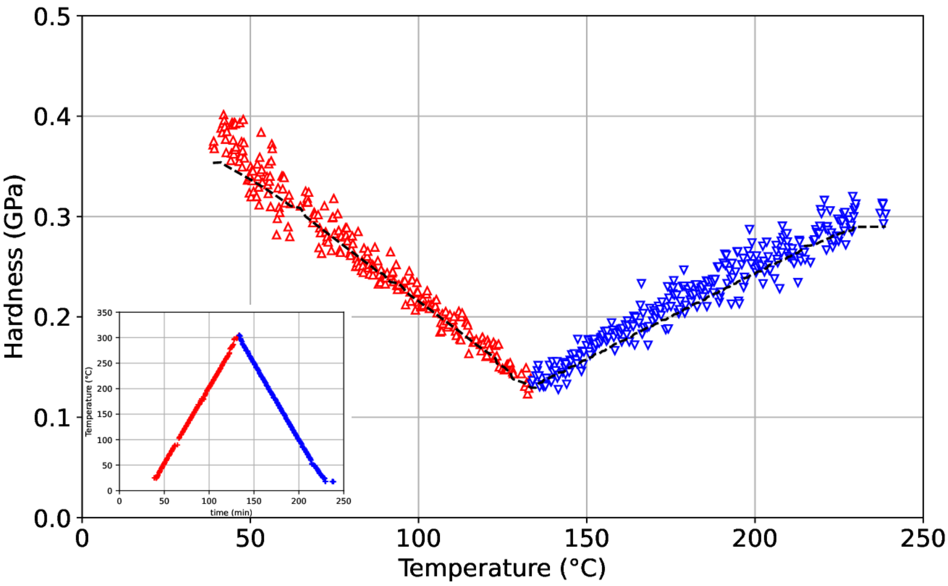

Figure 4.17: Modeling of hardness changes of sample Al#7. Static recovery and the thermal activation of plasticity are responsible for the hardness changes along the thermal cycle.

recrystallization kinetic. Here again, the identification factor is higher than 2: to get better modeling, work is required to improve the recrystallization model. However, as presented in figure 4.18, the parameters quantified for static recovery and recrystallization enable reconstituting the hardness of the samples employed to evaluate them.
Nevertheless, contrary to copper, changing the heating rate impacts the recrystallization kinetic as static recovery is occurring during heating. As it can be noticed in the table 4.6, the parameters of nucleation and growth of sample Al#8 have changed compared to sample Al#4 but stay in the same order. The thing is that because of static recovery, the dislocation density decreases so nucleation is expected to be more difficult and recrystallization is pushed back to a higher temperature. So, the recrystallization kinetic has to be characterized at each applied heating rate. Once again, the model leads to good hardness prediction (see figure 4.19).

Prediction of hardness changes depending on thermal cycles The hardness variations of samples Al#2 and Al#3 can be predicted, using the parameters determined on sample Al#4. As

Table 4.6: Recrystallization parameters of cold-rolled aluminum samples obtained by PSO optimization.

Sample	r	Heating rate ($°\mathrm{C\,min^{-1}}$)	t_0 (min)	b_0 (min^{-1})	Q_b (kJ/mol)	n	I
Al#4	85%	3	80	10^{10}	127	1	4.19
Al#5	60%	3	100	10^{10}	127	1	4.81
Al#6	40%	3	122	10^{10}	127	1	4.95
Al#8	85%	1	72	8.64×10^9	139	1.22	18.3

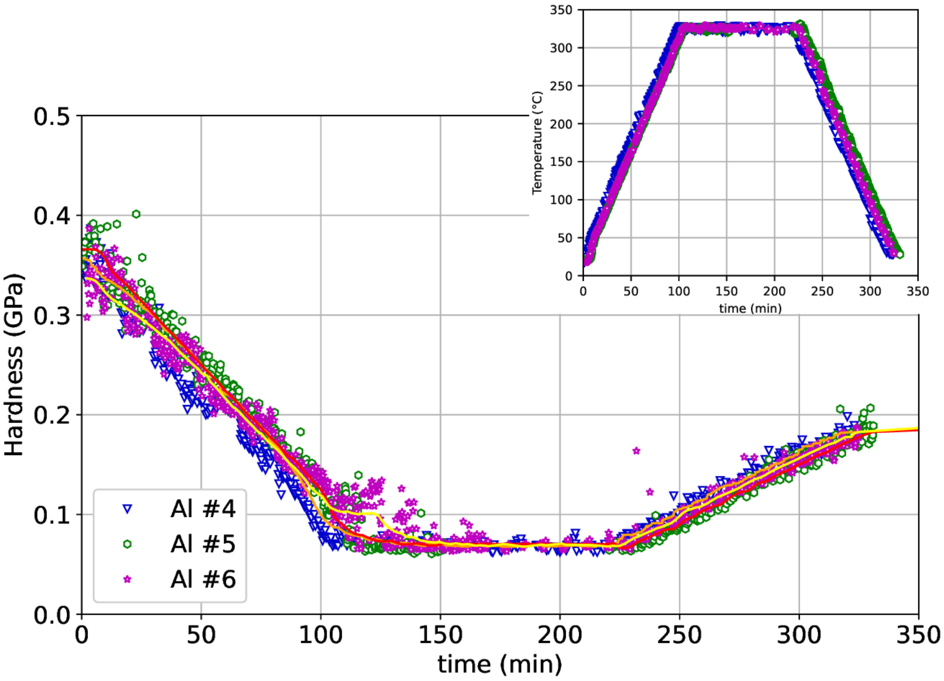

Figure 4.18: Modeling of hardness changes of sample Al#4 (orange), Al#5 (red) and Al#6 (yellow). The parameters determined using a PSO algorithm allow getting a good reconstruction of hardness variations on the samples.

it can be seen in figure 4.20, the reconstruction is really good during heating and holding but there is a gap visible during cooling. It may come from an overestimation of the recrystallized fraction and the mixture law used on the slope of the thermal activation.
Another explanation would be that the tests on samples Al#1, #2, and #3 have been made at really distinct times compared to samples Al#4, #5, and #6. As the tip has been changed and calibrated multiple times between tests, it may also explain the difference in hardness absolute values.

To predict the hardness variations of a material, one could use the HTSI method to assess the phenomena taking place in the sample and then predict them depending on the thermal cycle. Here, only two phenomena have been studied: static recovery and static recrystallization. Depending on the phenomena that take place in the sample, the evaluation could be really simple or quite complicated. On pure copper, recrystallization is the only detected phenomenon. The quantification is quite simple since, for a specific initial state, the kinetic does not depend on the heating rate (in the studied range). One HTSI test is enough to quantify the kinetic of recrystallization. It allows good prediction of the microstructure changes depending on the thermal cycle. However, if static recovery happens before recrystallization, things become trickier. As seen on aluminum, for a given initial state, static recovery kinetic does not depend on the heating rate but recrystallization kinetic does. So, more HTSI experiments should be used to predict the microstructure variations completely for a given initial state.

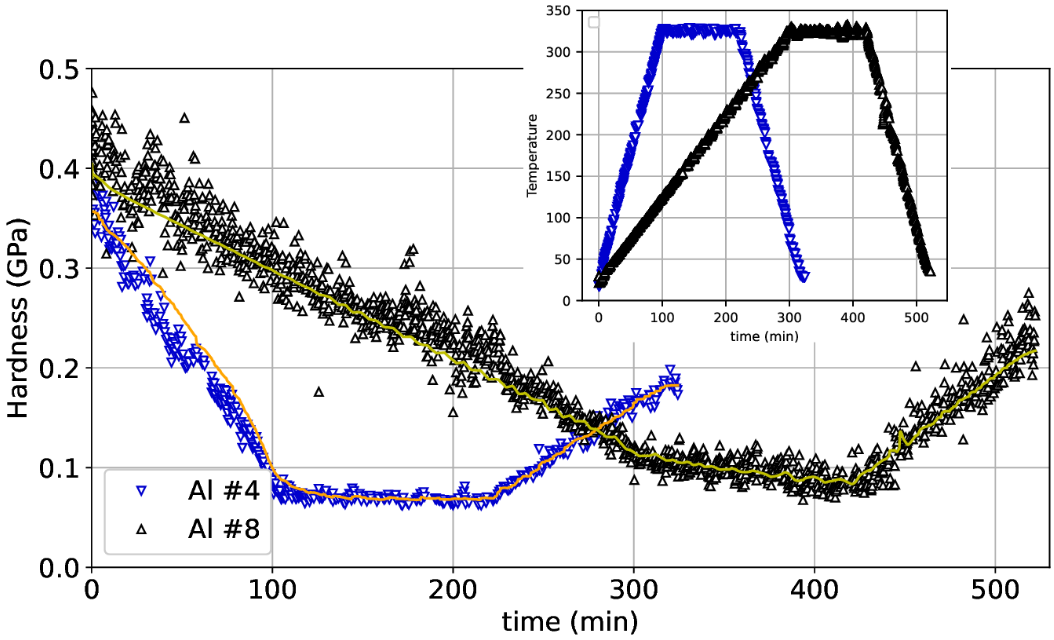

Figure 4.19: Modeling of hardness variations of sample Al#4 (orange) and Al#8 (yellow). The reconstruction is good but recrystallization kinetic needs to be determined for each sample, depending on the heating rate.

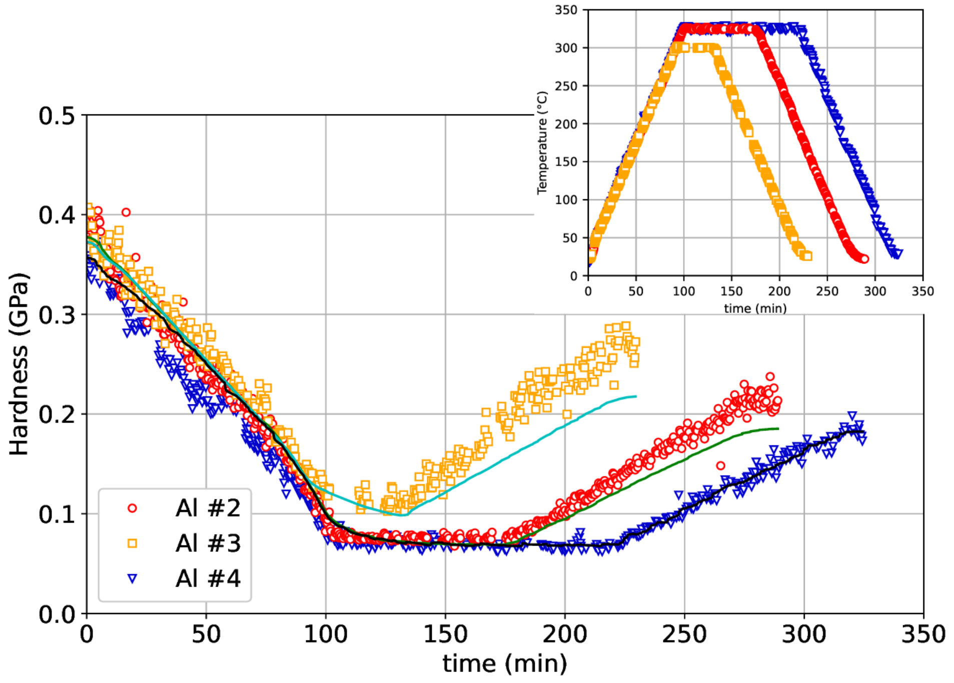

Figure 4.20: Modeling of hardness changes of sample Al#2 (cyan), Al#3 (green) and Al#4 (black). The reconstruction is consistent on heating and holding but a gap can be observed during cooling on samples Al#2 and Al#3.

Moreover, the initial state clearly impacts the kinetic of those phenomena. However, some dependencies on the parameters with the initial state may be determined, which would allow reducing the number of tests to pass from one initial state to another. For instance, on pure aluminum, it looks like the activation energy of static recovery is independent of the initial state and the activation volume seems to depend linearly on the logarithm of the initial deformation state (see values of table 4.5 and [116, 127, 128]). Concerning recrystallization, on aluminum again, the growth state appears independent of the initial state for a given heating rate. Moreover, when working on the thermal activation of plasticity, the creep results may be used to determine the slope of the deformed state knowing the one of the recrystallized state. These observations require to be confirmed and validated but could help reduce the number of HTSI tests needed to predict microstructure changes of a sample with various initial deformation states, submitted to different thermal cycles.

V. Conclusions of the chapter

Thanks to nanoindentation, one can measure the hardness changes of materials during in-situ annealing [106]. It then allows quantifying the kinetics of the microstructure modifications of the studied material. As conducting classical indentation tests is time-consuming, it “only” enables characterizing slow kinetics compared to the indentation time.

The HTSI method previously presented in this manuscript allows determining the hardness of a material in temperature. A huge number of 1-second indents are obtained in a few hours. So, this methodology can give access to in-situ microstructural changes. Through the 1-second indentation cycle, mechanical properties data are quantified in a few seconds. It gives access to more rapid variations compared to classical indentation. To prove the interest of the HTSI technique for such characterization, static recovery and recrystallization kinetics were evaluated on pure copper and pure aluminum.

The application on deformed pure copper allows studying the static recrystallization. It is detected through the huge drop in hardness observed during heating. The heating rate also impacts the onset of recrystallization. Through modeling, static recrystallization parameters are quantified and are assessed to be independent of the heating rate. A unique HTSI test on copper enables determining the kinetic parameters and so to predict the microstructure changes of the material, whatever the thermal cycle. The results are consistent with post-mortem EBSD measurements and creep measurements.

When studying pure deformed aluminum, two phenomena are detected: static recovery and recrystallization. Those two phenomena impact the hardness and strain rate sensitivity during the thermal cycle. The effect of the heating rate was investigated, as well as that of the initial deformation state. Modeling allows characterizing of the static recovery and the recrystallization. Static recovery parameters are affected by the initial deformed state but not by the heating rate. Contrary to copper results, the recrystallization parameters are here dependent on the heating rate and the initial state. This is due to the presence of static recovery. Having two mechanisms responsible for microstructure changes complicates the determination of their kinetics. Nevertheless, the results are consistent with literature data and with post-mortem EBSD measurements. Thanks to a few well-designed HTSI measurements, the design of materials may be eased as one would quantify the microstructure state of its material after an applied thermal cycle.

As observed, the obtained predictions are consistent with measurements but so discrepancies are detected on the aluminum samples not fully recrystallized. Furthermore, the obtained parameters are not unique: improvement of the modeling seems necessary. The present analysis only focuses on static recovery and recrystallization of model materials. As precipitation, oxidation, or phase transition are also possible, these phenomena must be studied and modeled.
Moreover, the indentation tests applied here are load-controlled. The maximum applied load stays constant so the maximum depth is increasing with temperature. The tested volume then changes with temperature. As the material behaviors may be modified a lot at swallow depths, improvements are required in the indentation cycle. Hopefully, as tests were conducted at 1 µm-depth, it should not impact the results.
Finally, some deviation around the mean hardness values at a given temperature can be observed all along the thermal cycle. Such variations come from the microstructure of the sample. Analyzing them and their changes should give information on the local microstructure. Doing experiments at different indentation sizes compared to the characteristic size of the structure will give various types of information on it.

5

Characterization of thin-film metallic glasses in temperature

The aim of this chapter is to study the behavior of metallic glasses at temperatures higher than their glass transition temperature.

Chapter's content

I. Goals of the chapter

Through the hardness variations of metals in temperature, one can quantify the microstructure changes using a few well-designed HTSI tests. However, these tests also give access to the creep properties of a sample. Viscoplastic as well as plastic properties give information about the physical state of a material. For instance, for an amorphous glass, having a strain rate sensitivity m equal to 1 means that the specimen behaves as a Newtonian fluid. Using the HTSI method may give more details on the properties of amorphous structures in temperature.

As there are not a lot of studies on what happens to a metallic glass above its glass transition temperature, experiments will be conducted not only to observe this transition but also to characterize what occurs at higher temperatures, in terms of plastic and creep properties. The experimentations were performed in collaboration with Solène Comby-Dassonneville and Philippe Steyer from MATEIS (France). Part of the results has already been published [229].

II. Materials and methods

II.A. Samples

Let's consider a model metallic glass: ZrCu. As obtaining bulk metallic glass (BMG) is quite difficult, samples were thin-film metallic glasses (TFMG) [229].

Film deposition ZrCu thin-film metallic glasses were deposited by Alejandro Borroto from the Institut Jean Lamour (France). The deposition was performed using DC magnetron co-sputtering of Zr and Cu metallic targets in the presence of argon. The sputtering chamber was pumped down via mechanical and turbo-molecular pumps, resulting in a base vacuum of 1×10^{-6} Pa. To ensure good lateral homogeneity of the film composition and thickness, the depositions were performed with the substrate holder in rotation mode. The cathodes were mounted in a confocal configuration, and the target-to-substrate distance was fixed at 9 cm. An argon flow rate of 30 sccm and a working argon pressure of 0.5 Pa were used. Zirconium and copper targets (50.8 mm. diameter, 3 mm-thick, and purity higher than 99.9%) were powered by a Maxim 10 0 0 DC generator. Under these conditions, ZrCu thin films with a Cu content of 50 at% were obtained by applying discharge currents of 0.3 A to the Zr target and 0.056 A to the Cu target. The films were deposited without external heating.

Substrates As the indentation measurements are compared with other characterization techniques, different substrates are used. For the nanoindentation, X-ray Diffraction (XRD), and Scanning Electron Microscopy (SEM), 6 µm-thick ZrCu TFMGs were deposited onto fused silica and silicon substrates during the same deposition batch.

In addition, samples for Differential Scanning Calorimetry (DSC) measurements were deposited onto sodium chloride substrates, ensuring 5 mg of material for each specimen. Substrate-free samples for DSC were then easily obtained by dissolving the NaCl substrate in distilled water.

Furthermore, a 70 nm thin film was deposited onto a dedicated Nano-Chip from DENS solutions for transmission electron microscopy (TEM) observations [230].

II.B. Methods

Indentation measurements The indentation tests were conducted using the InSEM HT nanoindenter at the LTDS, provided by KLA Nanomechanics. This system is under vacuum (1×10^{-2} Pa), inside a VEGA 3 SEM (Tescan). A Berkovich sapphire tip was mounted to make those tests. Calibration of temperature setting was performed before carrying out any HTSI experiments [79].

Different indentation tests were conducted. First, some CSM measurements were carried out at RT, 200 °C, 300 °C, 350 °C, and 400 °C, at a constant loading rate of $0.05\,\mathrm{s}^{-1}$. Some isotherm HTSI tests were also carried out at those temperatures for comparison purposes. As thermal history greatly impacts the properties of amorphous glass [231], a new sample was used for each testing temperature. Then, the different HTSI tests described in the table 5.1 were conducted. The samples #1 and #2 were heated for RT to 450 °C at 3 °C/min before holding at this temperature for 2 h and cooling down at 3 °C/min. The samples #3, #4, #5 and #6 were heated quickly (15 °C/min) up to 350 °C before being heated at 3 °C/min up to a maximum temperature. They were then annealed at this temperature for 5 h before being cooled down at 15 °C/min. The quarter sinus loading indentation cycle was used, with a maximum load of 25 mN and a creep segment of 0.1 s. As the sample configuration is a soft 6 µm film on a hard substrate, the substrate should have a very limited impact on the hardness values of the film [232, 233]. As the load frame stiffness seems to fluctuate in temperature and as the authors are interested in the relative changes of properties instead of the absolute value, Loubet's model was used to analyze the indentation results.

XRD characterization The crystallographic structure of the films before and after HTSI was investigated through X-ray Diffraction (XRD) at MATEIS (France), using an AXS Bruker D8 Advance diffractometer with Cu Kα radiation ($\lambda = 0.154\,06$ nm) in Bragg-Brentano geometry. For comparison with high-temperature nanoindentation testing, the thermal stability of ZrCu TFMGs was also investigated using in situ high-temperature XRD (HT-XRD) in an Anton

Table 5.1: Thermal cycle applied on the different samples during the HTSI tests.

Sample	T$_{min}$ (°C)	T$_{max}$ (°C)	Heating rate (°C/min)	Holding time (min)
#1	RT	450	3	120
#2	RT	450	3	120
#3	350	400	3	300
#4	350	410	3	300
#5	350	400	3	300
#6	350	435	3	300

Paar HTK 1200 oven chamber operating under vacuum (1×10^{-3} Pa). XRD measurements were performed with a locked coupled scan (2θ from 27° to 47°) during the same thermal cycle as for HTSI (heating up to 450 °C with a 3 °C/min equivalent rate, 2 h plateau at 450 °C, and cooling down to room temperature at a −3 °C/min equivalent rate). For each XRD diffractogram, the crystallization fraction F_x was estimated using equation 5.1, where I_a and I_x correspond to the integrated intensities of the amorphous phase and crystallized phases, respectively, after deconvolution of each contribution from the total diffraction intensity [234, 235].

$$F_x = \frac{I_x}{I_a + I_x} \tag{5.1}$$

Microstructure characterization The initial state of the samples was characterized through SEM observations utilizing a field-emission gun from Zeiss (SUPRA 55 VP) as well as by TEM using a FEI-TITAN eTEM operating at 300 kV under high vacuum. The characterization was carried out at MATEIS (France).

III. Verification of the initial state

Prior to carrying out experiments, a check of the amorphous structure of the samples was conducted. Firstly, the amorphous behavior at the macroscopic scale was confirmed using XRD measurements (see figure 5.1 a)). A characteristic hump is centered at 38.6° on the 2θ scale, as assessed in literature [236–238]. SEM observations at the mesoscopic scale validate the amorphous behavior (see figure 5.1 b)): the coating surface is homogeneous. A substructure due to the columnar growth of the film (figure 5.1 c)) can be noted. Moreover, focusing on the cross-section after the substrate cleavage, a characteristic vein-like pattern [237] is presented. Finally, no micron-scale precipitates are found in those samples. As nanocrystals may be present but not detected using the SEM, TEM observations were carried out. As it can be seen in figure 5.4 d), those statements confirm the amorphous atomic distributions of the initial state of the specimens.

IV. Physical changes of TFMGs during ramping

IV.A. Results

Let's considered samples ZrCu #1 and #2. They were submitted to the thermal cycles displayed in figure 5.2 during the High-Temperature Scanning Indentation measurements. Let's analyze the hardness and strain rate sensitivity modifications in all the thermal cycles. As can be seen in figure 5.3 and 5.4, those properties change a lot during the thermal cycle. Four steps can be distinguished.

First, during the heating up to 230 °C, hardness is quite constant with increasing temperature. The strain rate sensitivity is really low. The sample is in its solid amorphous state. Then, at 230 °C, sample ZrCu #2 hardness decreases while the one of sample ZrCu #1 stays constant up

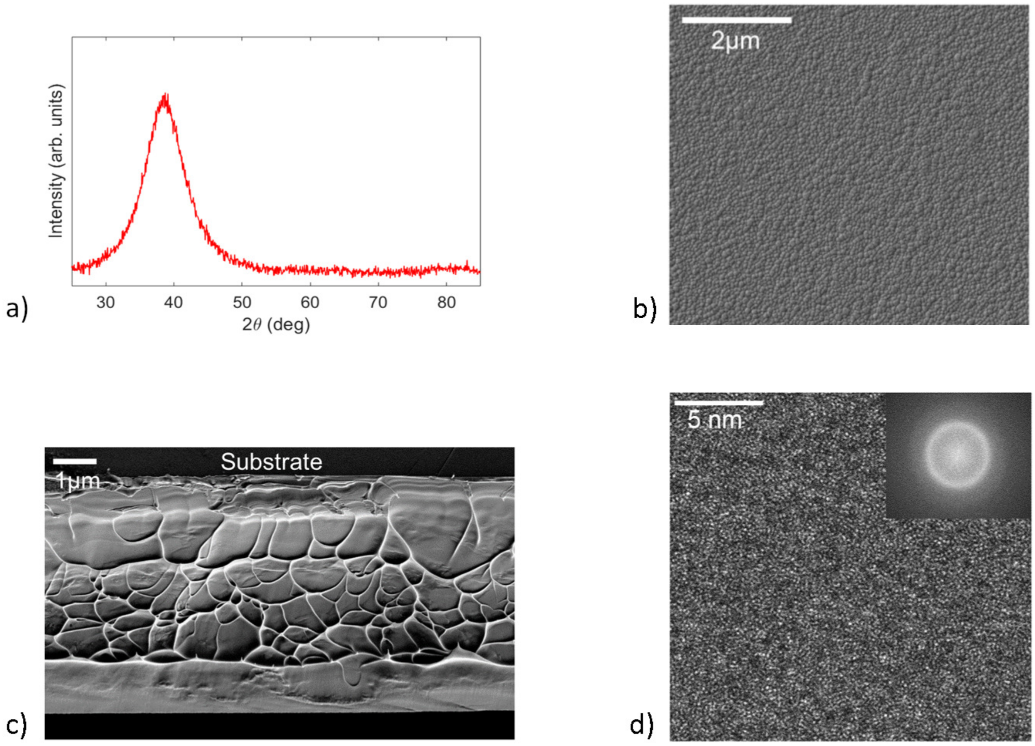

Figure 5.1: Characterization of the initial amorphous state of our ZrCu specimens (a) via XRD, (b,c) via SEM observations, and (d) via TEM measurements.

to 350 °C. The two specimens present a huge drop of hardness from around 350 °C to 430 °C: hardness is divided by almost 10 between those two temperatures. At the same time, strain rate sensitivity increases a lot. The increase of m is split into two regimes: slow increases up to 0.1 (at 350 °C) followed by a huge increase up to 1, linked with the huge drop in hardness. This second step corresponds to the glass transition observed on the samples: it changes from the solid amorphous state to a supercooled-liquid state. The state at really low hardness and high strain rate sensitivity (around 430 °C) quickly changes again.

At temperatures higher than 430 °C, the hardness suddenly increases a lot, up to 2 GPa before keeping a constant value until the end of the heating. At the same time, the strain rate sensitivity drops to 0.2 before stabilization. During the annealing at 450 °C, the hardness restarts to increase slowly and reaches 4.0 GPa after 2 h. Moreover, the strain rate slowly decreases again during the annealing. Finally, during the cooling, hardness and strain rate sensitivity decrease slowly, back to RT. The sample is no longer evolving.

IV.B. Amorphous state at low temperature

At low temperatures, the samples are in the amorphous metallic glass state. Hardness and strain rate sensitivity are roughly constant, up to 230 °C. According to DSC measurements (see table 5.2), the glass transition temperature of those samples should be 385 °C. Having the measured mechanical properties staying constant up to $0.76T_g$ is consistent with literature [146, 239–241]:

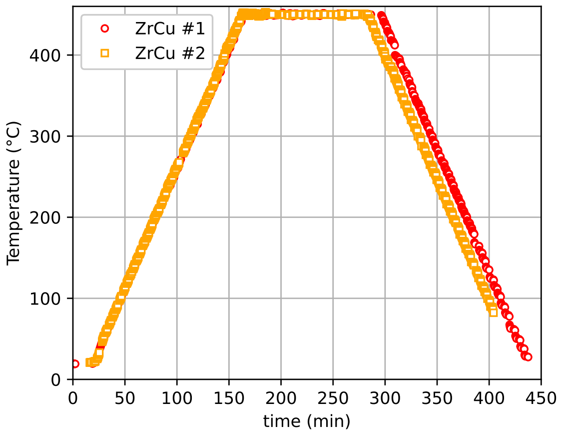

Figure 5.2: Thermal cycles applied on specimens ZrCu #1 and #2.

hardness of metallic glasses should be constant up to 0.7T$_g$.

Glass transition temperature Through the HTSI measurements, the glass transition temperature of the thin film can be determined. Around this temperature, the glass is starting to behave more like a liquid. The sample changes from the amorphous solid state to the supercooled-liquid state. It explains the huge decrease in hardness and the huge increase in strain rate sensitivity at this temperature. As in thermomechanical analysis [242, 243], one can assess the glass transition temperature using the thermal derivative of hardness and strain rate sensitivity.

It is considered that the changes of slope around 400 °C are the moment where this transition occurs. Table 5.2 presents the values obtained via this method. Values acquired by HTSI tests are consistent with DSC measurements at 3 °C/min. However, the quantification of T$_g$ on hardness can be tricky. In [229], the authors evaluate a lower T$_g$ value using the same hardness set of data. The scattering of data may cause a difference in the determination of T$_g$. Nevertheless, the strain rate sensitivity data give the same value in the two analyses. Some precautions should be taken if one is only employing the hardness data to get the glass transition temperature of thin-film metallic glass.

Table 5.2: Glass transition and crystallization temperatures determined using DSC or HTSI method.

Sample	Method	Heating rate (°C/min)	T$_g$(°C)	T$_X$ (°C)
-	DSC	3	385	407
-	DSC	15	395	429
#1	HTSI on hardness	3	389	427
#2	HTSI on hardness	3	385	430
#1	HTSI on strain rate sensitivity	3	389	424
#2	HTSI on strain rate sensitivity	3	389	426

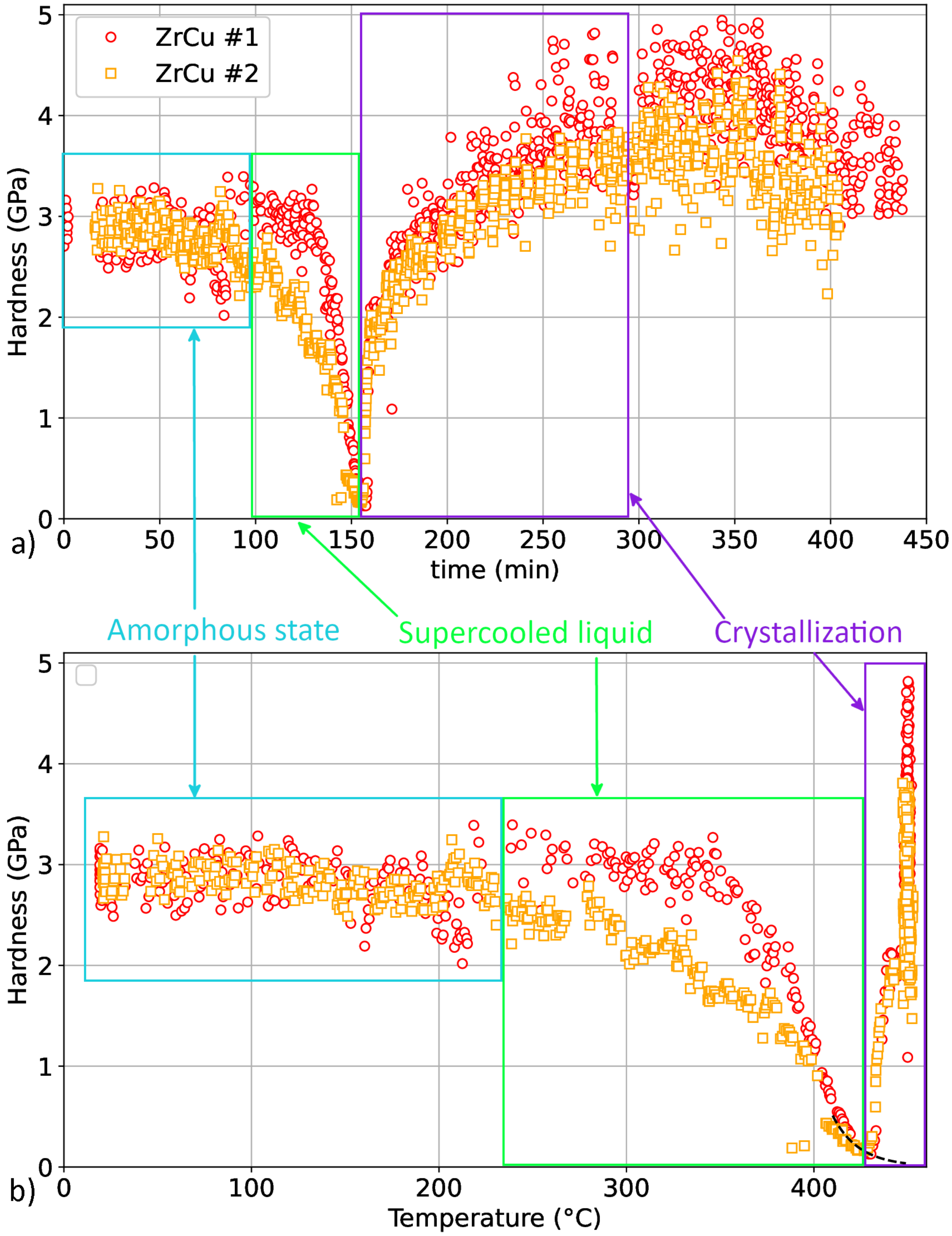

Figure 5.3: Hardness changes during the thermal cycles presented in figure 5.2. (a) against time, (b) against temperature. In (b), only the data during heating and holding at 450 °C are plotted.

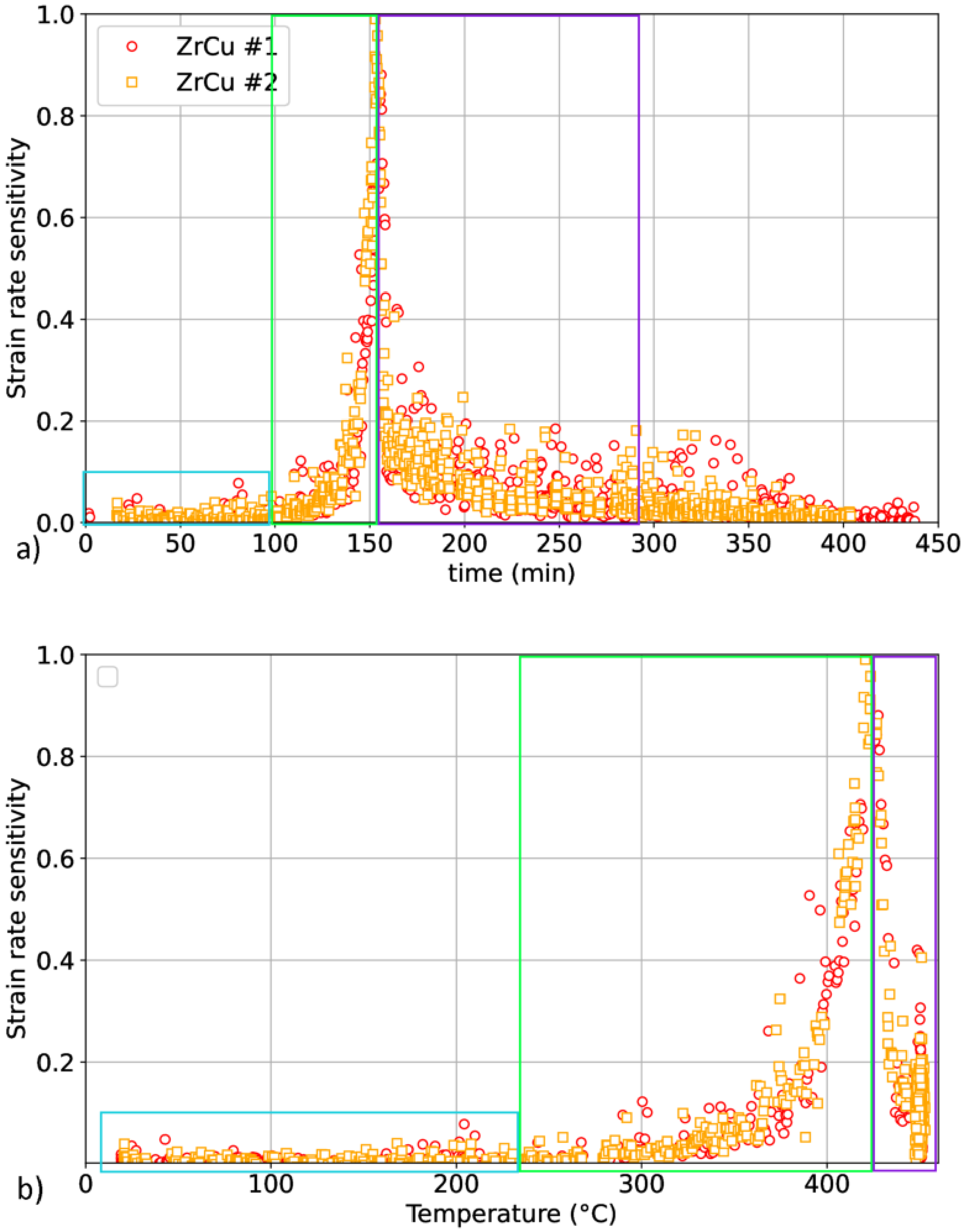

Figure 5.4: Strain rate sensitivity changes during the thermal cycles displayed in figure 5.2. (a) against time, (b) against temperature. In (b), only the data during heating and holding at 450 °C are plotted.

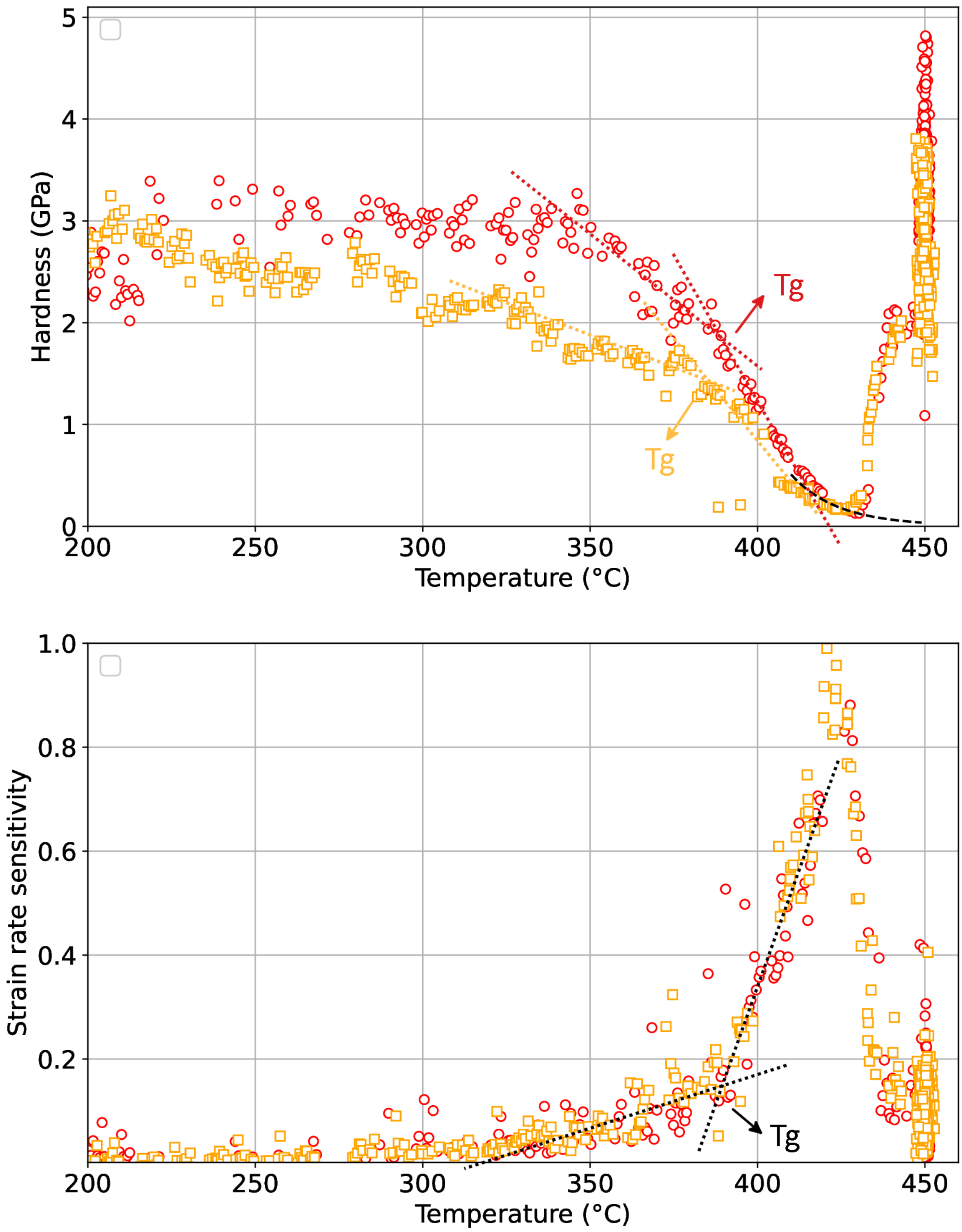

Figure 5.5: Hardness and strain rate sensitivity of ZrCu in temperature. Glass transition temperature is evaluated through the modifications of the slope of hardness or strain rate sensitivity with temperature.

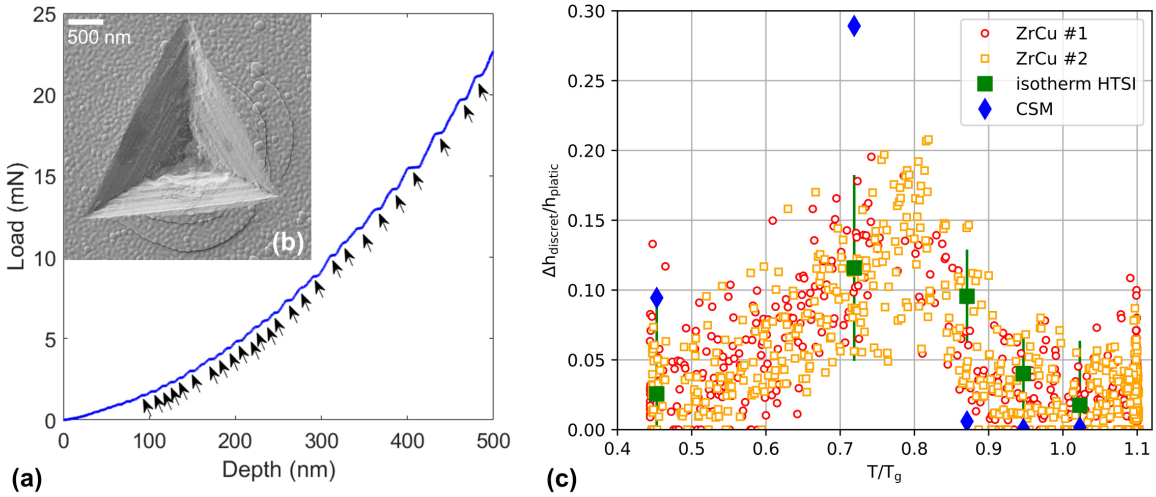

Figure 5.6: Examples of typical serrated flow during indentation of metallic glass (CSM mode at 200°C), with several discrete events indicated by black arrows (a) and resulting emerging shear bands on post-mortem SEM images (b), from [229]. The contribution of these serrations to the total deformation of the ZrCu TFMG indented under different testing conditions (strain rate and temperature) is given in (c). $T_g = 385\,°C$. The strain rate is 0.05/s in the CSM experiments and 2/s in the HTSI measurements.

Before the glass transition, the hardness changes of the two samples are not reproducible. The hardness of sample ZrCu #1 stays constant up to 350 °C before reducing near T_g. On the opposite, sample ZrCu #2 has a hardness that starts to decrease slowly around 230 °C. At 350 °C, its hardness has already been divided by 2/3 compared to RT. Nevertheless, at the glass transition temperature, the drop is quite similar to the one of sample ZrCu #1. The supercooled-liquid behaviors seem to be quite homogeneous while there is some heterogeneity at lower temperatures [244]. It is suspected that since the samples are amorphous, their initial structures differ at the local scale. As nanoindentation is a local probe, those variations may be detected. However, more analyses are needed to confirm those observations.

Brittle to ductile transition Under the glass transition temperature, the bulk metallic glasses present a brittle-to-ductile transition, occurring between 0.7 and 1.1 T_g [7, 146, 239–241]. Such transition could be responsible for the decrease of hardness and increase of strain rate sensitivity between 250 °C (0.79 T_g) and 400 °C (1.02 T_g), observed in figure 5.5. The mechanical properties of the ZrCu thin-film metallic glasses studied here have similar behavior to bulk metallic glass. As the sample thickness (6 µm) is above the characteristic size of the initial shear bands [245], such behavior was expected here.
The brittle-to-ductile transition is also detected through the changes in the serrated plastic flow. As viewed in figure 5.6 a), inhomogeneous plastic flow and discrete plastic events [145, 246–249] can be observed on nanoindentation curves on metallic glass. Such serrations are linked with the activation of shear bands during the deformation [146, 250–252]. Some of those serrations can be detected on post-mortem SEM imprints (see figure 5.6 b)). The contribution of these

serrations to the total plastic deformation can be computed [145, 146, 247] as the sum of the total length of each event ($\Delta h_{discret}$) divided by the final plastic depth ($h_{plastic}$). As presented in figure 5.6 c), this ratio firstly increases from RT (0.45 T_g) up to approximately 250 °C (0.79 T_g) before decreasing when reaching the glass transition temperature. Bell-shaped curves are obtained.

Such behavior can be explained by the competition between two thermally dependent mechanisms [146, 253]. Firstly, as the energy barrier to produce a shear band decreases with increasing temperature, an increase in shear bands contribution to deformation is observed when increasing temperature. At the same time, if the temperature is high enough, the metallic glass behaves more like a fluid: the deformation becomes more homogeneous and the contribution of shear bands to the deformation greatly decreases. So when increasing temperature, the serrations contribution increases with temperature up to 250 °C, where the deformation is still heterogeneous. At higher temperatures, the transition to a more homogeneous deformation mechanism greatly decreases those serrations. This transition in deformation mechanisms is the transition between a brittle-to-ductile behavior of the material. This transition seems to be near 0.8-0.9 T_g here, which is consistent with literature [7, 146, 239–241].

As seen in figure 5.6 c), the strain rate impacts the amplitude and the temperature of the transition. It is clearly visible when comparing results from CSM experiments with HTSI tests during isotherm annealing. The CSM experiments give access to a constant strain rate of 0.05/s while the HTSI tests correspond to tests at 2/s approximately. Let's notice that the HTSI tests do not give access to constant strain rates because of the quarter-sinus loading function used in the indentation test.

In figure 5.6 c), the decrease in strain rates clearly increases the serration contribution to the plastic deformation. It is consistent with literature [146, 239–241]. Such behavior is explained in literature through the dynamic of the formation and propagation of the shear bands. At low strain rates, as the deformation is slow, it is possible to localize and initiate a unique shear band that will grow and accommodate the deformation. This phenomenon allows detecting of a unique strain burst on the indentation curve. Then, with the increase of deformation, a new shear band may be nucleated and propagated, leading to another burst. Here, the sample has time to accommodate the deformation step by step. On the opposite, at high strain rates, the sample does not have time to nucleate and propagate shear bands one by one. As the deformation levels increase quickly, multiple shear bands are nucleated and propagated simultaneously. The sample has a much more homogeneous behavior here [146, 147, 246]. Correlation with post-mortem images was carried out [251, 254].

The impact of temperature and strain rate observed here is consistent with the temperature and strain rate deformation map proposed by Schuh *et al.* [146, 147].

IV.C. Supercooled-liquid state

Once the glass transition temperature is crossed, the hardness of the sample decreases drastically and its strain rate sensitivity increases up to the unit. The sample is in the supercooled-liquid state. Once the glass transition is crossed, the strain rate sensitivity is around 0.2. The material behaves as a non-Newtonian fluid. As its strain rate sensitivity then reaches the unit, it will comport as a Newtonian fluid.

Contrary to the hardness decreases observed before the glass transition, the change of behavior to the supercooled liquid is homogeneous for the two samples: the drop of hardness and the increase of strain rate sensitivity is quite reproducible after T_g. The supercooled-liquid behavior seems less affected by the initial amorphous state of the samples.

Finally, let's focus on the creep behavior of the sample in this regime. Using the Sherby and Amstrong analysis [171], one can obtain information on the activation energy of the mechanism responsible for creep in the supercooled-liquid state.

$$\dot{\varepsilon}_r = B \exp\left(-\frac{Q}{RT}\right) \sigma^{1/m} \tag{5.2}$$

To determine the mechanism allowing the accommodation of plastic deformation during the indentation creep segment in the supercooled-liquid region, one should study the activation energy of this phenomenon. When investigating this property between T_g and T_X, one gets an activation energy of 150±30kJ/mol or 1.6±0.3eV [229]. It is close to what is obtained by Faupel *et al.* [255] for the activation energy of the diffusion of copper atoms in ZrNi metallic glasses. Moreover, it is of the order of magnitude of the activation energy of the relaxation process linked with the diffusion of the smallest atom in a metallic glass [244, 256].

IV.D. Crystallization

Detection of crystallization Crystallization of the sample is caught through the huge increase of hardness and decrease of strain rate sensitivity observed near 430 °C. It is also extremely visible on the load-displacement curves (see figure 5.7). It can be clearly detected here that during the supercooled-liquid state, the maximum depth increases with temperature. The depth increases a lot during the creep segment of 0.1s. Moreover, adhesion is quite high in this regime and increases with temperature [257]. And suddenly, the maximum depth decreases with increasing temperature, creep and adhesion are greatly reduced. Here, the change of physical state happens quite abruptly.

Focusing on the crystallization stage in figure 5.3, this phenomenon seems to occur in two regimes. Firstly, at the end of heating, the huge increase in hardness [231] marks the first stage of crystallization. Then, during holding at the maximum temperature, hardness still increases slowly, going from 2 GPa to 3.8 GPa. At the same time, the strain rate sensitivity decreases abruptly back to 0.2: the material losses the Newtonian behavior. It next decreases slowly during the holding in temperature. Such modification in flow behavior was observed by Gravier *et al.* [258]. They show that partial crystallization decreases atomic mobility. It also increases the Newtonian viscosity and promotes the non-Newtonian regime in viscoplastic deformation. It seems that at the end of heating, the strain rate sensitivity and the hardness stay constant before changing slowly during the holding. This may be the sign that crystallization is detected near 430 °C, stopped shortly after the first phase, and then slowly restarts and continues during

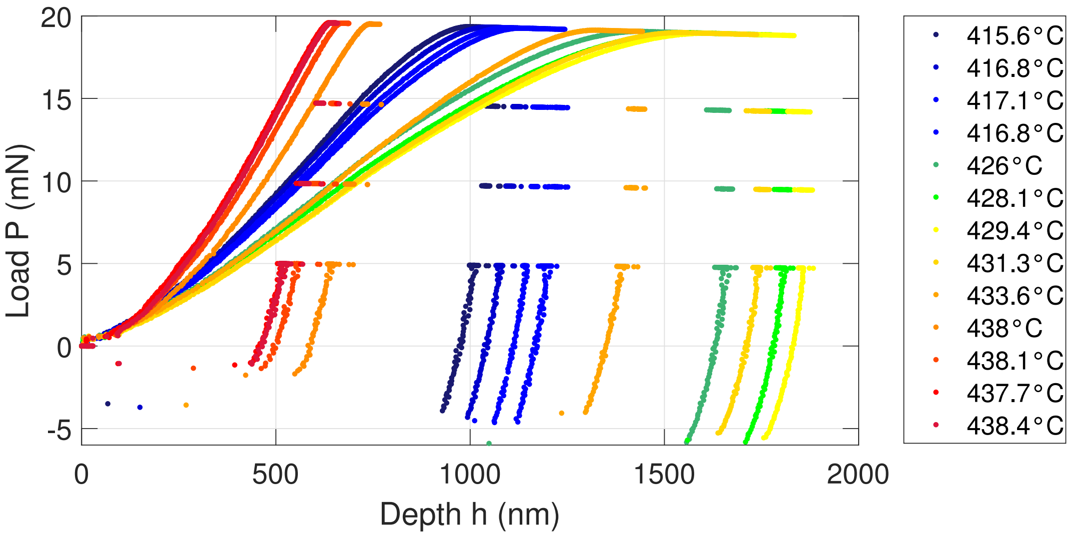

Figure 5.7: Load-displacement curves on ZrCu TFMG near the temperature of crystallization.

the holding.

As presented in the table 5.2, the recrystallized temperature is measured to be near 425-430 °C. For comparison, the DSC measurement at 3 °C/min gives an onset of crystallization at 407 °C. Such a difference can be explained by the nature of the indentation testing. First, nanoindentation tests give a mean value of the properties, detected on a testing volume of a few μm^3. As at the beginning of the crystallization, nuclei and small grains are not numerous inside the supercooled-liquid matrix, the indentation test may not be sensitive enough to detect them. Moreover, nanoindentation is a local probe. As crystallization is a heterogeneous phenomenon, it is not certain that the testing zone is the one where crystallization starts. All of this may explain the differences measured here.

Post-mortem structure Post-mortem XRD was performed on the samples (see figure 5.8). As revealed by the diffractogram, the sample is roughly 80% crystallized after a whole thermal cycle. As expected for the material, the body-centered orthorhombic (bco) $Cu_{10}Zr_7$ and tetragonal (t) Zr_2Cu phases are detected here. However, there are also traces of the cubic (c) ZrCu phase. Thermodynamically, bco-$Cu_{10}Zr_7$ and t-Zr_2Cu are the two phases stable at 450 °C [237, 259, 260]. Nevertheless, the c-ZrCu is stable at temperatures higher than 730 °C: it is metastable here and it would be assumed to decompose back to bco-$Cu_{10}Zr_7$ and t-Zr_2Cu during cooling [261]. Nonetheless, Yamamoto *et al.* [262] show evidence of the presence of the metastable c-ZrCu phase in a ZrCu metallic glass if rapidly heated and quenched at those working temperatures. This metastable phase is also presented in the metallic glass if it exhibits a slow diffusion rate and high viscosity. It was also observed by Cullinan *et al.* [157] during linear heating (10 °C/min) of $Zr_{50}Cu_{50}$.

Crystallized fraction To understand better the crystallization behavior of those glasses during the applied thermal cycle, the crystallized fraction is computed from the hardness measurements.

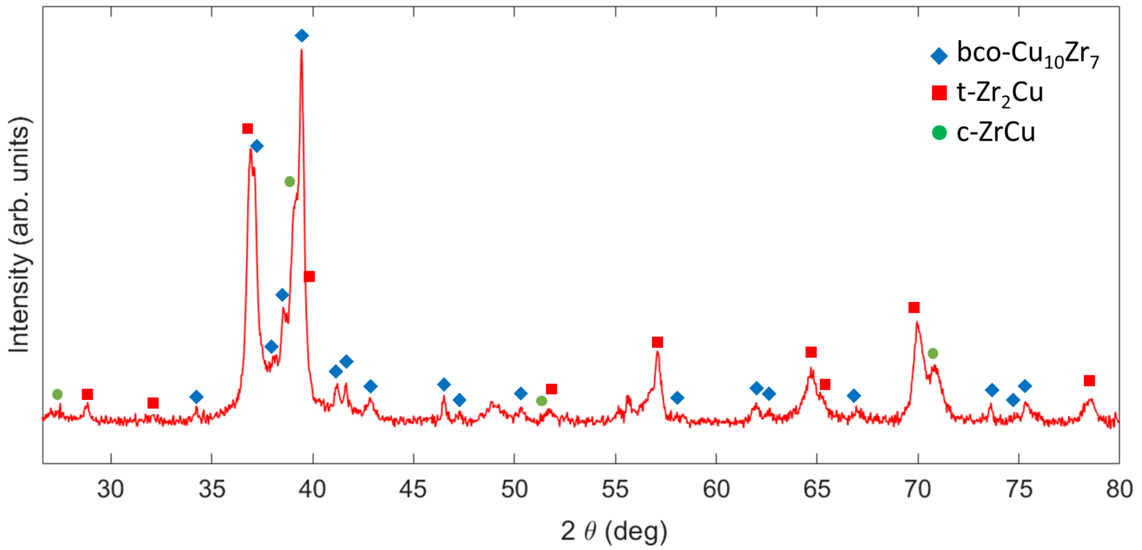

Figure 5.8: Post-mortem XRD diffractogram of partially crystallized ZrCu thin films, showing evidence of body-centered orthorhombic $Cu_{10}Zr_7$, tetragonal Zr_2Cu, and cubic ZrCu phases, form [229]. The crystallization fraction is approximately 80%.

Assuming an iso-strain hypothesis during the indentation of the ZrCu TFMG, a mixture law describes the hardness of a system composed of the supercooled-liquid matrix and crystallites.

$$H = XH_X + (1-X)H_A \tag{5.3}$$

with X the crystallized fraction, H_X the hardness of the fully crystalline sample and H_A the hardness of the amorphous liquid. The crystalline fraction is then:

$$X = \frac{H - H_A}{H_X - H_A} \tag{5.4}$$

H_X and H_A are temperature-dependent. To compute the crystallized fraction, one should correctly determine their changes with temperature. As observed in figure 5.3, the hardness of the amorphous phase depends a lot on the temperature in the supercooled-liquid region. This hardness is fitted following an Arrhenius law (dot line on figure 5.3): it will give the expected value of H_A on the interesting temperature scale.

On the other side, the hardness of the sample is roughly constant during cooling: the hardness of the crystalline phase should not vary in the studied temperature scale. As the measured value indicates a sample crystallized at %80, one can compute H_X using equation 5.3. The obtained value for H_X is approximately 4.5 GPa.

Having evaluated the laws of H_A and H_X, one can now calculate the crystallized fraction during the end of heating and the holding at 450 °C. As XRD tests were conducted to get a similar heating rate, a comparison between both results is presented in figure 5.9. As expected, the crystallized fraction increases rapidly during the heating phase, from 0 to approximately 40%.

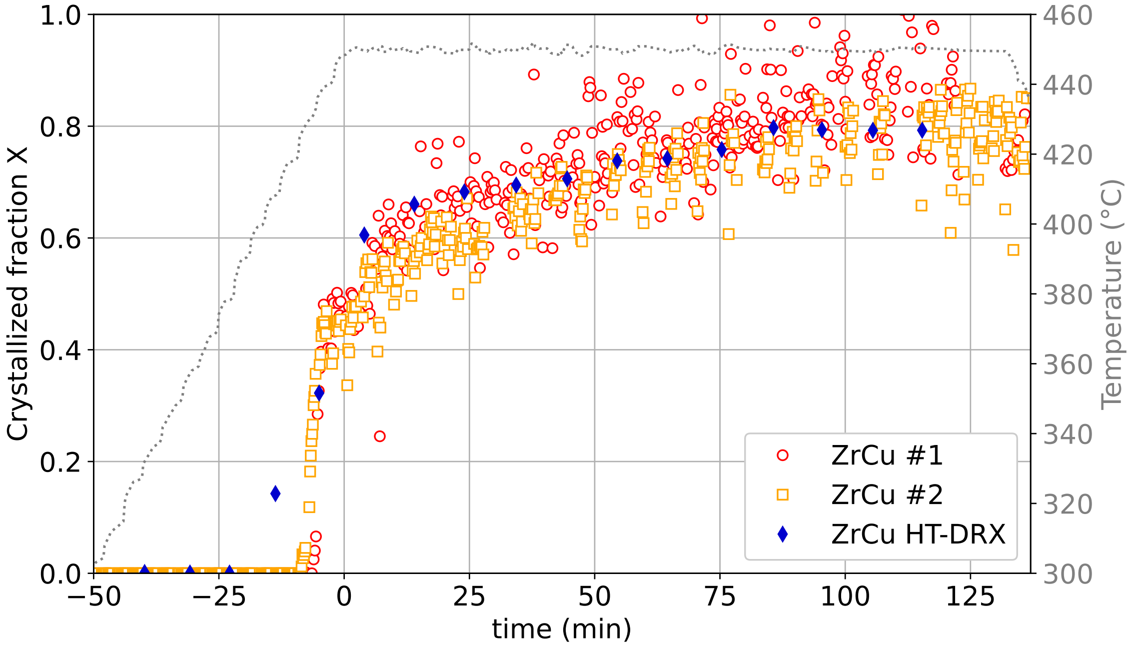

Figure 5.9: Crystallized fraction determined from HTSI and HT-XRD measurements on ZrCu TFMG. The corresponding temperature versus time curve is in gray. The time $t = 0$ min is here defined as the beginning of the holding at 450 °C.

Moreover, during the holding at 450 °C, the fraction still increases up to 80%, but the changes are slower. The huge number of data points of the HTSI method allows detecting of these two phases in the crystallization process. This is an advantage of this technique.

Besides, the indentation and HT-XRD results compare nicely during holding. Nevertheless, a huge difference is observed in the first stage of crystallization. According to the HT-XRD data, the beginning of crystallization is detected roughly at 400 °C. At this temperature, the HTSI data do not catch any signs of crystallization yet. This is consistent with what is monitored when comparing outcomes with DSC experiments. The HTSI method does not give access to the information at the beginning of the crystallization here.

The two phases in the crystallization, observed through the HTSI measurements, are not that clear on the HT-XRD results in figure 5.9. One could say that the change in the slope comes from the transition from anisotherm measurements to isotherm ones. However, it is not the case. As presented in the HT-XRD diffractograms of figure 5.10, there are two phases in the crystallization. Firstly, as viewed in the zoomed picture, one can notice the apparition of two peaks between t = -13 min and t = 5 min, corresponding to the formation of three phases bco-$Cu_{10}Zr_7$, t-Zr_2Cu and c-ZrCu. Then, during the holding, there is a decrease of the peak of c-ZrCu and an increase of those of bco-$Cu_{10}Zr_7$ and t-Zr_2Cu. The metastable c-ZrCu that is crystallized with bco-$Cu_{10}Zr_7$ and t-Zr_2Cu during the first crystallization step is thus consumed to form both bco-$Cu_{10}Zr_7$ and t-Zr_2Cu. At the same time, the amorphous hump is observed to decrease: the crystallization of the amorphous structure continues. Two phenomena are present

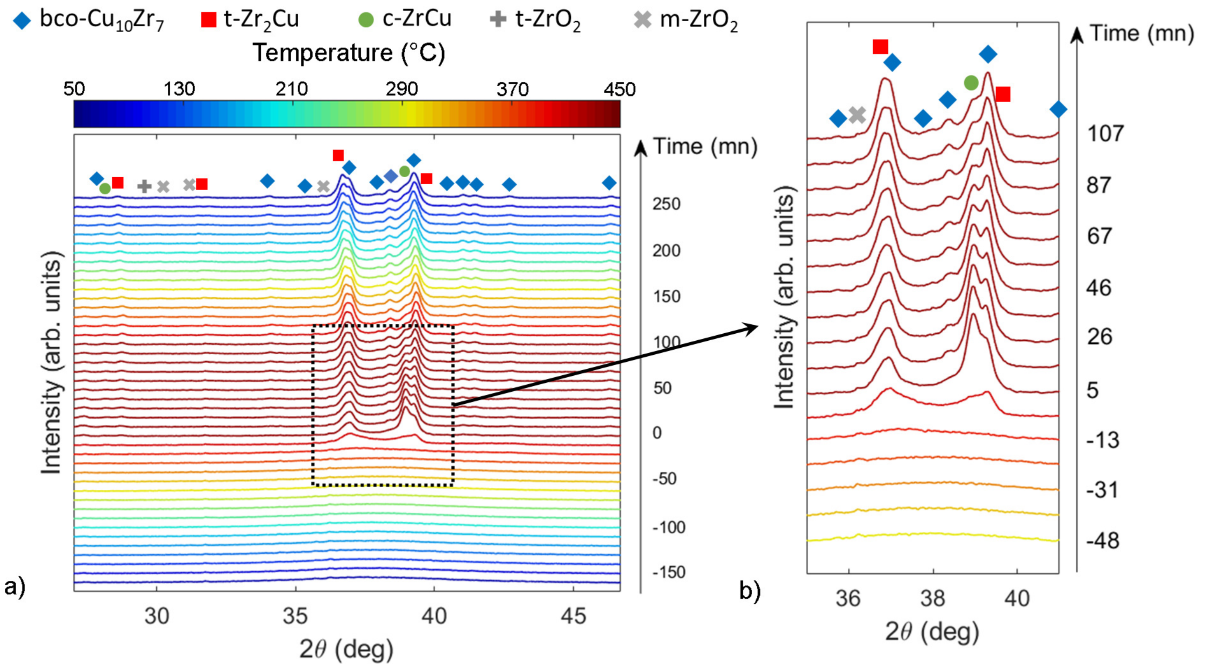

Figure 5.10: HT-XRD diffractograms of ZrCu coatings measured during an entire thermal cycle (a) with the color scale corresponding to the temperature, from [229]. The diffractograms are shifted along the y-axis according to the testing time, with time = 0 for the beginning of the 2 h plateau at 450 °C. A zoomed-in version of the diffractograms during the crystallization process (end of the heating ramp and plateau) is given in (b).

during this step: crystallization of the amorphous structure and decomposition of the metastable crystallized phase c-ZrCu in favor of bco-$Cu_{10}Zr_7$ and t-Zr_2Cu, the two thermodynamically stable phases at this temperature. Cullinan *et al.* [157] monitor a similar behavior on $Zr_{50}Cu_{50}$. During annealing for 80 min at 400 °C, they relate the increase of the crystallized fraction with the formation of $Cu_{10}Zr_7$, $CuZr_2$, and CuZr. Moreover, during heating at 10 °C/min after that, CuZr decomposed in favor of $Cu_{10}Zr_7$ and $CuZr_2$, until reaching 727 °C, where ZrCu becomes the thermodynamically stable phase [157, 259].

V. Crystallization kinetics during holding at maximum temperature

To focus more on the crystallization phenomenon, other experiments were carried out. The idea is to quickly heat the sample quickly 350 °C (at 15 °C/min) and then focus on the heating at 3 °C/min up to a maximum temperature, prior to a 5 h holding at this temperature. The samples ZrCu #3, #4, #5 and #6 were submitted to the thermal cycle presented in figure 5.11. In the following, time $t = 0$ min will always refer to the beginning of the annealing at the maximum temperature.

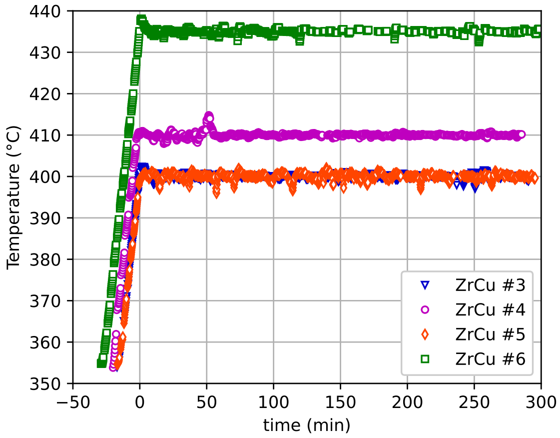

Figure 5.11: Thermal cycle applied on samples #3, #4, #5 and #6. Time $t = 0$ min is defined as the beginning of holding at the maximum temperature.

V.A. Results

ZrCu #3 Let's first focus on the hardness and strain rate sensitivity of sample ZrCu #3, presented in figure 5.12.

At the end of heating, as expected, the hardness decreases from 2.5 GPa at 350 °C to 1.3 GPa at 400 °C. At the same time, the strain rate sensitivity increases from 0.1 to 0.3. During the holding at the maximum temperature, hardness starts by oscillating between 1.2 and 1.6 GPa until 150 min of annealing. Then, the oscillations continue but the amplitude greatly increases, with a maximum value achieving 4.0 GPa and the lower value slowly increasing from 1.5 GPa to 2.0 GPa at the end of the annealing phase. During the first 150 min of the annealing, the strain rate sensitivity stays more or less constant around 0.25-0.3 with an important scattering of the data. And after 150 min, it starts oscillating with the same period as the hardness (approximately 25 min). Moreover, the minimum in hardness corresponds to the maximum in strain rate sensitivity. Finally, its values also decrease to values between 0.03 and 0.2 at the end of the studied thermal cycle.

As observed on samples ZrCu #1 and #2, the increase of hardness and decrease of strain rate sensitivity is expected to be linked with the crystallization of the sample.

ZrCu #4 Let's then study hardness and strain rate sensitivity of sample ZrCu #4, heated at 410 °C, presented in figure 5.13.

As the temperature of annealing is higher than the one of ZrCu #3, the crystallization is expected to happen sooner during the annealing. In figure 5.13, at the end of heating, the hardness decreases from 3.5 GPa at 350 °C to 2 GPa at 410 °C. Those values are quite high compared to what was obtained on the other samples at this temperature. At the same time, the strain rate sensitivity increases from 0.05 to 0.2 in the same temperature range. Once again, it is low compared to the other samples. Then, during the annealing, the hardness never goes to values lower than 1.8 GPa. It linearly increases from 1.8-2.0 GPa to 2.5 GPa after 5 h of

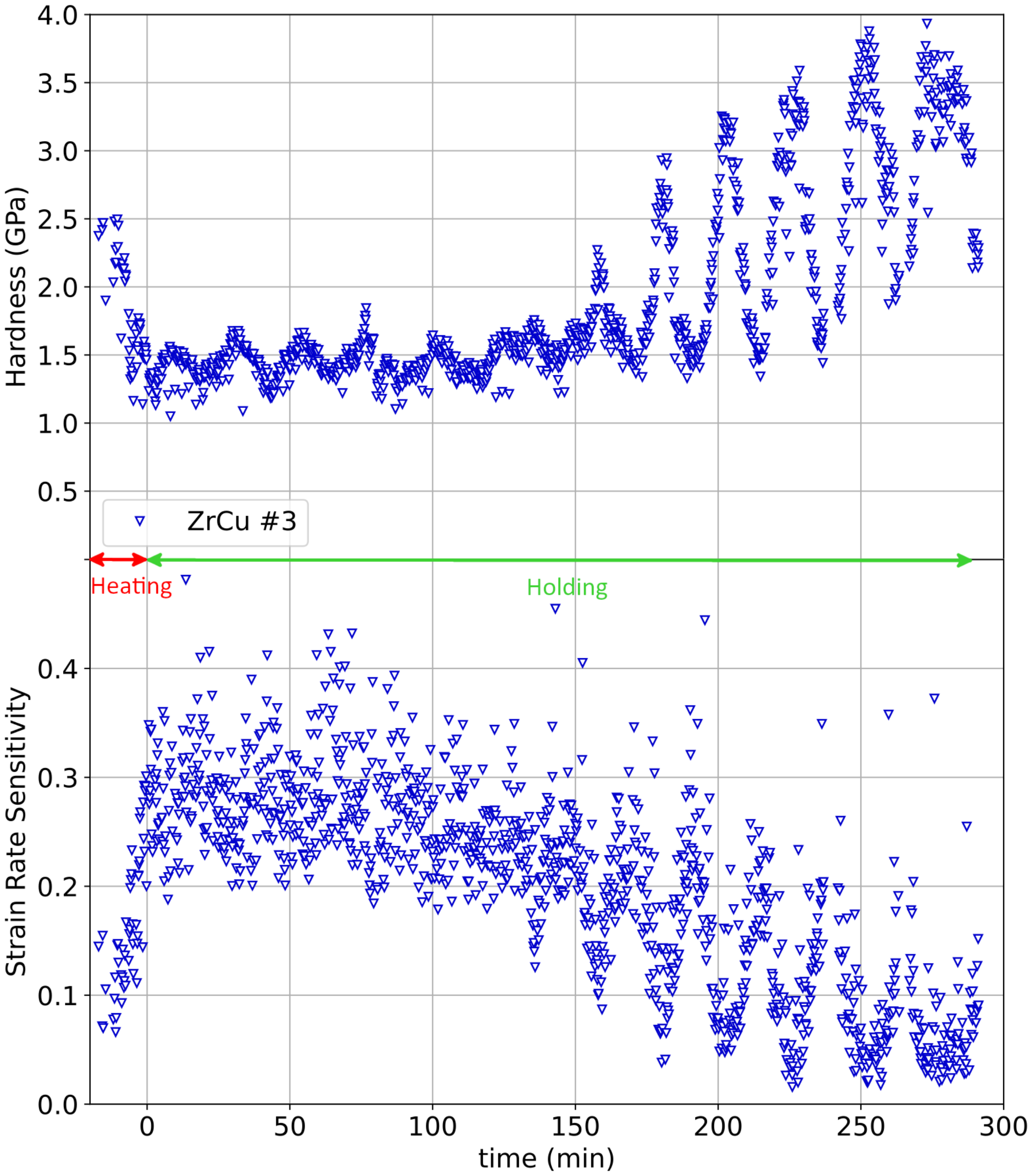

Figure 5.12: Hardness and strain rate sensitivity against time of sample ZrCu #3, during heating at 3 °C/min from 350 °C to 400 °C prior to 5 h annealing at 400 °C.

annealing. Moreover, during this phase, the strain rate sensitivity quickly decreases from 0.2 to 0.05 before staying stable until the end of the tests.

ZrCu #5 Let's now focus on sample ZrCu #5 and its hardness and strain rate sensitivity presented in figure 5.14. The annealing temperature (400 °C) was decided during the heating at 3 °C/min when a hardness value lower than 1.0 GPa was measured.

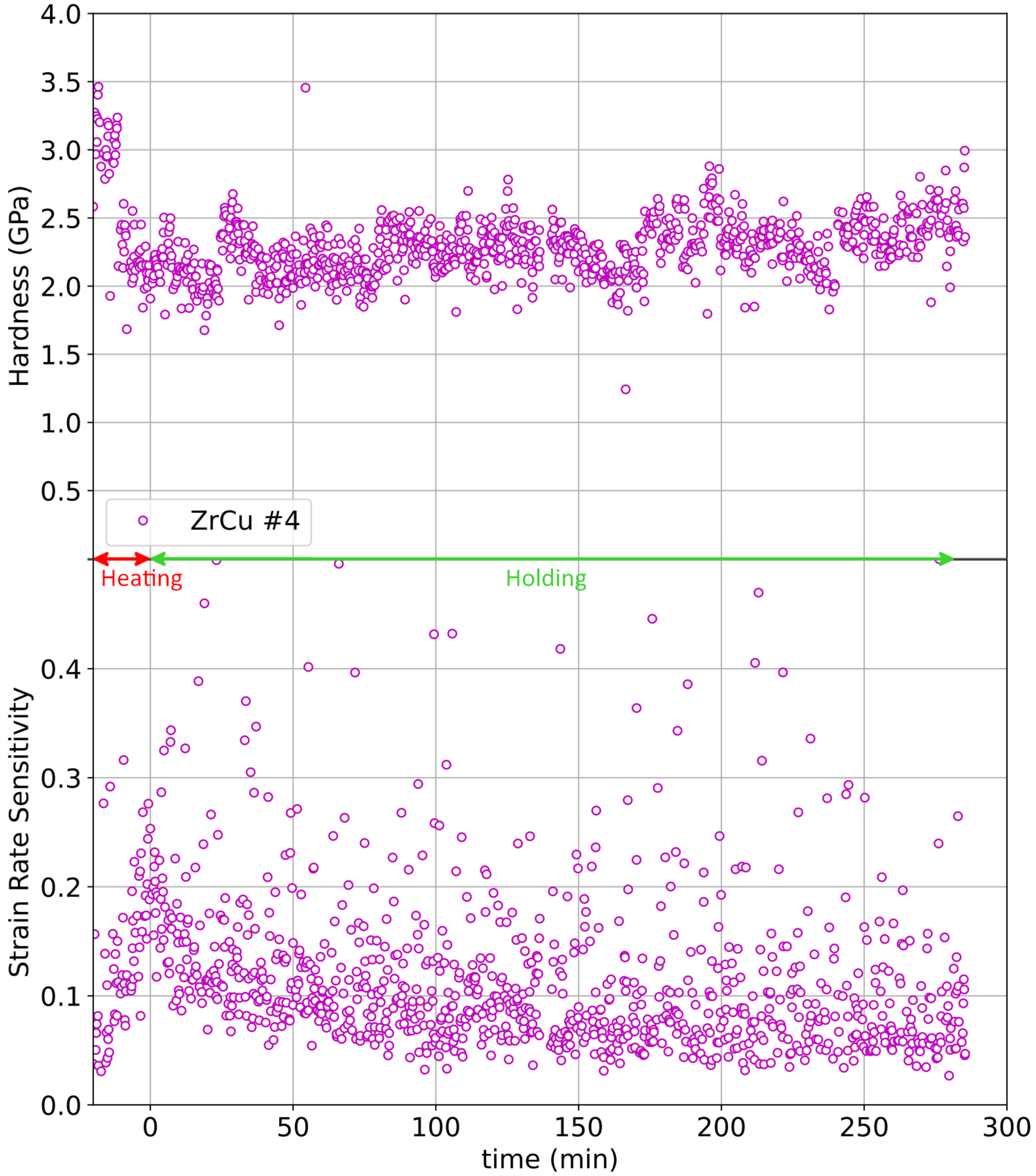

Figure 5.13: Hardness and strain rate sensitivity against time of sample ZrCu #4 during heating at 3 °C/min from 350 °C to 410 °C prior to 5 h annealing at 410 °C.

In figure 5.14, at the end of heating, the hardness decreases from 2.5 GPa at 350 °C to 0.7 GPa at 400 °C. At the same time, the strain rate sensitivity increases from 0.05 to near 0.5. At the beginning of holding, the hardness stays approximately constant for 10 min, before increasing rapidly to 2.0 GPa. A more or less constant value is then maintained for a few minutes before a second rapid increase (to 3.0 GPa at 50 min annealing) and then a slow increase up to 4.0 GPa takes place until the end of the annealing. Concerning the strain rate sensitivity, during the

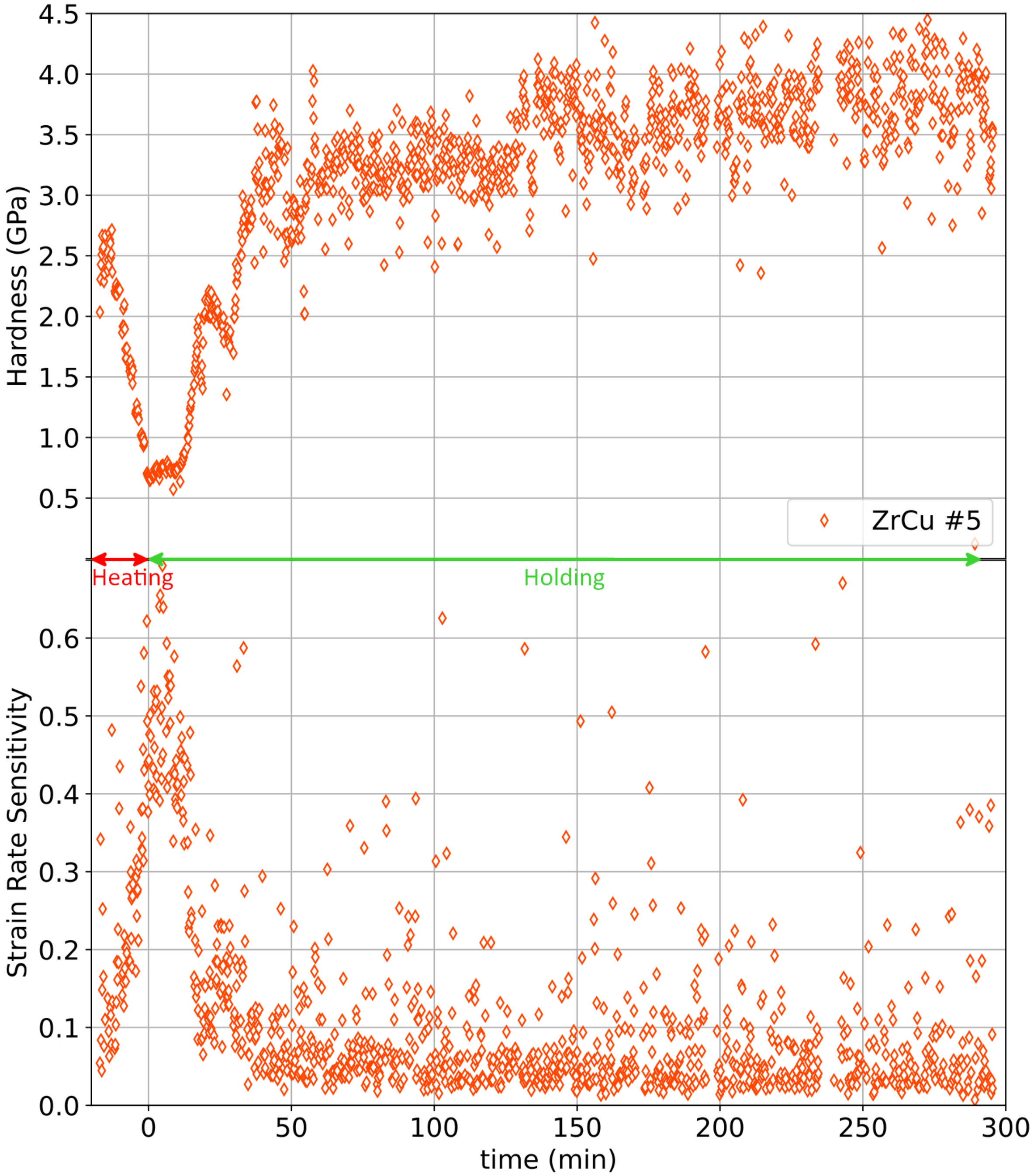

Figure 5.14: Hardness and strain rate sensitivity against time of sample ZrCu #5, 3 °C/min from 350 °C to 400 °C prior to 5 h annealing at 400 °C.

first 10 min of annealing, strain rate sensitivity values are quite scattered between 0.4 and 0.6. Then, with the huge increase in hardness, a huge drop in strain rate sensitivity is observed (down to approximately 0.15). The strain rate sensitivity slowly decreases to 0.05 until 50 min of annealing. During the last slow hardness-increasing phase, the strain rate sensitivity stays constant. The changes of hardness and strain rate sensitivity examined here remind clearly what is monitored on samples ZrCu #1 and #2.

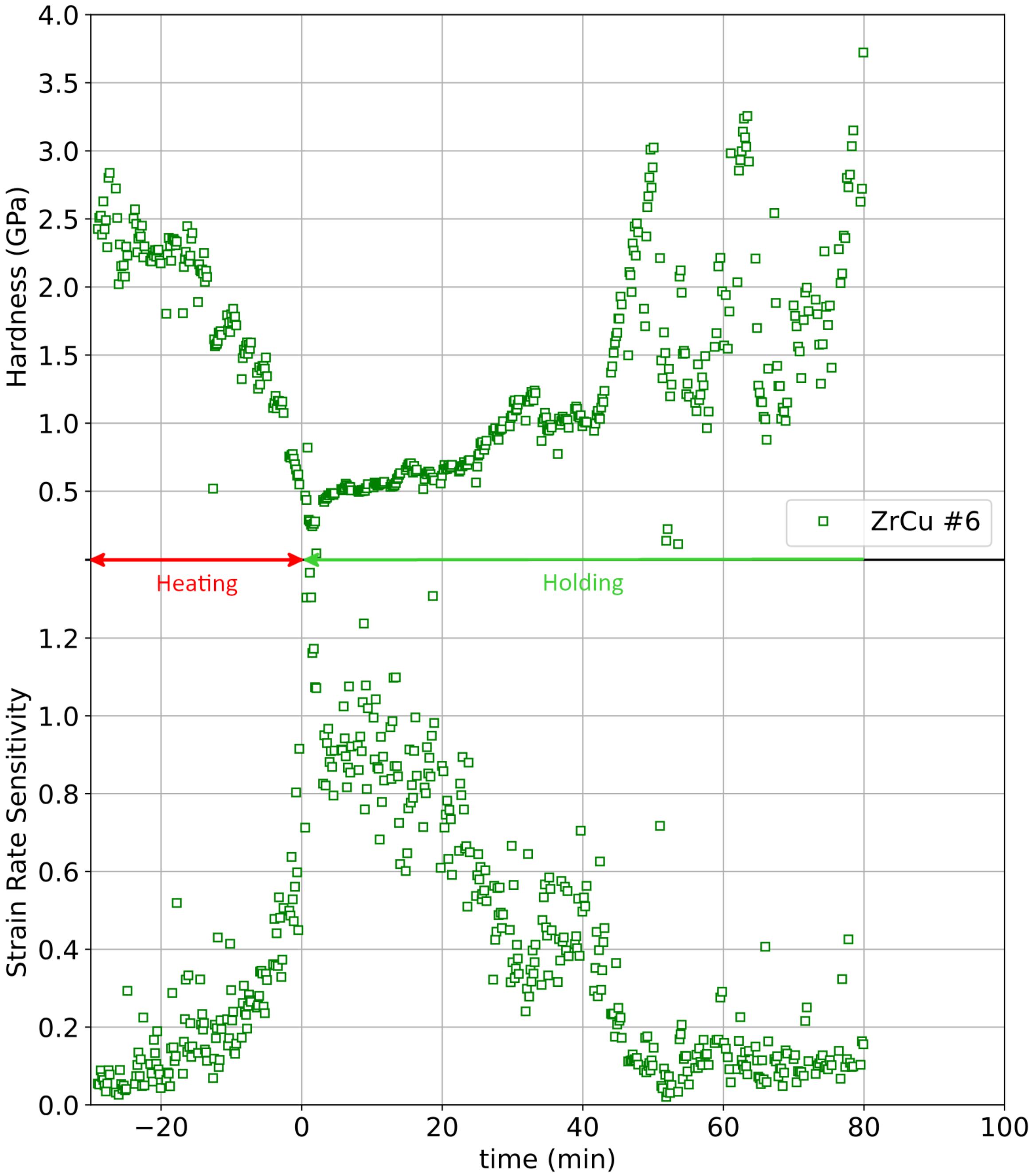

Figure 5.15: Hardness and strain rate sensitivity against time of sample ZrCu #6 , 3 °C/min from 350 °C to 435 °C prior to 5 h annealing at 435 °C.

ZrCu #6 Finally, let's focus on the hardness and strain rate sensitivity of sample ZrCu #6, presented in figure 5.15. The annealing temperature (435 °C) was once again decided during the heating at 3 °C/min when a hardness value lower than 1.0 GPa was measured. Unfortunately, the sapphire tip breaks after 80 min of annealing, so only the beginning of the thermal cycle can be analyzed.

As samples ZrCu #3 and #5, hardness at 350 °C is around 2.5 GPa. However, near 400 °C, the

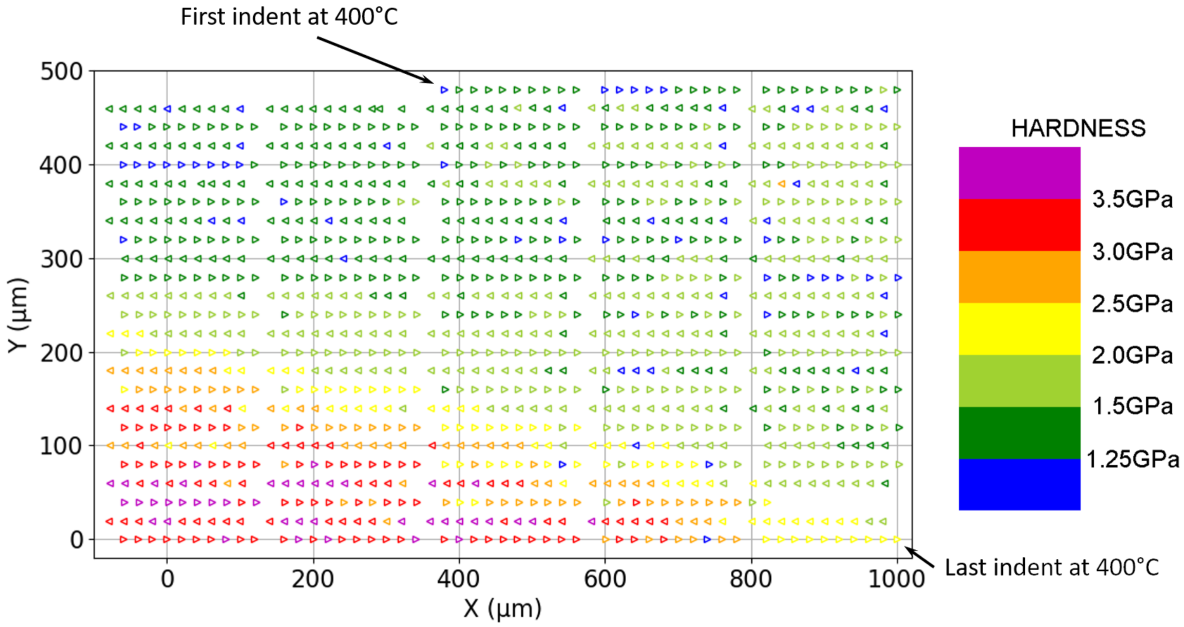

Figure 5.16: Hardness variations on the sample during the annealing at 400 °C of sample ZrCu #3. Time flows from the first indent, following the arrows. The color indicates the measured hardness. The position (x=0, y=0) represents the theoretical center of the sample.

hardness was near 2.0 GPa on this sample while it was much lower on the two other samples. Then, near 435 °C, the hardness has fallen down to 0.3 GPa. At the same time, the strain rate sensitivity greatly increases, passing from 0.05 to 0.6 at the end of heating. At the beginning of holding at the maximum temperature, the hardness increases quickly to 0.5 GPa and slowly increases to 1.0 GPa in 40 min. Then huge oscillations can be observed on hardness, between 1.0 GPa and 3.0 GPa. The strain rate sensitivity, which presents really high values at the beginning of the holding (near 1) decreases linearly for 50 min (back to 0.05) before staying quite constant until the tip breaks.

The different samples present really different behaviors. Within the next paragraph, several explanations will be given to explain such differences.

V.B. Local heterogeneities on a given sample

ZrCu #3 On this sample, important oscillations are measured on hardness and strain rate sensitivity. Such behavior is quite surprising at first but can be explained by plotting the spatial hardness values (see figure 5.16). In this figure, the indents are plotted at their (x,y) positions on the sample and the color indicates the measured hardness values. The first indent corresponds to the first indent performed during the annealing at 400 °C. The time then flows following the arrows. All the indents on one line take approximately 10 to 15 minutes to be carried out. Let's consider the two lines at y = 80 and 100 µm. Starting from x = 1000 µm, the hardness slowly increases from values near 1.3 GPa to values of 3.2 GPa at the end of the line. Taking the following line, hardness decreases back from 3.2 °C to 1.7 °C. Such changes explain the oscillations on the hardness against time previously observed. As the sample crystallization is

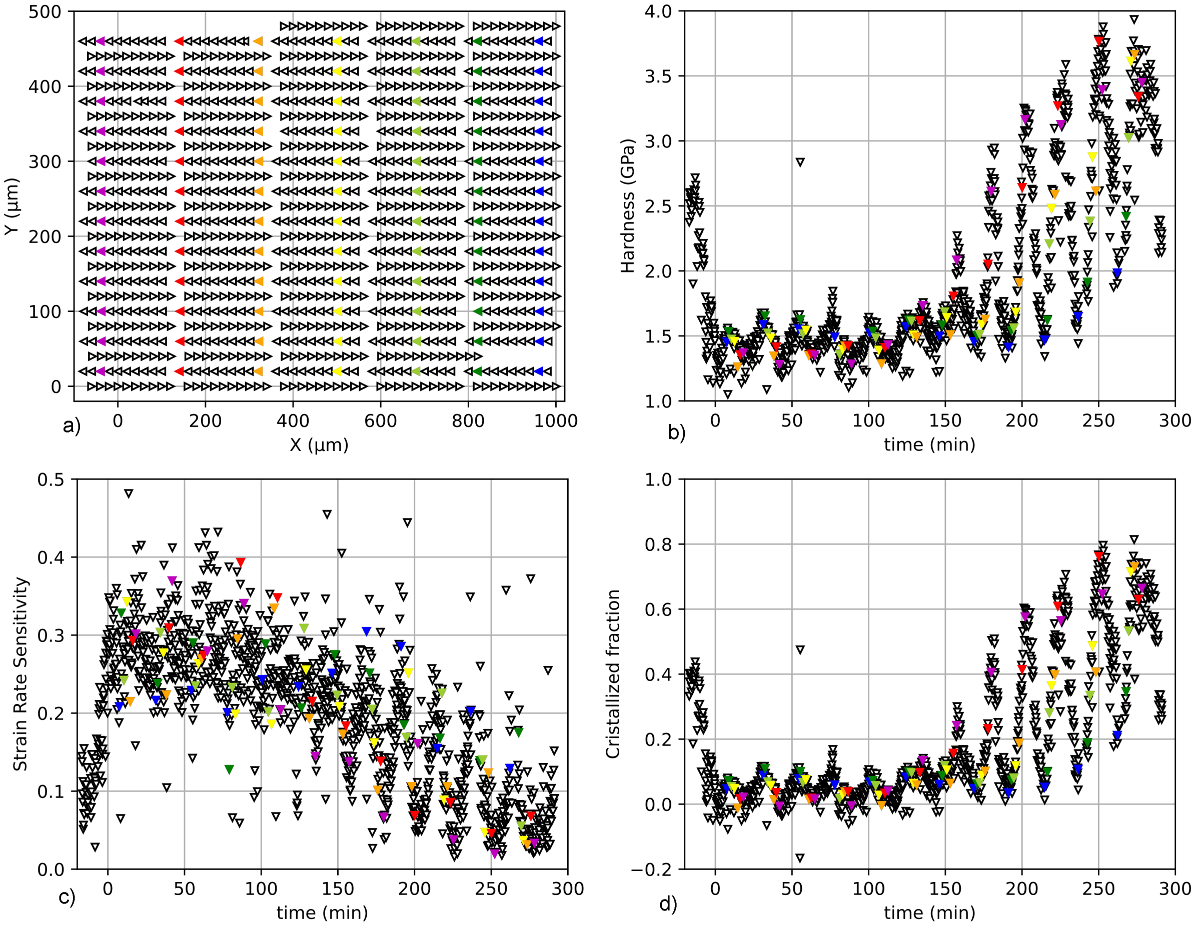

Figure 5.17: (a) Highlight of a few columns on the sample. (b) Hardness, (c) strain rate sensitivity, and (d) crystallized fraction against time of sample ZrCu #3. The local heterogeneity of the sample is clearly seen if observing the changes in those properties.

detected by the high increase in hardness, the heterogeneity of this phenomenon is clearly seen here.

To better understand the phenomena, columns have been highlighted by colors in figure 5.17 a). Tendencies can be observed. First, at the beginning of the holding (before 150 min), the region in red always has a hardness value lower than 1.5 GPa while in the blue ones, it stays higher than that (figure 5.17 b)). This difference in behavior is also observed in the strain rate sensitivity (figure 5.17 c)). The red regions have high strain rate sensitivity when the blue ones stay under 0.25 during the beginning of the annealing ($t < 100$ min). Then, the strain rate sensitivity of the red point decreases and its hardness increases. For the blue ones stay, m stays high before decreasing ($t > 200$ min). Seeing these observations and the behavior of the other samples, it is clear that crystallization depends on some local conditions. It looks like a local zone on the sample need to go to a "liquid enough" state to crystallize. In a certain way, it seems that to observe crystallization in the present conditions, the sample should locally reach a given state.

A simple temperature-dependent Arrhenius law is not enough to describe the local hardness variations of the amorphous state. A constant value of 1.3 GPa was chosen for H_A to compute

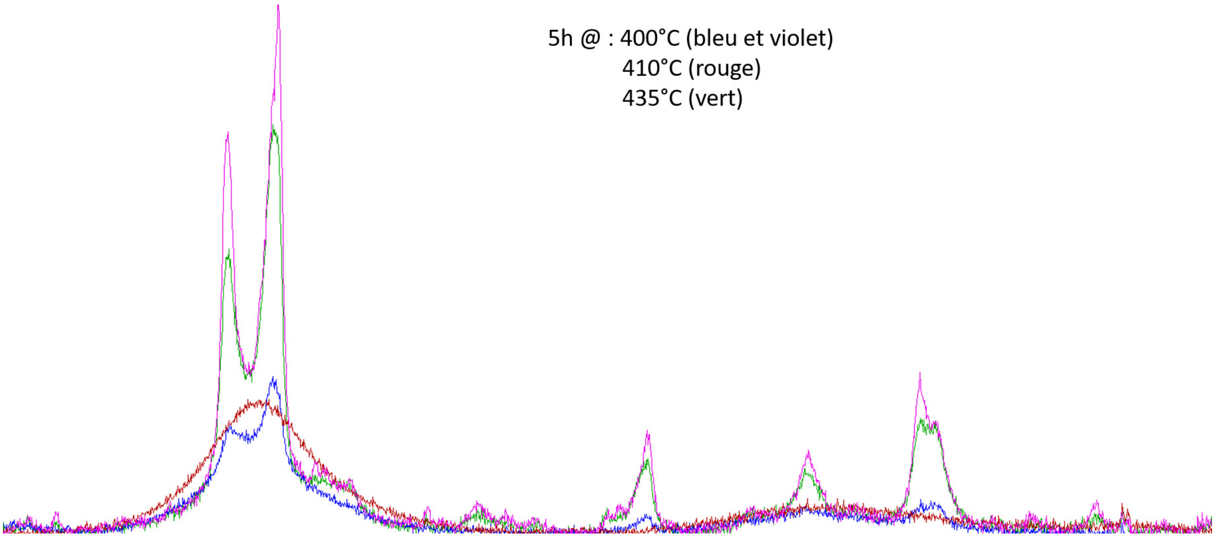

Figure 5.18: Post-mortem diffractogram from XRD measurements on samples ZrCu #3 (blue), #4 (red), #5 (purple) and #6 (green).

the crystallized fraction (figure 5.17 d)). However, this leads to the conclusion that some crystallization would take place in the first minutes of annealing, which is greatly unlikely, regarding the hardness and strain rate sensitivity values.

According to post-mortem XRD measurements, the sample is crystallized at 19% (see table 5.3). By considering the mean value measured by HTSI at the end of the cycle, it would be 40%. Localization of crystallization is clearly observed here. And the indentation tests give local characterization of the specimen while global information on the sample comes from XRD measurements. Better understanding and modeling are required to analyze deeper those results.

V.C. Comparison between samples

ZrCu #4 This sample has a really different behavior compared to the other ones, tested in similar conditions. As it was heated up to 410 °C, it was expected to crystallize with a quicker kinetic compared to samples ZrCu #3 and #5. However, the hardness and strain rate sensitivity values indicate that nothing is detected. Contrary to sample ZrCu #3, hardness always stays high and strain rate sensitivity is globally under 0.25. The values of 1.5 GPa and 0.25 that

Table 5.3: Post-mortem composition of samples after the different HTSI tests. The crystallized fraction is estimated at ± 5%.

Sample	Crystallized fraction (%)	ZrCu	Zr_2Cu	$Cu_{10}Zr_7$
#1	77	present (majority)	present	present
#3	19	present (majority)	not detected	present
#4	0	-	-	-
#5	64	present (majority)	present	present
#6	59	present (majority)	present	present

Table 5.4: Reminder of the hardness and strain rate sensitivity measured at the beginning of the holding phase, on the ZrCu samples.

Sample	$T_{holding}$ (°C)	$H(t = 0\,\text{min})$ (GPa)	$m(t = 0\,\text{min})$
#3	400	1.2-1.5	0.2-0.3
#4	410	2.0-2.5	0.15-0.25
#5	400	0.7	0.4-0.6
#6	435	0.5	1

separated the red and blue points in sample ZrCu #3 are not reached here. Post-mortem XRD characterization confirms that no crystallization happens on this sample (see figure 5.18 and table 5.3), contrary to sample ZrCu #3. The amorphous hump is clearly visible and no characteristic peaks are present on sample #4.

If comparing those hardness values with the one of sample ZrCu #1, it seems that the glass transition of this sample was not reached during the thermal cycle. According to [231], hardness is expected to increase slowly under T_g because of structural relaxation. As the sample was heated up at 15 °C/min from RT to 350 °C before being heated at 3 °C/min at a higher temperature, an increase of T_g is anticipated, compared to ZrCu #1. But with the observations made on sample #3 and DSC measurements, it was assumed to be lower than 400 °C.

Those variations may come from the different amorphous initial states between the samples, which still need to be understood since both samples were obtained from the same deposition batch.

ZrCu #5 This sample was submitted to the same cycle that sample ZrCu #3. However, their behavior clearly differs. Lower hardness value and high strain rate sensitivity are reached at 400 °C here, contrary to sample ZrCu #3. Nevertheless, the hardness and strain rate changes remind a lot of the ones of samples #1 and #2 during the crystallization process. The crystallization process is expected to follow the one proposed for those samples.

According to post-mortem XRD measurement, this sample is crystallized at 65% at the end of the indentation cycle, less than sample ZrCu #1 and #2. Same as for sample #3, if observing the HTSI crystallization results only, the sample seems to be crystallized at 80% (see figure 5.19). Localization of crystallization may explain the difference between the indentation and XRD results. Moreover, as noted on figure 5.18 and table 5.3, bco-$Cu_{10}Zr_7$, t-Zr_2Cu and c-ZrCu are present in the sample. Both bco-$Cu_{10}Zr_7$, t-Zr_2Cu are detected but appears to be in low proportion compared to c-ZrCu.

Differences are also observed with sample #3, while submitted to the same thermal cycle. In figure 5.18 the peaks of the phases clearly differ. And on the table 5.3, the final crystallized fraction is three times less on sample #3. Same as for sample ZrCu #4, the differences obtained on two samples submitted to the same thermal cycle might originate from different initial amorphous structure, which would impact the following measurements. More studies are required to understand better those observations.

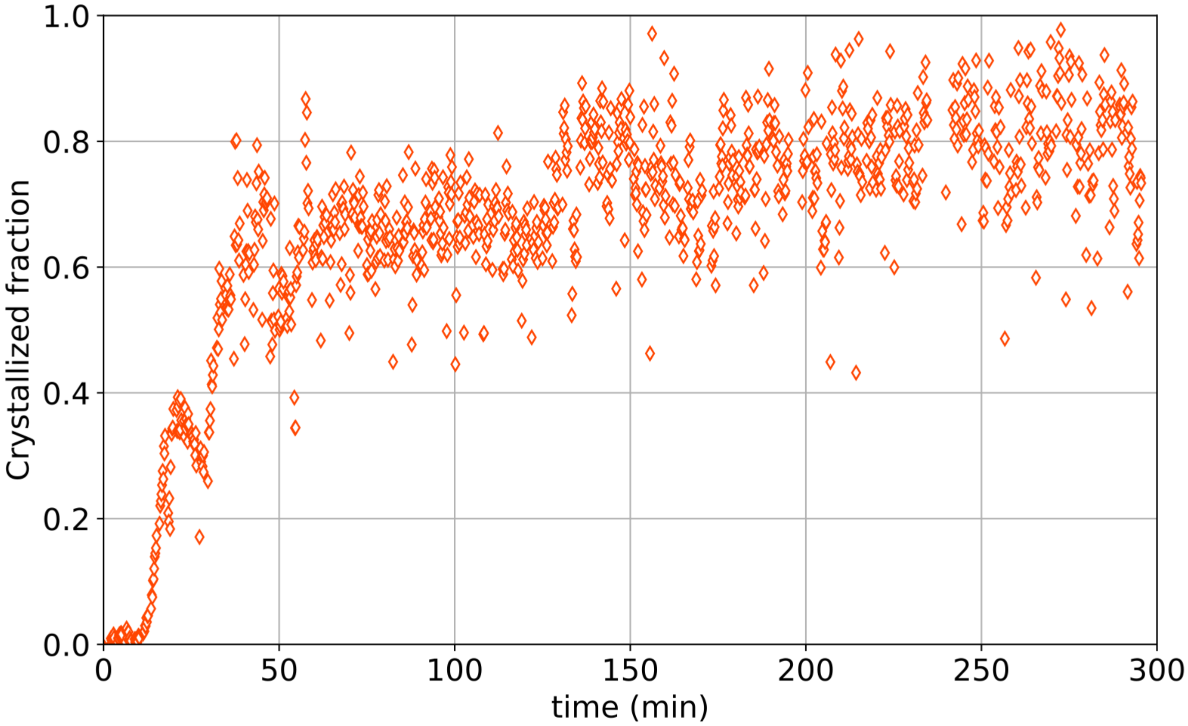

Figure 5.19: Crystallized fraction of sample ZrCu #5.

ZrCu #6 Contrary to sample #5, the low hardness value (under 1.0 GPa) was not detected at 400 °C but at a higher temperature (435 °C). Seen the low hardness and high strain rate value measured here, it is expected that the sample would be crystallized. The first increase of hardness with the decrease of strain rate sensitivity is assumed to be the beginning of this crystallization. The oscillations coming next are likely to be the sign of local crystallization, as observed on sample #3.

As sample #6 was heated at 15 °C/min up to 350 °C, it is normal that its crystallization temperature is higher than the one of samples #1 and #2. However, it behaves differently compared to samples #3 and #5, which were also submitted to this heating rate.

Seen the crystallized fraction of the samples and the proportion of bco-$Cu_{10}Zr_7$, t-Zr_2Cu and c-ZrCu, the crystallization process and the competition between the phases are far to be easily interpreted. The observed variations are not easy to understand but it seems that the local heterogeneity in the samples are a key point to address these issues.

VI. Conclusions of the chapter

The High-Temperature Scanning Indentation method presents a high interest to study changes in metallic glasses. Applying such methodology enables accessing to the variations of the mechanical properties along a whole temperature scale through 1-day experiments. Using a few numbers of well-designed HTSI tests allows focusing on specific behavior to understand better what is observed.

By using this technique on ZrCu-based thin-film metallic glasses, it is possible to monitor the physical transformations in the samples. Here, the modifications of the hardness and the strain rate sensitivity with temperature give access to more information. For instance, one can detect the brittle-to-ductile transition through the apparition and disappearance of serration flow on the indentation curves. It is the mark of the change in deformation behavior (from heterogeneous to homogeneous) with increasing temperature. Moreover, through the drop in hardness and the huge increase in strain rate sensitivity, the supercooled-liquid region is caught and the glass transition temperature is determined. Then, the sharp increase of hardness linked with the drop in the strain rate sensitivity is related to the crystallization of the sample.

As the HTSI gives access to a huge number of indentation data, the two-step crystallization of the ZrCu specimens is observed. Contrary to what is thermodynamically expected, three crystallized phases are formed during the crystallization process. They are the two stable phases bco-$Cu_{10}Zr_7$ and t-Zr_2Cu and the metastable phase c-ZrCu. The two-step kinetics is then explained by the crystallization of the amorphous phases in the three phases and the transformation of the c-ZrCu into the bco-$Cu_{10}Zr_7$ and t-Zr_2Cu phases. The obtained results are consistent with other characterization methods (DSC and HT-XRD). The HTSI technique is a local testing procedure. It may detect the local heterogeneity of the sample. As observed, the onset of crystallization is not detected. The measured properties are not representative of the whole structure but only of the local one.

Through the different performed experiments, some variability in the behavior of the samples is detected when submitted to similar thermal cycles. It questions the repeatability of the measurements. Contrary to copper or aluminum samples analyzed in the previous chapter, it seems that even if the samples are from the same deposition batch, some variations remain. Maybe the local amorphous structure differs between the samples and explains some of the observed differences.

The present study shows an interest in the HTSI method to characterize the properties of thin-film amorphous structures in temperature. However, more work would be necessary to understand better the observed behaviors, the mechanisms taking place, and the differences between samples. Some atomic simulations may be a way to propose an explanation for some of the observed behaviors.

Moreover, the present study was carried out on thin film: some of its behaviors may defer greatly from the ones of bulk metallic glasses. So, another following step would be to use this methodology to compare the behavior of a thin film and the corresponding bulk material to identify their similarities and differences.

Finally, here the characterized thin films were 6-μm thin. The indentation tests were conducted in a way to avoid the substrate effect on mechanical properties. However, they were performed with a constant maximum load: the maximum depth greatly changes with temperature. To reduce its impact, it could have on the results, implementing a maximum controlled depth indentation experiment is of great importance for future research.

Conclusions and Perspectives

Through the recent developments in high-temperature nanoindentation, determining the mechanical properties of a material in temperature is now possible. However, conducting classical indentation experiments typically takes a few minutes to a few hours by test. As it is long, extremely good control of temperature is necessary to reduce the impact of thermal drift on the measurement. Therefore, getting consistent results in temperature is quite time-consuming.

Usually, a day is required to evaluate the properties at a given temperature, as thermal stability is achieved in a few hours. Moreover, as material commonly changes at HT, it is not possible to quantify those changes with classical methods.

In the present work, a different approach is chosen to carry out nanoindentation tests in temperature. The idea is to use a 1-second indentation cycle. The cycle is based on a 0.5-second half-sinus loading function, followed by a creep segment of 0.1 second before a quick 3-steps unloading. This procedure is less sensitive to thermal drift since it lasts only 1 second. Applying multiple indentation cycles during a "slow" heating rate (a few degrees per minute) is the High-Temperature Scanning Indentation (HTSI) method. Computing the quasi-continuously changes of mechanical properties (Young's modulus, hardness, creep properties, etc.) of a material on a large temperature scale now takes a few hours only. The implementation of such methodology is presented in chapter 2. Validation steps were performed on fused silica, pure aluminum, and pure copper. The following chapters present different applications of this technique in diverse materials to study specific behavior in temperature.

The aim of chapter 3 is to use the HTSI method to characterize the creep properties of CaF_2 and silver samples on large temperature scales. Comparing the HTSI experiments with indentation creep and relaxation tests and with literature data gives consistent results. The equivalence between time and temperature is observed in the two materials. Such a method gives access to information (strain rate sensitivity, activation energy, activation volume) on the deformation mechanisms taking place in the materials in temperature.

However, as assessed on CaF_2, the strain rate may greatly impact the properties of the material at a given temperature. Unfortunately, the indentation cycle used in the methodology does not allow performing tests at a constant strain rate during loading. Moreover, the Indentation Size Effect is also observed in the studied materials. Conducing tests at a constant maximum depth is compulsory to reduce the influence of this phenomenon on the results.

To quantify the kinetics of restoration in metals, the HTSI method was applied on cold-rolled pure aluminum and copper, in chapter 4. Through the variations in hardness during the applied thermal cycle, static recovery and static recrystallization were identified. A simple model was proposed to identify the impact of each mechanism on the microstructure changes. The obtained modeling parameters allow predicting the hardness modifications correctly if applying different thermal cycles on the material. A few well-designed HTSI tests on a given deformed material should enable predicting its final microstructure. It will greatly help the material design.

The proposed model is quite simple. Further studies are required to better model the studied phenomena. Moreover, modeling the impact of the initial state on the parameters would allow reducing the number of experiments to help the design of new materials. Furthermore, the materials studied here are model materials. The proposed methodology should be applied to other materials to complete the model. Precipitation, phase transformations, and other phenomena should be identified. Taking their kinetic into account is essential to complete the model.

Finally, the High-Temperature Scanning Indentation technique was applied to a model ZrCu-based thin-film metallic glass to study its behaviors in temperature (see chapter 5). Different thermal cycles were applied and the changes in hardness and strain rate sensitivity in temperature were studied. Such analysis allows identifying the glass transition temperature, the crystallization temperature, and the temperature of the brittle-to-ductile transition, for a given heating rate. Moreover, the supercooled-liquid zone was clearly observed before the crystallization of the sample. Thanks to HT-XRD analyses, a better understanding of the crystallization process was achieved.

The thin films used here were 6 µm-thick: it enables conducting tests at 600 nm depth to have no impact of the substrate on hardness. However, as hardness greatly decreases in the supercooled-liquid zone, the indentation cycle, controlled in load, leads to great increases in the maximum depth. Being able to perform those tests at constant maximum depth (and so tested volume) would be of great interest to study thinner thin films and other materials.

Further developments and studies can be conducted after the present work. To always test the same volume of material in temperature, modifications of the indentation cycle should be performed. A first modification is proposed. To always carry out tests at the same maximum depth, an idea is to modify the maximum applied load in temperature. As the hardness is linked with the load and the area of contact, under the hypothesis that hardness does not change too much between one indent and the following one, one can use the current indentation cycle to modify the maximum load to the next test. Such an approach works well on materials with no spatial variation of hardness on the material (single crystal for instance). However on polycrystals, because of the modifications of hardness with the microstructure, the proposed method is not sufficient.

Nevertheless, the main modification would be to implement a high-speed indentation test with a constant strain rate during loading. Ideally, implementing high-speed CSM tests would allow people to have access to more properties of materials. Moreover, it may allow to perform all the tests at the same maximum depth. Nonetheless, with a Berkovich tip, such tests required exponential loading at high strain rates. During the loading, the deformation is no longer elastic [40–42] (see figure 1.10 p38). Finding a way to overcome or correct this effect is compulsory to implement such high-speed indentation cycles. Nonetheless, such high-speed indentation loading may not allow carrying out a creep segment and so to determine the creep properties of the materials. But it may give information on the internal friction of materials.

As nanoindentation is a local characterization method, it may be used to evaluate the properties of thin films. Indeed, metallic glasses present interesting properties compared to crystallized metals. However, as they are quite difficult to produce in large sizes, utilizing them as thin films may be easier. But characterizing them at micro- or nanometric size is necessary. Nanoindentation and the HTSI method are promising tools to quantify their mechanical behavior, especially if utilized in temperature.

Nonetheless, during tribological contact, some new materials can be manufactured near the contact. A nanometric tribological film can be formed, but its behaviors are not yet understood. How is it formed? What are its properties? How does it change? How does it impact the contact? Using the HTSI methods on such films may give some answers. Being able to characterize locally this layer in temperature may help understand how it is formed and how it may evolve in contact.

Nevertheless, huge needed developments concern the indentation tip. As a diamond tip cannot be applied at high temperatures because of oxidation, other materials (sapphire, WC, etc.) have been proposed. Unfortunately, the scientific community only has a few years of experience with those tips. Sadly, even if sapphire has interesting properties in temperature, presents issues with some materials because of chemical reactivity. The tungsten carbide is known to be brittle and difficult to cut. And to the author’s knowledge, no article using other tip material has been published yet. To continue to develop indentation experiments at high temperatures, it is necessary to have tips that can be employed at those temperatures.

A

Pile-up versus sink-in

I. Pile-up versus sink-in

Kermouche conducted a numerical study to determine which model between the one of Oliver and Pharr and the one of Loubet to prefer depending of the material. He considers an elasto-plastic solid with isotope non-linear cold-work (Holomon law with two parameters, Y and n). As it can be seen in figure A.1, the cold-rolled exponent n greatly impact the pile-up or sink-in comportment of the material. However, as it can be seen in figure A.2, the model of Oliver and Pharr or of Loubet are not really sensitive to this exponent. Those methods would give consistent results on certain materials, depending of their characteristics.

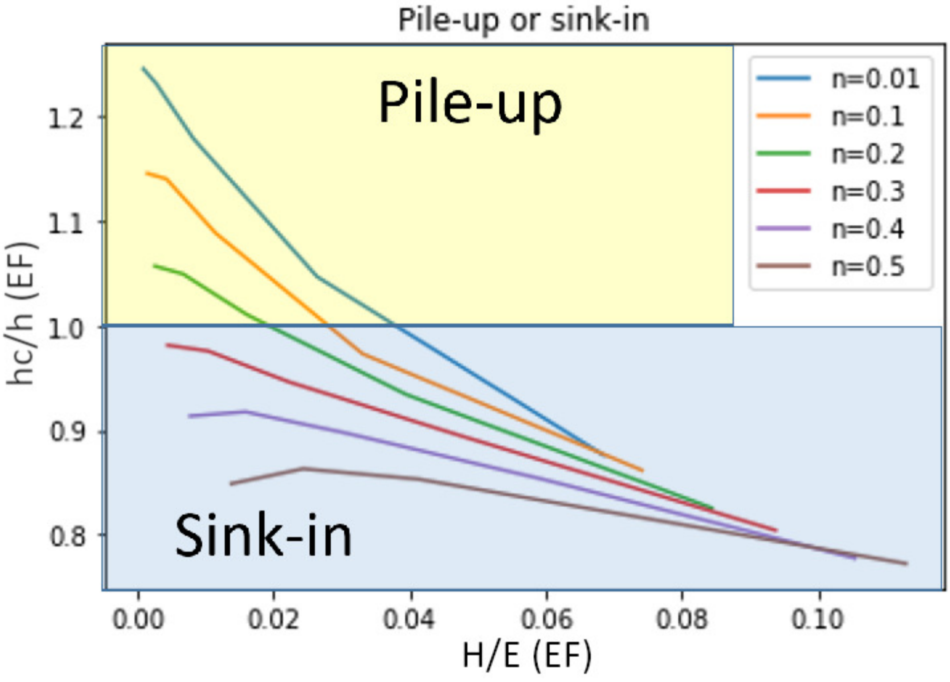

H

Figure A.1: Impact of the cold-work exponent n on the contact depth depending on hardness over Young modulus ratio, determined by numerical study using finite elements.

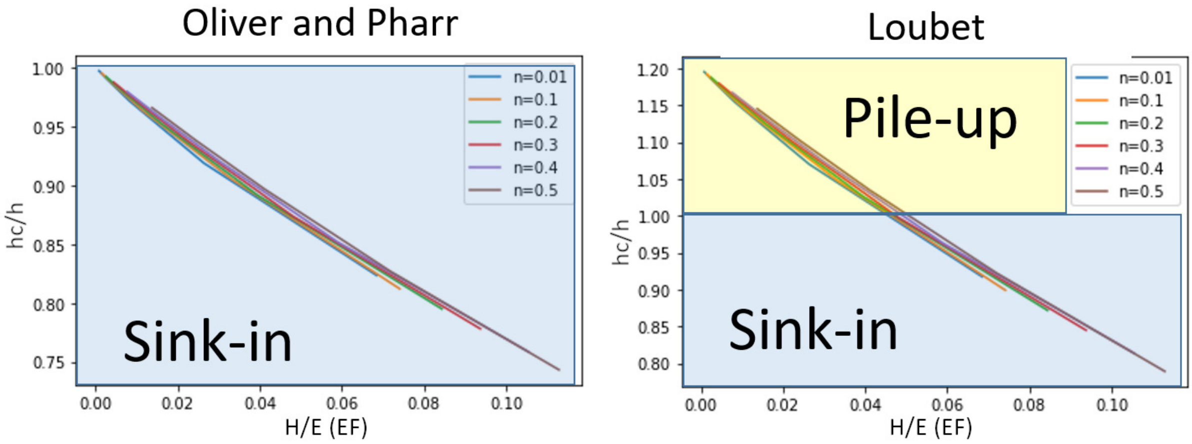

Figure A.2: Impact of the cold-work exponent n on the contact depth depending on hardness over Young modulus ratio, determined using Oliver and Pharr's model (left) or Loubet's model (right).

Let's compared the difference of hardness obtained using Oliver and Pharr's model or Loubet's model with the hardness obtained by finite elements (see figure A.3). According to those results, one should use Oliver and Pharr's model when the material has a high cold-work exponent or have a high H/E ratio. It would correspond to recrystallized metals, some hard steels or to silicate or metallic glasses. On the opposite, one should prefer Loubet's model for ductile materials with low cold-work exponent or with high H/E ratio. It would correspond to metals that could not work-harden a lot or that were cold-rolled up to saturation. It also includes glassy polymers and silicate or metallic glasses. For instance, both models give the same results on fused silica which presents sink-in [30].

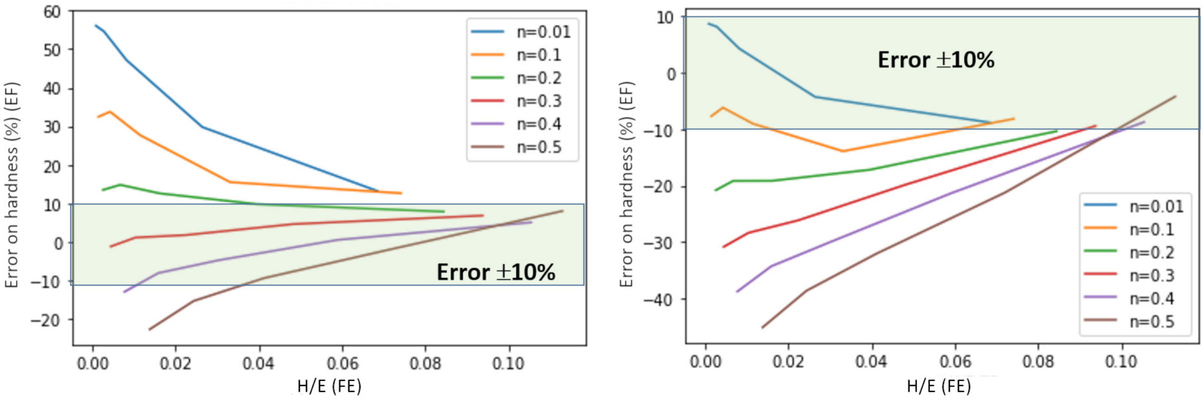

Figure A.3: Impact of the cold-work exponent n on the hardness error determined using Oliver and Pharr's model (left) or Loubet's model (right) depending on hardness over Young modulus ratio.

B

Optimization

I. Determination of the parameters of a model

I.A. From observation to modeling

Usually, once a phenomenon is observed, it is modeled for better understanding. Such an approach allows one to quantify the occurring mechanism.

Some models are established following the laws that have already been established. For instance, in chapter 1 section III.E., Verdier's model considered that recovery is the same as applying a deformation. By using Orowan relation, the authors can propose an explanation of the process and a law that governs its. The point is then to quantify the parameters of this law to characterize this phenomenon. This is on this quantification process that the following paragraphs will focus on.

I.B. Formulation of the problem

Let's first focus on the definition and the verification of the obtained parameters before studying a few algorithms that are useful to perform optimization.

I.B.1. Definition of the cost function

To apply optimization algorithms to obtain a good estimation of the parameters, one should first well define the problem. The objective is to find the parameters of the model that will reproduce the experimental data. The goal is in fact to minimize the difference between those data and the model: the cost function is defined based on that.

The cost function that is used in this manuscript is known as the X^2 function:

$$X^2 = \frac{1}{N}\sum_{i=0}^{N}\left(y_{experiment}(t_i, T_i, ...) - y_{model}(\theta, t_i, T_i, ...)\right)^2 \tag{B.1}$$

Where $y_{experiment}$ contains all the experimental data. y_{model} is the corresponding model, depending on the p parameters $\theta = (\theta_i)_{(0 \leq i \leq p)}$. The goal is to obtain the p parameters that minimize the function X^2.

I.B.2. Uniqueness and stability of the solution

Once a solution is obtained, one should verify that this is the only one possible in the studied solution space. An (easy) way to verify uniqueness is to run again the algorithm to see if it gives back the same set of parameters. As some cost functions will present local minima, changing the initial point is compulsory not to be trapped by those minima. More, it is important to have a unique solution but also to know if the solution is stable. A little variation of the parameters should only lead to a little variation of the result.
As verifying uniqueness and stability can become very time consuming, one can use the identification factor defined by Richard *et al.* [226]. Once a solution is identified, one will calculate the impact of a perturbation of 5% on each parameter on the solution. By determining the identification factor I:

$$I = \log_{10}\left(\frac{\lambda_{max}}{\lambda_{min}}\right) \tag{B.2}$$

with λ_{max} and λ_{min} the maximum and minimum eigenvalues of the cost function Hessian matrix H near the solution.

$$H_{ij} = \sum_{s=0}^{nbDot} \frac{\partial f(t_s)}{\partial \theta_i}\frac{\partial f(t_s)}{\partial \theta_j} \tag{B.3}$$

with $\theta = (\theta_i)$ the parameters of the function f that need to be determined. A problem is considered well posed if $I \leq 2$. For more detailed explanations, see [226–228].

I.C. A few algorithms to determine the best parameters of a model

Let's study some classical algorithms to obtain the parameters of a model.

I.C.1. Least square method

Really simple to implement, the least square method is widely used to determine the parameter of a model. The goal is to minimize the function X^2 where σ_{var} is the variance of the data. In the manuscript, it is considered that $\sigma_{var} = N$.

$$X^2 = \sum_{i=0}^{N}\left(\frac{y_{experiment}(t_i, T_i, ...) - y_{model}(\theta, t_i, T_i, ...)}{\sigma_{var}}\right)^2 \tag{B.4}$$

When the model y_{model} depends linearly on the parameter θ, the resolution is quite easy: one should find the parameters that give $grad(X^2) = 0$. When the model becomes more complex, the least square method could give the parameters using Gauss-Newton or Levenberg-Marquardt algorithms. However, such models present local minima that can trap the algorithm. One should verify that the obtained solution is the global minimum and not a local minimum. Such methodology can become really time consuming, so one could have to go for more complex algorithms in this case.

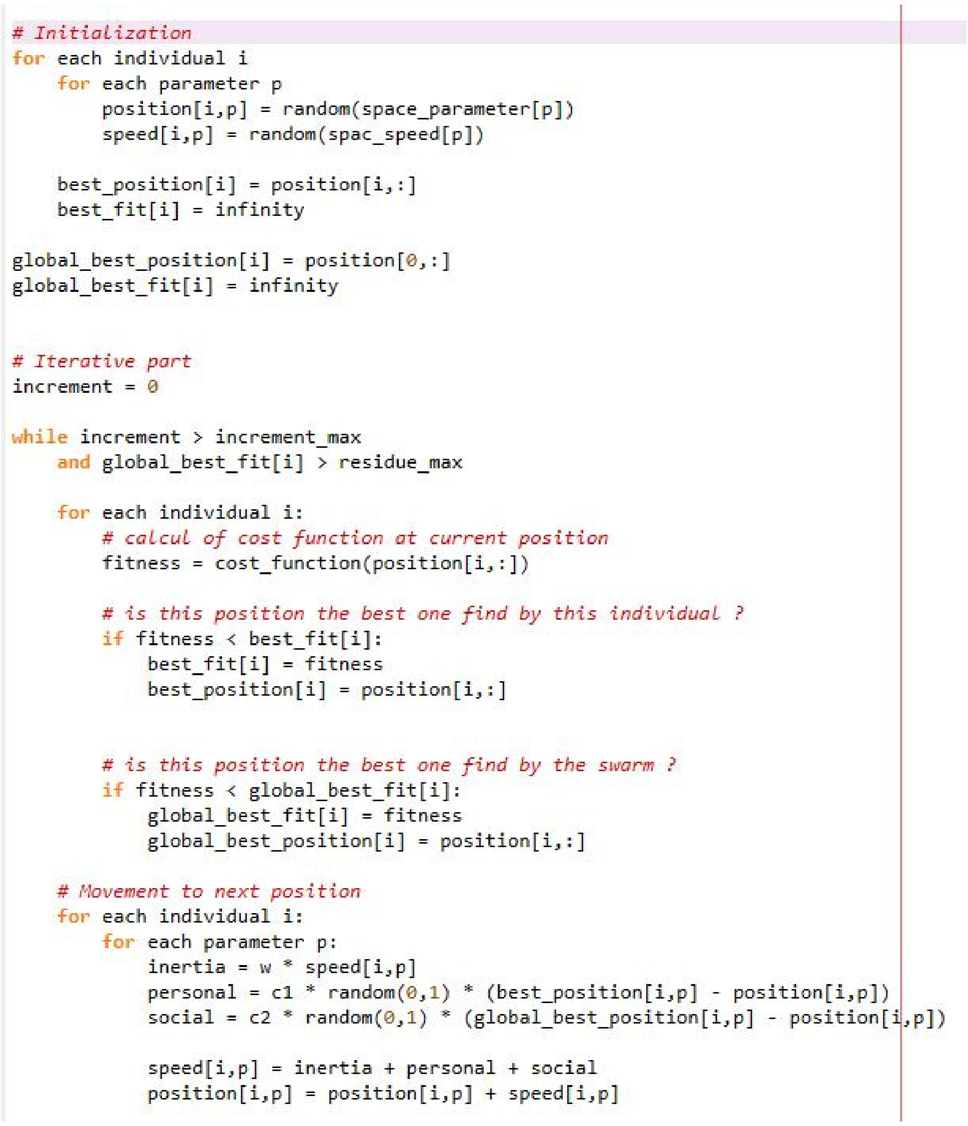

```
# Initialization
for each individual i
    for each parameter p
        position[i,p] = random(space_parameter[p])
        speed[i,p] = random(spac_speed[p])

    best_position[i] = position[i,:]
    best_fit[i] = infinity

global_best_position[i] = position[0,:]
global_best_fit[i] = infinity


# Iterative part
increment = 0

while increment > increment_max
    and global_best_fit[i] > residue_max

    for each individual i:
        # calcul of cost function at current position
        fitness = cost_function(position[i,:])

        # is this position the best one find by this individual ?
        if fitness < best_fit[i]:
            best_fit[i] = fitness
            best_position[i] = position[i,:]


        # is this position the best one find by the swarm ?
        if fitness < global_best_fit[i]:
            global_best_fit[i] = fitness
            global_best_position[i] = position[i,:]

    # Movement to next position
    for each individual i:
        for each parameter p:
            inertia = w * speed[i,p]
            personal = c1 * random(0,1) * (best_position[i,p] - position[i,p])
            social = c2 * random(0,1) * (global_best_position[i,p] - position[i,p])

            speed[i,p] = inertia + personal + social
            position[i,p] = position[i,p] + speed[i,p]
```

Figure B.1: Algorithm to implement a PSO methodology.

I.C.2. Particle Swarm Optimization Algorithms

To overcome the issue of local minima, one can use the Particle Swarm Algorithm (PSO), developed in the 1990s [216–220]. The idea of the algorithm is to reproduce swarm comportment. By effective shares of information, one can then quickly find the optimal solution. The algorithm is presented in figure B.1. Each individual n of the swarm starts at a random position p_0^n (set of parameters) in the solution space, with a certain speed s_0^n. At each iteration i, each individual will calculate the cost of the function cost $fitness_i^n$ depending of its actual position. It will then compare it with the result of the best position in memory $position_{best}^n$ and replace it if it is better. Then it will interact with the whole swarm to find who has found the best position in the swarm and save this global best solution $position_{best}^{global}$. Each individual will then change its speed and direction to move to the next position and repeat the process until converging globally to the best solution. See figure B.2 to understand better the three contributions to

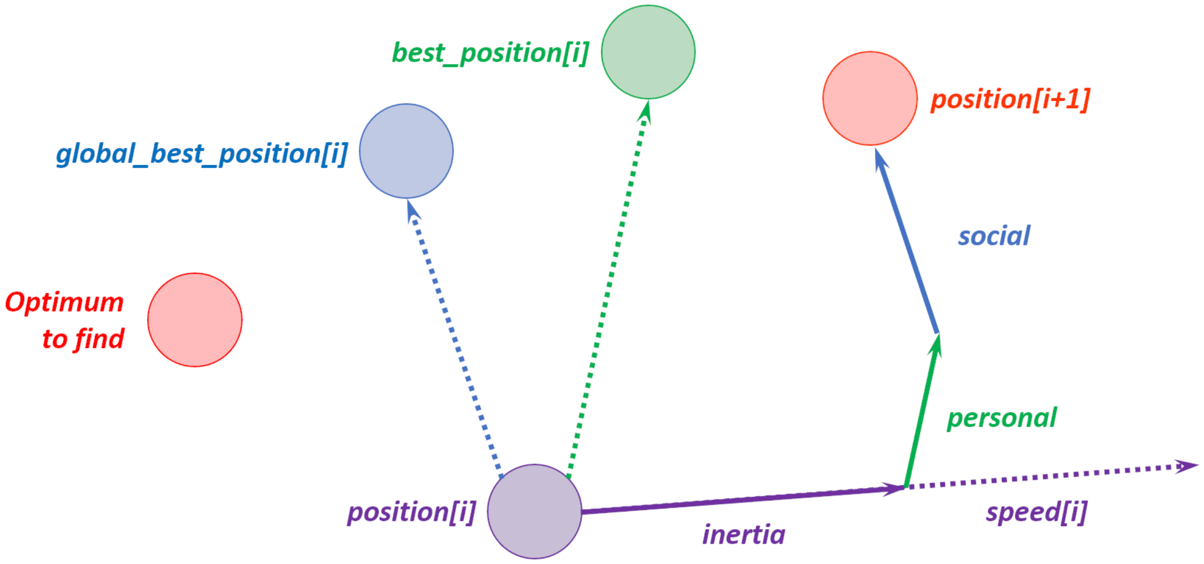

Figure B.2: Schematic representation of the movement of one particle in a PSO algorithm.

movement of each particle between time i and $i+1$.
Such a method allows one to overcome the issue of the local minima thanks to this information sharing. However, it can become time consuming if increasing the number of individuals in the swarm and the number of iterations. This algorithm is used to determine the parameters of a model that presents a non-linearity on its parameters.

I.D. Conclusions

When modeling a phenomenon, one should verify that his problem is well formulated to get unique and stable parameters to describe it. Using the identification index defined in [226, 227] allows knowing if one has enough data to extract such unique parameters. Moreover, when models are simple, linear, using a least square optimization is a simple, easy and quick way to get those parameters. As a model becomes more complex, the issue of local minima occurs. In this manuscript, a Particles Swarm Optimization algorithm [216–220] has been implemented to overcome it. There are other algorithms allowing one to solve the issue of the local minima (Simulated Annealing [263–265], Genetic Algorithms [266, 267], etc.).

Bibliography

[1] T. Turner. "The Hardness of Metals". In: *Scientific American Supplement* 602 (1887).

[2] H. Hertz. *Miscellaneous Papers*. MACMILLAN AND CO., 1896.

[3] "Hardness". In: *Mechanical Properties and Working of Metals and Alloys*. Vol. 264. Springer Singapore, 2018, pp. 119–171. DOI: 10.1007/978-981-10-7209-3_3. (Visited on 01/24/2022).

[4] G. A. Hankins. "A Synopsis of the Present State of Knowledge of the Hardness and Abrasion Testing of Metals with Special Reference to the Work Done during the Period 1917–27, and a Bibliography". In: *Proceedings of the Institution of Mechanical Engineers* 116.1 (1929), pp. 317–387. DOI: 10.1243/PIME_PROC_1929_116_017_02. (Visited on 02/01/2022).

[5] F. Knoop, C. G. Peters, and W. B. Emerson. "A Sensitive Pyramidal-Diamond Tool for Indentation Measurements". In: *Journal of Research of the National Bureau of Standards* 23.1 (1939), p. 39. DOI: 10.6028/jres.023.022. (Visited on 02/01/2022).

[6] W. Klement, R. H. Willens, and P. Duwez. "Non-Crystalline Structure in Solidified Gold–Silicon Alloys". In: *Nature* 187.4740 (1960), pp. 869–870. DOI: 10.1038/187869b0. (Visited on 07/04/2022).

[7] J.-M. Pelletier and Jichao Q. "Metallic Glasses". In: *Springer Handbook of Glass*. Ed. by J. D. Musgraves, J. Hu, and L. Calvez. Springer Handbooks. Cham: Springer International Publishing, 2019, pp. 617–643. DOI: 10.1007/978-3-319-93728-1_18. (Visited on 07/04/2022).

[8] D. Tabor. *The Hardness of Metals*. Oxford, 1951.

[9] D. Tabor. "The Hardness of Solids". In: *Reviews of Physics in Technology* 1.3 (1970), pp. 145–179. DOI: 10.1088/0034-6683/1/3/I01. (Visited on 10/05/2020).

[10] J. B. Pethicai, R. Hutchings, and W. C. Oliver. "Hardness Measurement at Penetration Depths as Small as 20 Nm". In: *Philosophical Magazine A* 48.4 (1983), pp. 593–606. DOI: 10.1080/01418618308234914. (Visited on 01/25/2022).

[11] J. L. Loubet et al. "Vickers Indentation Curves of Magnesium Oxide (MgO)". In: *Journal of Tribology* 106.1 (1984), pp. 43–48. DOI: 10.1115/1.3260865. (Visited on 01/25/2022).

[12] M. F. Doerner. “A Method for Interpreting the Data from Depth-Sensing Indentation Inst Rurnen Ts”. In: *Journal of Materials Research* 1.4 (1986), p. 9. DOI: `10.1557/JMR.1986.0601`.

[13] L. Odoni. “Propriétés mécaniques et effets d’échelle”. PhD thesis. Ecole centrale de Lyon, 1999.

[14] Micro Star Technologies. *Nano Indenters.*

[15] A. C. Fischer-Cripps. “Critical Review of Analysis and Interpretation of Nanoindentation Test Data”. In: *Surface and Coatings Technology* 200.14-15 (2006), pp. 4153–4165. DOI: `10.1016/j.surfcoat.2005.03.018`. (Visited on 02/04/2022).

[16] G. Kermouche, J.-L. Loubet, and J.-M. Bergheau. “Cone Indentation of Time-Dependent Materials: The Effects of the Indentation Strain Rate”. In: *Mechanics of Materials* 39.1 (2007), pp. 24–38. DOI: `10.1016/j.mechmat.2006.02.005`. (Visited on 10/23/2020).

[17] I. N. Sneddon. “The Relation between Load and Penetration in the Axisymmetric Boussinesq Problem for a Punch of Arbitrary Profile”. In: *International Journal of Engineering Science* 3 (1965), pp. 47–57. DOI: `10.1016/0020-7225(65)90019-4`.

[18] W. C. Oliver and G. M. Pharr. “An Improved Technique for Determining Hardness and Elastic Modulus Using Load and Displacement Sensing Indentation Experiments”. In: *Journal of Materials Research* 7.6 (1992), pp. 1564–1583. DOI: `10.1557/JMR.1992.1564`.

[19] G. M. Pharr, W. C. Oliver, and F. R. Brotzen. “On the Generality of the Relationship among Contact Stiffness, Contact Area, and Elastic Modulus during Indentation”. In: *Journal of Materials Research* 7.3 (1992), pp. 613–617. DOI: `10.1557/JMR.1992.0613`. (Visited on 01/31/2022).

[20] D. L. Joslin and W. C. Oliver. “A New Method for Analyzing Data from Continuous Depth-Sensing Microindentation Tests”. In: *Journal of Materials Research* 5.1 (1990), pp. 123–126. DOI: `10.1557/JMR.1990.0123`. (Visited on 02/08/2022).

[21] N. A. Stilwell and D. Tabor. “Elastic Recovery of Conical Indentations”. In: *Proceedings of the Physical Society* 78.2 (1961), pp. 169–179. DOI: `10.1088/0370-1328/78/2/302`. (Visited on 01/27/2022).

[22] P. Baral. “Caractérisation mécanique des phénomènes dépendants du temps par nanoindentation instrumentée en température”. PhD thesis. Ecole centrale de Lyon, 2018.

[23] K. Kese and Z. C. Li. “Semi-Ellipse Method for Accounting for the Pile-up Contact Area during Nanoindentation with the Berkovich Indenter”. In: *Scripta Materialia* 55.8 (2006), pp. 699–702. DOI: `10.1016/j.scriptamat.2006.06.030`. (Visited on 02/01/2022).

[24] J.-L. Loubet et al. “Nanoindentation with a Surface Force Apparatus”. In: *Mechanical Properties and Deformation Behavior of Materials Having Ultra-Fine Microstructures.* Ed. by M. Nastasi, D. M. Parkin, and H. Gleiter. Dordrecht: Springer Netherlands, 1993, pp. 429–447. DOI: `10.1007/978-94-011-1765-4_28`. (Visited on 09/28/2020).

[25] S. Bec et al. “Improvements in the Indentation Method with a Surface Force Apparatus”. In: *Philosophical Magazine A* 74.5 (1996), pp. 1061–1072. DOI: `10.1080/01418619608239707`. (Visited on 12/07/2020).

[26] K. Demmou. “Nanoindentation, Viscoplasticité & Piézo-Mécanique de Films de Dithio-Phosphate de Zinc Triboformés”. These. Ecole centrale de Lyon, 2007. (Visited on 10/12/2020).

[27] G. Guillonneau. “Nouvelles Techniques de Nano-Indentation Pour Des Conditions Expérimentales Difficiles : Très Faibles Enfoncements, Surfaces Rugueuses, Température”. These. Ecole centrale de Lyon, 2012. (Visited on 10/12/2020).

[28] G. Tiphéne et al. “High-Temperature Scanning Indentation: A New Method to Investigate in Situ Metallurgical Evolution along Temperature Ramps”. In: *Journal of Materials Research* 36 (2021), pp. 2383–2396. DOI: `10.1557/s43578-021-00107-7`. (Visited on 03/22/2021).

[29] K. W. McElhaney, J. J. Vlassak, and W. D. Nix. “Determination of Indenter Tip Geometry and Indentation Contact Area for Depth-Sensing Indentation Experiments”. In: *Journal of Materials Research* 13.5 (1997), pp. 1300–1306. DOI: `10.1557/JMR.1998.0185`. (Visited on 01/31/2022).

[30] G. Guillonneau et al. “Determination of the True Projected Contact Area by in Situ Indentation Testing”. In: *Journal of Materials Research* 34.16 (2019), pp. 2859–2868. DOI: `10.1557/jmr.2019.236`.

[31] A. Bolshakov and G. M. Pharr. “Influences of Pileup on the Measurement of Mechanical Properties by Load and Depth Sensing Indentation Techniques”. In: *Journal of Materials Research* 13.4 (1998), pp. 1049–1058. DOI: `10.1557/JMR.1998.0146`. (Visited on 01/31/2022).

[32] F. Roudet. “Propriétés mécaniques par indentation multi-échelles des matériaux biosourcés aux céramiques”. HDR. Université Lille 1, 2015.

[33] C. Kleesattel. “Resonant Sensing Devices”. 3,153,338. 1964.

[34] C. Kleesattel. “Compliance of Mechanical Contacts and Its Significance for Ultrasonic Hardness Testing and for Vibration-Amplitude Measurements”. In: *The Journal of the Acoustical Society of America* 39.2 (1966), pp. 404–405. DOI: `10.1121/1.1909907`. (Visited on 01/28/2022).

[35] S. Comby-Dassonneville. “Développement et Application d’un Nanoindenteur in Situ MEB Couplé à Des Mesures Électriques”. PhD thesis. SIMaP, Grenoble INP, 2018.

[36] Gaylord Guillonneau et al. “A New Method to Determine the True Projected Contact Area Using Nanoindentation Testing”. In: *Comptes Rendus Mécanique* 343.7-8 (2015), pp. 410–418. DOI: `10.1016/j.crme.2015.06.004`. (Visited on 01/06/2023).

[37] K. W. Siu and A. H. W. Ngan. “The Continuous Stiffness Measurement Technique in Nanoindentation Intrinsically Modifies the Strength of the Sample”. In: *Philosophical Magazine* 93.5 (2013), pp. 449–467. DOI: `10.1080/14786435.2012.722234`. (Visited on 02/03/2022).

[38] M. J. Cordill, N. R. Moody, and W. W. Gerberich. “Effects of Dynamic Indentation on the Mechanical Response of Materials”. In: *Journal of Materials Research* 23.6 (2008), pp. 1604–1613. DOI: `10.1557/JMR.2008.0205`. (Visited on 02/03/2022).

[39] G. M. Pharr, J. H. Strader, and W. C. Oliver. “Critical Issues in Making Small-Depth Mechanical Property Measurements by Nanoindentation with Continuous Stiffness Measurement”. In: *Journal of Materials Research* 24.3 (2009), pp. 653–666. DOI: `10.1557/jmr.2009.0096`. (Visited on 02/03/2022).

[40] B. Merle, V. Maier-Kiener, and G. M. Pharr. “Influence of Modulus-to-Hardness Ratio and Harmonic Parameters on Continuous Stiffness Measurement during Nanoindentation”. In: *Acta Materialia* 134 (2017), pp. 167–176. DOI: `10.1016/j.actamat.2017.05.036`. (Visited on 02/03/2022).

[41] B. Merle, W. H. Higgins, and G. M. Pharr. “Critical Issues in Conducting Constant Strain Rate Nanoindentation Tests at Higher Strain Rates”. In: *Journal of Materials Research* 34.20 (2019), pp. 3495–3503. DOI: `10.1557/jmr.2019.292`. (Visited on 02/03/2022).

[42] B. Merle, W. H. Higgins, and G. M. Pharr. “Extending the Range of Constant Strain Rate Nanoindentation Testing”. In: *Journal of Materials Research* 35.4 (2020), pp. 343–352. DOI: `10.1557/jmr.2019.408`. (Visited on 02/03/2022).

[43] P. S. Phani, W. C. Oliver, and G. M. Pharr. “An Experimental Assessment of Methods for Mitigating Plasticity Error during Nanoindentation with Continuous Stiffness Measurement”. In: *Materials & Design* 194 (2020), p. 108924. DOI: `10.1016/j.matdes.2020.108924`. (Visited on 02/03/2022).

[44] P. S. Phani, W. C. Oliver, and G. M. Pharr. “Understanding and Modeling Plasticity Error during Nanoindentation with Continuous Stiffness Measurement”. In: *Materials & Design* 194 (2020), p. 108923. DOI: `10.1016/j.matdes.2020.108923`. (Visited on 02/03/2022).

[45] W. C. Oliver and G. M. Pharr. “Measurement of Hardness and Elastic Modulus by Instrumented Indentation: Advances in Understanding and Refinements to Methodology”. In: *Journal of Materials Research* 19.1 (2004), p. 18. DOI: `10.1557/jmr.2004.19.1.3`.

[46] M. R. VanLandingham, T. F. Juliano, and M. J. Hagon. “Measuring Tip Shape for Instrumented Indentation Using Atomic Force Microscopy”. In: *Measurement Science and Technology* 16.11 (2005), pp. 2173–2185. DOI: `10.1088/0957-0233/16/11/007`. (Visited on 02/01/2022).

[47] G. Cailletaud. “Mécanique des Matériaux Solides - Notes de Cours - MINES ParisTech”. MINES ParisTech, 2012.

[48] K. L. Johnson. “The Correlation of Indentation Experiments”. In: *Journal of the Mechanics and Physics of Solids* 18.2 (1970), pp. 115–126. DOI: `10.1016/0022-5096(70)90029-3`. (Visited on 02/08/2022).

[49] G. Kermouche, J.-L. Loubet, and J.-M. Bergheau. “An Approximate Solution to the Problem of Cone or Wedge Indentation of Elastoplastic Solids”. In: *Comptes Rendus Mécanique* 333.5 (2005), pp. 389–395. DOI: `10.1016/j.crme.2005.04.001`. (Visited on 02/08/2022).

[50] M. J. Mayo and W. D. Nix. “A Micro-Indentation Study of Superplasticity in Pb, Sn, and Sn-38 Wt% Pb”. In: *Acta Metallurgica* 36.8 (1988), pp. 2183–2192. DOI: `10.1016/0001-6160(88)90319-7`. (Visited on 02/08/2022).

[51] T. P. Weihs and J. B. Pethica. “Monitoring Time-Dependent Deformation in Small Volumes”. In: *MRS Proceedings* 239 (1991), p. 325. DOI: `10.1557/PROC-239-325`. (Visited on 02/08/2022).

[52] B. N. Lucas et al. “Time Dependent Deformation During Indentation Testing”. In: *MRS Online Proceedings Library* 436.1 (1996), pp. 233–238. DOI: `10.1557/PROC-436-233`.

[53] J. L. Bucaille, E. Felder, and G. Hochstetter. “Identification of the Viscoplastic Behavior of a Polycarbonate Based on Experiments and Numerical Modeling of the Nano-Indentation Test”. In: *Journal Of Materials Science* 37 (2002), pp. 3999–4011. DOI: `10.1023/A:1019644630927`.

[54] H. Conrad. “Thermally Activated Deformation of Metals”. In: *JOM* 16.7 (1964), pp. 582–588. DOI: `10.1007/BF03378292`. (Visited on 08/26/2022).

[55] *Creep Classification of Grade 91 Steel.* https://tetra-eng.com/en/resources/30-white-papers/183-creep-classification. (Visited on 01/06/2023).

[56] C. Su et al. “Measurement of Power-Law Creep Parameters by Instrumented Indentation Methods”. In: *Journal of the Mechanics and Physics of Solids* 61.2 (2013), pp. 517–536. DOI: `10.1016/j.jmps.2012.09.009`. (Visited on 02/10/2022).

[57] P. Baral et al. “A New Long-Term Indentation Relaxation Method to Measure Creep Properties at the Micro-Scale with Application to Fused Silica and PMMA”. In: *Mechanics of Materials* 137 (2019), p. 103095. DOI: `10.1016/j.mechmat.2019.103095`. (Visited on 03/03/2021).

[58] V. Maier et al. “An Improved Long-Term Nanoindentation Creep Testing Approach for Studying the Local Deformation Processes in Nanocrystalline Metals at Room and Elevated Temperatures”. In: *Journal of Materials Research* 28.9 (2013), pp. 1177–1188. DOI: `10.1557/jmr.2013.39`. (Visited on 03/03/2021).

[59] V. Maier et al. “Nanoindentation Strain-Rate Jump Tests for Determining the Local Strain-Rate Sensitivity in Nanocrystalline Ni and Ultrafine-Grained Al”. In: *Journal of Materials Research* 26.11 (2011), pp. 1421–1430. DOI: `10.1557/jmr.2011.156`. (Visited on 02/10/2022).

[60] O. Prach et al. “A New Nanoindentation Creep Technique Using Constant Contact Pressure”. In: *Journal of Materials Research* 34.14 (2019), pp. 2492–2500. DOI: `10.1557/jmr.2019.188`. (Visited on 02/10/2022).

[61] W. R. LaFontaine et al. “Indentation Load Relaxation Experiments with Indentation Depth in the Submicron Range”. In: *Journal of Materials Research* 5.10 (1990), pp. 2100–2106. DOI: `10.1557/JMR.1990.2100`. (Visited on 02/22/2022).

[62] B. Xu, Z. Yue, and X. Chen. “Characterization of Strain Rate Sensitivity and Activation Volume Using the Indentation Relaxation Test”. In: *Journal of Physics D: Applied Physics* 43.24 (2010), p. 245401. DOI: `10.1088/0022-3727/43/24/245401`. (Visited on 02/22/2022).

[63] D. E. Stegall et al. “Repeated Load Relaxation Testing of Pure Polycrystalline Nickel at Room Temperature Using Nanoindentation”. In: *Applied Physics Letters* 104.4 (2014), p. 041902. DOI: `10.1063/1.4862799`. (Visited on 02/22/2022).

[64] P. Baral et al. “Theoretical and Experimental Analysis of Indentation Relaxation Test”. In: *Journal of Materials Research* 32.12 (2017), pp. 2286–2296. DOI: `10.1557/jmr.2017.203`. (Visited on 02/22/2022).

[65] C. A. Schuh and A. C. Lund. “Application of Nucleation Theory to the Rate Dependence of Incipient Plasticity during Nanoindentation”. In: *J. Mater. Res.* 19.7 (2004), pp. 2152–2158. DOI: `10.1557/JMR.2004.0276`. (Visited on 03/08/2022).

[66] D. Lorenz et al. “Pop-in Effect as Homogeneous Nucleation of Dislocations during Nanoindentation”. In: *Phys. Rev. B* 67.17 (2003), p. 172101. DOI: `10.1103/PhysRevB.67.172101`. (Visited on 03/08/2022).

[67] A. Barnoush. “Correlation between Dislocation Density and Nanomechanical Response during Nanoindentation”. In: *Acta Materialia* 60.3 (2012), pp. 1268–1277. DOI: `10.1016/j.actamat.2011.11.034`. (Visited on 03/08/2022).

[68] A. Montagne, V. Audurier, and C. Tromas. “Influence of Pre-Existing Dislocations on the Pop-in Phenomenon during Nanoindentation in MgO”. In: *Acta Materialia* 61.13 (2013), pp. 4778–4786. DOI: `10.1016/j.actamat.2013.05.004`. (Visited on 03/08/2022).

[69] G. M. Pharr, E. G. Herbert, and Y. Gao. “The Indentation Size Effect: A Critical Examination of Experimental Observations and Mechanistic Interpretations”. In: *Annu. Rev. Mater. Res.* 40.1 (2010), pp. 271–292. DOI: `10.1146/annurev-matsci-070909-104456`. (Visited on 03/08/2022).

[70] K. Durst, M. Göken, and G. M. Pharr. “Indentation Size Effect in Spherical and Pyramidal Indentations”. In: *J. Phys. D: Appl. Phys.* 41.7 (2008), p. 074005. DOI: `10.1088/0022-3727/41/7/074005`. (Visited on 03/08/2022).

[71] J.-W. Lu et al. “Thermally Activated Pop-in and Indentation Size Effects in GaN Films”. In: *J. Phys. D: Appl. Phys.* 45.8 (2012), p. 085301. DOI: `10.1088/0022-3727/45/8/085301`. (Visited on 03/08/2022).

[72] T. T. Zhu et al. “Indentation Size Effect at the Initiation of Plasticity for Ceramics and Metals”. In: *J. Phys. D: Appl. Phys.* 41.7 (2008), p. 074004. DOI: 10.1088/0022-3727/41/7/074004. (Visited on 03/08/2022).

[73] W. D. Nix and H. Gao. “Indentation Size Effects in Crystalline Metrials A Law for Strain Gradient Plasticity”. In: *J. Mech. Phys. So/id.i,* 46.3 (1998), pp. 411–425. DOI: 10.1016/S0022-5096(97)00086-0.

[74] K. Durst, B. Backes, and M. Göken. “Indentation Size Effect in Metallic Materials: Correcting for the Size of the Plastic Zone”. In: *Scripta Materialia* 52.11 (2005), pp. 1093–1097. DOI: 10.1016/j.scriptamat.2005.02.009. (Visited on 03/08/2022).

[75] B. N. Lucas and W. C. Oliver. “Time Dependent Indentation Testing At Non-Ambient Temperatures Utilizing the High Temperature Mechanical Properties Microprobe”. In: *MRS Proc.* 356 (1994), p. 645. DOI: 10.1557/PROC-356-645. (Visited on 03/09/2022).

[76] J. F. Smith and S. Zheng. “High Temperature Nanoscale Mechanical Property Measurements”. In: *Surface Engineering* 16.2 (2000), pp. 143–146. DOI: 10.1179/026708400101517044. (Visited on 03/09/2022).

[77] J. S. K.-L. Gibson et al. “On Extracting Mechanical Properties from Nanoindentation at Temperatures up to 1000 °C”. In: *Extreme Mechanics Letters* 17 (2017), pp. 43–49. DOI: 10.1016/j.eml.2017.09.007. (Visited on 10/08/2020).

[78] B. D. Beake and A. J. Harris. “Nanomechanics to 1000 °C for High Temperature Mechanical Properties of Bulk Materials and Hard Coatings”. In: *Vacuum* 159 (2019), pp. 17–28. DOI: 10.1016/j.vacuum.2018.10.011. (Visited on 10/08/2020).

[79] C. Minnert, W. C. Oliver, and K. Durst. “New Ultra-High Temperature Nanoindentation System for Operating at up to 1100 °C”. In: *Materials & Design* 192 (2020), p. 108727. DOI: 10.1016/j.matdes.2020.108727. (Visited on 12/08/2020).

[80] C. A. Schuh, C. E. Packard, and A. C. Lund. “Nanoindentation and Contact-Mode Imaging at High Temperatures”. In: *J. Mater. Res.* 21.3 (2006), pp. 725–736. DOI: 10.1557/jmr.2006.0080. (Visited on 09/24/2020).

[81] N. M. Everitt, M. I. Davies, and J. F. Smith. “High Temperature Nanoindentation – the Importance of Isothermal Contact”. In: *Philosophical Magazine* 91.7-9 (2011), pp. 1221–1244. DOI: 10.1080/14786435.2010.496745.

[82] K. Demmou et al. “Temperature Effects on Mechanical Properties of Zinc Dithiophosphate Tribofilms”. In: *Tribology International*. Interactions of Tribology and the Operating Environment: Proceedings of the 32nd Leeds-Lyon Symposium on Tribology (Lyon, 2005) 39.12 (2006), pp. 1558–1563. DOI: 10.1016/j.triboint.2006.01.025. (Visited on 09/07/2022).

[83] J. M. Wheeler. “High Temperature Nanoindentation: The State of the Art and Future Challenges”. In: *Current Opinion in Solid State and Materials Science* 19.6 (2015), pp. 354–366. DOI: 10.1016/j.cossms.2015.02.002.

[84] J. M. Wheeler and J. Michler. "Elevated Temperature, Nano-Mechanical Testing *in Situ* in the Scanning Electron Microscope". In: *Review of Scientific Instruments* 84.4 (2013), p. 045103. DOI: `10.1063/1.4795829`. (Visited on 12/08/2020).

[85] S. Korte et al. "Deformation of Silicon – Insights from Microcompression Testing at 25–500°C". In: *International Journal of Plasticity* 27.11 (2011), pp. 1853–1866. DOI: `10.1016/j.ijplas.2011.05.009`. (Visited on 03/10/2022).

[86] S. Korte et al. "High Temperature Microcompression and Nanoindentation in Vacuum". In: *J. Mater. Res.* 27.1 (2012), pp. 167–176. DOI: `10.1557/jmr.2011.268`. (Visited on 03/10/2022).

[87] J. M. Wheeler and J. Michler. "Indenter Materials for High Temperature Nanoindentation". In: *Review of Scientific Instruments* 84.10 (2013), p. 101301. DOI: `10.1063/1.4824710`.

[88] F. P. Bundy et al. "Review Article - The Pressure-Temperature Phase And Transformation Diagram For Carbon; Updated Through 1994". In: *Carbon* 34.2 (1996), pp. 141–153. DOI: `10.1016/0008-6223(96)00170-4`.

[89] F. S. Phinney. "Graphitization of Diamond". In: *Science* 120.3114 (1954), pp. 394–395. DOI: `10.1126/science.120.3114.393`. (Visited on 03/14/2022).

[90] M. Seal. "Graphitization and Plastic Deformation of Diamond". In: *Nature* 182.4645 (1958), pp. 1264–1267. DOI: `10.1038/1821264a0`. (Visited on 03/14/2022).

[91] M. Seal. "Graphitization of Diamond". In: *Nature* 185.4712 (1960), pp. 522–523. DOI: `10.1038/185522a0`.

[92] V. R. Howes. "The Graphitization of Diamond". In: *Proc. Phys. Soc.* 80.3 (1962), pp. 648–662. DOI: `10.1088/0370-1328/80/3/310`. (Visited on 03/14/2022).

[93] T. Evans. "A Study of the Transformation of Diamond to Graphite". In: *Proc. R. Soc. Lond. A* 277 (1963), pp. 260–269. DOI: `10.1098/rspa.1964.0020`.

[94] G. Davies. "Graphitization of Diamond at Zero Pressure and at a High Pressure". In: *Proc. R. Soc. Lond. A* 328.1574 (1972), pp. 413–427. DOI: `10.1098/rspa.1972.0086`. (Visited on 03/14/2022).

[95] T. Evans and C. Phaal. "The Kinetics Of The Diamond - Oxygen Reaction". In: *Proceedings of the Fifth Conference on Carbon*. Elsevier, 1962, pp. 147–153. DOI: `10.1016/B978-0-08-009707-7.50025-X`. (Visited on 03/14/2022).

[96] C. E. Johnson, M. A. S. Hasting, and W. A. Weimer. "Thermogravimetric Analysis of the Oxidation of CVD Diamond Films". In: *J. Mater. Res.* 5.11 (1990), pp. 2320–2325. DOI: `10.1557/JMR.1990.2320`. (Visited on 03/14/2022).

[97] A. Joshi, R. Nimmagadda, and J. Herrington. "Oxidation Kinetics of Diamond, Graphite, and Chemical Vapor Deposited Diamond Films by Thermal Gravimetry". In: *Journal of Vacuum Science & Technology A: Vacuum, Surfaces, and Films* 8.3 (1990), pp. 2137–2142. DOI: `10.1116/1.577028`. (Visited on 03/14/2022).

[98] C. Q. Sun et al. "Preferential Oxidation of Diamond {111}". In: *J. Phys. D: Appl. Phys* 33 (2000), pp. 2196–2199. DOI: 10.1088/0022-3727/33/17/316.

[99] J.-C. Pu, S.-H. Wang, and J. C. Sung. "High-Temperature Oxidation Behaviors of CVD Diamond Films". In: *Applied Surface Science* 256.3 (2009), pp. 668–673. DOI: 10.1016/j.apsusc.2009.08.042. (Visited on 03/14/2022).

[100] J.-C. Pu, S.-F. Wang, and J. C. Sung. "High-Temperature Oxidation Behavior of Nanocrystalline Diamond Films". In: *Journal of Alloys and Compounds* 489.2 (2010), pp. 638–644. DOI: 10.1016/j.jallcom.2009.09.140. (Visited on 03/14/2022).

[101] T. Ando et al. "Vapour-Phase Oxidation of Diamond Surfaces in O2 Studied by Diffuse Reflectance Fourier-transform Infrared and Temperature-programmed Desorption Spectroscopy". In: *Journal of the Chemical Society, Faraday Transactions* 89 (1993), pp. 3635–3640. DOI: 10.1039/FT9938903635.

[102] P. E. Pehrsson, T. W. Mercer, and J. A. Chaney. "Thermal Oxidation of the Hydrogenated Diamond (100) Surface". In: *Surface Science* 497.1-3 (2002), pp. 13–28. DOI: 10.1016/S0039-6028(01)01677-6. (Visited on 03/14/2022).

[103] J. M. Wheeler, R. A. Oliver, and T. W. Clyne. "AFM Observation of Diamond Indenters after Oxidation at Elevated Temperatures". In: *Diamond and Related Materials* 19.11 (2010), pp. 1348–1353. DOI: 10.1016/j.diamond.2010.07.004. (Visited on 03/14/2022).

[104] C. A. Schuh, J. K. Mason, and A. C. Lund. "Quantitative Insight into Dislocation Nucleation from High-Temperature Nanoindentation Experiments". In: *Nature Mater* 4.8 (2005), pp. 617–621. DOI: 10.1038/nmat1429. (Visited on 03/03/2021).

[105] O. Franke, J. C. Trenkle, and C. A. Schuh. "Temperature Dependence of the Indentation Size Effect". In: *J. Mater. Res.* 25.7 (2010), pp. 1225–1229. DOI: 10.1557/JMR.2010.0159. (Visited on 10/08/2020).

[106] P. Baral et al. "In Situ Characterization of AA1050 Recrystallization Kinetics Using High Temperature Nanoindentation Testing". In: *Materials & Design* 152 (2018), pp. 22–29. DOI: 10.1016/j.matdes.2018.04.053. (Visited on 09/24/2020).

[107] Extrudesign. *Principal Metallic Crystal Structures BCC, FCC, and HCP*. https://extrudesign.com/princ
metallic-crystal-structures-bcc-fcc-and-hcp/. 2022.

[108] Université le Mans. *Liaison Chimique et Empilements*. http://ressources.univ-lemans.fr/AccesLibre/UM
2005.

[109] Wikipedia. *Dislocation*. https://en.wikipedia.org/wiki/Dislocation.

[110] K.-I. Ikeda et al. "Grain Boundary Structure of Ultrafine Grained Pure Copper Fabricated by Accumulative Roll Bonding". In: *Mater Trans* 49 (2008), pp. 24–30. DOI: 10.2320/matertrans.ME200715.

[111] E. Orowan. In: *Zeitschrift für Physik* 89 (1934), pp. 605–613, 614–633, 634–659.

[112] M. Polanyi. In: *Zeitschrift für Physik* 89 (1934), p. 660.

[113] G. I. Taylor. "The Mechanism of Plastic Deformation of Crystals. Part I.—Theoretical". In: *Proceedings of the Royal Society of London. Series A, Containing Papers of a Mathematical and Physical Character* 145.855 (1934), pp. 362–387. DOI: 10.1098/rspa.1934.0106. (Visited on 08/26/2022).

[114] E. O. Hall. "The Deformation and Ageing of Mild Steel: III Discussion of Results". In: *Proc. Phys. Soc. B* 64.9 (1951), pp. 747–753. DOI: 10.1088/0370-1301/64/9/303. (Visited on 09/05/2022).

[115] G. Saada. "Sur le durcissement dû à la recombinaison des dislocations". In: *Acta Metallurgica* 8.12 (1960), pp. 841–847. DOI: 10.1016/0001-6160(60)90150-4. (Visited on 09/05/2022).

[116] M. Verdier, Y. Brechet, and P. Guyot. "Recovery of AlMg Alloys: Flow Stress and Strain-Hardening Properties". In: *Acta Mater.* 47.1 (1998), pp. 127–134. DOI: 10.1016/S1359-6454(98)00350-4. (Visited on 01/27/2021).

[117] J. Friedel. *Dislocations.* Vol. 3. PERGAMON PRESS, 1964.

[118] F. J. Humphreys and M. Hatherly. *Recrystallization and Related Annealing Phenomena.* Elsevier, 2004. DOI: 10.1016/B978-0-08-044164-1.X5000-2. (Visited on 10/14/2020).

[119] L. E. Murr. *Interfacial Phenomena in Metals and Alloys.* United States: Addison-Wesley Publishing Company, Reading, MA, 1975.

[120] E. Nes. "Recovery Revisited". In: *Acta Metall. Mater.* 43.6 (1995), pp. 2189–2207. DOI: 10.1016/0956-7151(94)00409-9.

[121] M. Richou et al. "Recrystallization at High Temperature of Two Tungsten Materials Complying with the ITER Specifications". In: *Journal of Nuclear Materials* 542 (2020), p. 152418. DOI: 10.1016/j.jnucmat.2020.152418. (Visited on 10/21/2020).

[122] N. Bozzolo, S. Jacomet, and R. E. Logé. "Fast In-Situ Annealing Stage Coupled with EBSD: A Suitable Tool to Observe Quick Recrystallization Mechanisms". In: *Materials Characterization* 70 (2012), pp. 28–32. DOI: 10.1016/j.matchar.2012.04.020. (Visited on 10/14/2020).

[123] L. Karanja et al. "An Attempt to Assess Recovery/Recrystallization Kinetics in Tungsten at High Temperature Using Statistical Nanoindentation Analysis". In: *Crystals* 11.1 (2020), p. 37. DOI: 10.3390/cryst11010037. (Visited on 03/17/2022).

[124] C. Kerisit et al. "EBSD Coupled to SEM in Situannealing for Assessing Recrystallization and Grain Growth Mechanisms in Pure Tantalum". In: *Journal of Microscopy* 250.3 (2013), pp. 189–199. DOI: 10.1111/jmi.12034. (Visited on 03/17/2022).

[125] M. A. Lopez-Sanchez et al. "Dislocation-Driven Recrystallization in AZ31B Magnesium Alloy Imaged by Quasi-in Situ EBSD in Annealing Experiments". In: *Materials Characterization* 165 (2020), p. 110382. DOI: 10.1016/j.matchar.2020.110382. (Visited on 03/17/2022).

[126] D. Kuhlmann, G. Masing, and J. Raffelsieper. “Zur Theorie Der Erholung”. In: *International Journal of Materials Research* 40.7 (1949), pp. 241–246. DOI: `10.1515/ijmr-1949-400701`.

[127] J. Go et al. “Modelling Recovery and Recrystallisation during Annealing of AA 5754 Aluminium Alloy”. In: *Mater. Sci. Technol.* 19.10 (2003), pp. 1361–1368. DOI: `10.1179/026708303225005980`. (Visited on 08/23/2021).

[128] M. Seyed Salehi and N. Anjabin. “Modeling and Experimental Study of Static Recovery and Mechanical Behavior of AA5052 Alloy During Cold-Working and Subsequent Annealing”. In: *Iran. J. Mater. Form.* 4.1 (2017), pp. 28–38. DOI: `10.22099/ijmf.2017.3997`.

[129] W. A. Johnson and R. F. Mehl. “Reaction Kinetics in Processes of Nucleation and Growth”. In: *Transactions of the American Institute of Mining and Metallurgical Engineers* 135 (1939), pp. 416–442.

[130] A. Kolmogoroff. “Zur Statistik der Kristallisationsvorgange in Metallen”. In: *Izv. Akad. Nauk SSSR Ser. Mat.* 1.3 (1937), pp. 355–359.

[131] M. Avrami. “Kinetics of Phase Change. I General Theory”. In: *J. Chem. Phys.* 7.12 (1939), pp. 1103–1112. DOI: `10.1063/1.1750380`. (Visited on 08/31/2021).

[132] M. J. Starink and A.-M. Zahra. “An Analysis Method for Nucleation and Growth Controlled Reactions at Constant Heating Rate”. In: *Thermochimica Acta* 292.1-2 (1997), pp. 159–168. DOI: `10.1016/S0040-6031(96)03135-8`. (Visited on 12/07/2020).

[133] J. Farjas and P. Roura. “Modification of the Kolmogorov–Johnson–Mehl–Avrami Rate Equation for Non-Isothermal Experiments and Its Analytical Solution”. In: *Acta Materialia* 54.20 (2006), pp. 5573–5579. DOI: `10.1016/j.actamat.2006.07.037`. (Visited on 12/07/2020).

[134] F. M. B. Fernandes, S. Denis, and A. Simon. “Mathematical Model Coupling Phase Transformation and Temperature Evolution during Quenching of Steels”. In: *Mater. Sci. Technol.* 1 (1985), pp. 838–844. DOI: `10.1179/mst.1985.1.10.838`.

[135] R. A. Vandermeer and N. Hansen. “Recovery Kinetics of Nanostructured Aluminum: Model and Experiment”. In: *Acta Mater.* 56.19 (2008), pp. 5719–5727. DOI: `10.1016/j.actamat.2008.07.038`. (Visited on 01/27/2021).

[136] J. C. Qiao and J. M. Pelletier. “Dynamic Mechanical Relaxation in Bulk Metallic Glasses: A Review”. In: *Journal of Materials Science & Technology* 30.6 (2014), pp. 523–545. DOI: `10.1016/j.jmst.2014.04.018`. (Visited on 07/04/2022).

[137] Centre national de la recherche scientifique (France) and Societe francaise de physique, eds. *Les Amorphes Metalliques: Ecole d’hiver, Aussois, 13-22 Janvier 1983.* Les Ulis, France: Editions de physique, 1984.

[138] J. M. Pelletier and B. Van de Moortèle. "Mechanical Properties of Bulk Metallic Glasses: Elastic, Visco-Elastic and Visco-Plastic Components in the Deformation". In: *Journal of Non-Crystalline Solids* 353.32-40 (2007), pp. 3750–3753. DOI: 10.1016/j.jnoncrysol.2007.05.141. (Visited on 07/04/2022).

[139] J. M. Barandiarán et al. "Free Volume Driven Crystallization in Metallic Glasses". In: *Thermochimica Acta* 63.2 (1983), pp. 255–260. DOI: 10.1016/0040-6031(83)80091-4. (Visited on 07/04/2022).

[140] H. S. Chen and D. Turnbull. "Evidence of a Glass–Liquid Transition in a Gold–Germanium–Silicon Alloy". In: *J. Chem. Phys.* 48.6 (1968), pp. 2560–2571. DOI: 10.1063/1.1669483. (Visited on 07/04/2022).

[141] W. L. Johnson. "Bulk Amorphous Metal—An Emerging Engineering Material". In: *JOM* 54.3 (2002), pp. 40–43. DOI: 10.1007/BF02822619. (Visited on 07/04/2022).

[142] M. F. Ashby and A. L. Greer. "Metallic Glasses as Structural Materials". In: *Scripta Materialia*. Viewpoint Set No: 37. On Mechanical Behavior of Metallic Glasses 54.3 (2006), pp. 321–326. DOI: 10.1016/j.scriptamat.2005.09.051. (Visited on 07/04/2022).

[143] W. H. Wang. "Bulk Metallic Glasses with Functional Physical Properties". In: *Advanced Materials* 21.45 (2009), pp. 4524–4544. DOI: 10.1002/adma.200901053. (Visited on 07/04/2022).

[144] J. Schroers. "Processing of Bulk Metallic Glass". In: *Advanced Materials* 22.14 (2010), pp. 1566–1597. DOI: 10.1002/adma.200902776. (Visited on 07/04/2022).

[145] T. G. Nieh et al. "Strain Rate-Dependent Deformation in Bulk Metallic Glasses". In: *Intermetallics* 10.11-12 (2002), pp. 1177–1182. DOI: 10.1016/S0966-9795(02)00146-2. (Visited on 07/04/2022).

[146] C. A. Schuh, A. C. Lund, and T. G. Nieh. "New Regime of Homogeneous Flow in the Deformation Map of Metallic Glasses: Elevated Temperature Nanoindentation Experiments and Mechanistic Modeling". In: *Acta Materialia* 52.20 (2004), pp. 5879–5891. DOI: 10.1016/j.actamat.2004.09.005. (Visited on 07/04/2022).

[147] C. A. Schuh, T. Hufnagel, and U. Ramamurty. "Mechanical Behavior of Amorphous Alloys". In: *Acta Materialia* 55.12 (2007), pp. 4067–4109. DOI: 10.1016/j.actamat.2007.01.052. (Visited on 07/04/2022).

[148] C. A. Schuh, T. G. Nieh, and Y. Kawamura. "Rate Dependence of Serrated Flow During Nanoindentation of a Bulk Metallic Glass". In: *J. Mater. Res.* 17.7 (2002), pp. 1651–1654. DOI: 10.1557/JMR.2002.0243. (Visited on 07/04/2022).

[149] B. Moser et al. "Observation of Instabilities during Plastic Deformation by In-Situ SEM Indentation Experiments". In: *Adv. Eng. Mater.* 7.5 (2005), pp. 388–392. DOI: 10.1002/adem.200500049. (Visited on 03/08/2022).

[150] K.-W. Chen et al. “A Study of the Relationship between Semi-Circular Shear Bands and Pop-Ins Induced by Indentation in Bulk Metallic Glasses”. In: *Intermetallics* 18.8 (2010), pp. 1572–1578. DOI: 10.1016/j.intermet.2010.04.010. (Visited on 03/08/2022).

[151] M. Heilmaier and J. Eckert. “Elevated Temperature Deformation Behavior of Zr-Based Bulk Metallic Glasses”. In: *Adv. Eng. Mater.* 7.9 (2005), pp. 833–841. DOI: 10.1002/adem.200500080. (Visited on 07/04/2022).

[152] J.-J. Pang et al. “Nanoindentation Study of Size Effect and Loading Rate Effect on Mechanical Properties of a Thin Film Metallic Glass Cu49.3Zr50.7”. In: *Physica B: Condensed Matter* 407.3 (2012), pp. 340–346. DOI: 10.1016/j.physb.2011.10.050. (Visited on 07/04/2022).

[153] M. Idriss et al. “Evolution of the Elastic Modulus of Zr–Cu–Al BMGs during Annealing Treatment and Crystallization: Role of Zr/Cu Ratio”. In: *Journal of Non-Crystalline Solids* 421 (2015), pp. 35–40. DOI: 10.1016/j.jnoncrysol.2015.04.028. (Visited on 10/14/2020).

[154] M. Apreutesei, A. Billard, and P. Steyer. “Crystallization and Hardening of Zr-40at.% Cu Thin Film Metallic Glass: Effects of Isothermal Annealing”. In: *Materials & Design* 86 (2015), pp. 555–563. DOI: 10.1016/j.matdes.2015.07.149. (Visited on 10/14/2020).

[155] J. Perez et al. “Viscoelastic And Plastic Behaviour Of Metallic And Other Glasses Near The Glass Transition”. In: *J. Phys. Colloques* 41.C8 (1980), pp. C8-850-C8–853. DOI: 10.1051/jphyscol:19808209. (Visited on 07/04/2022).

[156] G. V. Afonin et al. “Structural Relaxation and Related Viscous Flow of Zr–Cu–Al-based Bulk Glasses Produced from the Melts with Different Glass-Forming Ability”. In: *Intermetallics* 19.9 (2011), pp. 1298–1305. DOI: 10.1016/j.intermet.2011.04.012. (Visited on 07/04/2022).

[157] T. Cullinan et al. “Kinetics and Mechanisms of Isothermal Devitrification in Amorphous Cu50Zr50”. In: *Metall and Mat Trans A* 46.2 (2015), pp. 600–613. DOI: 10.1007/s11661-014-2661-y. (Visited on 07/04/2022).

[158] Q. Gao et al. “Crystallization Kinetics of the Cu50Zr50 Metallic Glass under Isothermal Conditions”. In: *Journal of Solid State Chemistry* 244 (2016), pp. 116–119. DOI: 10.1016/j.jssc.2016.09.023. (Visited on 10/14/2020).

[159] G. Feng and A. H. W. Ngan. “Effects of Creep and Thermal Drift on Modulus Measurement Using Depth-sensing Indentation”. In: *J. Mater. Res.* 17.3 (2002), pp. 660–668. DOI: 10.1557/JMR.2002.0094. (Visited on 07/08/2022).

[160] A. H. W. Ngan and B. Tang. “Viscoelastic Effects during Unloading in Depth-Sensing Indentation”. In: *J. Mater. Res.* 17.10 (2002), pp. 2604–2610. DOI: 10.1557/JMR.2002.0377. (Visited on 07/08/2022).

[161] A. H. W. Ngan et al. “Correcting Power-Law Viscoelastic Effects in Elastic Modulus Measurement Using Depth-Sensing Indentation”. In: *International Journal of Solids and Structures* 42.5-6 (2005), pp. 1831–1846. DOI: `10.1016/j.ijsolstr.2004.07.018`.

[162] P. Sudharshan Phani and W. C. Oliver. “A Critical Assessment of the Effect of Indentation Spacing on the Measurement of Hardness and Modulus Using Instrumented Indentation Testing”. In: *Materials & Design* 164 (2019), p. 107563. DOI: `10.1016/j.matdes.2018.107563`. (Visited on 10/01/2020).

[163] S. Spinner. “Elastic Moduli of Glasses at Elevated Temperatures by a Dynamic Method”. In: *Journal of The American Ceramic Society* 39.3 (1955), p. 6. DOI: `10.1111/j.1151-2916.1956.tb15634.x`.

[164] A. Polian, D. Vo-Thanh, and P. Richet. “Elastic Properties of A-SiO $_2$ up to 2300 K from Brillouin Scattering Measurements”. In: *Europhys. Lett.* 57.3 (2002), pp. 375–381. DOI: `10.1209/epl/i2002-00470-4`. (Visited on 07/21/2022).

[165] B. D. Beake and J. F. Smith. “High-Temperature Nanoindentation Testing of Fused Silica and Other Materials”. In: *Philosophical Magazine A* 82.10 (2002), pp. 2179–2186. DOI: `doi.org/10.1080/01418610208235727`.

[166] J. M. Wheeler et al. “Activation Parameters for Deformation of Ultrafine-Grained Aluminium as Determined by Indentation Strain Rate Jumps at Elevated Temperature”. In: *Materials Science and Engineering: A* 585 (2013), pp. 108–113. DOI: `10.1016/j.msea.2013.07.033`. (Visited on 10/12/2020).

[167] G. Simmons and H. Wang. *Single Crystal Elastic Constants and Calculated Aggregate Properties: A Handbook*. Cambridge, Mass., M.I.T. Press, 1971. (Visited on 09/29/2020).

[168] P. Ludwik. “Über Die Änderung Der Inneren Reibung Der Metalle Mit Der Temperatur”. In: *Zeitschrift für Physikalische Chemie* 91U.1 (1916), pp. 232–247. DOI: `10.1515/zpch-1916-9112`. (Visited on 10/19/2020).

[169] Z. Huang, L. Y. Gu, and J. R. Weertman. “Temperature Dependence of Hardness of Nanocrystalleve Copper in Low-Temperature Range”. In: *Scripta Materialia* 37.7 (1997), pp. 1071–1075. DOI: `10.1016/S1359-6462(97)00209-1`.

[170] P. S. Phani and W. C. Oliver. “A Direct Comparison of High Temperature Nanoindentation Creep and Uniaxial Creep Measurements for Commercial Purity Aluminum”. In: *Acta Materialia* 111 (2016), pp. 31–38. DOI: `10.1016/j.actamat.2016.03.032`. (Visited on 10/20/2020).

[171] O. D. Sherby and P. E. Armstrong. “Prediction of Activation Energies for Creep and Self-Diffusion from Hot Hardness Data”. In: *Metall Mater Trans B* 2.12 (1971), pp. 3479–3484. DOI: `10.1007/BF02811630`. (Visited on 10/20/2020).

[172] M.J. Mayo and W.D. Nix. "Measuring and Understanding Strain Rate Sensitive Deformation with the Nanoindenter". In: *Strength of Metals and Alloys (ICSMA 8)*. Elsevier, 1989, pp. 1415–1420. DOI: `10.1016/B978-0-08-034804-9.50224-2`. (Visited on 03/14/2023).

[173] R. Goodall and T.W. Clyne. "A Critical Appraisal of the Extraction of Creep Parameters from Nanoindentation Data Obtained at Room Temperature". In: *Acta Materialia* 54.20 (2006), pp. 5489–5499. DOI: `10.1016/j.actamat.2006.07.020`. (Visited on 03/14/2023).

[174] J. Dean et al. "A Procedure for Extracting Primary and Secondary Creep Parameters from Nanoindentation Data". In: *Mechanics of Materials* 65 (2013), pp. 124–134. DOI: `10.1016/j.mechmat.2013.05.014`. (Visited on 03/14/2023).

[175] J. Dean et al. "A Critical Assessment of the "Stable Indenter Velocity" Method for Obtaining the Creep Stress Exponent from Indentation Data". In: *Acta Materialia* 80 (2014), pp. 56–66. DOI: `10.1016/j.actamat.2014.07.054`. (Visited on 03/14/2023).

[176] Xiazi Xiao and Long Yu. "Effect of Primary Creep on the Relationship between Indentation and Uniaxial Creep: A Theoretical Model". In: *International Journal of Solids and Structures* 206 (2020), pp. 114–123. DOI: `10.1016/j.ijsolstr.2020.09.017`. (Visited on 03/14/2023).

[177] J. Chua et al. "High-Temperature Nanoindentation Size Effect in Fluorite Material". In: *International Journal of Mechanical Sciences* 159 (2019), pp. 459–466. DOI: `10.1016/j.ijmecsci.2019.06.020`. (Visited on 04/20/2021).

[178] P. Baral et al. "Indentation Creep vs. Indentation Relaxation: A Matter of Strain Rate Definition?" In: *Materials Science and Engineering: A* 781 (2020), p. 139246. DOI: `10.1016/j.msea.2020.139246`. (Visited on 09/24/2020).

[179] Z. Y. Liang, S. S. Xiang, and G. M. Pharr. "Effects of Crystal Orientation on the Indentation Creep of β-Tin". In: *Journal of Materials Research* 36.12 (2021), pp. 2434–2443. DOI: `10.1557/s43578-021-00165-x`. (Visited on 11/21/2022).

[180] A. F. Bower et al. "Indentation of a Power Law Creeping Solid". In: *Proc. R. Soc. Lond. A* 441.1911 (1993), pp. 97–124. DOI: `10.1098/rspa.1993.0050`.

[181] G. Guillonneau et al. "Nanomechanical Testing at High Strain Rates: New Instrumentation for Nanoindentation and Microcompression". In: *Materials & Design* 148 (2018), pp. 39–48. DOI: `10.1016/j.matdes.2018.03.050`. (Visited on 10/26/2022).

[182] D. L. Deadmore. "Hardness of CaF2 and BaF2 Solid Lubricants at 25 to 670 °C". In: *NASA Technical Memorandum* (1987).

[183] N. Miyazaki et al. "Birefringence Simulations of Annealed Ingot of Calcium Fluoride Single Crystal by Considering Creep Behavior of Ingot during Annealing Process". In: *2009 4th International Microsystems, Packaging, Assembly and Circuits Technology Conference*. Taipei, Taiwan: IEEE, 2009, pp. 2–5. DOI: `10.1109/IMPACT.2009.5382295`. (Visited on 04/20/2021).

[184] K. Kishan Rao and D. B. Sirdeshmukh. “Microhardness and Interatomic Binding in Some Cubic Crystals”. In: *Bull. Mater. Sci.* 5.5 (1983), pp. 449–452. DOI: 10.1007/BF02743923. (Visited on 10/25/2022).

[185] W. L. Phillips. “Deformation and Fracture Processes in Calcium Fluoride Single Crystals”. In: *Journal of The American Ceramic Society* 44.10 (1961), p. 8. DOI: 10.1111/j.1151-2916.1961.tb13713.x.

[186] Q. Zhang and J. C. Lambropoulos. “Residual Stress Model for CaF $_2$”. In: *J. Mater. Res.* 22.10 (2007), pp. 2796–2808. DOI: 10.1557/JMR.2007.0348. (Visited on 10/26/2022).

[187] J. B. O’Neill, B. A. W. Redfern, and C. A. Brookes. “Anisotropy in the Hardness and Friction of Calcium Fluoride Crystals”. In: *Journal Of Materials Science* 8 (1973), pp. 47–58. DOI: 10.1007/BF00755582.

[188] A. Aruga et al. “Mechanical Properties of CaF $_2$ Single Crystal Substrates Determined from Nanoindentation Techniques”. In: *MRS Proc.* 436 (1996), p. 213. DOI: 10.1557/PROC-436-213. (Visited on 10/25/2022).

[189] M. A. Lodes et al. “Influence of Dislocation Density on the Pop-in Behavior and Indentation Size Effect in CaF2 Single Crystals: Experiments and Molecular Dynamics Simulations”. In: *Acta Materialia* 59.11 (2011), pp. 4264–4273. DOI: 10.1016/j.actamat.2011.03.050. (Visited on 03/08/2022).

[190] P. Sadrabadi, K. Durst, and M. Göken. “Study on the Indentation Size Effect in CaF2: Dislocation Structure and Hardness”. In: *Acta Materialia* 57.4 (2009), pp. 1281–1289. DOI: 10.1016/j.actamat.2008.11.015. (Visited on 09/13/2022).

[191] G. Guillonneau et al. “Plastic Flow Under Shear-Compression at the Micron Scale-Application on Amorphous Silica at High Strain Rate”. In: *JOM* 74.6 (2022), pp. 2231–2237. DOI: 10.1007/s11837-021-05142-7. (Visited on 11/04/2022).

[192] P. S. Phani et al. “On the Measurement of Hardness at High Strain Rates by Nanoindentation Impact Testing”. In: *Journal of the Mechanics and Physics of Solids* 170 (2023), p. 105105. DOI: 10.1016/j.jmps.2022.105105. (Visited on 11/04/2022).

[193] G. A. Keig and R. L. Coble. “Mobility of Edge Dislocations in Single-Crystal Calcium Fluoride”. In: *Journal of Applied Physics* 39.13 (1968), pp. 6090–6095. DOI: 10.1063/1.1656121. (Visited on 11/03/2022).

[194] S. R. Mekala. “Analysis of Creep Transients in Calcium Fluoride Single Crystals Following Stress Changes”. Doctoralthesis. Friedrich-Alexander-Universität Erlangen-Nürnberg (FAU), 2006.

[195] P. Sadrabadi et al. “Evolution of Dislocation Structure and Deformation Resistance in Creep Exemplified on Single Crystals of CaF2”. In: *Materials Science and Engineering A* 510–511 (2009), pp. 16/50. DOI: 10.1016/j.msea.2008.04.086.

[196] A. G. Evans. “Thermally Activated Dislocation Motion in Ceramic Materials”. In: *Deformation of Ceramic Materials*. Ed. by R. C. Bradt and R. E. Tressler. Boston, MA: Springer US, 1975, pp. 127–149. DOI: `10.1007/978-1-4613-4431-5_5`. (Visited on 09/19/2022).

[197] P. Feltham and R. Ghosh. “High-Temperature Stress Relaxation of CaF2 Crystals”. In: *Phys. Stat. Sol. (a)* 5.1 (1971), pp. 279–284. DOI: `10.1002/pssa.2210050130`. (Visited on 11/03/2022).

[198] D. Caillard and J.-L. Martin. *Thermally Activated Mechanisms in Crystal Plasticity*. Pergamon Materials Series 8. Amsterdam ; Boston, Mass: Pergamon, 2003.

[199] C. Tian, G. Dehm, and C. Kirchlechner. “Influence of Strain Rate on the Activation of {110}, {112}, {123} Slip in Ferrite of DP800”. In: *Materialia* 15 (2021), p. 100983. DOI: `10.1016/j.mtla.2020.100983`. (Visited on 11/21/2022).

[200] A. S. Khan et al. “Strain Rate Effect of High Purity Aluminum Single Crystals: Experiments and Simulations”. In: *International Journal of Plasticity* 67 (2015), pp. 39–52. DOI: `10.1016/j.ijplas.2014.10.002`. (Visited on 11/21/2022).

[201] V. Maier et al. “Microstructure-Dependent Deformation Behaviour of Bcc-Metals – Indentation Size Effect and Strain Rate Sensitivity”. In: *Philosophical Magazine* 95.16-18 (2015), pp. 1766–1779. DOI: `10.1080/14786435.2014.982741`. (Visited on 11/21/2022).

[202] P. El Ters and M. A. Shehadeh. “On the Strain Rate Sensitivity of Size-Dependent Plasticity in BCC Iron at Elevated Temperatures: Discrete Dislocation Dynamics Investigation”. In: *Mechanics of Materials* 148 (2020), p. 103494. DOI: `10.1016/j.mechmat.2020.103494`. (Visited on 11/21/2022).

[203] A. Munoz, A. Dom, and J. Castaing. “Slip Systems and Plastic Anisotropy in CaF2”. In: *Journal Of Materials Science* 29 (1994), pp. 6207–6211. DOI: `10.1007/BF00354561`.

[204] K. Kishan Rao and D. B. Sirdeshmukh. “Indentation Studies on Alkaline Earth Fluoride Crystals at Elevated Temperatures”. In: *Pramana* 34 (1990), pp. 151–156. DOI: `10.1007/BF02847199`.

[205] S. H. Goods and W. D. Nix. “The Coalescence of Large Grain Boundary Cavities in Silver during Tension Creep”. In: *Acta Metallurgica* 26.5 (1978), pp. 753–758. DOI: `10.1016/0001-6160(78)90025-1`. (Visited on 09/13/2022).

[206] R. W. Logan, R. G. Castro, and A. K. Mukherjee. “Mechanical Properties of Silver at Low Temperatures”. In: *Scripta Metallurgica* 17.1 (1983), pp. 63–66. DOI: `10.1016/0036-9748(83)90071-6`.

[207] M. E. Kassner. “The Rate Dependence and Microstructure of High-Purity Silver Deformed to Large Strains between 0.16 and 0.30 Tm”. In: *Metallurgical Transactions A volume* 20 (1989), pp. 2001–2010. DOI: `10.1007/BF02650286`.

[208] R. P. Carreker. “Tensile Deformation of Silver as a Function of Temperature, Strain Rate, and Grain Size”. In: *JOM* 9.1 (1957), pp. 112–115. DOI: 10.1007/BF03398466. (Visited on 09/19/2022).

[209] F. Bachmann, R. Hielscher, and H. Schaeben. “Grain Detection from 2d and 3d EBSD Data—Specification of the MTEX Algorithm”. In: *Ultramicroscopy* 111.12 (2011), pp. 1720–1733. DOI: 10.1016/j.ultramic.2011.08.002. (Visited on 10/28/2020).

[210] F. J. Humphreys. “Review Grain and Subgrain Characterisation by Electron Backscatter Diffraction”. In: *Journal of Materials Science* 36.16 (2001), pp. 3833–3854. DOI: 10.1023/A:1017973432592. (Visited on 12/08/2022).

[211] A. Lens, C. Maurice, and J. H. Driver. “Grain Boundary Mobilities during Recrystallization of Al–Mn Alloys as Measured by in Situ Annealing Experiments”. In: *Materials Science and Engineering: A* 403.1 (2005), pp. 144–153. DOI: 10.1016/j.msea.2005.05.010. (Visited on 10/14/2020).

[212] S. Primig et al. “Influence of the Heating Rate on the Recrystallization Behavior of Molybdenum”. In: *Mater. Sci. Eng. A* 535 (2012), pp. 316–324. DOI: 10.1016/j.msea.2011.12.099. (Visited on 07/01/2021).

[213] Y. Wang et al. “Influence of Cold Rolled Deformation Degree and Heating Rates on Crystallite Dimension and Recrystallization Fraction of Aluminum Plates”. In: *Crystals* 11.11 (2021), p. 1428. DOI: 10.3390/cryst11111428. (Visited on 12/09/2022).

[214] C. Schäfer, V. Mohles, and G. Gottstein. “Modeling of Non-Isothermal Annealing: Interaction of Recrystallization, Recovery, and Precipitation”. In: *Acta Materialia* 59.17 (2011), pp. 6574–6587. DOI: 10.1016/j.actamat.2011.07.003. (Visited on 12/09/2022).

[215] A. Durif. “Modélisation de la durée de vie de composants face au plasma dans les réacteurs à fusion thermonucléaire”. PhD thesis. Mines Saint Etienne, 2019.

[216] R. Eberhart and J. Kennedy. “A New Optimizer Using Particle Swarm Theory”. In: *MHS’95. Proceedings of the Sixth International Symposium on Micro Machine and Human Science*. Nagoya, Japan: IEEE, 1995, pp. 39–43. DOI: 10.1109/MHS.1995.494215. (Visited on 06/15/2021).

[217] J. Kennedy and R. Eberhart. “Particle Swarm Optimization”. In: *Proceedings of ICNN’95 - International Conference on Neural Networks*. Vol. 4. Perth, WA, Australia: IEEE, 1995, pp. 1942–1948. DOI: 10.1109/ICNN.1995.488968. (Visited on 06/15/2021).

[218] P. J. Angeline. “Using Selection to Improve Particle Swarm Optimization”. In: *1998 IEEE International Conference on Evolutionary Computation Proceedings. IEEE World Congress on Computational Intelligence (Cat. No.98TH8360)*. Anchorage, AK, USA: IEEE, 1998, pp. 84–89. DOI: 10.1109/ICEC.1998.699327. (Visited on 06/15/2021).

[219] Y. Shi and R. Eberhart. “A Modified Particle Swarm Optimizer”. In: *1998 IEEE International Conference on Evolutionary Computation Proceedings. IEEE World Congress on Computational Intelligence (Cat. No.98TH8360)*. Anchorage, AK, USA: IEEE, 1998, pp. 69–73. DOI: `10.1109/ICEC.1998.699146`. (Visited on 06/15/2021).

[220] X. Xu et al. “Incremental Particle Swarm Optimization”. In: *Physics Procedia* 24 (2012), pp. 1369–1376. DOI: `10.1016/j.phpro.2012.02.204`. (Visited on 06/15/2021).

[221] A. M. Wusatowska-Sarnek, H. Miura, and T. Sakai. “Influence of Deformation Temperature on Microstructure Evolution and Static Recrystallization of Polycrystalline Copper”. In: *Materials Transactions* 42.11 (2001), pp. 2452–2459. DOI: `10.2320/matertrans.42.2452`.

[222] E. A. Jägle and E. J. Mittemeijer. “The Kinetics of and the Microstructure Induced by the Recrystallization of Copper”. In: *Metall and Mat Trans A* 43.4 (2012), pp. 1117–1131. DOI: `10.1007/s11661-011-0959-6`. (Visited on 09/16/2022).

[223] W. Pantleon. “Thermal Stability of the Microstructure in Rolled Tungsten for Fusion Reactors”. In: *Phys. Scr.* 96.12 (2021), p. 124036. DOI: `10.1088/1402-4896/ac2854`. (Visited on 01/14/2022).

[224] G. Benchabane et al. “Recrystallization of Pure Copper Investigated by Calorimetry and Microhardness”. In: *Materials Characterization* 59.10 (2008), pp. 1425–1428. DOI: `10.1016/j.matchar.2008.01.002`. (Visited on 09/16/2022).

[225] A. Pérez et al. “Isoconversional Analysis of Copper Recrystallization”. In: *J Therm Anal Calorim* 125.2 (2016), pp. 667–672. DOI: `10.1007/s10973-016-5307-z`. (Visited on 09/16/2022).

[226] F. Richard, M. Villars, and S. Thibaud. “Viscoelastic Modeling and Quantitative Experimental Characterization of Normal and Osteoarthritic Human Articular Cartilage Using Indentation”. In: *J. Mech. Behav. Biomed. Mater.* 24 (2013), pp. 41–52. DOI: `10.1016/j.jmbbm.2013.04.012`. (Visited on 09/09/2021).

[227] S. Breumier et al. “High Strain Rate Micro-Compression for Crystal Plasticity Constitutive Law Parameters Identification”. In: *Mater. Des.* 193 (2020), p. 108789. DOI: `10.1016/j.matdes.2020.108789`. (Visited on 09/09/2021).

[228] S. Breumier. https://github.com/simonBreumier/Play_with_I.git. GitHub. 2020.

[229] S. Comby-Dassonneville et al. “Real-Time High-Temperature Scanning Indentation: Probing Physical Changes in Thin-Film Metallic Glasses”. In: *Applied Materials Today* 24 (2021), p. 101126. DOI: `10.1016/j.apmt.2021.101126`. (Visited on 08/19/2021).

[230] J. R. Jinschek. “Advances in the Environmental Transmission Electron Microscope (ETEM) for Nanoscale in Situ Studies of Gas–Solid Interactions”. In: *Chem. Commun.* 50.21 (2014), pp. 2696–2706. DOI: `10.1039/C3CC49092K`. (Visited on 10/18/2022).

[231] Z. Zhang and J. Xie. “Influence of Relaxation and Crystallization on Micro-Hardness and Deformation of Bulk Metallic Glass”. In: *Materials Science and Engineering: A* 407.1 (2005), pp. 161–166. DOI: `10.1016/j.msea.2005.07.020`. (Visited on 10/14/2020).

[232] R. Saha and W. D. Nix. “Effects of the Substrate on the Determination of Thin Film Mechanical Properties by Nanoindentation”. In: *Acta Materialia* 50.1 (2002), pp. 23–38. DOI: `10.1016/S1359-6454(01)00328-7`. (Visited on 10/18/2022).

[233] N. Tayebi, A. A. Polycarpou, and T. F. Conry. “Effects of Substrate on Determination of Hardness of Thin Films by Nanoscratch and Nanoindentation Techniques”. In: *J. Mater. Res.* 19.6 (2004), pp. 1791–1802. DOI: `10.1557/JMR.2004.0233`. (Visited on 10/18/2022).

[234] P. Wesseling, B. C. Ko, and J. J Lewandowski. “Quantitative Evaluation of α-Al Nano-Particles in Amorphous Al87Ni7Gd6—Comparison of XRD, DSC, and TEM”. In: *Scripta Materialia* 48.11 (2003), pp. 1537–1541. DOI: `10.1016/S1359-6462(03)00127-1`. (Visited on 11/25/2022).

[235] S. Gravier et al. “Evaluation of the Crystal Volume Fraction in a Partially Nanocrystallized Bulk Metallic Glass”. In: *Journal of Alloys and Compounds*. 16th International Symposium on Metastable, Amorphous and Nanostructured Materials 504 (2010), S226–S229. DOI: `10.1016/j.jallcom.2010.05.008`. (Visited on 11/25/2022).

[236] P. Coddet et al. “On the Elastic Modulus and Hardness of Co-Sputtered Zr–Cu–(N) Thin Metal Glass Films”. In: *Surface and Coatings Technology* 206.17 (2012), pp. 3567–3571. DOI: `10.1016/j.surfcoat.2012.02.036`. (Visited on 10/19/2022).

[237] M. Apreutesei et al. “Zr–Cu Thin Film Metallic Glasses: An Assessment of the Thermal Stability and Phases’ Transformation Mechanisms”. In: *Journal of Alloys and Compounds* 619 (2015), pp. 284–292. DOI: `10.1016/j.jallcom.2014.08.253`. (Visited on 10/19/2022).

[238] P. Zeman et al. “Amorphous Zr-Cu Thin-Film Alloys with Metallic Glass Behavior”. In: *Journal of Alloys and Compounds* 696 (2017), pp. 1298–1306. DOI: `10.1016/j.jallcom.2016.12.098`. (Visited on 10/19/2022).

[239] C. A. Pampillo. “Flow and Fracture in Amorphous Alloys”. In: *J Mater Sci* 10.7 (1975), pp. 1194–1227. DOI: `10.1007/BF00541403`. (Visited on 10/20/2022).

[240] G. Abrosimova et al. “The Structure and Mechanical Properties of Bulk Zr50Ti16.5Cu15Ni18.5 Metallic Glasses”. In: *Journal of Materials Science* 36.16 (2001), pp. 3933–3939. DOI: `10.1023/A:1017918121205`. (Visited on 10/20/2022).

[241] T. C. Hufnagel. “Preface to the Viewpoint Set on Mechanical Behavior of Metallic Glasses”. In: *Scripta Materialia*. Viewpoint Set No: 37. On Mechanical Behavior of Metallic Glasses 54.3 (2006), pp. 317–319. DOI: `10.1016/j.scriptamat.2005.10.004`. (Visited on 10/20/2022).

[242] T. W. Tang et al. "On Thermomechanical Properties of Au–Ag–Pd–Cu–Si Bulk Metallic Glass". In: *Materials Chemistry and Physics* 116.2 (2009), pp. 569–572. DOI: 10.1016/j.matchemphys.2009.04.032. (Visited on 12/14/2022).

[243] L. Yang and J. L. Thomason. "The Thermal Behaviour of Glass Fibre Investigated by Thermomechanical Analysis". In: *J Mater Sci* 48.17 (2013), pp. 5768–5775. DOI: 10.1007/s10853-013-7369-7. (Visited on 12/14/2022).

[244] J. C. Qiao et al. "Structural Heterogeneities and Mechanical Behavior of Amorphous Alloys". In: *Progress in Materials Science* 104 (2019), pp. 250–329. DOI: 10.1016/j.pmatsci.2019.04.005. (Visited on 10/21/2022).

[245] O. Glushko et al. "Exceptional Fracture Resistance of Ultrathin Metallic Glass Films Due to an Intrinsic Size Effect". In: *Sci Rep* 9.1 (2019), p. 8281. DOI: 10.1038/s41598-019-44384-z. (Visited on 11/28/2022).

[246] C. A. Schuh and T. G. Nieh. "A Nanoindentation Study of Serrated Flow in Bulk Metallic Glasses". In: *Acta Materialia* 51.1 (2003), pp. 87–99. DOI: 10.1016/S1359-6454(02)00303-8. (Visited on 11/28/2022).

[247] C. A. Schuh and T. G. Nieh. "A Survey of Instrumented Indentation Studies on Metallic Glasses". In: *Journal of Materials Research* 19.1 (2004), p. 4. DOI: 10.1557/jmr.2004.19.1.46. (Visited on 11/28/2022).

[248] T. Burgess and M. Ferry. "Nanoindentation of Metallic Glasses". In: *Materials Today* 12.1 (2009), pp. 24–32. DOI: 10.1016/S1369-7021(09)70039-2. (Visited on 11/28/2022).

[249] C. A. Schuh. "Nanoindentation Studies of Materials". In: *Materials Today* 9.5 (2006), pp. 32–40. DOI: 10.1016/S1369-7021(06)71495-X. (Visited on 11/28/2022).

[250] Y. I. Golovin et al. "Serrated Plastic Flow during Nanoindentation of a Bulk Metallic Glass". In: *Scripta Materialia* 45.8 (2001), pp. 947–952. DOI: 10.1016/S1359-6462(01)01116-2. (Visited on 11/28/2022).

[251] W. H. Jiang and M. Atzmon. "Rate Dependence of Serrated Flow in a Metallic Glass". In: *Journal of Materials Research* 18.4 (2003), pp. 755–757. DOI: 10.1557/JMR.2003.0103. (Visited on 11/28/2022).

[252] A. L. Greer et al. "Nanoindentation Studies of Shear Banding in Fully Amorphous and Partially Devitrified Metallic Alloys". In: *Materials Science and Engineering: A* 375–377 (2004), pp. 1182–1185. DOI: 10.1016/j.msea.2003.10.032. (Visited on 11/28/2022).

[253] A. L. Greer. "Metallic Glasses…on the Threshold". In: *Materials Today* 12.1 (2009), pp. 14–22. DOI: 10.1016/S1369-7021(09)70037-9. (Visited on 11/28/2022).

[254] D. Xing et al. "The Characterization of Plastic Flow in Three Different Bulk Metallic Glass Systems". In: *Journal of Alloys and Compounds* 433.1 (2007), pp. 318–323. DOI: 10.1016/j.jallcom.2006.06.077. (Visited on 11/28/2022).

[255] F. Faupel et al. "Diffusion in Metallic Glasses and Supercooled Melts". In: *Rev. Mod. Phys.* 75.1 (2003), pp. 237–280. DOI: 10.1103/RevModPhys.75.237. (Visited on 11/28/2022).

[256] H. B. Yu et al. “Correlation between $\ensuremath{\beta}$ Relaxation and Self-Diffusion of the Smallest Constituting Atoms in Metallic Glasses”. In: *Phys. Rev. Lett.* 109.9 (2012), p. 095508. DOI: `10.1103/PhysRevLett.109.095508`. (Visited on 11/28/2022).

[257] J. M. Wheeler, R. Raghavan, and J. Michler. “In Situ SEM Indentation of a Zr-based Bulk Metallic Glass at Elevated Temperatures”. In: *Materials Science and Engineering: A* 528.29-30 (2011), pp. 8750–8756. DOI: `10.1016/j.msea.2011.08.057`. (Visited on 11/25/2022).

[258] S. Gravier et al. “Sensitivity of Viscoplastic and Viscoelastic Properties to Nanocrystallization in a Zr Bulk Metallic Glass”. In: *Reviews on Advanced Materials Science* 18.2 (2008), pp. 144–148.

[259] H. Okamoto. “Section III: Supplemental Literature Review”. In: *JPE* 19.5 (1998), pp. 486–486. DOI: `10.1007/BF02700865`. (Visited on 11/22/2022).

[260] H. R. Wang et al. “Crystallization Processes in Amorphous Zr54Cu46 Alloy”. In: *Journal of Non-Crystalline Solids* 311.1 (2002), pp. 36–41. DOI: `10.1016/S0022-3093(02)01326-1`. (Visited on 11/22/2022).

[261] N. Zou et al. “Thermodynamic Assessment and Glass Forming Ability Prediction of the Zr-Fe-Cu System”. In: *Calphad* 64 (2019), pp. 175–184. DOI: `10.1016/j.calphad.2018.12.007`. (Visited on 11/22/2022).

[262] T. Yamamoto et al. “Precipitation of the ZrCu B2 Phase in Zr50Cu50–xAlx (x = 0, 4, 6) Metallic Glasses by Rapidly Heating and Cooling”. In: *Journal of Materials Research* 25.4 (2010), pp. 793–800. DOI: `10.1557/JMR.2010.0105`. (Visited on 11/22/2022).

[263] S. Kirkpatrick, C. D. Gelatt, and M. P. Vecchi. “Optimization by Simulated Annealing”. In: *Science* 220.4598 (1983), pp. 671–680. DOI: `10.1126/science.220.4598.671`.

[264] A. Collin and B. Batiot. “Chapitre 8. OPTIMISATION DE PARAMETRES”. In: (2018), p. 12.

[265] X. Garrido. “Méthode d’optimisation : Simulated Annealing ou le “recuit simulé””. In: (), p. 6.

[266] S. Forrest. “Genetic Algorithms”. In: *ACM Computing Surveys* 28.1 (1996). DOI: `10.1145/234313.234350`.

[267] M. Mitchell. “Genetic Algorithms: An Overview”. In: *SIGEVOlution* 8.2 (2016), pp. 4–4. DOI: `10.1145/2907674.2907678`. (Visited on 07/21/2022).

List of the author's publications

Articles

- P. Baral et al. "Indentation Creep vs. Indentation Relaxation: A Matter of Strain Rate Definition?" In: *Materials Science and Engineering: A* 781 (2020), p. 139246. DOI: `10.1016/j.msea.2020.139246`.
- G. Tiphéne et al. "High-Temperature Scanning Indentation: A New Method to Investigate in Situ Metallurgical Evolution along Temperature Ramps". In: *Journal of Materials Research* 36 (2021), pp. 2383–2396. DOI: `10.1557/s43578-021-00107-7`.
- S. Comby-Dassonneville et al. "Real-Time High-Temperature Scanning Indentation: Probing Physical Changes in Thin-Film Metallic Glasses". In: *Applied Materials Today* 24 (2021), p. 101126. DOI: `10.1016/j.apmt.2021.101126`.

dernière page de la thèse

AUTORISATION DE SOUTENANCE

Vu les dispositions de l'arrêté du 25 mai 2016 modifié par l'arrêté du 26 août 2022,

Vu la demande du directeur de thèse

Monsieur J-L. LOUBET

et les rapports de

Mme S. KORTE-KERZEL
Professeure - RWTH Aachen University - Templergraben 55 - 52053 Aachen - Allemagne

et de

M. G-M. PHARR
Professeur - Texas A&M University College of Engineering - 3127 TAMU College Station TX USA

Madame TIPHENE Gabrielle

est autorisée à soutenir une thèse pour l'obtention du grade de **DOCTEUR**

Ecole doctorale Mécanique, Energétique, Génie Civil, Acoustique

Fait à Ecully, le 20 février 2023

Pour le directeur de l'Ecole centrale de Lyon
Le directeur de la Recherche

Christophe CORRE